Production and investigation of quasi-two-dimensional Bose gases

Steffen Patrick Rath

To cite this version:

Steffen Patrick Rath. Production and investigation of quasi-two-dimensional Bose gases. Atomic Physics [physics.atom-ph]. Université Pierre et Marie Curie - Paris VI, 2010. English. NNT : . tel-00469991

HAL Id: tel-00469991
https://theses.hal.science/tel-00469991

Submitted on 2 Apr 2010

Doctoral thesis
at Université Pierre et Marie Curie

Specialty: Quantum Physics

Presented by
Steffen Patrick RATH

In partial fulfillment of the requirements to obtain the title of
Docteur de l'Université Pierre et Marie Curie

Production and investigation of quasi-two-dimensional Bose gases

Thesis defence date: February 19th, 2010

Members of the dissertation committee:

Antoine BROWAEYS	Rapporteur
Hélène PERRIN	Rapporteur
Roland COMBESCOT	Examinateur
Wilhelm ZWERGER	Examinateur
Jean DALIBARD	Supervisor

Alles Vergängliche
Ist nur ein Gleichnis;
Das Unzulängliche,
Hier wirds Ereignis

JOHANN WOLFGANG
VON GOETHE (1749–1832)
Faust II, Act V

Contents

Preface

> If we offend, it is with our good will.
> That you should think, we come not to offend,
> But with good will. To show our simple skill,
> That is the true beginning of our end.
> Consider then, we come but in despite.
> We do not come, as minding to content you,
> Our true intent is. All for your delight
> We are not here. That you should here repent you,
> The actors are at hand; and, by their show,
> You shall know all, that you are like to know.
>
> WILLIAM SHAKESPEARE (1564–1616)
> *A Midsummer Night's Dream, Act V, Scene 1*

RESEARCH on ultracold atoms has given new vigour to the investigation of quantum many-body systems ever since the first realisations of Bose-Einstein condensates (BECs) in dilute atomic vapours [1, 2]. Before, BECs have usually been associated with superfluid helium. The connection between superfluidity and Bose-Einstein condensation has first been mentioned by London [3, 4]. However, superfluid helium is a strongly interacting system so that the condensed fraction is low and difficult to measure—an experimental determination of the condensate fraction using neutron diffraction by Sears and Svensson dates from 1979 [5].

In this respect, BECs in dilute atomic gases were not the first BECs to be discovered, but they were much closer to Einstein's original idea of a condensate [6] in that they were only weakly interacting (and thus closer to the ideal gas than superfluid helium) so that they could be described quite satisfactorily by a macroscopic wave function [7] governed by a nonlinear Schrödinger equation, the celebrated Gross-Pitaevskii equation [8, 9]. During the first years of experimental research on Bose-Einstein condensates, the main focus consequently lay on phenomena that can be well described within this framework, such as collective oscillations, coherence properties and the behaviour of quantised vortices which provide striking evidence for the superfluidity of Bose-Einstein condensates. Exhaustive reviews of this research may be found in [10, 11, 12, 13][1].

---

[1] It should be mentioned that the study of ultracold atoms is not restricted to bosonic isotopes: the first realisation of a degenerate Fermi gas was reported in 1999 [14], and the research of these system has attracted ever more interest in the meantime (see, *e.g.* [15] for a recent review).

In the following, the interest shifted back towards more strongly correlated systems (see [16] for a review) with the idea in mind to take advantage of the diverse manipulation methods offered by atomic physics to simulate problems from less accessible systems such as solids, where the word "simulation" is meant in the broader sense as used by Feynman [17]. Since dilute gases are intrinsically weakly correlated, one has to subject them to an appropriate external influence to obtain strongly correlated regimes. An example is the rapid rotation of an anisotropic trap [18, 19], that could ultimately lead to strongly correlated vortex phases [20]. A second means is provided by Feshbach resonances which permit to tune the atomic interaction strength using an external magnetic field. Their use was first reported in 1998 [21, 22], theoretical propositions to this effect have been made even earlier (see, *e.g.* [23]). The use of Feshbach resonances permitted amongst other things to achieve Bose-Einstein condensation of molecules made up by two fermions [24, 25] and study the associated regime of the BEC-BCS crossover [26].

Still another way to obtain strongly correlated states was pointed out by Jaksch *et al.* in 1998 [27]: using far-detuned laser beams, one can create versatile potentials for neutral atoms which are caused by the dipole force. In particular, such potentials permit the creation of optical lattices which mimic the structure of a solid. This was used by the Munich group to demonstrate the quantum phase transition from a superfluid to a Mott isolator four years later [28].

Another possible application for optical lattices—or optical dipole potentials in general—is the confinement of the atomic sample in a geometry of reduced dimensionality. For this work, it is above all the aspect of reduced dimensionality that is important. The possibility of realising ultracold Bose gases in lower-dimensional traps has first been considered by Bagnato and Kleppner in 1987 [29]. The earliest experimental data on this subject dates from 2001 when the MIT group first demonstrated trapping geometries in which the level spacing in one or more direction approaches the thermal energy [30]. Greater aspect ratios permitting to enter more deeply the low-dimensional regime were reported in 2004 when two different groups succeeded in realising deeply one-dimensional (1d) [31] and two-dimensional (2d) [32] Bose gases.

There is a considerable variety of methods for the production of quasi-two-dimensional samples: Rychtarik *et al.* used a gravito-optical trap using an evanescent wave [32]. Orzel *et al.* used a one-dimensional optical lattice to slice up a BEC into an array of quasi-two-dimensional Bose gases [33], a technique that was later adopted by our group [34]. The first production of a deeply 2d Bose gas using an optical plus magnetic potential as in our recent experiments has been reported by Smith *et al.* in 2005 [35]. Another successful method for the production of low-dimensional Bose gases is the use of radio-frequency dressed potentials [36, 37, 38].

Up to now, two-dimensional Bose gases have been used to study such diverse phenomena as the superfluid-Mott transition [39, 40] and the Berezinskii-Kosterlitz-Thouless transition [41] as well as the behaviour in the critical region around the latter [42, 43]. The work described in this manuscript follows the latter line of research, with the focus on the equation of state.

My thesis work was carried out in the cold atoms group at Laboratoire Kastler Brossel under the supervision of Jean Dalibard. The present manuscript is divided into two parts. The first part describes what may be seen as the aftermath of the finished construction of a new experimental setup (the construction itself has been described in detail by my predecessors [44, 45]). In particular, it describes experimental techniques that we elaborated during the first year of operation as well as prospective studies regarding possible future uses of the setup. Most of the latter material is still prospective at the end of my thesis work. However this is not the case for the preliminary studies of phase plates for the creation of versatile dipole potentials presented in chapter 4 which are a direct preparation for the second part—even more so since it simultaneously prepares the ground for the discussion of our imaging optics in chapter 7.

Moreover, we describe the first experiment that has been attempted with our new setup: the realisation of an isotropic harmonic trap to verify a longstanding prediction by Ludwig Boltzmann [46] concerning the non-damping of the breathing mode of a classical gas confined in such a potential. Even if we did not succeed in pushing this study to its very end, it permitted us to learn a lot about the way our setup is working so that it is worthwhile describing our findings in some detail.

The second part describes experiments on quasi-two-dimensional Bose gases that have been carried out during the first half of 2009 on our new setup. Originally, the purpose was a direct measurement of the equation of state of the quasi-two-dimensional Bose gas. Unlike the three-dimensional one, the two-dimensional equation of state is a directly measurable quantity since when taking images one does not need to take into account the integration over the imaging axis. Such a measurement should be directly comparable to theoretical predictions [47, 48]. Our results show significant deviations from theory—and since two independently derived predictions agree very well with each other, it is safe to assume that both are correct—so our focus gradually shifted to an analysis of the differences between experiment and theory and their possible reasons. At first, we suspected the effects to be caused by imperfections of the imaging optics which would be a somewhat prosaic explanation the plausibility of which is investigated in chapter 7. The result being essentially negative, we now suppose that the observed effects are caused by the high atomic density of our samples so that the object of study has shifted to the interaction of flat and dense atomic samples with resonant light. Since these last developments coincided with the end of my thesis, they are presented here as far as we were able to progress.

Part I

Experimental techniques

Introduction

> Haueisen, mer stahel und scher,
> wetzstein; vernemt, wan er gestemt,
> wil ich euch weiter weisen.
>
> HANS SACHS (1494–1576)
> *Der rock*

EXPERIMENTAL physics may be seen as a craft, in both the literal and the figurative sense of the word. Not only is the construction of an experimental apparatus (as well as all ulterior modifications of the same) done by hand, but also one has first to pass through a phase of "apprenticeship" to master the usage of the apparatus which is made up of a multitude of different tools. This apprenticeship applies not only to the individual experimentalist but also to the team as a whole when it concerns a new setup.

This metaphor is quite appropriate to describe the work done during the first half of my thesis which will be described in the present part of this thesis. Since the construction of our setup has begun in 2006, the basic construction process is well finished and has been described in detail by my predecessors [44, 45], but it has taken a certain time to fully apprehend the working of the apparatus, from both the principal and the practical point of view.

The four chapters of this part can be divided into two categories: on the one hand, concrete experimental work (chapters 1, 3 and the last sections of chapter 4) and on the other hand , theoretical studies to explore the possibilities of the setup (chapter 2 and the major part of chapter 4).

Chapter 1 gives a rather succinct presentation of the basic experimental apparatus which is necessary for the comprehension of actual experiments described in later chapters. Chapter 2 is a summary of theoretical studies concerning the possibilities offered by the Time-averaged Orbiting Potential (TOP) trap used on our setup. Most of the material is well known, with the exception of an extensive discussion of a method to create anisotropies of arbitrary rotational symmetry by means of rapid phase modulation which is original.

The first experiment we attempted on the new setup is described in chapter 3: using gravity, it should in principle be possible to create a completely isotropic TOP trap, permitting to verify a peculiar phenomenon in the physics of the classical Boltzmann equation: the breathing mode of a classical gas trapped in an isotropic harmonic trap should be undamped. While we were not able to reach our experimental goal, we made considerable progress in this direction and gained valuable insight into the working details of the experimental apparatus.

Finally, chapter 4 is a preliminary study (both theoretical and experimental) for the experiments presented in the second part of this thesis: using phase plates, *i.e.* plates which imprint a given phase distribution on an incident light field, one may create a multitude of intensity distributions which can be used to create versatile trapping potentials for cold atoms. The chapter describes in detail the effects of four different types of such phase plates (which correspond to the plates actually at our disposition) and presents measurements done on the real counterparts. In order to prepare the ground for the discussion of the effect of imperfections in the imaging optics in chapter 7 in the second part of this thesis, chapter 4 begins with some extensive reminders on light propagation within the paraxial approximation and Gaussian beams.

Chapter One

The experimental apparatus

My liege, and madam, to expostulate
What majesty should be, what duty is,
Why day is day, night is night, and time is time,
Were nothing but to waste night, day, and time.
Therefore, since brevity is the soul of wit,
And tediousness the limbs and outward flourishes,
I will be brief.

WILLIAM SHAKESPEARE (1564–1616)
Hamlet, Act II, Scene 2

ALL the work described in this thesis revolves around our group's experimental setup. The original conception of the setup has been described in Baptiste Battelier's PhD thesis [44], but the actual realisation has changed considerably in the meantime. A description of the experiment in its current state is given in Marc Cheneau's PhD thesis [45], the actual design of the modifications has mainly been carried out by Tarik Yefsah. With these modifications, we were able to produce a first BEC in February 2008 and then gradually pass from the phase of understanding and mastering the basic functioning of the setup[1] to its actual usage for new experiments.

While it is necessary for the comprehension of the following chapters to provide an overview of the setup and its principal characteristics, it would be superfluous to reproduce in detail what has already been written in previous theses. We will thus limit ourselves to a summary of the most important aspects of the setup in its present state, referring the reader to Baptiste Battelier's PhD thesis [44] for general design considerations and technical choices and to Marc Cheneau's thesis [45] for details of the experimental sequence permitting to reach the quantum degenerate regime on this setup. In addition to this summary, we will describe some details regarding the coils around the science cell and the security electronics which have not been characterised in the above-mentioned works.

---

[1] The setup still underwent a certain number of modifications in the year following the first BEC before reaching the state described by Marc Cheneau. In the course of this chapter, we will state differences regarding the data in chapter 3 which has been taken directly after the first condensate.

1.1 Overview of the setup

The general idea of the setup is that of a two chamber system: a first chamber to trap an atomic sample and perform preliminary cooling, and a second one, the "science cell", in which cooling is continued until the regime of quantum degeneracy is reached, preparing the ground for actual experiments.

The separation into two distinct chambers has the advantage of decoupling the used "tools", thus freeing a maximum of access to the science cell for experimental work. However, it entails the necessity of transferring the atoms from the first to the second chamber. This is achieved by using a magnetic transport system following the model of the Munich group [49].

A to-scale drawing of the setup (vacuum chamber, omitting the pumps and part of the tubing, and coil holders) is given in figure 1.1, including an indication of the principal constituents the usage of which will be explained briefly in what follows.

Preparation of an atomic sample

The following paragraphs are in essence a summary of the far more detailed description in Marc Cheneau's PhD thesis up to some minor differences.

All our sequences start with a magneto-optical trap (MOT) [50] charged from a background vapour of ^{87}Rb in the MOT chamber (to the left in figure 1.1). The MOT consists of six cooling beams detuned by $-21\,$MHz with respect to the $F=2 \mapsto F'=3$ transition and six repumping beams tuned to the $F=1 \mapsto F'=2$ transition. Its magnetic field gradient is $6.8\,$G/cm (on the axis of symmetry). Since the writing of Marc Cheneau's PhD thesis, the loading time of the MOT has been prolonged to $30\,$s to give the magnetic trap around the science cell more time to cool down after each cycle.

The MOT is then compressed [51] by increasing the cooling beams' detuning and decreasing their intensity (as well as the one of the repumping beams) in $10\,$ms while maintaining a constant gradient. Once the final values are reached, they are kept constant for another $10\,$ms. This permits to reach the regime of sub-Doppler cooling [52, 53] and to cool the cloud down to about $40\,\mu$K.

An optical pumping phase of $1\,$ms follows which transfers up to 80% of the atoms into the $F=2, m_F=2$ hyperfine state which is the most strongly confined in a magnetic trap (see chapter 2 for a short review of magnetic trapping). The atoms are magnetically trapped by rapidly ramping up a quadrupole field using a second, more powerful supply connected to the MOT coils, then magnetically transported [49] over to the science cell in $5.6\,$s. The transport takes place in a narrow tube to which two ion pumps are connected, forming a differential pumping stage. Thus, the vacuum in the science cell is far better than the one in the MOT chamber. We have measured atom life times of at least $80\,$s.

In the science cell, the atoms shall be loaded into a TOP trap (see chapters 2 and 3 for a detailed description of this trap type). Since a TOP trap is quite shallow, this necessitates antecedent cooling of the sample which is achieved using radio-frequency (rf) evaporation in the quadrupole at maximum gradient for $10\,$s. The TOP trap is then switched on at maximum current while the quadrupole gradient is reduced. Once the atoms are loaded into the TOP,

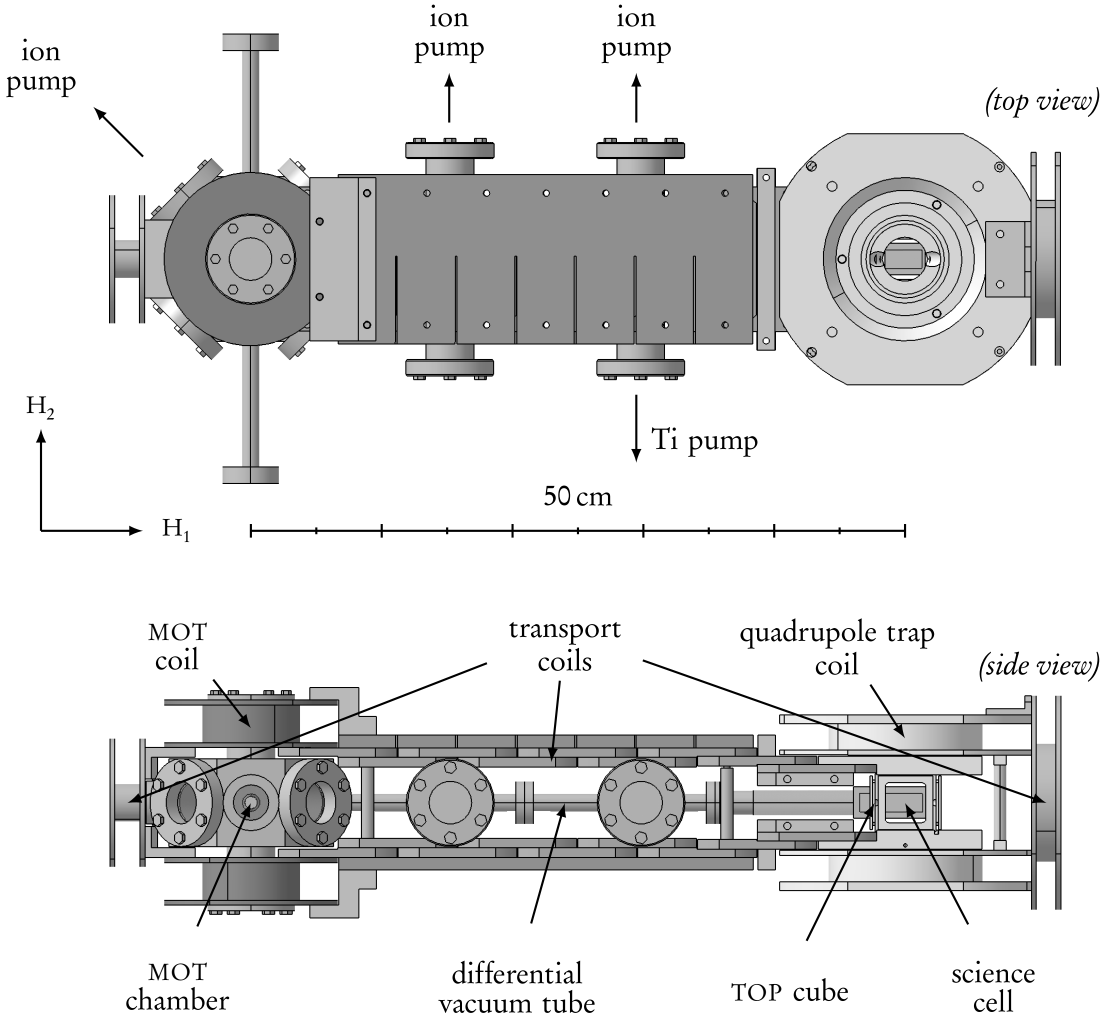

FIGURE 1.1: *Top and side view of the basic experimental apparatus with indication of the most important elements. Photographs of the real setup would be considerably less clear since the view would be obstructed by a multitude of cables, optics elements and cooling water tubes.*

a second rf cooling phase of 30 s follows during which the TOP and quadrupole currents are reduced.

This sequence permits the creation of a BEC [1, 2] with typically about 10^5 atoms which constitutes the starting point for actual experiments (evidently, not all possible experiments require a BEC to start off, so one can equally stop the evaporation sooner and work on a cold albeit non degenerate sample).

When the experiment as such is terminated, an image of the atomic sample is taken using the technique of absorption imaging (see chapter 6 for a short discussion of this technique) along either a horizontal or the vertical axis. The imaging may take place "in situ", *i.e.* with the magnetic trap still switched on, or after a ballistic expansion of up to 36 ms (so-called "Time Of Flight" (TOF) measurement) which, depending on the nature of the sample, permits a "magnification" of the atomic cloud (as in the case of a three-dimensional BEC) or the observation of momentum distribution in the trap (in the case of a thermal gas for $\omega\tau \gg 1$, where τ is the TOF duration, and ω the trapping frequency.

Around the science cell

The science cell, as is clear from its name, is the very place where actual experiments on the atomic sample take place. In order to enhance the possibilities, we have strived for a maximum of means to manipulate the cloud. This means on the one hand that optical access was the primary design priority and on the other hand that we tried to accommodate as many independent coil pairs as possible in the space close to the cell. These fall into two categories: the quadrupole coil pair on the one hand, of which there cannot be more than one by its sheer size, and a set of smaller coils wound on a plastic cube surrounding the cell (the TOP cube), or otherwise placed in its direct vicinity.

A list of this second kind of coils is given in table 1.1, specifying the names given to them, the coil pair's axis of symmetry, the number of windings and the magnetic field produced per unit current in the cube's centre[2]. The directions of space in the laboratory are labeled in the following way: the axis of the magnetic transport is called H_1, the horizontal axis perpendicular to it H_2 and the vertical axis V.

Such a number of coils may seem abusive, but they are rapidly put to use: the TOP coils are reserved for the generation of the rotating field, the "internal" coils on the vertical axis for the generation of the rf field used for evaporative cooling. The other coils may be used for the compensation of the magnetic field at the location of the atoms (on all three axes, a priori), the compensation of the gravitational "sag" of the TOP trap for low gradients (see chapter 3) and the excitation of oscillations of the atomic sample so that one rapidly runs short on available coils. Indeed, it has already happened more than once that we introduced a temporary supplementary coil on one of the horizontal axes.

The current in the TOP coils is produced using two stereo audio amplifiers (Crest CPX 2600), one for each coil pair. In bridged mode (where both channels are used in series), each amplifier has a nominal power of 1.5 kW and requires a minimum impedance of 4 Ω at its output. The

---

[2] The data in chapter 3 was taken with a slightly different version of the cube which had less and different coils that do not appear in table 1.1.

Name	axis	windings	B/I (G/A)
TOP	H_1, H_2	6	0.95
Bonus	H_1, H_2	1	0.16*
Circular	V	6	0.82
Internal	V	3	0.48*
External	V	4	0.63*

TABLE 1.1: *Coil pairs mounted on the plastic cube around the science cell with their axis, winding number and magnetic field (produced by the pair). The values marked with an asterisk are not measured, but inferred from the geometry (which comes close to that of the* TOP *coils) and the winding number.*

ohmic resistance of the coils being about 0.1 Ω and the inductive impedance being negligible for the experimentally relevant frequencies of some kHz, the major part of the power is dissipated in a water cooled 4 Ω series resistor. The actual power is considerably lower than the nominal one since the nominal power of audio amplifiers is attributed according to guidelines which are inspired by their primary usage, *i.e.* the reproduction of music with its typical spectral properties and fluctuations of loudness. A rule of thumb (communicated by a Crest technician) is to divide the nominal power by a factor of eight to obtain the power that can be continuously sustained with a sine signal. With our numbers, this means that in a continuous regime we can run currents with an amplitude of up to 10 A. When the input signal becomes too large, the CPX 2600 automatically reduces the gain to avoid clipping of the output signal, which is signalled by lighting up an LED on its front panel. The sine and cosine signals for the TOP trap are created by a programmable signal generator (Tabor WW 1072) which shall permit us to use the TOP trap also for more elaborate potentials (see chapter 2 for examples)[3].

The concept of the quadrupole coils at the science cell has changed radically between the original design [44] and the current one [45]: instead of compact, tightly wound coils with a lot of windings close to the science cell we now have considerably larger coils with less windings which are farther removed from the science cell to maximise optical access. Thus, to achieve comparable gradients, we need notably higher currents. Specifically, a gradient of 180 G/cm necessitates a current of 300 A. Taking into account the electrical resistivity of our coils, we need a total power of 12 kW to run such a current.

To this end, we use two 6 kW power supplies (SM 45-140 fabricated and custom-tuned to deliver 150 A each by the Delta Elektronika company) in parallel[4]. The switching of so large currents is outside the reach of the MOSFET technology we used up to then, so we opted for the

---

[3] The data presented in chapter 3 was taken before the acquisition of this generator. At that time, we used two function generators (Stanford Research Systems (SRS) DS 345), one for each coil pair, using the possibility to synchronize the clocks of the two generators to ensure a stable relative phase between the coil pairs. Unlike the Tabor generator, these two did not permit to have a reproducible initial phase from one experiment to the other since they run continuously and cannot be triggered.

[4] Actually, there was an intermediate version of the new magnetic trap with which the data presented in chapter 3 was taken. In this version, two 3 kW units (model SM 15-200 by the same company) were used in series, permitting to run currents up to 200 A.

usage of two IGBTs[5] (Mitsubishi CM 600 HA-24 H) in parallel, a technology well established in Christophe Salomon's group [54] who generously shared their knowledge with us (the overall disposition as well as the design of their driving circuit). With this system, we are capable of switching off the current in the coils within 500 µs. A single IGBT of the same type is used for the switching of the magnetic trap current in the MOT coils[6]. To dissipate the power, the coils are realised as hollow copper tubes that are water-cooled from the inside. To increase the flow, each coil is made up of two sub-coils each of which has its own cooling circuit.

1.2 Security electronics

Considering the power dissipated in the experiment and the fact that data acquisition series often have to run for hours without an experimenter present, the necessity of a security system that automatically shuts down all current sources in case of overheating goes without saying. An electronic system that was adapted to the first version of this setup has been described in [44] (and in [55] in more detail). This system has been largely revised in the course of the rebuilding of the setup in its current version. Most modifications are mere details of realisation, so we will not discuss them here. In return, there are two modifications related to an increased attention to the water cooling system which will be exposed in the following paragraphs.

The first modification is the introduction of flow meters (SWK 2108 and SWK 2118 fabricated by the Kobold company) on all arms of the water cooling circuit. These are equipped with reed relays that change their state when the flow falls below an adjustable threshold value. By connecting these relays to an appropriate electronic circuit, one can generate error flags that can be used to shut down the current sources in case of insufficient cooling water flow.

While a substantial reduction in cooling water flow is certainly a sufficient reason for an emergency shutdown, a constant flow is not enough to guarantee that all is well: in fact, despite our efforts, the cooling of the magnetic trap coils is still not enough to stabilise the temperature at a reasonable value at maximum current when 12 kW are dissipated. We therefore decided to monitor the cooling water temperature as well as its flow. In return, we do not measure any more the temperature of the coil holders as we did in the first version of the electronics [55]—such measurements are only feasible on even surfaces and the coils that are most susceptible to overheat do not permit to attach a temperature probe.

To monitor the cooling water temperature, we conceived an electronic device that reads out the temperature measured using a type LM 35 temperature probe, compares it to a manually adjustable reference temperature and creates an error flag as soon as the temperature exceeds its threshold. Since this is one of the more intricate of our home-made electronic circuits, it seems worthwhile to spend some paragraphs on an explanation of its working principle to facilitate future maintenance.

---

[5] Insulated-gate bipolar transistor, rugged devices for the fast switching of high currents.

[6] One should add that the magnetic field takes longer than this (typically some ms to disappear completely. We do not know whether this is due to eddy currents or to the existence of a second time scale in the switching process. The stated 500 ms are the typical time scale of the first part of the decay.

The basic idea of the device is the following: the LM 35 chip has an output voltage that is given by 10 mV/°C times the temperature. This voltage is then multiplied by an adjustable factor and the result fed into a Schmitt trigger[7]. The multiplication is done by a standard non-inverting operational amplifier circuit the gain of which is rendered adjustable by replacing one resistor by a potentiometer. In order for the device to be usable in practice, it must be possible to display the measured temperature as well as the user-set threshold value which is achieved using a DPM 340 LCD display. For reasons of compactness, we use the same display for both the measured temperature and the set threshold since there is no need to see them simultaneously. The essential part of the electronic circuit that serves to generate the signal sent to the Schmitt trigger and to display temperature and threshold is shown in figure 1.2 (of course, the whole circuit is somewhat larger, but the rest is straightforward).

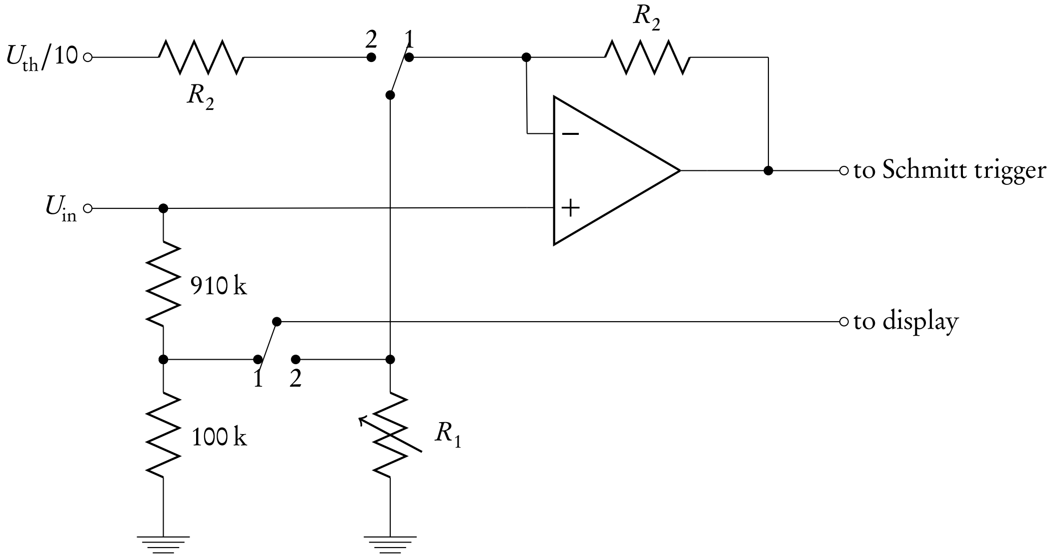

FIGURE 1.2: *Electronic circuit of the crucial part of the temperature security system. The two switches are operated by the same push button and change their state simultaneously. When the switches are in position 1, the temperature is measured and displayed. When they are in position 2, the threshold temperature is displayed and the measurement is suspended.*

The main component of this circuit is the operational amplifier used as a non-inverting amplifier [56]. Its amplification is given by $A = 1 + R_2/R_1$, where R_1 is chosen to be the potentiometer. The threshold temperature is thus given by $T_{th}/°\mathrm{C} = A^{-1} \times U_{th}/10\,\mathrm{mV}$. It increases with increasing R_1, *i.e.* when the user turns the potentiometer clockwise which is the intuitive sense. The threshold voltage U_{th} is a built-in property of the Schmitt trigger. For a

---

[7] A Schmitt trigger is an electronic device whose output is equal to the positive source voltage for input voltages below a fixed threshold value U_{th}, and equal to the negative source voltage for input voltages above that threshold. A special and useful property of Schmitt triggers is their hysteresis: the threshold is slightly lower when coming from above than when coming from below which avoids oscillations in the case of near-threshold signals.

source voltage of 15 V as used in our circuit, it is 8 V. We have chosen the values $R_1 = 0 \ldots 1\,\mathrm{k\Omega}$ and $R_2 = 10\,\mathrm{k\Omega}$ so that the threshold temperature can be varied between 0 and 73 °C.

The DPM 340 display is basically nothing but a digital voltmeter the scale of which can be changed with a set of jumpers at its rear. We chose a setting in which the number displayed is just the input voltage in millivolts. To correctly display the measured temperature, it is sufficient to pass the output voltage of the LM 35 chip by a 1/10 voltage divider. Likewise, the threshold temperature can be displayed by passing a tenth of the threshold voltage (corresponding to the 10 mV/°C) through a voltage divider made up of R_1 and R_2. Thus, one must arrange for the potentiometer to be part of the amplification and of the threshold display circuit. Our solution can be seen in figure 1.2: two switches operated by the same push button on the device's panel connect simultaneously the potentiometer to a tension divider and the display to the potentiometer. When this happens, the amplifier circuit becomes a voltage follower with unit gain which is smaller than all values that occur with connected potentiometer so that the Schmitt trigger will not change its state. This is important since otherwise each adjustment of the threshold temperature would result in an involuntary emergency shutdown of the power supplies.

This circuit is reproduced eight times to read out the signals from eight probes. The outputs are combined into a single error flag that is triggered as soon as one probe signals overheating. The whole device is subdivided into two groups of four, each with one display, a selector switch permitting to view any of the four temperatures and a set of push buttons (one per probe) to pass from temperature to threshold display. Overheating signals are visualised by a set of red LEDs.

For a reliable operation, there are two peculiarities of the LM 35 chip to be taken into account: firstly, the results become unreliable when the chip is connected by a cable that is more than some 10 cm long. It turns out this can be circumvented by putting a hefty capacitor (we use a 1 µF one) in parallel between the output and the ground pin in the direct vicinity of the chip. Secondly, these chips are primarily designed to measure the temperature of the ambient air (plastic package, no plane surface). For a reliable measurement one has to ensure that they are enclosed in a reasonably tight volume close to the body that shall be measured (in our case, some copper and brass pieces the cooling water runs through after the coils). Even so, the measured temperature will be somewhat below the temperature of the body which has to be taken into account when setting the threshold values.

Coming back from these quite technical issues to a larger perspective, the "basic" parts of the experiment have now stopped to be modified for more than one year so that we may assume that they have reached their definite state. After this overview of the experimental setup, the stage is set for discussing its actual use. We will expose experiments that have been performed on the setup in chapters 3 and 6. For each of these chapters, there is a second one (chapter 2 for chapter 3 and chapter 4 for chapter 6) that serves to "prepare the ground" by discussing underlying concepts.

Chapter Two

Creating versatile potentials using a TOP *trap*

> Das sehn wir auch den Rädern ab,
> den Rädern!
> Die gar nicht gerne stille stehn,
> Die sich mein Tag nicht müde drehn,
> Die Räder.
>
> WILHELM MÜLLER (1794–1827)
> *Die schöne Müllerin: 1. Das Wandern*

THE TOP (Time-averaged Orbiting Potential) trap was first used by Petrich *et al.* in 1994 [57] to circumvent the atom losses that cold samples trapped in a magnetic quadrupole field suffer due to Majorana spin flips. By adding a rapidly rotating homogeneous field to the quadrupole, they obtained a time-dependent potential in which the zero of the total magnetic field—the very cause of Majorana spin flips—is rotating around the atoms rather than sitting still in the middle of the cloud. At the same time, the resulting trapping potential is tightly confining, an essential property for the application of forced evaporative cooling. Indeed, the TOP trap permitted the group to create the first Bose-Einstein condensate [1] in a dilute atomic gas of rubidium atoms[1].

The flexibility and ease of use of the TOP have led our group to the decision of using this trap type on our new setup. In parallel with actual experimental work, I have carried out bibliographic research and proof-of-principle calculations to have an idea of the possibilities this trap offers. They are summarised in this chapter which is organised as follows: after some reminders on the principles of magnetic trapping, I reproduce the motivation for and the principle of the TOP trap as outlined in reference [57]. The following sections are devoted to possible future uses of this trap by generalising its working principle, such as the creation of rotating anisotropic potentials and radio frequency-dressed potentials. While most of the material in this chapter is essentially a bibliographic review, section 2.4 on the creation of higher-order anisotropies and their rotation presents original albeit unpublished calculations that I carried out based on Jean Dalibard's idea of using rapid phase modulation in a TOP trap. Throughout this chapter, I will neglect the influence of gravity. This is justified as long as the force caused by the vertical gradient of the quadrupole potential which is part of the TOP trap

---

[1] Shortly afterwards, the Ketterle group produced a sodium BEC using an optical "plug" for its quadrupole trap [2]. Later on, BECs were produced in purely magnetic, static traps of the Ioffe-Pritchard type [58]. It was not until 2001 that condensation could be achieved in a crossed-beam optical trap [59].

is considerably stronger than the gravitational force. I will discuss the role of gravity in some detail in the following chapter.

2.1 Magnetic trapping

A classical magnetic dipole $\boldsymbol{\mu}$ in a magnetic field $\boldsymbol{B}(\boldsymbol{r})$ has the potential energy $-\boldsymbol{\mu}\cdot\boldsymbol{B}(\boldsymbol{r})$ which gives rise to a "torque" that tries to align the magnetic moment with the magnetic field and to a force on the centre of mass of its carrier. In a homogeneous field only the "torque" is present, causing the magnetic moment to precess around the field direction with the *Larmor frequency* $\omega_{\mathrm{L}} = \boldsymbol{\mu}\cdot\boldsymbol{B}/\hbar$. The force on the centre of mass is caused by the inhomogeneity of spatially varying fields. For a magnetic moment aligned with the magnetic field, it is proportional to the negative gradient of the field's modulus, *i.e.* it points towards regions of low field strength. Since the modulus of a magnetic field may have a minimum (but not a maximum according to Earnshaw's theorem), this permits to trap particles having a magnetic dipole moment with static magnetic fields.

In our experiment, the objects of interest are ^{87}Rb atoms with a mass of $m = 1.45\times 10^{-25}\,$kg and a state-dependent quantised magnetic moment $\mu = g_F m_F \mu_{\mathrm{B}}$, where g_F is the Landé factor and m_F the magnetic quantum number associated with the hyperfine level F while $\mu_{\mathrm{B}} = 9.27\times 10^{-24}\,$J/T is the Bohr magneton. For ^{87}Rb, due to the nuclear spin $I = 3/2$, there are two hyperfine states $F = 1, 2$ in the electronic ground state. The corresponding Landé factors are $g_1 = -1/2$ and $g_2 = +1/2$ [60], so that the states $F = 1, m_F = -1$ and $F = 2, m_F = +1, +2$ can be magnetically trapped since the projection of their magnetic moments on the magnetic field is positive. In our experiment, the atoms are optically pumped to the $F = 2, m_F = 2$ hyperfine state so that their magnetic moment equals μ_{B}.

The Larmor frequency corresponding to one Bohr magneton is $2\pi \times 1.4\,$MHz/G. Thus the time scale for spin alignment is typically very small compared to the time scale of the centre of mass motion even in quite weak magnetic fields. This leads in a natural way to the *adiabatic approximation*: as long as the variation of the magnetic field "seen" by an atom is slow compared to its Larmor frequency, one can assume that the spin projection on the local magnetic field follows adiabatically. The approximation breaks down when either the atom is too fast or the magnetic field strength is too low. If this is the case, the atom can undergo Landau-Zener type transitions [61, 62] to other (in general untrapped) hyperfine states and be lost from the trap. As long as the adiabatic approximation is valid (a theoretical investigation of the physics beyond the adiabatic approximation in a TOP trap has been made by Franzosi *et al.* [63]), the potential energy can be written in the form $-\mu|\boldsymbol{B}|$.

The simplest magnetic trap that one can imagine—and that is in fact a major building block of all existing static magnetic traps—is the quadrupole trap which one gets by running equal currents in opposite directions in two circular coils (so-called Anti-Helmholtz configuration in contrast to the Helmholtz configuration where the currents run in the same direction). To be explicit, let the axis between these two coils be the z axis with the origin in the centre of the configuration so that each coil is parallel to the xy plane. By symmetry, the magnetic field must vanish at the origin, and a power-law expansion of the field on the z axis may only have odd terms (whereas in the Helmholtz configuration only even terms appear): $B(z) = bz + cz^3 + \cdots$. For a pair of circular coils with radius R a distance d apart carrying a current I, a straightforward calculation from the Biot-Savart law yields

$$b = \frac{3}{4}\mu_0 I \frac{R^2 d}{(R^2 + d^2/4)^{5/2}} . \tag{2.1}$$

In the plane perpendicular to the axis, the field must vary linearly as well in order to satisfy Maxwell's equation $\nabla \cdot \boldsymbol{B} = 0$. By symmetry, the gradient must be the same in every direction of the plane and equal to half the vertical gradient. To first order, the field of a quadrupole trap can thus be written in the form

$$\boldsymbol{B} = \frac{b}{2}(x\boldsymbol{u}_x + y\boldsymbol{u}_y) - bz\boldsymbol{u}_z \quad \Longrightarrow \quad B = \frac{b}{2}\sqrt{x^2 + y^2 + 4z^2} . \tag{2.2}$$

The small parameter in the power-law expansion is $\Delta r \times d/(R^2 + d^2/4)$, where Δr is the distance from the centre of the trap. Since typical atomic samples are smaller than 1 mm while typical coil sizes are about 10 cm, this linear approximation is sufficient for all practical purposes. Actual realisations of quadrupole traps consist of a certain number of (approximately circular) windings carrying the same current. The total field is then obtained by summing up the contributions from all these windings.

2.2 *The basic* TOP *trap*

The quadrupole trap is both simple and tightly confining[2], but it has the major disadvantage that the magnetic field vanishes in the centre, and with it the Larmor frequency. Inside an ellipsoid whose size depends on the gradient and the temperature of the cloud, the rate of change of the direction of the magnetic field seen by the atom $\mathrm{d}/\mathrm{d}t\{\boldsymbol{B}[\boldsymbol{r}(t)]/|\boldsymbol{B}[\boldsymbol{r}(t)]|\}$ is comparable to the Larmor frequency. By considering the flux through this ellipsoid and making use of the Virial theorem, Petrich *et al.* estimate the loss rate due to spin flips to be characterised by the time $\tau \sim m\ell^2/\hbar$, where ℓ is the characteristic size of the cloud [57]. For ^{87}Rb, τ drops below one second when $\ell < 27\,\mu\mathrm{m}$. It turns out this makes Bose-Einstein condensation in a quadrupole trap impossible, since loss rates become too high before the temperature can be lowered sufficiently to reach the degenerate regime.

Now, the basic idea of the TOP trap is to move the zero of the magnetic field out of the atomic cloud, which is readily achieved by superimposing on the quadrupole a homogeneous magnetic field created with a pair of Helmholtz coils. But, as is clear from (2.2), this will only shift the potential without altering its form. Using two pairs of Helmholtz coils on perpendicular axes, one can generate a homogeneous field of magnitude B_0 the direction of

---

[2] The trapping potential seen by an atomic cloud of size ℓ scales as $(\ell/R_c)^n$, where R_c is the characteristic size of the coil configuration and n is the leading order of the potential [57]. According to what we said in the preceding section, ℓ/R_c is a small parameter, so higher order traps are less tightly confining than lower order ones.

which is rotating at a frequency ω. If we choose the axis of symmetry of the quadrupole as the axis of rotation, the total magnetic field reads

$$\boldsymbol{B}(t)=(bx/2-B_0\cos\omega t)\boldsymbol{u}_x+(by/2-B_0\sin\omega t)\boldsymbol{u}_y-bz\boldsymbol{u}_z\,, \tag{2.3}$$

its instantaneous modulus is

$$B(t)=\frac{br_0}{2}\left(1+\frac{x^2+y^2+4z^2}{r_0^2}-\frac{2}{r_0}(x\cos\omega t+y\sin\omega t)\right)^{1/2}\,, \tag{2.4}$$

where $r_0=2B_0/b$ is the radius of the circle on which the point of vanishing magnetic field is moving. Since atoms passing nearby this circle can undergo spin flips just as in the case of a stationary zero point, r_0 is also called the "radius of death".

If one chooses the frequency ω sufficiently high, the motion of the atoms is governed by a time-averaged potential. Expanding (2.4) up to second order in the spatial coordinates and calculating the average over one period $(\omega/2\pi)\int_0^{2\pi/\omega}\mathrm{d}t\,B(t)$, one obtains the effective modulus

$$B\simeq\frac{br_0}{2}\left(1+\frac{x^2+y^2+8z^2}{4r_0^2}\right)\,. \tag{2.5}$$

This is a harmonic, axially symmetric field[3] that gives rise to a trapping potential $U=g_Fm_F\mu_\mathrm{B}B=|m_F|\mu_\mathrm{B}B/2$ with the trapping frequencies

$$\omega_z=\left(\frac{|m_F|\mu_\mathrm{B}b^2}{2mB_0}\right)^{1/2}\quad;\quad\omega_\perp=\left(\frac{|m_F|\mu_\mathrm{B}b^2}{16mB_0}\right)^{1/2}=\frac{\omega_z}{2\sqrt{2}}\,. \tag{2.6}$$

The atomic cloud in such a trap is equally axially symmetric and slightly flattened with an aspect ratio of $1:2\sqrt{2}$. The trapping frequencies are directly proportional to the gradient and inversely proportional to the square root of the rotating field. For typical experimental values such as $b=100\,\mathrm{G/cm}$ and $B_0=5\,\mathrm{G}$, the radial frequency is 20.1 Hz and the axial one 56.9 Hz while the radius of death is 1 mm. Having calculated the trapping frequencies, one can check the consistency of the time averaging procedure. On our experiment, the TOP frequency is $\omega=2\pi\times10\,\mathrm{kHz}$, so we satisfy indeed the double constraint $\omega_{z,\perp}\ll\omega\ll\omega_L$ (with $\omega_L=2\pi\times1.4\,\mathrm{MHz}\times B_0/\mathrm{G}$) that is necessary in order for our equations to hold.

On first sight, it might seem inconsistent to derive a potential up to second order in the spatial coordinates using fields that are themselves only calculated up to first order. However, the length scales of the expansions are not the same: the fields are calculated to first order with respect to the extension of the coils while the quadratic expansion of the field is with respect to the radius of death which itself is small compared to the coils.

---

[3] This symmetry is due to the choice of the axis of rotation. One can in fact choose the axis of rotation perpendicular to the strong axis of the quadrupole to obtain a TOP trap with three distinct trapping frequencies [64, 65]. Generalising this principle, one may apply oscillating magnetic fields on three axes simultaneously to obtain a so-called zTOP which offers an increased control over the aspect ratio of the atomic cloud [66].

It is worthwhile to note a fundamental difference between the TOP trap and other dynamic traps such as the Paul trap for ions [67] and earlier ac magnetic trapping schemes for neutral atoms [68, 69, 70]: in those traps, the average of the potential actually vanishes—the trapping comes from an effective potential that arises from the interplay between the oscillating potential and a short timescale motion of the particles. Such an effective potential is equally present in the TOP and gives rise to a micromotion of the atoms that is superposed on the macroscopic motion governed by the average potential (see [71] for a detailed theoretical analysis and [72] for an experimental investigation): in short, the instantaneous quadrupole force acts as a centripetal force corresponding to a circular motion with velocity $v = \mu_B b/m\omega$. In practical use, the average potential dominates by far this effective potential so that we only consider the average here.

For the charging of the TOP trap, it is important to know its depth. It is reasonable to define the circle of death as the limit of the trap, so the depth is just the difference between the average potential on a point on this border, where the instantaneous magnetic field is equal to $2B_0|\cos\omega t|$, and the centre, where it is always equal to B_0. Averaging over one period yields

$$\Delta U = \frac{|m_F|\mu_B B_0}{2}\left(\frac{4}{\pi}-1\right) . \tag{2.7}$$

The trapping depth is independent of the gradient. In order for the TOP trap to be practicable, this depth must be sufficient to load an atomic sample from a quadrupole where it still has an appreciable life time. If we require the sample to have a temperature equivalent to one third of ΔU so that it will be well inside the trap, its FWHM extension in the xy plane in a quadrupole will be 128 µm at equal gradient. According to the estimations stated above, this corresponds to a life time of the order of ten seconds. Thus, it is plausible that the charging of a TOP from a quadrupole at equal gradient should be feasible, as is the case experimentally. It is clear from this discussion that the loading requires careful optimisation of the magnetic fields and the temperature for maximum efficiency.

Considering the possibilities of modern electronics, it is natural to wonder what kind of potentials can be realised using the same principles by applying wave forms more complicated than mere sines and cosines. In the following sections, we will discuss some examples of such potentials. To this end, it is convenient to note that the potential created by a given TOP configuration is entirely specified by the trajectory of the magnetic field's zero x_t, y_t, z_t. For the basic TOP trap discussed up to now, one has $x_t = 2B_0/b \times \cos\omega t$, $y_t = 2B_0/b \times \sin\omega t$ and $z_t = 0$. For the general case of arbitrary trajectories, the instantaneous magnetic field reads (to second order in the coordinates)

$$B(t) = \frac{b r_t}{2}\left(1 + \frac{x^2+y^2+4z^2}{2r_t^2} - \frac{x x_t + y y_t + 4 z z_t}{r_t^2} - \frac{(x x_t + z z_t + 4 z z_t)^2}{2r_t^4}\right) + \mathscr{O}[(x/r_t)^3] , \tag{2.8}$$

where $r_t^2 = x_t^2 + y_t^2 + 4z_t^2$. In order to be able to calculate meaningful averages, all three components of the trajectory should be periodic functions with a common period $2\pi/\omega$. If r_t

is not constant (which is the case whenever the trajectory does not move on a flattened ellipsoid with aspect ratio 2:1), the calculation of the averaged potential becomes computationally involved and may not be feasible to carry out analytically any more. In this chapter, we will only regard cases where r_t is at least approximately constant.

2.3 *Rigid rotation of a* TOP *trap*

Setting a quantum gas into rotation is a conceptually simple method to probe its superfluid properties: if the gas is superfluid, its velocity field $v = \hbar\nabla\phi/m$ must be irrotational, so angular momentum can only be built up by the nucleation of vortices with a quantised angular momentum around each vortex core. A vortex is easy to see on a cloud since the density drops to zero at its core. The first evidence for vortices was given by Matthews *et al.* who generated vortices in a BEC using a coherent process between two internal states [73]. Another very successful technique was the "stirring" of the atomic sample in a static magnetic trap using a rotating blue-detuned laser beam [74, 75]. The creation of a rotating anisotropy using nothing but a TOP trap was demonstrated by the Oxford group as soon as 1999 [76], but it was not until 2001 that they succeeded in nucleating vortices with this technique [77]. The creation of the rotating anisotropy with the TOP trap has the great advantage of not taking up any optical access which is always a precious good in cold atom experiments.

The interest of cold atomic gases under rotation goes far beyond its use as a probe for superfluidity: in fact, the Hamiltonian of a gas under rotation is equivalent to that of a charged particle in an electromagnetic field, permitting to explore the physics of the quantum Hall effect with rotating samples of neutral atoms [78, 20]. In the regime of critical rotation, where the rotation frequency equals the trapping frequency so that the latter is entirely compensated by the centrifugal force, the ground state becomes infinitely degenerate and the system is effectively in the lowest Landau level. Reaching this regime is experimentally challenging since it requires a very precise control both of the trap's geometry and of the rotation frequency. Several experiments have succeeded in coming quite near the critical frequency [18, 19]. However it turned out to be very difficult to maintain a stable critical rotation long enough to reach a stationary state.

The method of rotation used by the Oxford group [76, 77] can be seen as a rigid rotation: first of all, in order for a rotation to have an effect, one has to introduce an anisotropy. A static anisotropy is readily achieved by choosing

$$x_t = r_0(1+2\epsilon)\cos\omega t \quad ; \quad y_t = r_0(1-2\epsilon)\sin\omega t \,, \tag{2.9}$$

resulting in an averaged magnetic field of

$$B = \frac{b\,r_0}{2}\left(1 + \frac{x^2+y^2+8z^2}{4r_0^2}(1+\epsilon^2) - \epsilon\frac{x^2-y^2}{4r_0^2}(1+3\epsilon^2/2)\right) + \mathcal{O}(\epsilon^4)\,. \tag{2.10}$$

The modification of x_t and y_t has been chosen such that the geometric average of the frequencies remains constant to first order in ϵ. The trapping frequencies in x and y direction are multiplied by $\sqrt{1\pm\epsilon}$, respectively.

This anisotropy can be rotated by applying a rotation matrix on x_t and y_t:

$$\begin{pmatrix} X_t \\ Y_t \end{pmatrix} = \begin{pmatrix} \cos\Omega t & -\sin\Omega t \\ \sin\Omega t & \cos\Omega t \end{pmatrix} \begin{pmatrix} x_t \\ y_t \end{pmatrix}, \tag{2.11}$$

where $\Omega \ll \omega$ is the frequency at which the trap is to be rotated. Plugging X_t and Y_t into (2.8) and averaging (treating $\sin\Omega t$ and $\cos\Omega t$ as constants) yields

$$B = \frac{b r_0}{2}\left(1 + \frac{x^2+y^2+8z^2}{4r_0^2}(1+\epsilon^2) - \epsilon\frac{(x^2-y^2)\cos 2\Omega t + 2xy\sin 2\Omega t}{4r_0^2}(1+3\epsilon^2/2)\right) + \mathcal{O}(\epsilon^4), \tag{2.12}$$

which is the desired outcome[4].

For the practical implementation of this configuration it is convenient to rewrite the coordinates of the zero point using the addition theorems:

$$X_t = r_0\{\cos[(\omega+\Omega)t] + 2\epsilon\cos[(\omega-\Omega)t]\} \quad ; \quad Y_t = r_0\{\sin[(\omega+\Omega)t] - 2\epsilon\sin[(\omega-\Omega)t]\} \tag{2.13}$$

All one has to do is to generate a sum of sines or cosines of slightly different frequency. The general structure is that of a carrier with one side band. While Arlt *et al.* propose an electronic circuit to carry out this procedure starting from pure sine waves [76], the entire signal can conveniently be generated by a programmable signal generator such as the Tabor WW 1072 used on our setup.

2.4 *Rotating a* TOP *with rapid phase modulation*

From a radio technician's point of view, the coordinates of the "rigid rotation" trajectory are a combination of amplitude and phase modulation of the carrier. Each type of modulation individually would result in *two* side bands whereas the signals in (2.13) only have one, the second being cancelled out by the interplay of phase and amplitude modulation.

We now consider an alternative approach which is—to our knowledge—original. It is based on pure phase modulation of the standard TOP trajectory. The idea is the following: we restrict the motion of the magnetic field's zero to a circle of radius r_0, but let it run along this circle with varying angular velocity. The trajectory will thus be described by

$$X_t = r_0\cos[\omega t + \epsilon\cos(\Omega t + \phi)] \quad ; \quad Y_t = r_0\sin[\omega t + \epsilon\cos(\Omega t + \phi)] \, . \tag{2.14}$$

The role of the frequency Ω is quite different from the rigid rotation case: in the latter, Ω was directly related to the rotation frequency of the anisotropic trap. Here, the cosine terms depending on Ω serve to make the zero point run slower in certain regions of the circle of death. Having $\Omega \neq 0$ does not necessarily imply that one has a rotating potential: if Ω is an integer multiple of ω, it will always be the same zones where the zero moves faster or slower,

---

[4] One might wonder why the dependence of the potential is on 2Ω. This is due to the two-fold rotational symmetry of the potential: after one half-period, it has regained its original shape.

respectively. Thus, after averaging the potential remains static. We will pass most of this section discussing this static case since it contains the essential physics. The constant phase ϕ determines the orientation of the resulting potential. Later on we shall add a slowly varying linear term which sets the potential into rotation.

Static anisotropies of arbitrary order

The rapid modulation scheme opens up new possibilities since it permits—at least in principle—the creation of anisotropies of arbitrary polynomial order n. For the type of anisotropy we are interested in, it is at the same time the order of the rotational symmetry: an anisotropy of order n is invariant under rotations of $2\pi/n$ around the trap centre (see figure 2.1 for an illustration for $n = 2$ where the potential has a two-fold rotational symmetry and $n = 3$ where the symmetry is threefold). The maximum order that can be practically achieved is limited by the bandwidth of the amplifiers used to produce the actual currents for the TOP coils: an expansion to first order in the modulation parameter ϵ yields

$$X_t \simeq \cos\omega t - \epsilon\cos(\Omega t + \phi)\sin\omega t \quad ; \quad Y_t \simeq \sin\omega t + \epsilon\cos(\Omega t + \phi)\cos\omega t\ , \qquad (2.15)$$

which means that one has ω as a carrier frequency and side bands at $\Omega - \omega$ and $\Omega + \omega$ (higher order expansions in ϵ would yield more side bands). Since $\Omega = n\omega$ (it is in fact the same n as the order of the anisotropy that comes out of it), this means that $(n+1)\omega$ must be within the bandwidth of the amplifier. Since we use audio amplifiers, the bandwidth is 20 kHz, so, for an example, $n = 3$ is feasible if one chooses a TOP frequency of 5 kHz. Of course, it would be advisable in an actual realisation to correct for the dependence of the amplifier's gain on frequency, since carrier and side bands are quite far from each other.

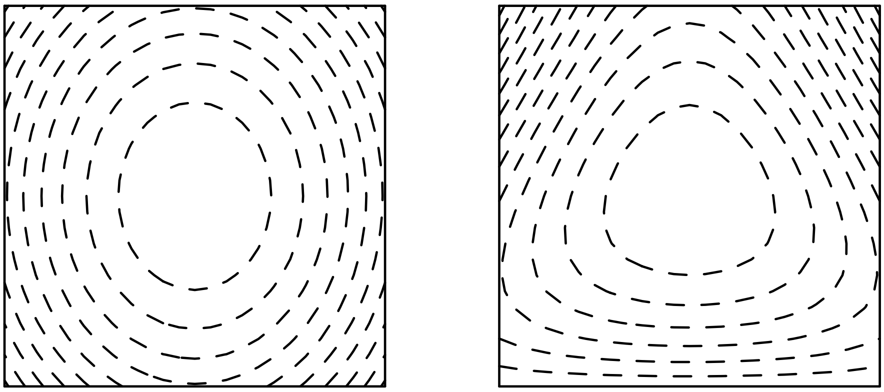

FIGURE 2.1: *Left: contour lines of a harmonic potential with a quadratic anisotropy* ($n = 2$). *The isopotential lines become ellipses. Right: contour lines of a harmonic potential with a symmetric cubic anisotropy* ($n = 3$). *The contour lines take on a "triangular" shape.*

To analyse potentials of higher order than two, we have to extend the expansion of the TOP potential to higher orders. Rigorously speaking, we would have to start by using more exact expressions for the quadrupole and the rotating field than the expressions used up to now which are only correct to second and first order in the distance from the trap centre, respectively[5]. However, apart from the fact that the effect is smaller than it seems due to the argument of different length scales given earlier in this chapter, we are principally interested in the anisotropic components of the resulting potential, and corrections to the constituent fields will only change the isotropic part. Since we are going to present an analytical treatment to first order in ϵ only (which permits to get an impression of how things work), it seems pointless to strive for numerical accuracy in such a way and we will continue to use the idealised expressions for the basic fields. Using the fact that for perfectly circular trajectories one has $r_t \equiv r_0$, one calculates the instantaneous magnetic field modulus to fourth order in the spatial coordinates:

$$\begin{aligned} B = \frac{b r_0}{2} \Bigg[1 + \frac{X_t x + Y_t y}{r_0^2} + \frac{x^2+y^2+4z^2}{2r_0^2} - \frac{(X_t x + Y_t y)^2}{2r_0^4} \\ + \frac{X_t x + Y_t y}{r_0^2} \left(\frac{x^2+y^2+4z^2}{2r_0^2} - \frac{(X_t x + Y_t y)^2}{2r_0^4} \right) \\ - \frac{(x^2+y^2+4z^2)^2}{8r_0^4} + 3r_0^2 (X_t x + Y_t y)^2 \frac{x^2+y^2+4z^2}{4r_0^8} - \frac{5(X_t x + Y_t y)^4}{8r_0^8} \Bigg] + \mathscr{O}[(x/r_0)^5] \, . \end{aligned} \tag{2.16}$$

To obtain the effective potential, one has to average this expression over one rotation period. Since all the time dependence is in X_t and Y_t, this means that the potential is completely characterised by the dimensionless *moments*

$$M_{k\ell} \equiv \frac{\omega}{2\pi r_0^{k+\ell}} \int_0^{2\pi/\omega} \mathrm{d}t \, X_t^k Y_t^\ell \, . \tag{2.17}$$

It is not possible to carry out these integrals analytically using the exact expressions (2.14), so we will use the expressions to first order in ϵ (2.15). As concerns an experimental realisation, this is not necessarily an approximation: one can decide freely which version one wants to implement as a wave form. Furthermore, the higher order side bands will be increasingly suppressed by the amplifier's bandwidth so that one cannot possibly hope to get an ideal realisation of (2.14) in terms of actual currents. We will regard the moments and their effect order by order in X_t and Y_t (not to be confused with the order in ϵ. The order of the moments is a classification, not a degree of approximation). A graphical representation up to fourth order is given in figure 2.2.

First order moments The first order moments M_{10} and M_{01} are just the averages of X_t/r_0 and Y_t/r_0, respectively. They appear in two places in our expansion (2.16): as coefficient of the linear part of the potential (the effect of which is to displace the trap's center) and in the first of

---

[5] If the coils generating the rotating field were in a perfect Helmholtz configuration, *i. e.* circular coils separated by their radius, the expression would be correct up to third order. We carried out all preceding calculations as if this were the case, which works well since the second order contribution is quite small.

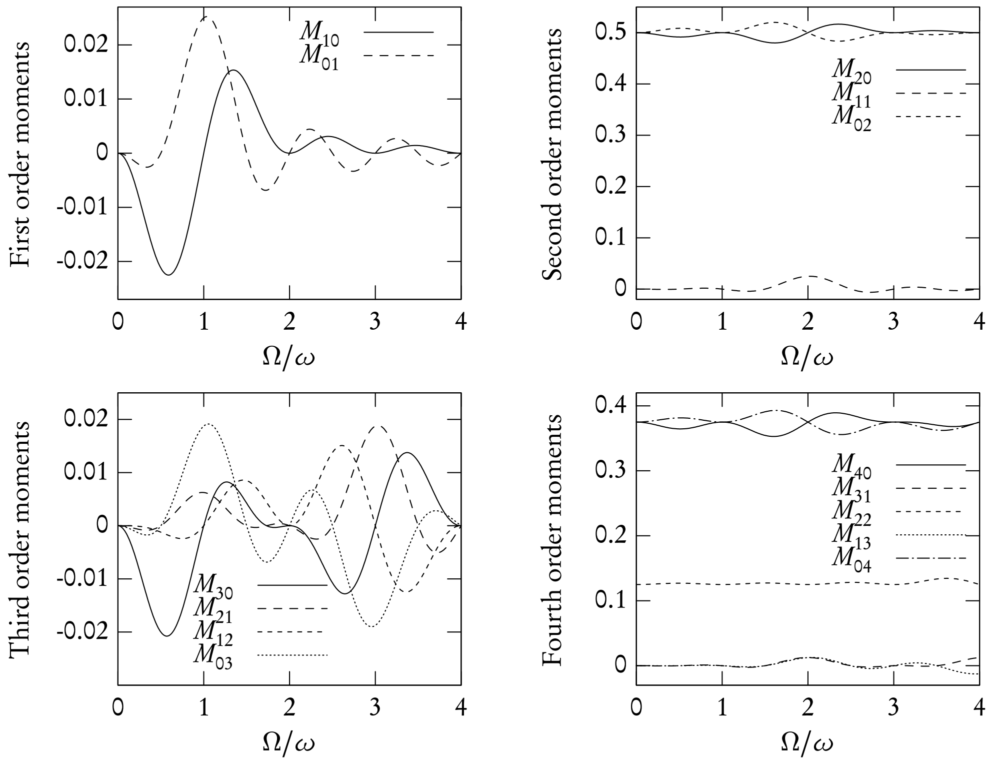

FIGURE 2.2: *First to fourth order (in X_t and Y_t) moments to first order in ϵ for $\epsilon = 0.05$ and $\phi = 0$. Note the special role played by the points for which Ω is an integer multiple of ω.*

the third order (in x) terms. We shall come back to the effects of this latter term later on. The actual values are:

$$M_{10} = \frac{\epsilon}{\pi} \frac{\sin(\pi\Omega/\omega)\sin(\pi\Omega/\omega + \phi)}{(\Omega/\omega)^2 - 1} \quad ; \quad M_{01} = \frac{\epsilon}{\pi} \frac{\sin(\pi\Omega/\omega)\cos(\pi\Omega/\omega + \phi)\Omega/\omega}{(\Omega/\omega)^2 - 1} \, . \tag{2.18}$$

As we already stated, we are mainly interested in the case $\Omega = n\omega$. One immediately sees that for all $n > 1$, both first order moments vanish identically, so for static anisotropies one needs not bother with its effects on the cubic part of the potential (the case of turning anisotropies requires a more careful discussion). The case $n = 1$ must be regarded in the sense of de l'Hôpital's rule: the denominators vanish linearly, while the numerators are sums of linearly and quadratically vanishing terms (depending on the value of ϕ). Thus, the first order moments remain finite for all values of Ω at $n = 1$.

Second order moments In the magnetic field, the second order moments appear in the second quadratic term (the one that generates the anisotropic part) as coefficients of x^2, $2xy$ and y^2 (note the binomial coefficient in the cross term) and in the first quartic term. A straightforward calculation yields

$$\begin{aligned} M_{20} &= \frac{1}{2} + \frac{\epsilon}{\pi} \frac{\cos\phi - \cos(2\pi\Omega/\omega + \phi)}{(\Omega/\omega)^2 - 4} \\ M_{11} &= -\frac{\epsilon}{2\pi} \frac{[\sin\phi - \sin(2\pi\Omega/\omega + \phi)]\Omega/\omega}{(\Omega/\omega)^2 - 4} \\ M_{02} &= \frac{1}{2} - \frac{\epsilon}{\pi} \frac{\cos\phi - \cos(2\pi\Omega/\omega + \phi)}{(\Omega/\omega)^2 - 4} \,. \end{aligned} \tag{2.19}$$

For all $n \neq 2$, one has $M_{20} = M_{02} = 1/2$ and $M_{11} = 0$, *i. e.* the usual "softening" of the trapping frequencies in the plane leading to the habitual TOP aspect ratio of $1 : 2\sqrt{2}$. In this case the second order contribution remains isotropic. The case $n = 2$ is reminiscent of the $n = 1$ case for the first order moments, and treated in the same way. Here again, all moments remain finite and simplify to

$$M_{20} = \frac{1 + \epsilon \sin\phi}{2} \quad ; \quad M_{11} = \frac{\epsilon \cos\phi}{2} \quad ; \quad M_{02} = \frac{1 - \epsilon \sin\phi}{2} \,. \tag{2.20}$$

Substituting these expressions as coefficients of x^2, $2xy$ and y^2, one immediately recovers an expression of the same kind as (2.10). This proves that one can produce a quadratic anisotropy with pure phase modulation.

Third order moments As far as we have carried out the expansion, the third order moments appear only once in (2.16), in the second third order term (the first being proportional to the first order moments). They are thus the coefficients of x^3, $3x^2y$, $3xy^2$ and y^3, respectively. Explicit calculation gives

$$\begin{aligned} M_{30} &= \frac{3\epsilon}{\pi} \frac{[(\Omega/\omega)^2 - 3] \sin(\pi\Omega/\omega) \sin(\pi\Omega/\omega + \phi)}{(\Omega/\omega)^4 - 10(\Omega/\omega)^2 + 9} \\ M_{21} &= \frac{\epsilon}{\pi} \frac{[(\Omega/\omega)^2 - 3] \sin(\pi\Omega/\omega) \cos(\pi\Omega/\omega + \phi)\Omega/\omega}{(\Omega/\omega)^4 - 10(\Omega/\omega)^2 + 9} \\ M_{12} &= -\frac{2\epsilon}{\pi} \frac{\sin(\pi\Omega/\omega) \sin(\pi\Omega/\omega + \phi)(\Omega/\omega)^2}{(\Omega/\omega)^4 - 10(\Omega/\omega)^2 + 9} \\ M_{03} &= -\frac{6\epsilon}{\pi} \frac{\sin(\pi\Omega/\omega) \cos(\pi\Omega/\omega + \phi)\Omega/\omega}{(\Omega/\omega)^4 - 10(\Omega/\omega)^2 + 9} \,. \end{aligned} \tag{2.21}$$

The common denominator vanishes linearly for $n = 1$ and $n = 3$, the numerators all vanish linearly for all n. Thus, the overall moments vanish for all n except 1 and 3. For $n = 3$ these expressions simplify to

$$M_{30} = \frac{3}{8}\epsilon \sin\phi \quad ; \quad M_{21} = \frac{3}{8}\epsilon \cos\phi \quad ; \quad M_{12} = -\frac{3}{8}\epsilon \sin\phi \quad ; \quad M_{03} = -\frac{3}{8}\epsilon \cos\phi \,. \tag{2.22}$$

It is readily verified that the expression

$$x^3 \sin\phi + 3x^2 y \cos\phi - 3xy^2 \sin\phi - y^3 \cos\phi \tag{2.23}$$

is invariant under a rotation by $2\pi/3$, *i.e.* the cubic anisotropy corresponding to this term has threefold rotational symmetry. For $n = 3$, this is the only cubic term that survives since the first order moments vanish. Thus, this configuration produces a maximally symmetric cubic anisotropy which is a good starting point for rotations.

One can continue calculating higher order moments, but with respect to the technical limitations mentioned earlier, it becomes increasingly pointless. Summing up our results for the moments up to third order, we have two cases of interest: the case $n = 2$ where one has only a quadratic anisotropy (and also a quartic one, but the quadratic one will be dominating) and the case $n = 3$ where all anisotropies except the cubic one vanish.

Setting the anisotropy into rotation

We now turn to the case of a *rotating* cubic anisotropy. To understand how such a rotation comes about we remark that the constant phase ϕ actually does rotate the magnetic field since it displaces the regions of slow and fast motion in a uniform manner. A uniform rotation can thus be achieved by making the replacement

$$\Omega \mapsto \Omega(1+\delta) \quad \Longrightarrow \quad \phi \mapsto \phi + \Omega\delta t\ . \tag{2.24}$$

In this way, the signal is no more $2\pi/\omega$-periodic, but accumulates a small phase $2\pi n\delta$ (for $\Omega = n\omega$) on each turn, which does the same effect as if one varied ϕ linearly with time. Thus, after a time $2\pi/(n\omega\delta)$, the potential regains its original shape, which happens after a rotation by $2\pi/n$ for a potential with n-fold symmetry. This means that the anisotropy of order n will rotate at the angular frequency $\omega\delta$.

It is clear that this permits us to rotate the anisotropy of our choice, but at the same time it will create rotating anisotropies of other orders as well since we are deliberately moving away from the “magic frequencies” which are plain integer multiples of the TOP frequency. We are not moving far, though, since the order of magnitude for rotational speeds is given by the trapping frequencies: if we assume a TOP frequency of 5 kHz and trapping frequency of 20 Hz, we get $\delta \leq 0.04$. If we substitute (2.24) into (2.18) and (2.19), we can thus do a linear expansion in δ. If we then set $\Omega = 3\omega$ we obtain

$$M_{10} = \frac{3\epsilon\delta}{8}\sin\phi \quad ; \quad M_{01} = \frac{9\epsilon\delta}{8}\cos\phi \tag{2.25}$$

$$M_{20} = \frac{1}{2} + \frac{6\epsilon\delta}{5}\sin\phi \quad ; \quad M_{11} = \frac{9\epsilon\delta}{5}\cos\phi \quad ; \quad M_{02} = \frac{1}{2} - \frac{6\epsilon\delta}{5}\sin\phi\ . \tag{2.26}$$

Evidently, there is also a slight modification of the third moments, but we are more interested in the appearance of undesired lower order anisotropies. One sees that anisotropies of first and second order appear as well as a non-symmetric one at third order (from the first cubic term in (2.16) which is a function of the first order moments), all of them rotating along with the desired symmetric cubic anisotropy. But the amplitudes of *all* those components are of order $\epsilon\delta$, *i. e.* a factor of δ smaller than the amplitude of the symmetric cubic anisotropy. Since δ is quite small for typical experimental parameters, it seems plausible that in such a system the symmetric cubic anisotropy should be predominating (all other anisotropies would be comparable to or small against residual static anisotropies due to experimental imperfections).

Stability in a rotating tripod potential

To supplement the above considerations, we analyse the stability of atom trajectories in the xy plane in a trap with a rotating cubic anisotropy. In the static case, for $n = 3$ and $\phi = 0$, one has the following magnetic field:

$$B = \frac{b r_0}{2}\left(1 + \frac{x^2 + y^2 + 8z^2}{4r_0^2} - 9\epsilon\frac{3x^2y - y^3}{16r_0^3}\right) . \tag{2.27}$$

In the xy plane, this will give rise to a potential of the form

$$V(x,y) = m\omega_\perp^2\left(\frac{x^2 + y^2}{2} + \frac{\eta}{3r_0}(3x^2y - y^3)\right) , \tag{2.28}$$

where we have introduced $\eta = 27\epsilon/8$ for convenience.

Now let us imagine that this potential is rotated at an angular velocity $\alpha\omega_\perp$ so that $V(x,y)$ is actually the potential in the corotating frame (we will disregard for these considerations the slight deformations of the static potential that occur in the rotating case). In this frame, there will be two pseudo forces, the Coriolis and the centrifugal force. To the latter one can attribute a pseudo potential $-m(\alpha\omega_\perp)^2r^2/2$, permitting us to define the dimensionless effective potential

$$\tilde{V}(x',y') = \frac{V(x,y)}{m\omega_\perp^2 r_0^2} - \alpha^2\frac{x'^2 + y'^2}{2} = (1-\alpha^2)\frac{x'^2 + y'^2}{2} + \frac{\eta}{3}(3x'^2y' - y'^3) , \tag{2.29}$$

where $x' = x/r_0$ and $y' = y/r_0$. Using this potential, the centrifugal force is completely taken into account. A graphical representation of this effective potential is shown in figure 2.3.

The case of the Coriolis force which cannot be derived from a pseudo potential is less obvious. In the case of a rotating *quadratic* anisotropy of the form (2.12), it is well known that there are three regimes for the stability of a particle [79]: the effective trapping potential is of the form $m[(1+\epsilon-\alpha^2)\omega_x^2x^2 + (1-\epsilon-\alpha^2)\omega_y^2y^2]/2$. As long as $\alpha < \sqrt{1-\epsilon}$ (we assume $\epsilon > 0$), the effective potential is confining in both directions and trajectories are stable. For $\sqrt{1-\epsilon} < \alpha < \sqrt{1+\epsilon}$, the effective potential is confining in one direction and repulsive in the other, thus creating an unstable regime. Quite surprisingly, trajectories become stable again for $\alpha > \sqrt{1+\epsilon}$. In this latter case, the effective potential is repulsive in both directions, and the particles are dynamically stabilised by the Coriolis force that "pushes" them along the

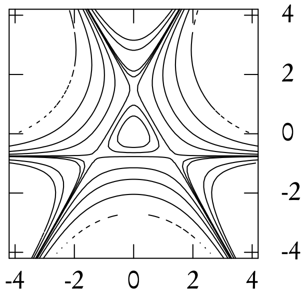

FIGURE 2.3: *Effective potential* $\tilde{V}(x',y')$ *for* $\alpha = 0.5$ *and* $\eta = 0.5$ *(these values have been chosen in order to render the qualitative behaviour of the potential more clearly discernible). In the middle of the potential, there is an approximately harmonic well, further outside the potential takes the form of a triangular "ash tray". The potential becomes negative on the top, the lower left and the lower right of this contour plot so that particles whose energy exceeds the depth of the central well will leave the trap in one of these directions.*

equipotential lines of the effective potential (it might be doing the same thing in the slowly rotating regime, but there trajectories are already stable). It can only do this because there are closed equipotential lines. In the unstable regime, such lines do not exist since the effective potential takes the form of a saddle point and equipotential lines are hyperbolas extending to infinity. The Coriolis force cannot possibly do more than force particles on equipotential lines since by its very mathematical structure it cannot do work.

Thus, for our purposes, we can say that trajectories are guaranteed to be stable when the effective potential is globally attractive and guaranteed to be unstable when it takes the form of a saddle point. The case of a globally repulsive effective potential is not clear from such arguments, but since we are interested by the behaviour of atomic *gases* in which particles collide, the issue of dynamic stabilisation is more complicated even for a quadratic anisotropy. To be on the safe side, we will only regard trivially stable configurations.

According to these considerations, we only need to know the stationary points of the effective potential and its behaviour in their vicinity. The stationary points are readily found:

$$\begin{gathered} \boldsymbol{r}'_1 = 0 \quad ; \quad \boldsymbol{r}'_2 = \frac{1-\alpha^2}{\eta}\boldsymbol{u}_y \\ \boldsymbol{r}'_3 = \sqrt{3}\frac{1-\alpha^2}{2\eta}\boldsymbol{u}_x - \frac{1-\alpha^2}{2\eta}\boldsymbol{u}_y \quad ; \quad \boldsymbol{r}'_4 = -\sqrt{3}\frac{1-\alpha^2}{2\eta}\boldsymbol{u}_x - \frac{1-\alpha^2}{2\eta}\boldsymbol{u}_y \,. \end{gathered} \tag{2.30}$$

We find one stationary point in the centre of the trap and three which are evenly distributed on a circle with radius

$$R' = \frac{1-\alpha^2}{\eta} \,. \tag{2.31}$$

Since these are points of symmetry (they are just $2\pi/3$ apart), it is sufficient to regard one of these points. Expanding the effective potential around $\boldsymbol{r}_2'$ up to second order in x' and y' yields

$$\tilde{V}\left(x', \frac{1-\alpha^2}{\eta} + y'\right) = (1-\alpha^2)\frac{3x'^2 - y'^2}{2} + \frac{(1-\alpha^2)^3}{6\eta^2} + \mathcal{O}(x'^3)\,. \tag{2.32}$$

Since x'^2 and y'^2 appear with opposing signs, the three stationary points on the circle are always saddle points for $\alpha \neq 1$ as opposed to the stationary point in the trap center which is a minimum of the effective potential for all $\alpha = \Omega/\omega_\perp < 1$. Thus, there is a stable zone which extends from the trap centre up to the radius R'. This situation is very different from the case of a rotating *quadratic* anisotropy: there, depending on the value of the rotating frequency, either trajectories are stable at all energies (for $|\Omega - \omega|/\omega > \sqrt{1+\epsilon}$), or they are unstable at all energies (for $|\Omega - \omega|/\omega \leq \sqrt{1+\epsilon}$) so that there is nothing like a zone of stability in space. In the case of the rotating tripod, for Ω arbitrarily close to ω, we do have a spatial region of stability the size of which depends on the rotation frequency.

To see what this means for actual experiments, we resubstitute our units: for a gradient $b = 100\,\mathrm{G/cm}$, a rotating field $B_0 = 5\,\mathrm{G}$, a near-critical rotation with $\alpha = 0.99$ and a modulation parameter $\epsilon = 0.05$, one finds $R = r_0 R' = 354\,\mu\mathrm{m}$. The depth of the corresponding potential is given by the difference between the minimum value of the effective potential on the circle with radius R and the trap centre (the latter being already set to zero):

$$\Delta V = m\omega_\perp^2 r_0^2 \frac{(1-\alpha^2)^3}{6\eta^2}\,. \tag{2.33}$$

Since, as we said earlier this chapter, the given values for b and B_0 correspond to a trapping frequency $\omega_\perp = 2\pi \times 20\,\mathrm{Hz}$, the depth for the given parameters is $\Delta V = k_\mathrm{B} \times 69\,\mathrm{nK}$. This depth can be increased by increasing the magnitude of the rotating field: since $\omega_\perp$ scales as $b/\sqrt{B_0}$ while r_0 scales as B_0/b, the product $\omega_\perp^2 r_0^2$ scales as B_0. Thus, near-critical rotation of a cubic anisotropy seems to be feasible at least for very cold clouds. Of course, the stability of trajectories also depends on the slight quadratic anisotropy that comes along with the rotating cubic anisotropy as well as the inevitable slight imperfections of a concrete experimental realisation. As a consequence, the region of stability will at least be smaller than what can be expected from this analysis. If the mentioned effects become too strong, it will vanish altogether. Thus, although it seems easier to achieve near-critical rotation with a cubic anisotropy than with a quadratic one, a definitive answer can only be provided by an experimental test.

2.5 Evaporation and radio frequency-dressed potentials

As Petrich *et al.* pointed out, the TOP trap has a "built-in" means for evaporation given by the radius of death [57]. However, this method lacks some flexibility since evaporation only occurs on a small toroidal volume and one cannot change the radius of evaporation without changing at the same time the trapping geometry. Thus, evaporative cooling in a TOP trap is usually carried out using radio frequency (rf) waves.

Radio frequency cooling in a TOP trap is slightly different from the case in a static trap: in the latter, the potential "seen" by the atoms and by the rf waves is the same. In a TOP trap, due to the separation of time scales, the atoms see an averaged magnetic field whereas the rf sees the instantaneous one: when an rf field at a frequency ω_{rf} is applied, this defines an ellipsoidal surface centered on the instantaneous position of the magnetic field's zero. In the xy plane, this ellipse has a circular cross section the radius of which is $|g_F|\mu_B B = \hbar\omega_{\text{rf}}$. Atoms crossing this surface become resonant with the transitions between the hyperfine states. They are transferred to non-trapped states (in the case of the state $F = 2, m_F = 2$, this takes two photons) and leave the trap. When the TOP field rotates, this instantaneous evaporation surface rotates along with it, creating an *effective* evaporation surface which is just the surface of revolution of the instantaneous one around the trap centre. Figure 2.4 illustrates the instantaneous situation.

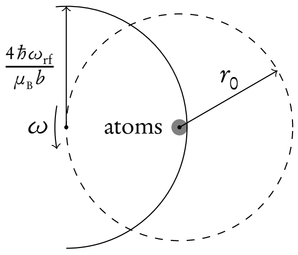

FIGURE 2.4: *Geometry of evaporative cooling in a* TOP *trap in the plane: The surface of evaporation is centered on the instantaneous zero of the magnetic field that is rotating around the atoms. The radius of evaporation r_0 is the distance from the origin to the evaporation surface.*

Since in the xy plane one has $B = br/2$, the radius from the trap centre to this effective surface is given by

$$r_{\text{ev}} = \frac{2}{b}\left(\frac{\hbar\omega_{\text{rf}}}{|g_F|\mu_B} - B_0\right). \tag{2.34}$$

The evaporation radius scales linearly with the rf frequency down to the trap centre, unlike the case of a static harmonic trap where it scales with the square root which renders the approach of the trap centre at the end of an evaporation sequence quite delicate. As Marc Cheneau has explained in his PhD thesis, this results in a conveniently large condensation range in a TOP trap (about 200 kHz on our setup) [45].

A different point of view on the same process consists in saying that the rf couples different magnetic substates on a certain surface, creating avoided crossings which results in an *adiabatic potential* with a local minimum in the trap centre surrounded by "trapping walls" of finite height [2, 80]. As Zobay and Garraway pointed out, this potential has a "twin" with a local maximum in the middle and an ellipsoidal minimum (called a "shell" by the authors) located at the evaporation surface of the "habitual" potential [36] (see figure 2.5 for an illustration of the principle). Starting from a static harmonic trap, they conjectured it should be possible to create two-dimensional gases on such a shell. Indeed, the Villetaneuse group succeeded in loading ultracold gases in such a potential (both in a harmonic trap [37] and in a pure quadrupole [81]).

On atom chips, considerable success was achieved by the Heidelberg group with similar techniques which permitted among other things interferometry between condensates and one-dimensional Bose gases [82, 83].

So far there is no published experimental work on adiabatic potentials in TOP traps, but there has been a proposal by Lesanovsky and von Klitzing who argue that such *time-averaged adiabatic potentials* can be quite versatile [84]. Of the diverse possible potentials they investigate in their article we will discuss the double well potential since it is tempting to try to use it for the production of a pair of 2d Bose gases.

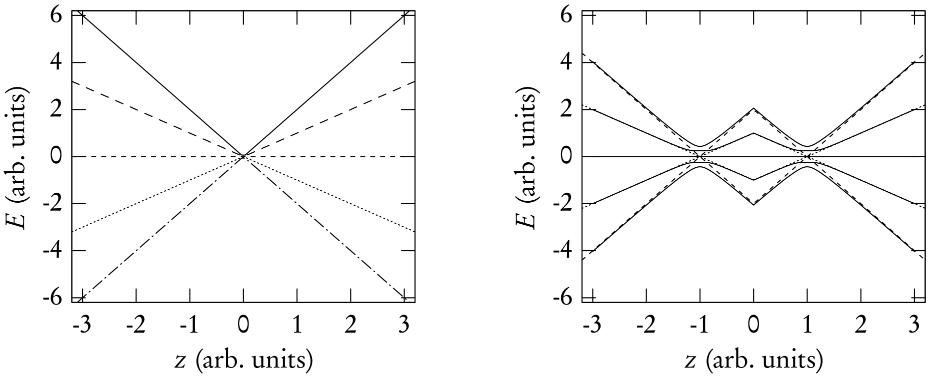

FIGURE 2.5: *Principle of rf dressed potentials. Left: the potentials seen in a quadrupole trap by the five substates of the $F = 2$ quintuplet, only two of which are confining. Right: if one adds an rf field, the energies in the dressed state picture are shifted and become degenerate in certain points (dashed and dotted line). The coupling between atoms and rf field lifts the degeneracy (solid lines) and creates double well potentials (upper half) as well as "evaporation" potentials (lower half). In the case of a* TOP *trap, the cusp in the middle would be rounded off.*

The production of a double-well potential requires no special efforts in a standard TOP trap since it is just the "twin" of the potential that naturally occurs during rf evaporation (provided that—as is the case on our setup—the rf field is directed along the axis of rotation z of the TOP): the instantaneous potential is a "shell" type one which is rotated about the trap centre. Anywhere but close to the z axis, this will "close" the shell, leaving two minima of the time-averaged potential above and below the trap centre. Note that without this dynamic effect, the shell would be "open" anywhere so that there would be only one global minimum (at the bottom of the shell, due to gravity).

Under the assumptions that the rf coupling is near-resonant and that the associated Rabi frequency Ω_{rf} is small compared to the radio frequency itself, the instantaneous potential can be calculated within the rotating wave approximation (RWA)[6]:

$$V(\boldsymbol{r}) = |m_F|\hbar\sqrt{[\omega_L(\boldsymbol{r}) - \omega_{\mathrm{rf}}]^2 + \Omega_{\mathrm{rf}}^2(\boldsymbol{r})}\,, \tag{2.35}$$

with the Rabi frequency $\Omega_{\mathrm{rf}} = |g_F \mu_{\mathrm{B}} \boldsymbol{B}(\boldsymbol{r}) \times \boldsymbol{B}_{\mathrm{rf}}|/|2\hbar \boldsymbol{B}(\boldsymbol{r})|$, where $\boldsymbol{B}_{\mathrm{rf}}$ is the magnetic field strength of the rf field. In the following, the direction of $\boldsymbol{B}_{\mathrm{rf}}$ is chosen to be along the z axis. The effective potential is the time average of (2.35) over one rotation period. It is convenient to define the constants

$$\beta = \frac{|g_F|\mu_{\mathrm{B}} B_0}{\hbar\omega_{\mathrm{rf}}} = \frac{\omega_{\mathrm{rf}}^{\mathrm{min}}}{\omega_{\mathrm{rf}}} \quad ; \quad \gamma = \frac{B_{\mathrm{rf}}}{B_0} \quad ; \quad \phi = \angle(\boldsymbol{B}, \boldsymbol{B}_{\mathrm{rf}}) \quad ; \quad \omega_0^2 = \frac{|m_F g_F|\mu_{\mathrm{B}} b^2}{2mB_{\mathrm{rf}}}\,, \tag{2.36}$$

where $\omega_{\mathrm{rf}}^{\mathrm{min}}$ corresponds to an evaporation exactly at the trap centre and ω_0 is, as we will see, a typical value for the resulting frequencies of oscillation. The parameter β which varies between 0 and 1 controls the radius of evaporation and thus the shape of the potential while γ characterises the rf coupling strength. The instantaneous potential for the double-well case takes the explicit form

$$\begin{aligned} V(\boldsymbol{r},t) &= |m_F|\hbar\omega_{\mathrm{rf}}^{\mathrm{min}} \\ &\times \left[\left(\sqrt{1 + \frac{x^2+y^2+4z^2}{r_0^2} - \frac{2}{r_0}(x\cos\omega t + y\sin\omega t)} - \frac{1}{\beta} \right)^2 + \left(\frac{\gamma}{2}\sin\phi(\boldsymbol{r},t) \right)^2 \right]^{1/2}, \end{aligned} \tag{2.37}$$

with the local angle ϕ the sine of which is given by

$$\sin\phi(\boldsymbol{r},t) = \left(\frac{x^2+y^2+r_0^2 - 2r_0(x\cos\omega t + y\sin\omega t)}{x^2+y^2+4z^2+r_0^2 - 2r_0(x\cos\omega t + y\sin\omega t)} \right)^{1/2}. \tag{2.38}$$

Since the time average only affects the x and y directions, the location of the minima on the z axis can be found directly from the instantaneous potential. For $z \sim r_0$, the angle ϕ can be regarded as a constant, and one finds

$$z_\pm = \frac{\sqrt{1-\beta^2}\,r_0}{2\beta} \quad ; \quad \omega_z = 2\sqrt{1-\beta^2}\,\omega_0 \tag{2.39}$$

To get the frequencies in the xy plane around the minima, one has to make the more careful approximation

$$\sin^2\phi\big|_{z=z\pm} \simeq \frac{x^2+y^2+r_0^2 - 2r_0(x\cos\omega t + y\sin\omega t)}{(r_0/\beta)^2}\,. \tag{2.40}$$

---

[6] This approximation can be and has been violated in experiment [85], so when considering an actual realisation of such a potential, it is advisable to regard the non-RWA corrections. Here, we are just dealing with principal questions of feasibility and will thus stick to the RWA.

Substituting this into (2.37), expansion to second order in x and y and averaging yields a radial frequency of

$$\omega_\perp = \frac{\beta\omega_0}{2}\sqrt{\frac{\gamma^2}{2}+2} \overset{\text{RWA}}{=} \frac{\beta\omega_0}{\sqrt{2}}\,, \tag{2.41}$$

where we have used the fact that within the RWA one must have $\gamma \ll 1$ so that to be consistent one has to use the simpler expression for $\omega_\perp$.

Two other quantities of interest are the trapping depth and the effective potential at the bottom of the wells—the latter has to be high enough to prevent the atoms from doing Landau-Zener transitions to the conjugated potential. The trapping depth can be defined as the difference between the potential in the centre of the trap (the barrier between the two wells) and at the bottom of one well, which can be calculated without approximations:

$$\Delta V = V(0) - V(0,z_\pm) = |m_F|\hbar\omega_{\text{rf}}^{\text{min}}\left(\sqrt{\left(1-\frac{1}{\beta}\right)^2+\left(\frac{\gamma}{2}\right)^2}-\frac{\beta\gamma}{2}\right)\,. \tag{2.42}$$

The potential at the bottom of a well is given by $|g_F m_F|\mu_B B_{\text{rf}}/2 = |m_F|\hbar\Omega_{\text{rf}}$. Thus, it is the rf field itself that plays the role of a bias field (or more precisely, that determines the size of the gap of the avoided crossing), and must be dimensioned accordingly.

We can now see whether such a potential can indeed serve the purpose of a pair of two-dimensional Bose gases. In order to be in the 2d regime one needs to satisfy the condition $\hbar\omega_z \gg k_B T$. The equivalent frequency for 100 nK is $2\pi \times 2.08$ kHz, so it would be desirable to be able to achieve $\omega_z = 2\pi \times 4$ kHz. If one is to make interferometric experiments with two 2d Bose gases, the distance between the two should not be much greater than 5 µm in order to have reasonably spaced interference fringes[7].

Owing to the great number of adjustable parameters, it is not easy to make definite statements on the feasibility of a given configuration, so we will try to do this step by step. To maximise the trapping frequency, the first (since unambiguous) step to take is to use the maximum gradient permitted by the trap. On our setup, the gradient provided by the quadrupole coils is 0.6 G/(cm A) and the maximum current that can be run by the power supplies is 300 A so that one cannot exceed $b = 180$ G/cm. If we fix the gradient at this maximum value, ω_0 still depends on the modulation parameter β and the rf field B_{rf} [see equation (2.39)]. The trapping frequency ω_z is maximum for vanishing β, so if we take $\beta = 0$ for a first estimation, we see that for $\omega_z = 2\pi \times 4$ kHz, we need $B_{\text{rf}} = 6.56$ mG. If we allow for finite β values [which is necessary since otherwise the two minima will disappear at infinity according to equation (2.39)], B_{rf} must become even smaller for the same trapping frequency. But this is by far too weak to prevent Landau-Zener transitions: the corresponding Rabi frequency is only

---

[7] If the original distance is d, the spacing between two interference maxima is asymptotically equal to $ht/(md)$. For an example, after 15 ms of free expansion, the fringe spacing between two rubidium clouds originally separated by 5 µm will be 13.7 µm. It is advantageous to have short expansion times for two reasons: the cloud will expand less and thus yield a higher signal, and its dropping velocity will be lower, causing less blurring during the exposure time for imaging.

$2\pi \times 2.29\,\text{kHz}$, while in similar experiments like [37, 81, 86], the lowest reported frequency is $2\pi \times 30\,\text{kHz}$. The probability for a Landau-Zener transition at one crossing is $1 - \exp(-\alpha\Omega_{\text{rf}}^2)$, where α depends on the trapping geometry. For the achievable gradient, one cannot have at the same time sufficient field strength in the minima and a trapping frequency permitting to do 2d physics.

In fact, this is not too surprising since the rf field in the minima plays a very similar role to the field B_0 in a normal TOP trap: in both cases, the "skeleton" of the potential is provided by the quadrupole's gradient which is then rounded off by the second field. By lowering towards the tip of the potential the area over which this rounding off takes place, one can increase the trapping frequency up to theoretically arbitrary values, but at the same time the lift of the degeneracy with the other m_F states becomes weaker and weaker.

As the examples discussed in this chapter show, the dynamic character of the TOP trap permits the creation of a large variety of potentials. While it seems hard to use it for the creation of two-dimensional gases (for which there exist other efficient methods, for example the optical potentials discussed in chapter 4), the feasibility of rotating anisotropies has already been demonstrated for the rigid rotation case.

As stated at the beginning of this chapter, we have systematically neglected the influence of gravity which, depending on the type of potential, can be either a minor complication or a major element. We will see in the following chapter how gravity can be used together with a TOP to create an approximately isotropic harmonic trap.

Chapter Three

Towards an isotropic TOP *trap*

> Never measure anything but frequency!
>
> ARTHUR LEONARD SCHAWLOW (1921–1999)

ISOTROPIC harmonic traps are a common ingredient in the theory of confined gases. In many cases, this is nothing but a matter of convenience and the general case of a trap with up to three distinct trapping frequencies can be related back to the results by simple changes of notation. In other cases, the isotropy of the trap may be a crucial prerequisite for the existence of a given effect. One of the latter cases was first described in 1909 by Ludwig Boltzmann [46] who found that in an isotropic harmonic trap the so-called monopole mode (or *breathing mode*) of an interacting classical gas is undamped.

The age of this intriguing prediction notwithstanding, an experimental verification has not yet been reported (the results reported in [87] come close, but they apply to two spatial directions in a three-dimensional trap, the third having a much lower trapping frequency). This is owed to the fact that the experimental realisation of an isotropic harmonic trap is not trivial: a quadrupole trap has an aspect ratio of $1:2$, and static magnetic traps made up by more than two coils rather tend to have three distinct frequencies than to reduce the aspect ratio. A TOP trap has a "natural" aspect ratio of $1:\sqrt{8}$ which is even more anisotropic than the quadrupole trap. However, this can be changed by decreasing the gradient to values where its effect is comparable to that of gravity.

We have performed experiments the goal of which was to render our TOP trap isotropic and to verify Boltzmann's prediction. While we were able to get quite near an isotropic trap, a problem of reproducibility prevented us from carrying out this program in its entirety. Since the setup has changed since then, addressing amongst other things the issue of stability, it is not excluded that the group shall come back to this experiment one day. To this end, the present chapter summarises the progress we were able to make and explains the techniques we developed. It begins with a brief account of collective modes in a trapped gas to make clear the original motivation, followed by the generalisation of the TOP magnetic field to the more realistic case taking into account gravity. The experimental realisation of an isotropic TOP trap is then discussed in detail as far as we were able to progress.

3.1 Collective modes in trapped gases

The atoms in a trapped gas are constantly oscillating. Owing to their great number and the dispersion of the amplitudes and phases, the density distribution at equilibrium is constant in time. By transferring energy to the gas, it is possible to generate collective excitations in which the density distribution becomes an oscillating function of time.

The totality of possible collective excitations of a trapped gas can be expanded on a set of basis modes classified by two numbers n and ℓ. For our purposes, only three of these modes are of interest: the monopole mode ($n = 1, \ell = 0$) where the cloud shape is altered only by a isotropic oscillating scaling factor, the dipole modes ($n = 0, \ell = 1$) which are nothing but a centre of mass oscillation of the entire atomic cloud without deformation of the latter (one mode per axis) and finally the quadrupole modes ($n = 0, \ell = 2$). Similarly to the dipole modes, the quadrupole modes exist in three linearly independent realisations. Among the possible bases we choose the one in which the basis functions are characterised by a principal axis: the cloud is compressed along this axis and simultaneously expands in the plane perpendicular to it during the first half of an oscillation, then the process is reversed. The monopole and quadrupole modes are schematically represented in figure 3.1.

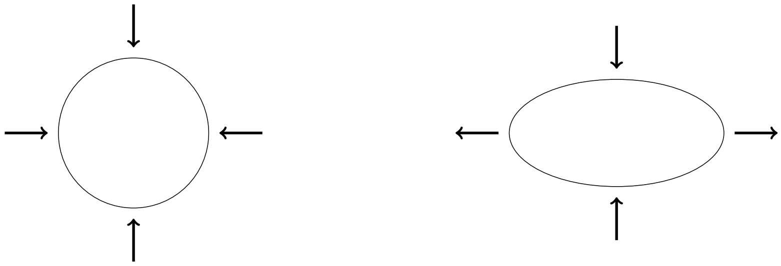

FIGURE 3.1: *Schematic representation of the cloud deformation in the quadrupole and monopole modes. A monopole oscillation will look as shown on the left seen from any direction. A quadrupole mode will look as shown on the right when seen from a direction normal to its principal axis, but as on the left when regarded along its principal axis.*

The interest of these modes for the purpose of this chapter is the following: a dipole mode is a mode of reference which permits to characterise the trap since it is easy to excite and observe and, just as importantly, its frequency does not depend on the particular regime of the atomic sample. The monopole mode is what we want to observe, so its importance needs not be stressed. The quadrupole modes, finally, are interesting for two reasons: firstly, to have a mode for comparison that exhibits clear damping (which requires a sufficient collision rate) and secondly, because in the actual observation of an atomic sample one cannot completely separate monopole and quadrupole modes: in the plane normal to the eigenaxis of a given quadrupole mode, the cloud is always either isotropically expanding or contracting so that it looks just like a monopole mode.

Apart from the corresponding deformation, the modes are characterised by their frequencies. The case of the dipole mode is simple: since it is just the centre of mass oscillation of the cloud, its frequency is equal to the trapping frequency regardless of the microscopic properties of the atomic sample. The monopole and quadrupole modes are more complicated in this respect since they concern the deformation of the sample itself which is intimately connected to its physical properties. The monopole and quadrupole frequencies for three limiting regimes—a strongly interacting BEC and a classical gas for the two extreme cases of the collision rate—are summarised in table 3.1.

Regime	Quadrupole	Monopole
Pure BEC ($T = 0$)	$\sqrt{2}\omega_0$	$\sqrt{5}\omega_0$
Classical gas (HD)	$\sqrt{2}\omega_0$	$2\omega_0$
Classical gas (CL)	$2\omega_0$	$2\omega_0$

TABLE 3.1: *Oscillation frequencies of the quadrupole and monopole mode in units of the dipole frequency ω_0 for a Bose-Einstein condensate, a classical gas in the hydrodynamic (HD) regime and a classical gas in the collisionless (CL) regime.*

A particularly clear account of the case of a classical gas has been given by Guéry-Odelin *et al.* [88] who distinguish two regimes: the collisionless regime in which the atoms undergo a large number of oscillations between two successive collisions and the hydrodynamic regime where there are several collisions per oscillation. In the collisionless regime, one essentially has an ideal gas in which the trajectories of particles are completely independent. Thus, there is no coupling between modes, and both monopole and quadrupole modes have the frequency $2\omega_0$ where ω_0 is the trapping frequency (we consider the isotropic case). In the hydrodynamic regime, the frequency of the monopole mode remains at $2\omega_0$ but the quadrupole frequency is lowered to $\sqrt{2}\omega_0$. The damping of the quadrupole mode is driven by binary collisions. Guéry-Odelin *et al.* find a relaxation time of $\tau = 5/4\gamma_{\text{coll}}$ where γ_{coll} is the elastic collision rate. The monopole mode is undamped, as already stated by Boltzmann. When the trap becomes anisotropic, the monopole and quadrupole modes become coupled which induces a damping of the monopole mode as well. We are principally interested in the hydrodynamic regime one since in the collisionless one all modes are trivially undamped.

The case of a pure Bose-Einstein condensate in the strongly interacting limit has been treated by Stringari [89]. Using a hydrodynamic formulation of the Gross-Pitaevskii equation, he derived a frequency of $\sqrt{2}\omega_0$ for the quadrupole—the same result as for a classical gas in the hydrodynamic regime—and a frequency of $\sqrt{5}\omega_0$ for the monopole mode, which is different from the frequency in a classical gas. His predictions (for the case of an anisotropic trap) are in fair agreement with experiment [90, 91, 87]. The experiments in [91] are only partially in the strongly interacting regime, so to fully explain their data a more elaborate theory is required [92, 93]. There also have been experimental as well as theoretical investigations of the excitation frequencies of a BEC at finite temperature (see *e.g.* [94, 10, 95]). In the case of a pure BEC, the monopole mode is undamped just as in a classical gas. In the intermediate situation of coexistence of a BEC and a thermal cloud the interaction between the respective monopole modes induces a damping of both of them.

3.2 *The* TOP *trap with gravity*

It turns out that a TOP trap, notwithstanding the fact that its natural aspect ratio is even larger than that of a quadrupole, can be rendered isotropic by taking advantage of the force of gravity. In order to see how gravity modifies the trapping frequencies of a TOP trap, we have to generalise the equations presented in chapter 2. To take into account gravity, we expand the magnetic field not around its zero, but around an arbitrary point on the z axis with a distance z_0 from the origin. To second order in the spatial coordinates, the magnetic field after averaging now reads

$$B = \frac{b}{2}\sqrt{r_0^2+4z_0^2}\left(1+\frac{r_0^2+8z_0^2}{4(r_0^2+4z_0^2)^2}(x^2+y^2)+\frac{2r_0^2}{(r_0^2+4z_0^2)^2}(\Delta z)^2-\frac{4z_0}{r_0^2+4z_0^2}\Delta z\right), \quad (3.1)$$

with $\Delta z = z - z_0$. The total potential experienced by the atoms is $V(\boldsymbol{r}) = \mu_{\rm B}|m_F|B(\boldsymbol{r})/2 + mg\Delta z$ up to a constant. The minimum of the harmonic trap is found at the point where the two terms linear in Δz cancel, *i.e.* for

$$z_0 = -\frac{r_0/2}{\sqrt{(b/b_0)^2-1}}, \quad (3.2)$$

where $b_0 = 2mg/\mu_{\rm B}|m_F|$ is the gradient that exactly compensates gravity. For $m_F = 2$, one has $b_0 = 15.3\,\mathrm{G/cm}$. Note that the ratio z_0/r_0 is a function of the gradient only and thus unchanged by the TOP field B_0. In the following, we will adopt the common practice of referring to z_0 as the gravitational "sag".

The trapping frequencies corresponding to the total potential expanded around this point are given by

$$\omega_\perp = \sqrt{\frac{|m_F|\mu_B b}{8m}\frac{r_0^2+8z_0^2}{(r_0^2+4z_0^2)^{3/2}}} \quad ; \quad \frac{\omega_z}{\omega_\perp} = \sqrt{\frac{8r_0^2}{r_0^2+8z_0^2}}. \quad (3.3)$$

In particular, one sees that the trap becomes isotropic for $z_0 = \sqrt{7/8}\,r_0$. The aspect ratio is a function of the ratio z_0/r_0 only and will thus equally be completely determined by the gradient, independently of B_0. The dependence of the sag on the gradient as well as the dependence of the aspect ratio on the sag are shown in figure 3.2.

One may inverse equation (3.2) to find the gradient that produces a given ratio z_0/r_0:

$$b = b_0\sqrt{1+\left(\frac{r_0}{2z_0}\right)^2}. \quad (3.4)$$

This has one important consequence: since an isotropic trap corresponds to a fixed ratio of z_0/r_0, there is only one possible value for the gradient (for a given m_F) that permits to obtain such a potential. For $m_F = 2$, the gradient for an isotropic trap is 17.4 G/cm which is only 14% above the value equivalent to gravity. The trapping frequency is now controlled by only one parameter—the TOP field B_0, or equivalently the radius of death $r_0 = 2B_0/b$. For $r_0 = 1\,\mathrm{mm}$,

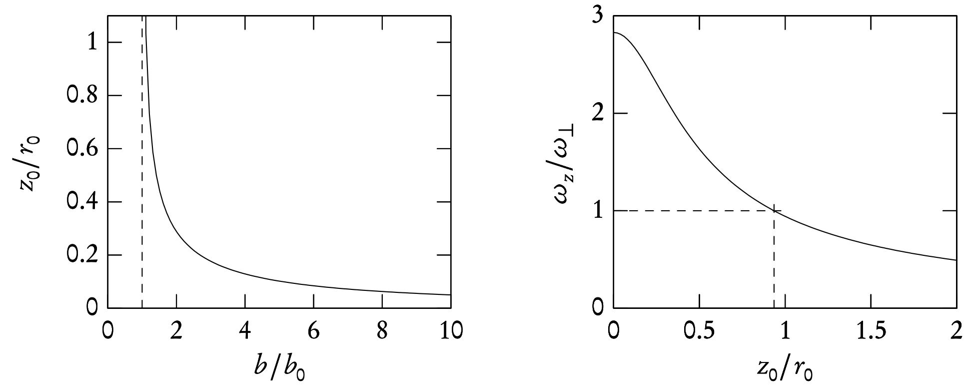

FIGURE 3.2: *Left: gravitational "sag" in units of the radius of death as a function of the magnetic gradient in units of the gradient that is equivalent to gravity. Right: aspect ratio of the resulting trap as a function of the sag (and hence of the gradient). An isotropic trap is obtained for* $z_0/r_0 = \sqrt{7/8}$.

one obtains a trapping frequency of 7.68 Hz, reference value from which all other possible frequencies can be calculated by noting that $\omega \propto 1/\sqrt{r_0}$. A radius of death of 1 mm is realised by choosing a TOP field amplitude of 0.87 G. Note that the field experienced by the atoms is no more $b\,r_0/2 = B_0$ as in the case of strong gradients, but $b(r_0^2 + 4z_0^2)^{1/2}/2$ which for the case of an isotropic trap is a factor of 2.12 higher.

In figure 3.3 we show a comparison of the effective field $B_{\mathrm{eff}} = B + b_0 z$ calculated from a numerical evaluation of the exact expression with the harmonic approximation (3.1). One sees that the harmonic approximation is excellent in the xy plane with no visible deviation up to the radius of death while in the vertical direction it is quite good "downwards" but fails sooner in the upward direction. This means that in experimental practice one has to make sure that oscillation amplitudes in the vertical direction be sufficiently small to guarantee that they take place in the isotropic harmonic regime.

After these preparations, we will now turn to the description of the actual experiments we performed. To verify Boltzmann's prediction, there are two experimental tasks to accomplish: firstly, to render the trap isotropic, and secondly, to excite the monopole and quadrupole modes in a cloud in the hydrodynamic regime and measure their frequencies and damping. We will begin our discussion with the excitation of the monopole mode which is directly connected to the dynamic compensation of the gravitational sag and then pass to the task of rendering the trap isotropic.

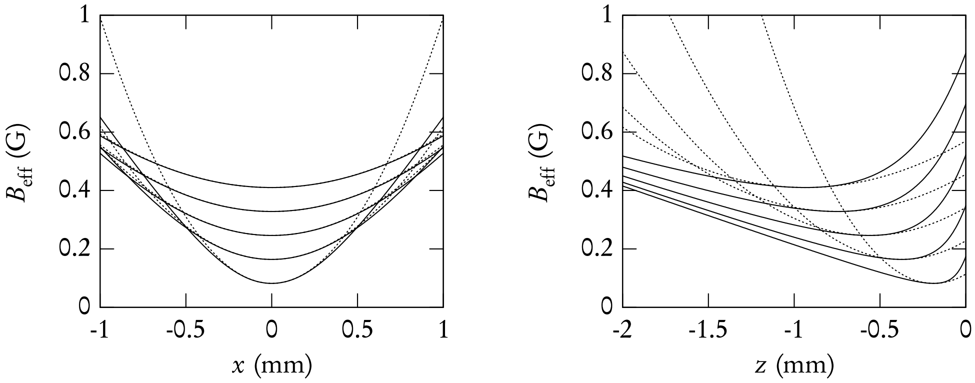

FIGURE 3.3: *Effective magnetic field* $B_{eff} = B + b_0 z$ *for* $b = 17.4\,\text{G/cm}$, i.e. *in the isotropic case. Solid lines show a numerical evaluation of the exact average field, dotted lines the harmonic approximation. The curves correspond to* $r_0 = 200\,\mu\text{m}, 400\,\mu\text{m} \ldots 1\,\text{mm}$ *(in our actual experiments,* r_0 *is somewhat larger, but the general tendency is clear from the values represented here). Left: Field in the horizontal plane around the minimum. Right: Field in the vertical direction.*

3.3 Sag compensation and monopole excitation

Experimentally speaking, the gravitational sag is inconvenient for several reasons: for the imaging system, it is advantageous to have the sample always at the same position to avoid having to displace optics elements each time the potential is changed (which means that it cannot easily be a varied parameter of a series). When the sag becomes too large, the time that can be used for a ballistic expansion becomes increasingly short since otherwise the sample will hit the bottom of the science cell. Moreover, a displacement of the trap position during decompression easily excites centre of mass oscillations in the vertical direction which are particularly undesirable since the harmonic range is smallest in this direction.

Compensating the sag

Conceptually, compensating the sag is simple: it is sufficient to add a homogeneous magnetic field of magnitude $b z_0 = B_0/[(b/b_0)^2 - 1]^{1/2}$ [see equation (3.2)] along the vertical direction which will effectively displace the quadrupole by the distance z_0. Note that this does not change the shape of the potential, it is only shifted as a whole.

It is not easy to carry this out in practice since the compensation of the sag needs to be quite precise in order to avoid excessive dipole oscillations. With a straightforward application of the theoretical formulae, we would be limited by the precision of our calibrations of our coils. The idea is thus to measure the compensation current I_{comp} needed to maintain the sample at a constant vertical position as a function of the quadrupole current I_q to which we can then fit the theoretical formula which permits at the same time to improve the precision of our coils' calibrations. For the generation of the compensation field, we use a coil pair in Helmholtz configuration (not listed in table 1.1 since it belongs to a preliminary version of the magnetic trap) on the vertical axis with a 150 W Delta current supply.

This procedure still leaves a free parameter which is a constant offset current. We can fix this offset by requiring that the trap centre of the TOP coincide with the one of the quadrupole. The latter is not easy to measure exactly due to the vertical asymmetry of a sample in a quadrupole trap, so we rather calculate the sag for one reference configuration which requires to inject a calibration of b and B_0 that has to be checked for consistency afterwards. The gradient (0.54 G/cm A) has been calibrated by a direct measurement of the coils' magnetic field before mounting. A calibration of B_0 is obtained by determining the evaporation frequency corresponding to the trap centre. The magnetic field there is equal to $[B_0^2 + (bz_0)^2]^{1/2}$ which has to be equal to $2h\nu_0/\mu_B$, where ν_0 is the frequency at which the atoms disappear. Since the sag appears in this formula, one has to solve for B_0 iteratively. For a given TOP current amplitude and a quadrupole current of 175 A we measure $\nu_0 = 2290 \pm 5$ kHz from which one calculates $B_0 = 3.23$ G and a sag of 56 µm, fixing the offset of the compensation current.

We can now carry out the procedure of keeping the sample in the same place, measuring I_{comp} as a function of I_q which we vary over a range from 32 A to 175 A. The result is shown in figure 3.4. We fit the function $I_{\text{comp}} = P_1/[(P_2 I_q)^2 - 1]^{1/2}$ to the resulting curve. The fit constants correspond to the gradient per unit current of the quadrupole, which is given by $P_2 b_0$ and found to be 0.53 G/cm A (just slightly smaller than the calibration stated above that we used up to then), and the magnetic field per unit current of the compensation coils given by B_0/P_1 with the best fit value 0.79 G/A.

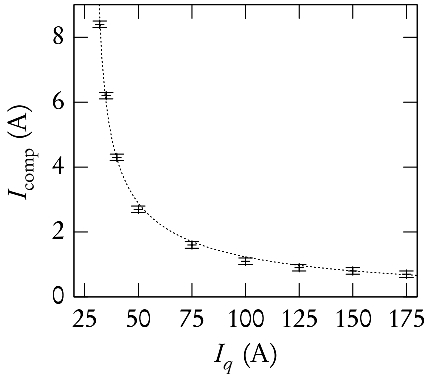

FIGURE 3.4: *Calibration of the sag compensation current: the necessary current I_{comp} is measured as a function of the quadrupole current I_q (error bars). The dotted line corresponds to a two parameter fit.*

Note that this calibration is done at constant B_0. It will remain correct as long as B_0 is well controlled. When there is a difference between the demanded and the real B_0 (due to nonlinearities in the response of electronic components such as the function generators), the compensation will equally show deviations.

Exciting the monopole mode

The sag compensation plays a critical role for the excitation of the monopole mode. This excitation can be accomplished by modulating the magnetic field B_0 at fixed gradient which will keep the aspect ratio constant but modulate the trapping frequency which is exactly what is needed. However, the sag will be modulated at the same time which can quickly lead to a strong excitation of the vertical dipole mode. We could not completely suppress this excitation (which is not a problem as long as the cloud stays in the harmonic part of the potential), but considerably reduce its amplitude by dynamically compensating the sag during the excitation. For the excitation, B_0 is modulated by 8% at the expected monopole frequency during five complete periods. The resulting dipole and monopole excitation of a quasi-pure BEC can be seen in figure 3.5. Like all data presented in this chapter, these images are taken after 25 ms of TOF. Here and in the following, the x axis is the axis of the magnetic transport (the H_1 axis), the y axis the horizontal axis perpendicular to it (H_2) and z the vertical axis (V).

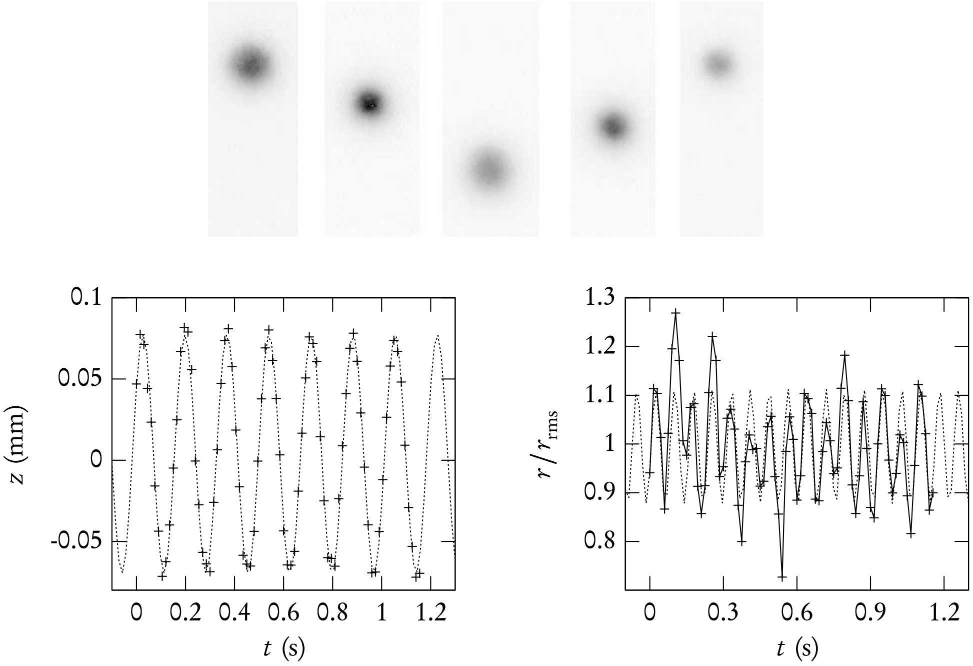

FIGURE 3.5: *Top: absorption images of an oscillating* BEC *at* 15, 30, . . . 75 ms *after an excitation of the monopole mode. The image plane is the* xz *plane. One clearly sees the oscillations of the cloud size and centre of mass. Left: vertical centre of mass position as a function of time. The dotted line corresponds to a sinusoidal fit with a frequency of* 5.83 Hz. *Right: Radius normalised by the rms radius* $r_{rms} = 25.3\ \mu\text{m}$. *The dotted line shows a sine fit with a frequency of* 12.9 Hz.

To extract quantitative information, we fit a two-dimensional Gaussian function to the condensate. Evidently, a Gaussian is not the correct form, but since the oscillations correspond only to displacements and scalings (the latter follows from the Castin-Dum equations [96]) we can at most make an error in the absolute numbers. We normalise the monopole amplitude to the root mean square radius $r_{\text{rms}} = \left(\overline{\Delta x^2 + \Delta z^2}\right)^{1/2}$ (the average is over all points in the series), so this poses no problem.

The amplitude of the dipolar motion is about 70 μm which is small compared to the radius of death which is equal to 1.7 mm so that the atoms only explore the harmonic part of the potential. Both the dipole and the monopole motion are conveniently fitted by a single sine curve which yields the frequencies 5.82 Hz for the vertical dipole motion and 12.9 Hz for the monopole mode. The ratio of these frequencies is 2.21, in excellent agreement with the theoretically expected value $\sqrt{5} \approx 2.24$.

The data shows no indication of a quadrupolar excitation: the quantity $(\Delta x^2 - \Delta z^2)/r_{\text{rms}}^2$ only shows erratic patterns with an amplitude of the order of 10^{-3}. The amplitude of the monopole exhibits some "overshoots", but they do not seem to stem from a quadrupole contribution either (we recall that the quadrupole mode whose principal axis coincides with the imaging axis looks just like a monopole mode) since when one tries to fit a sum of two sine curves, the second sine has a negligible amplitude and its frequency differs from the expected quadrupole frequency.

This shows that a modulation of B_0 with dynamic compensation of the sag is an efficient method for the excitation of the monopole mode. The simultaneous appearance of the vertical dipole mode is not a problem since its amplitude is sufficiently small thanks to the compensation. Note that the absence of quadrupole excitation is related to the lift of degeneracy between the monopole and quadrupole mode in a condensate. Indeed, we found experimentally that for a thermal gas in the collisionless regime, the quadrupole mode is excited appreciably with this scheme.

For reasons of symmetry, one would like to have a similar means to specifically excite the quadrupole mode. We do not have any data on this, but following the same logic this should be feasible by modulating the gradient at constant B_0 (equally with dynamic sag compensation): of course, this would at the same time excite the monopole mode since all trapping frequencies change in the same direction, but the change in the aspect ratio directly couples to the quadrupolar mode which has its principal axis along the vertical direction.

3.4 Rendering the trap isotropic

Our approach to the realisation of an isotropic trap can be divided into two steps: in a first step, we deliberately keep the frequency 5% higher along the vertical direction which decouples the vertical and horizontal degrees of freedom[1]. In this configuration we try to render the TOP trap as isotropic as possible in the xy plane. Once we are satisfied with this, we lower the gradient trying to equalise all three frequencies.

---

[1] The vertical frequency is nonetheless chosen close to the others since the idea is to have the TOP trap isotropic in the plane for the current amplitude used for an isotropic trap. In order to be able to use this amplitude without having an r_0 too small, the gradient must not be too high. This is especially important since the response of our function generators to the amplitude command is neither completely linear nor identical for the two generators.

In all cases, the frequencies are measured by exciting a dipolar motion and observing it for a given period of time. Since the absorption imaging technique is destructive, each measured point requires the generation of a new sample. The excitation of the dipolar motion in the TOP plane is done using a coil deliberately placed at an angle in which we induce a 50 µs current pulse. The vertical motion needs no excitation since it is already present due to the imperfection of the sag compensation.

Symmetrising the TOP *in its plane*

For the optimisation of the TOP with "high" vertical trapping frequency, we found graphs showing the projection of all points of one series on the imaging plane to be an excellent means for diagnostics: for a two-dimensional harmonic oscillator, the motion along the eigenaxes x' and y' is of the form $x'_0\cos(\omega_1 t+\phi_1)$ and $y'_0\cos(\omega_2 t+\phi_2)$. Due to the difference between the frequencies along the eigenaxes the trajectory will cover the entire rectangle $[-x'0, x'0]\times[-y'_0, y'_0]$ for sufficiently long times. If one regards the projection of the points of an experimental series on the xy plane, all points lie inside a rectangle the sides of which are parallel to the eigenaxes of the potential. The graphs permit at the same time to verify that the oscillation is well excited on both eigenaxes (hence the deliberate angle of the excitation coil) and to determine the angle between the eigenaxes of the potential and the x and y axes.

This angle permits to distinguish between the respective influences of the TOP currents' amplitudes and relative phase: if the TOP field is not the ideal one considered up to here, but has slight deviations in amplitude in phase such that

$$x_t = \frac{2(B_0+\Delta B/2)}{b}\cos(\omega t+\phi/2) \quad ; \quad y_t = \frac{2(B_0-\Delta B/2)}{b}\sin(\omega t-\phi/2)\,, \qquad (3.5)$$

with $\Delta B \ll B_0$ and $\phi \ll 1$, carrying out the expansion and averaging yields a potential of the type

$$V(x,y) = \frac{m\omega_0^2}{2}[(1+\alpha)x^2+(1-\alpha)y^2+2\epsilon xy] \qquad (3.6)$$

(we leave out the z direction for notational clarity). For a nearly isotropic TOP trap, one calculates $\alpha \simeq -0.104\Delta B/B_0$ and $\epsilon \simeq 0.208\phi$. The sag and aspect ratio between the mean frequency in the plane and the vertical one remain unaltered to first order in α and ϵ. A principal axis transformation of equation (3.6) yields the eigenfrequencies $\omega_\pm$ and the angles $\theta_\pm$ between the eigenaxes and the x axis:

$$\omega_\pm = \omega_0\sqrt{1\pm\sqrt{\alpha^2+\epsilon^2}} \quad ; \quad \tan\theta_\pm = -\frac{\alpha}{\epsilon}\pm\sqrt{\left(\frac{\alpha}{\epsilon}\right)^2+1}\,. \qquad (3.7)$$

When $\alpha \gg \epsilon$, the eigenaxes will almost coincide with the x and y axes. In the opposite case $\epsilon \gg \alpha$, the eigenaxes are rotated by 45° with respect to the x and y axes. Thus, the angle observed in a given measurement permits to see whether the phase or the amplitude is farther from the correct value. Two examples of such measurements are shown in figure 3.6.

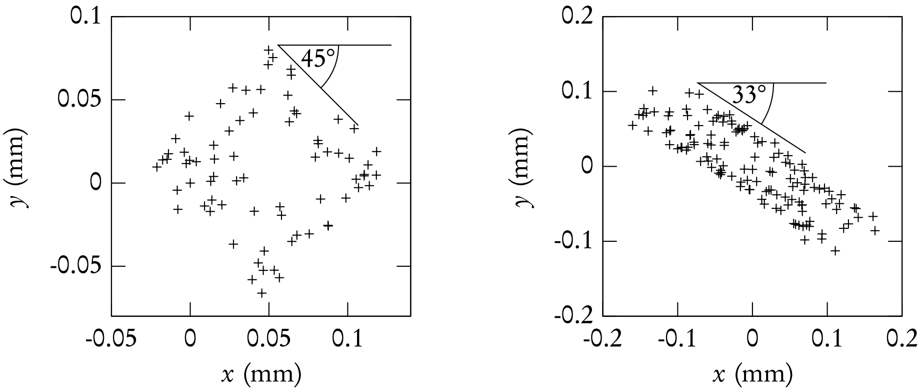

FIGURE 3.6: *Projection of all the points in one series in the xy plane. Left: case where the error in the relative phase dominates: the eigenaxes are turned by* $\sim 45°$. *Right: case where the errors in phase and amplitude are of equal order: the eigenaxes are turned by neither* 0° *nor* 45°. *Between these two datasets, the relative phase of the* TOP *currents has been corrected by* 4°.

This method is especially useful since the relative phase between the TOP coil pairs is hard to measure: while amplitudes can be measured sequentially using the same instrument, thus avoiding calibration errors, the relative phase can only be inferred from a simultaneous measurement of both channels. This implies the usage of two devices (even if they are two channels on the same instrument) which may have a relative dephasing themselves. Note that in the case of a perfectly isotropic trap there is no preferred referential, so the angle can take any value. One can nonetheless distinguish the isotropic case from one in which α and ϵ are of equal magnitude, but finite: in the isotropic case, the rectangle will shrink to a line since the axis of excitation is automatically an eigenaxis, whatever its orientation in the plane. Of course, when this occurs in experiment, one has to make sure that the excitation was not along an eigenaxis by accident which would have the same effect.

Owing to the finite rotation angle, the oscillations observed along any lab frame axis are actually superpositions of oscillations along the eigenaxes of the potential. When the frequencies get close, they exhibit clear beats. We have tried two different methods to extract the frequencies from such data: either we fit the sum of two sines with different frequencies to the oscillations along each of the measured axes or we rotate the measured points by the observed angle to obtain the oscillations along the eigenaxes and fit single sine curves to the result. The double sine method has the advantage of being considerably faster, but it treats the datasets as if they were independent so that there are redundant fit parameters. For both methods, the line of oscillation must turn by at least 90° in order to clearly discern the beats or the orientation of the rectangle's sides, respectively.

The three-dimensional case

Once the frequencies in the TOP plane are equal to better than within one percent, the only free parameter left is the gradient. It should thus be enough to precisely tune the quadrupole current to achieve an isotropic trap. Of course, there might be complications due to the imperfect geometry of the coils that introduces a coupling between different directions of space, but in a first step, all that one has to look at is the gradient.

It turns out that the current supply system (two current supplies in parallel delivering up to 200 A controlled by the experiment's computer using National Instruments PXI interface cards) we used in this version of the setup has a limited precision: the command voltage of a given channel can take on 1024 different values on the relevant range from 0 to 5 V (4096 values on the full range from −10 V to +10 V). This means that with a 200 A current supply the available precision is 0.2 A. The theoretical gradient of 17.4 G/cm is obtained for a current of 32.6 A according to the calibrations stated above. Thus, a precision of 0.2 A will permit to reach a precision of about 6×10^{-3}. In order to be able to do better, we use a coil pair (diameter ~ 6 cm, four windings each) on the vertical axis connected to a 150 W power supply (equally a Delta Elektronika unit) to fine-tune the gradient. The gradient per unit current of this supplementary coil pair is about 0.2 G/cm A. Taking together the factor of at least twenty between the peak currents of the power supplies (the 150 W Delta units exist in a 30 V, 5 A and a 15 V, 10 A version) and the factor of more than two of the specific gradients, this extra coil pair increases the possible precision by at least a factor of forty which is more than sufficient.

While decompressing the trap, one has to take care to avoid excessive excitation of dipole modes—especially the vertical one which easily acquires an amplitude of several hundreds of microns. Since the trapping frequencies become very low during decompression, it seems logical that it is advantageous to decompress very slowly. However, this is not what we found experimentally. The most likely explanation is the existence of mechanical resonances that transfer energy to the sample which does more harm when the trapping frequency is close to the resonance for a longer time. An obvious candidate for such a resonance is the 50 Hz frequency of the electric network.

To avoid this resonance, we adapted the sequence so that the vertical trapping frequency is already at 46 Hz (using a gradient of 93 G/cm and a TOP field of 6.7 G) after the 15 s decompression phase during evaporation. Of course, the frequency still passes by 50 Hz in this manner, but during evaporation the extra energy can be dissipated. During the subsequent second decompression phase, the gradient is varied as $(b_i - b_f)(1 + \cos\{\pi[1 - \exp(-t/\tau)]\})/2 + b_f$, where b_i and b_f are the initial and final value of the gradient, respectively, and τ is a time constant. B_0 is varied in the same manner. This functional form ensures a smooth variation of the sag compensation current. We found that vertical oscillations are minimised for a total duration of 10 s for this phase using a time constant $\tau = 2$ s.

When the gradient is lowered so that all three frequencies are approximately equal, the situation of the two-dimensional harmonic oscillator described above is generalised to three dimensions: the oscillations take place inside a cuboid the sides of which are parallel to the three eigenaxes of the potential. These eigenaxes form an orthonormal system that is rotated with respect to the lab frame, a rotation which can be described using the formalism of Euler angles. Just as in the two-dimensional case, an eigenaxis will almost coincide with a lab frame axis when the corresponding frequency is significantly different from the others—in fact, this is the reason why we could separate the system into a two-dimensional system and one lab frame axis by keeping the vertical frequency somewhat higher than the two others.

When one regards the projection of all points in a series on one imaging plane, the points will lie inside the projection of the cuboid on the plane. In the general case, this projection will have a hexagonal shape in which opposing sides are parallel, as can (approximately) be seen in figure 3.7 (right).

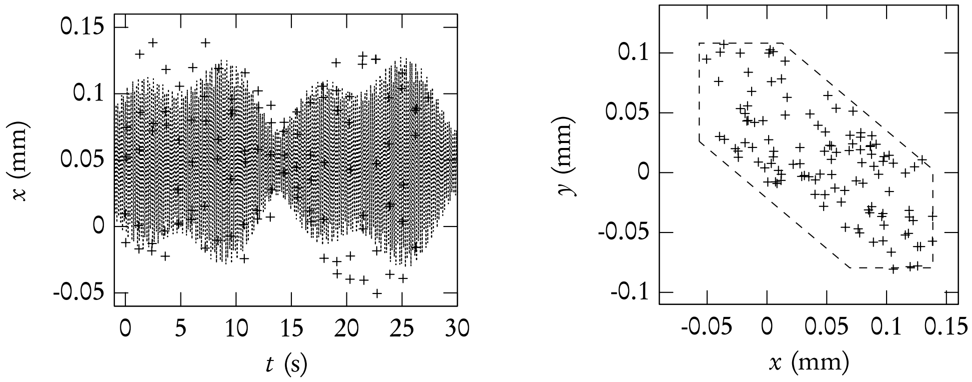

FIGURE 3.7: *Left: Oscillations in one spatial direction in a nearly isotropic situation. There are clear modulations in the amplitude corresponding to beats between the three frequencies. The rapidly oscillating dotted line corresponds to a simple three frequency fit to the data. Right: projection of all points of the oscillation on the* xy *plane. Since all three eigenaxes are at arbitrary angles, the projection takes on a hexagonal shape. The dashed line is just a rough guide to the eye and not supposed to render accurately the outline of the points.*

The oscillations along a given lab frame axis become quite complicated in the three-dimensional case since one now has a superposition of oscillations at three different frequencies. An example of such an oscillation can be seen in figure 3.7 (left). To extract the frequencies, one has to generalise one of the two methods stated above. Since the reconstruction of the Euler angles from two projections (or worse, from a single one) is not only mind-twisting but also hard to do accurately, we opted for a fit using a sum of sines. We improved the scheme by performing simultaneous fits using the same fit parameters on the oscillations on all observed axes. In this case, the fit parameters are three amplitudes, three frequencies, three phases and the three Euler angles.

To give an example, for the data shown in figure 3.7, this fitting procedure yields the following results: the "vertical" eigenaxis of the potential is tilted with respect to the vertical lab axis by 22°, the frequencies in the tilted "horizontal" plane are 5.97 Hz and 5.92 Hz while the frequency along the "vertical" axis is 5.86 Hz. Since the fitting procedure is quite complicated, it can get stuck in secondary minima so that different seed values may yield different results. We found that frequencies inferred from such a three-frequency fit typically vary by up to one percent.

Evidently, it is advantageous to have data on all three axes because otherwise there will be one frequency that is just a slight "admixture" along both observed directions. Since on one image one can only see a projection on one plane, one has to image the same series from two directions in order to obtain a complete data set. This can be done either by imaging simultaneously on two axes during the sequence or by repeating a series under identical conditions and changing the imaging axis between the runs. For a certain time, we tried the first possibility, but we were limited by the quality of the resulting images since for each imaging direction there is a motion of the cloud in the observed plane due to the radiation pressure from the other imaging beam. We thus abandoned this scheme and opted for the more time-consuming solution of repeating the series.

3.5 Limitations and open questions

In order to increase the measurement's precision, one has to observe the oscillations of the sample for increasingly long times. Basically, to measure a single frequency, one measures the accumulated phase per time. In order to be able to identify the phase, one has to take several points per period, and to increase the relative precision of the measurement, one has to measure over a long time interval. Depending on the quality of the data, one may try to leave out a part of the interval in order to get longer periods with a comparable number of points, but if there is noise, this can lead to errors in the count of periods which destroy the gain in precision. In the case of a measurement of several frequencies, the same considerations apply to the beats between the individual frequencies. In our experiments, we successively increased the total duration of our measurement interval up to 30 s. We experimented with schemes of leaving out part of the interval, but returned to a measurement of all points later on.

Such long measurement intervals are inconvenient for two reasons: the first one is that evidently the measurement will take considerably longer. The second and more fundamental one is that the measurements only make sense if they are reproducible which becomes increasingly difficult with increasing duration. While trying to improve the measurement precision beyond the one percent level, we eventually noticed that the frequencies coming out of two similar measurements did not agree. To see how this comes about we repeated one series with identical parameters within four days and explicitly compared the trajectories. The result is shown in figure 3.8.

One clearly sees that for short times on the order of a few seconds, the x component is reproducible from one series to the other, but beyond 6 s the normalised difference between the x components from both series becomes completely erratic. One might be tempted to accuse the atomic micro-motion in the TOP [72] that is not reproducible since the SRS generators cannot be triggered, but the amplitude of the micro-motion for a TOP frequency of 10 kHz after 25 ms of TOF is only $\sim 4\,\mu$m which is a small effect—besides, there is no reason why it should be a progressive effect. Thus, we allot the non-reproducibility mainly to thermal effects.

Given this situation, the question arises whether it is possible to carry out the measurements we have in mind nonetheless, *i.e.* whether the time during which the oscillations are repro-

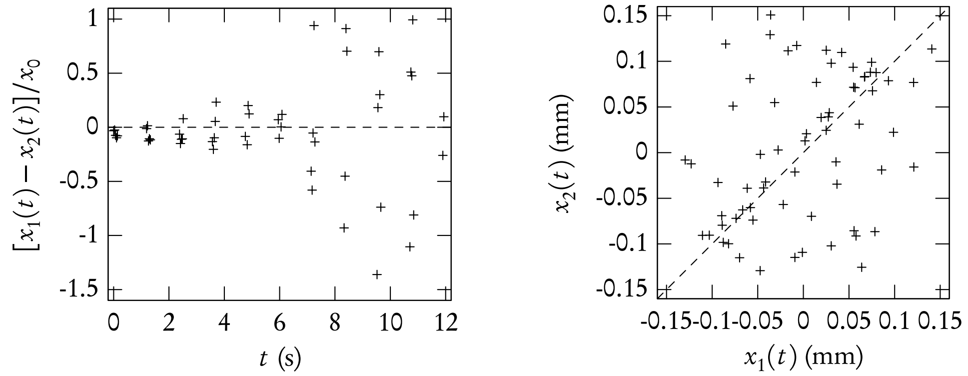

FIGURE 3.8: *Illustration of the reproducibility problem:* x_1 *and* x_2 *are the same coordinate for two series with identical parameters taken within four days. Left: Difference of both divided by the amplitude of oscillation. One sees that after about* 5 s *(about 30 periods) the difference becomes non-negligible. Right: The coordinate of the second series as a function of the coordinate of the first. Only for short times do the points lie close to the* $x_2 = x_1$ *line that corresponds to perfect reproducibility.*

ducible is sufficient to see an appreciable damping of the quadrupole mode. This would permit to discriminate between the trivial situation of non-damping due to the absence of collisions and the scenario described by Boltzmann where the non-damping is a specific property of the monopole mode only.

The thermal gases that we were able to load into the near-isotropic trap were typically quite close to quantum degeneracy with typical temperatures of 25 nK and atom numbers of 600 000. For a trapping frequency $\omega = 2\pi \times 8\,\mathrm{Hz}$, this corresponds to a central density of $1.27\,\mu\mathrm{m}^{-3}$. The collision rate is given by $\gamma = n(0) v_{\mathrm{th}} \sigma_{\mathrm{coll}}/2$, where $v_{\mathrm{th}} = (8kT/\pi m)^{1/2}$ is the thermal velocity and $\sigma_{\mathrm{coll}} = 8\pi a^2$ is the collisional cross section for pure s wave scattering (a is the scattering length). Substituting these definitions one finds that the scattering rate is given by $\gamma = 4a^2 N m \omega^3/\pi k T$. For the numerical values stated above, $\gamma = 1.02\,\mathrm{s}^{-1}$. We thus obtain $\omega/\gamma = 48.3$ which is deeply in the collisionless regime. According to Guéry-Odelin *et al.* [88], the damping time constant of the quadrupole mode in a classical gas is then approximately given by

$$\Gamma \simeq \frac{\tau}{2} \frac{\omega_{\mathrm{CL}}^2 - \omega_{\mathrm{HD}}^2}{1 + (\omega_{\mathrm{CL}}\tau)^2}, \tag{3.8}$$

where $\tau = 5/4\gamma$. For our numbers, $\Gamma = 0.21\,\mathrm{s}^{-1}$. Thus, in five seconds, the amplitude of the quadrupole should have decreased to less than a third which would be marginal but perhaps still acceptable. However, it turns out that for our near-degenerate clouds, the damping is considerably slower since we have observed appreciable quadrupole amplitudes even after more than ten seconds. Thus, we were not able to obtain a configuration where there was appreciable damping of the quadrupole over a duration during which measurements are reproducible.

We therefore decided to suspend this experimental project and to replace the quadrupole coils by the ones of the current version of the setup with enhanced water cooling. In doing so, we lost the absolute calibrations done up to this moment (even if we could redo them more quickly since we have had time to refine our methods), so we decided to put the priority on the work on two-dimensional Bose gases instead of carrying on the isotropic trap project. Since then, we have equally modified further parts of the setup and gained a more thorough understanding of other ones so that one may be optimistic that today we could achieve a better reproducibility. To be explicit, we have gained more control on the following aspects:

- Due to the improved water cooling system, the temperature of the quadrupole coils varies less during the sequence. Thus, there is less thermal dilatation of the coils.
- We have seen that (with the current version of the setup) it takes a certain time for the setup to enter a "stationary" regime. During that warm-up time, the equilibrium position of the atomic sample is displaced by about 30...45 μm (the displacement is larger for shorter MOT durations since the magnetic trap cools down during the MOT phase) in the vertical direction and about 12 μm in the x direction. After a "cold start", it takes between 45 minutes and an hour to reach the stationary regime. When the experimental cycle is interrupted (for example to change parameters), it takes some minutes until the stationary regime is reestablished. In order to have reproducible data, one has to ensure that the experiment is properly warmed up before taking data. However, it is not evident that there actually is a stationary regime when the duration of individual shots may differ by as much as 30 s.
- We have exchanged the TOP function generators by a single device that may be triggered so that the TOP phase is now reproducible from shot to shot. In this manner, the micromotion of the atoms is reproducible as well. At the same time, the usage of two channels of a single device should ensure an equal response of both channels to external commands.
- In the near future, we will implement a non-destructive phase contrast imaging system which will permit to take several images during one experimental cycle which will considerably reduce the duration of series so that thermal drifts will be less important.

Compared to the others, the third point is rather cosmetic, but it reduces the number of questions one might want to ask when data differs from expectations.

A complementary approach to reducing the problem of reproducibility is to try to increase the trapping frequency since it would permit to measure the same number of oscillations over shorter periods of time. Within the "TOP with gravity" scheme presented here, one cannot increase the trapping frequency much since otherwise the TOP field B_0 becomes too weak to ensure adiabatic following of the atomic magnetic moment. The Oxford group has shown that with a zTOP [66] it should be possible to produce an isotropic trap with a higher trapping frequency—however, the experimental feasibility of this approach has yet to be demonstrated.

In summary, we have developed a range of techniques that should permit to render a TOP trap isotropic to within a few 10^{-3}. We are equally able to excite a pure monopole mode in the trapped gas and to control residual dipole motion sufficiently to ensure that the sample remains in the harmonic part of the potential. Since the problem of reproducibility prevented us from going further, there remain a few questions that we have not yet addressed experimentally such as the excitation of the quadrupole mode and the observation of its damping (as well as the non-damping of monopole) as well as the creation of non-condensed samples with a sufficient collision rate to be in the hydrodynamic regime. The most difficult among these issues is certainly the obtention of an appreciable collision rate to increase the damping of the quadrupole mode, but in principle it should be possible to resolve all these problems. With the progress of understanding of our setup since the acquisition of the data shown here, there are chances that Boltzmann's prediction may finally be verified within the next years.

Chapter Four

Producing versatile optical potentials using phase plates

> Einen solchen Gebrauch also, der mit der Natur
> völlig übereinträfe, könnte man den symbolischen
> nennen, indem die Farbe ihrer Wirkung gemäss
> angewendet würde und das wahre Verhältnis
> sogleich die Bedeutung ausspräche.
>
> JOHANN WOLFGANG VON GOETHE (1749–1821)
> *Zur Farbenlehre*

THE principal tools used for the manipulation of neutral atoms are quasi-static magnetic fields and electromagnetic waves [97], the latter in the form of radio-frequency waves and coherent light from laser sources (the use of electro-static fields [98, 99] and microwaves [100] has been reported, but is far less common). Therefore, there are continuous efforts to render these tools more versatile and to enhance existing manipulation techniques. We have seen some examples of such efforts in chapter 2. In this chapter we will discuss a means to extend the possibilities of dipole potentials created with laser light: holographic plates that imprint a carefully chosen phase distribution on an incident light beam [101, 35, 102]. In fact, there is a second type of holographic pattern which changes the field amplitude rather than the phase [103, 104], but we will not consider these here since they have the disadvantage of reducing the available light intensity. The potentials tailored by holographic plates rapidly found applications for the production of multiple optical tweezers [105, 106] which may be used for the controlled manipulation of single atoms [107].

In order to appreciate the working principle of the phase plates, the chapter begins with some brief reminders on the dipole force (section 4.1), followed by some rather comprehensive reminders on wave optics in general and Gaussian beams in particular (section 4.2). We shall dwell on those somewhat longer than what is strictly necessary for the purposes of this chapter, hoping it will serve to clarify certain points such as the validity of the paraxial approximation. Besides, we will come back to the equations in this section for a different reason in chapter 7.

In section 4.3, having established the bases, we calculate analytically the electric field distributions created by the four types of phase plates that are at our disposition: the "phase step" plate where the phase jumps from 0 to π on a line that divides the plate in half, the "phase barrier" plate on which the phase is zero everywhere except on a stripe in the middle of the plate where it equals π, and two different kinds of "vortex" plates where the phase increases from 0 to $2\pi n$ (n an integer) when turning around the plate.

The results of these calculations are then compared to experimental measurements taken with our actual plates (which have been fabricated by the company Silios and are designed to be used with light at a wavelength of 532 nm) for all four types (section 4.4). Finally, we discuss the preparation of the phase step and barrier plates for the creation of two-dimensional Bose gases. This last section has its logical continuation in chapter 6 where we shall present and discuss experiments that we have conducted on two-dimensional Bose gases using the phase step plate. Possible future uses of the phase barrier and vortex plates will be mentioned in chapter 8.

4.1 The dipole force

Atoms plunged into a light field experience a force that can be divided into two qualitatively different components [108]: (i) the scattering force which is nonconservative and caused by fluorescence cycles, *i.e.* the absorption of a photons followed by the spontaneous emission of randomly directed photon, and (ii) the conservative dipole force caused by coherent photon scattering processes.

The dipole force scales broadly speaking as $-I/(\omega_0 - \omega)$ where ω_0 is an atomic transition frequency, ω the light frequency and I the intensity. If the light frequency is higher than the transition frequency (*blue-detuned* light), the potential is repulsive and atoms will be attracted to local intensity minima. In the opposite case (*red-detuned* light) the potential is attractive and atoms will accumulate in local maxima. The scattering force is just the momentum carried by a photon multiplied by the photon scattering rate, which falls off as $(\omega_0 - \omega)^{-2}$ for large detunings. Thus, if the frequency of the light is strongly detuned with respect to the atomic transition frequencies, photon absorption is strongly suppressed and the principal contribution comes from the dipole force.

For the calculation of the dipole force, there are two common approximations the validity of which has to be verified: the first one is the "Rotating Wave Approximation" (RWA) which consists in neglecting terms proportional to $1/(\omega_0 + \omega)$ (where ω_0 is a given resonance frequency) against terms proportional to $1/(\omega_0 - \omega)$ which is evidently correct for small detunings [109]. In our case, however, the transition frequencies corresponding to the D_1 and D_2 line of our ^{87}Rb atoms are $\omega_{D_1} = 2\pi \times 3.85 \times 10^{14}$ Hz and $\omega_{D_2} = 2\pi \times 3.77 \times 10^{14}$ Hz, respectively [60]. The laser frequency is $\omega = 2\pi \times 5.65 \times 10^{14}$ Hz (corresponding to the 532 nm wave length of our 10 W Verdi laser fabricated by the Coherent company) so that $|(\omega_{D_1} - \omega)/(\omega_{D_1} + \omega)| = 0.19$. Thus, one has to retain the non RWA terms in order to have results that are correct to better than within twenty percent.

The second approximation consists in neglecting the difference between the detunings with respect to the different fine structure energy levels of the atoms. This is nothing but the difference between the transition frequencies ω_{D_1} and ω_{D_2}. For our parameters, one has $|(\omega_{D_1} - \omega_{D_2})/(\omega_{D_1} - \omega)| = 0.045$, so this approximation is reasonable. In the following, we will set $\omega_0 \equiv 1/3\omega_{D_1} + 2/3\omega_{D_2} = 2\pi \times 3.80$ Hz (the factors correspond to the Clebsch-Gordan coefficients that appear when the atoms interact with linearly polarised light).

Under these conditions, the dipole potential U and the photon scattering rate Γ_{sc} are given by the expressions [110]

$$U = -\frac{3\pi c^2}{2\omega_0^3}\left(\frac{\Gamma}{\omega_0-\omega}+\frac{\Gamma}{\omega_0+\omega}\right)I \quad ; \quad \Gamma_{\mathrm{sc}} = \frac{3\pi c^2}{2\hbar\omega_0^3}\left(\frac{\omega}{\omega_0}\right)^3\left(\frac{\Gamma}{\omega_0-\omega}+\frac{\Gamma}{\omega_0+\omega}\right)^2 I\,, \tag{4.1}$$

where c is the speed of light in vacuum and $\Gamma \equiv 2/3\Gamma_{D_2}+1/3\Gamma_{D_1} = 2\pi\times 5.97\,\mathrm{MHz}$ is the natural line width of the rubidium D line [60]. In our case, the laser is blue-detuned with respect to the atomic transitions, so the potential U will be repulsive. In our actual experimental situation, all quantities except the intensity are fixed and can be absorbed into simple multiplicative constants: $U = \alpha I$, $\Gamma_{\mathrm{sc}} = \beta I$. Plugging in all constants, we obtain $\alpha = 8.09\times 10^{-37}\,\mathrm{Jm^2/W}$ and $\beta = 0.65\times 10^{-9}\,\mathrm{m^2/Ws}$.

Experimentally, one wants to minimise the photon scattering rate as it leads to heating of the sample. We will now estimate this rate for a relevant example: let us imagine an intensity distribution in one dimension which has a local harmonic minimum. The corresponding potential will be of the form $U = U_0 + m\omega_{\mathrm{ho}}^2 x^2/2$. The typical extension of a cold sample in this potential well will be the harmonic oscillator length $a = \sqrt{\hbar/m\omega_{\mathrm{ho}}}$. The average of the potential from $-a$ to $+a$ around the minimum is[1] $U_0 + \hbar\omega/6$. If the intensity vanishes in the minimum, the photon scattering rate will thus be around $\beta\hbar\omega_{\mathrm{ho}}/6\alpha$. Now, $\beta\hbar/6\alpha = 1.38\times 10^{-10}$, so the photon scattering rate is small against 1/s for any experimentally relevant trapping frequency. Likewise, an intensity corresponding to 1 mW focussed on a surface of $1\,\mathrm{mm}^2$ corresponds to a photon scattering rate of $\Gamma_{\mathrm{sc}} = 0.65\times 10^{-6}\,/\mathrm{s}$. Thus, for our Verdi operating at 532 nm, photon scattering remains a minor issue as long as the minima in which the atoms are trapped remain at reasonably low intensities.

4.2 *Reminders on wave optics*

In order to set the stage for the discussion of the phase plates, we will first review the equations of wave optics in the paraxial approximation [111, 112] and Gaussian light beams [113] on an introductory textbook level. This permits us to define all required concepts and notations for this chapter as well as for the imaging aspects discussed in chapter 6.

Propagation of light

The basis for the understanding of the phase plates' effect is to know how the electric field transforms along a propagating light beam. The electric field $\boldsymbol{E}(\boldsymbol{r},t)$ of a light wave can be described by a *d'Alembert wave equation*

$$\frac{\partial^2}{\partial t^2}\boldsymbol{E}(\boldsymbol{r},t) + c^2\Delta\boldsymbol{E}(\boldsymbol{r},t) = 0\,. \tag{4.2}$$

---

[1] The one-dimensional case is the most disadvantageous one: in 2d, when averaging over a disk of radius a, the second term is multiplied by 3/4.

This is a linear equation which does not induce any coupling between the different vector components of the electric field, so for all that follows it will not be necessary to heed its vectorial character and we will write scalar equations. We can further simplify the equation by noting that we are working with monochromatic light where the electric field takes the form[2] $E(\boldsymbol{r},t)=E(\boldsymbol{r})e^{i\omega t}$. The d'Alembert equation (4.2) thus simplifies to the *Helmholtz equation*

$$\Delta E(\boldsymbol{r})+k^2E(\boldsymbol{r})=0\,, \tag{4.3}$$

with the wave number $k=\omega/c$.

The general solution of this equation is conveniently expressed by its *Green function* (or *propagator*)

$$\mathscr{G}(\boldsymbol{r}'-\boldsymbol{r})=\mathscr{C}\frac{e^{-ik|\boldsymbol{r}'-\boldsymbol{r}|}}{|\boldsymbol{r}'-\boldsymbol{r}|}\,, \tag{4.4}$$

where $\mathscr{C}$ is a normalisation factor that we have yet to fix. This function permits us to calculate the electric field on a surface $\mathscr{S}'$ if we know it on a surface $\mathscr{S}$:

$$E(\boldsymbol{r}'\in\mathscr{S}')=\int_{\mathscr{S}}\mathrm{d}^2r\,E(\boldsymbol{r})\mathscr{G}(\boldsymbol{r}'-\boldsymbol{r})\,. \tag{4.5}$$

Physically speaking, this is nothing but Huygens's principle: each point on the surface $\mathscr{S}$ can be regarded as the origin of a spherical wave, and the electric field on a second surface $\mathscr{S}'$ is obtained by summing the contributions of all those "elementary waves"[3]. While the form of the surfaces $\mathscr{S}$ and $\mathscr{S}'$ can in principle be arbitrary, the only case of interest for our purposes will be planes perpendicular to the propagation axis. This situation is illustrated in figure 4.1.

In the following, we will focus on the propagation of light beams where in each plane perpendicular to the propagation direction the total power is concentrated in a finite area. Thus, distances L along the direction of propagation (for concreteness, let it be the z axis) will in general be far greater than distances perpendicular to it, permitting us to use the *paraxial approximation*

$$|\boldsymbol{r}'-\boldsymbol{r}|\simeq L\left(1+\frac{(\boldsymbol{\rho}'-\boldsymbol{\rho})^2}{2L^2}\right)\,, \tag{4.6}$$

where $\boldsymbol{\rho}^{(\prime)}$ denotes the projection of $\boldsymbol{r}^{(\prime)}$ on the xy plane and is thus a vector in a two-dimensional space. All vectors appearing in the following are such 2d vectors. Within this approximation, the Green function reads[4]

$$\mathscr{G}(\boldsymbol{\rho}'-\boldsymbol{\rho})=\frac{\mathscr{C}}{L}e^{-ikL}e^{-ik(\boldsymbol{\rho}'-\boldsymbol{\rho})^2/2L}\,. \tag{4.7}$$

---

[2] Rigorously speaking, the electric field is the real part of this quantity. The quantity of interest for dipole potentials is the time-averaged (over one period of oscillation) intensity which is proportional to the square of the real electric field. Since $\overline{(\Re\{E\,e^{i\omega t}\})^2}=|E|^2/2=\overline{(|E|\cos\omega t)^2}$, one can do all calculations as if the field was complex.

[3] Note that (4.4) corresponds to a retarded Green function. It will give correct results only when applied in the direction of propagation of the light field (in the other direction, one has to use the advanced Green function which differs from the retarded one by the sign inside the exponential).

[4] Note that we can just set the denominator equal to L since the correction is of second order in ρ/L. In the exponent, however, one has the product of ρ/L with kL which has no reason to be small since kL can be arbitrarily large so that the ρ^2 term is not negligible.

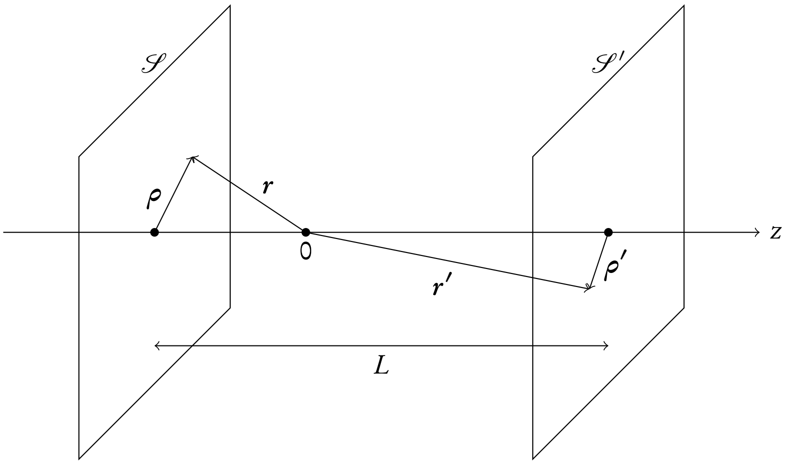

FIGURE 4.1: *Geometric conventions for the propagation of the light field. The field distribution is supposed to be known in a plane $\mathscr{S}$ and we want to calculate it in a second plane $\mathscr{S}'$ at a distance L along the z axis. The projection of the physical points $\mathbf{r}^{(\prime)}$ in the respective planes is denoted by $\boldsymbol{\rho}^{(\prime)}$.*

The argument of the Green function is now the difference of two 2d vectors, even though the physical points described by these vectors are in different planes.

Now, conservation of energy requires that

$$\int_{\mathscr{S}} \mathrm{d}^2\rho\, |E(\boldsymbol{\rho})|^2 = \int_{\mathscr{S}'} \mathrm{d}^2\rho'\, |E(\boldsymbol{\rho}')|^2 \,. \tag{4.8}$$

Substituting equation (4.5) for the electric field in the plane $\mathscr{S}$, one finds

$$\int_{\mathscr{S}'} \mathrm{d}^2\rho'\, |E(\boldsymbol{\rho}')|^2 = \int_{\mathscr{S}} \mathrm{d}^2\rho \int_{\mathscr{S}} \mathrm{d}^2\rho''\, E(\boldsymbol{\rho})E^*(\boldsymbol{\rho}'') \int_{\mathscr{S}'} \mathrm{d}^2\rho' \mathscr{G}[\boldsymbol{\rho}'] \mathscr{G}^*[\boldsymbol{\rho}' - (\boldsymbol{\rho}'' - \boldsymbol{\rho})] \,. \tag{4.9}$$

In order to reproduce equation (4.8) from equation (4.9), one has to require

$$\int_{\mathscr{S}'} \mathrm{d}^2\rho' \mathscr{G}(\boldsymbol{\rho}')\mathscr{G}^*(\boldsymbol{\rho}' - \boldsymbol{\rho}) = \delta(\boldsymbol{\rho}) \tag{4.10}$$

which readily gives $|\mathscr{C}| = 1/\lambda$. One can fix the phase of the propagator by requiring that a plane wave $E_0 e^{-ikz}$ be multiplied by e^{-ikL} when propagated over a distance L (conceptually, this approach is a bit doubtful since a perfect plane wave physically cannot be described within the paraxial approximation). The normalisation factor then becomes $\mathscr{C} = i/\lambda$. Thus, the final expression for the propagator in the paraxial approximation is

$$\mathscr{G}(\boldsymbol{\rho}' - \boldsymbol{\rho}) = \frac{i}{\lambda L} e^{-ikL} e^{-ik(\boldsymbol{\rho}'-\boldsymbol{\rho})^2/2L} \,. \tag{4.11}$$

The phase factor e^{-ikL} plays an important role in interferometric experiments in which a light beam is split up into several parts that are then recombined after running through different lengths, as in a Mach-Zehnder interferometer. For our purposes, all phase factors without explicit dependence on x and y will vanish in final results since we always regard the intensity in a single plane. Thus, we will not always bother to explicitly write down these global phases.

It is worthwhile to note [113] that in many cases the paraxial approximation is much less restrictive than the derivation presented here using the approximation (4.6) suggests: in particular, in the case of a well localised light beam (such as a Gaussian one), the propagator (4.11) may be used for arbitrarily short distances and will yield correct results. The reason is the following: the paraxial propagator will obviously give the correct answer when used over a large distance L from a plane $\mathscr{S}_1$ to a different one $\mathscr{S}_2$. If now the electric field in the plane $\mathscr{S}_2$ is well localised as well, there is no reason against calculating a propagation from $\mathscr{S}_2$ over a distance $L(1-\epsilon)$, with $\epsilon \ll 1$, in the opposite direction so that one obtains the field in a plane $\mathscr{S}_3$ which is at the small distance ϵL from the first plane $\mathscr{S}_1$. The result one obtains from this double propagation is the same as the one that is found using a direct propagation over the distance ϵL from $\mathscr{S}_1$ to $\mathscr{S}_3$. Thus, as long as it is possible to find a plane at a large distance where the power is well localised so that one can do a backward propagation from there using the paraxial approximation, it is justified to use the paraxial propagator over arbitrarily short distances [113]. This is the case for the unperturbed propagation of a well localised beam, but breaks down in general when diffraction occurs, since diffraction patterns usually have electric field distributions that fall off quite slowly. The same applies to the electric field after a phase plate that induces abrupt variations of the phase[5]. In such cases, it is still possible to calculate the field at a large distance from the perturbing object using the paraxial approximation (corresponding to the regime of *Fraunhofer diffraction*), but one cannot hope to obtain correct results for shorter distances.

Optical elements

In actual experiments, we use optical elements to change the shape of light beams. The two objects of interest here are lenses and phase plates. Evidently, mirrors are important experimentally, but since an ideal mirror will not alter the electric field distribution (of course, a real one will cause some attenuation as well as clipping on its borders), we will not consider them here. The same applies to retardation plates and polarisation cubes.

Lenses are used to change the beam's curvature, permitting for example to make it converge in a certain plane. An ideal lens conserves the total power. Thus, for an ideal, infinitely thin lens, the modulus of the electric field directly after the lens must be the same as the one directly before the lens. In other words, from the point of view of wave optics, a lens does nothing but imprint a certain phase distribution on the electric field. For an ideal lens with focal length f, the electric field transforms as

$$E(\boldsymbol{\rho}) \mapsto E(\boldsymbol{\rho}) e^{ik\rho^2/2f} \ . \tag{4.12}$$

---

[5] This is clearly the case for phase plates with phase jumps such as the step and barrier plates. For the vortex plates it is less evident, but it turns out to be similar.

This definition is chosen to reproduce as closely as possible the behaviour of an ideal lens as one would expect from geometrical optics. If one combines a lens and a propagation over the distance f, the two quadratic terms in the phase will cancel out and the resulting electric field will be (almost) the Fourier transform of the one incident on the lens:

$$E(f,\boldsymbol{\rho}') = \frac{e^{-ik\rho'^2/2f}}{\lambda L} \int_{\text{lens}} \mathrm{d}^2\rho\, E(0,\boldsymbol{\rho}) e^{ik\boldsymbol{\rho}\cdot\boldsymbol{\rho}'/f} \,, \tag{4.13}$$

up to a constant global phase. The focussing effect is thus achieved by a modification of the phase distribution. Broadly speaking, one may say that the phase determines "where the intensity will go". Now, one also obtains a Fourier transform by letting the beam propagate on a very long distance so that $k\rho^2/2L \ll 1$ for all values of $\boldsymbol{\rho}$ for which $E(\boldsymbol{\rho})$ gives a non-negligible contribution. This means that the intensity distribution in the focal plane of a lens is (up to a scale factor) the same one would find after an infinitely long propagation. This equivalence has the important consequence that the field in the focal plane of a lens may be calculated correctly within the paraxial approximation even if the physical distance is not large compared to the extension of the intensity distribution incident on the lens.

As can be seen from equation (4.13), the situation between the lens plane and the focal plane after the lens is not symmetric: if the incident field has a uniform phase, the field in the focal plane will have a finite curvature (which causes a displacement of the plane in which the intensity is most strongly confined). A more symmetric situation prevails between the two focal planes (the one before and the one after the lens): using two propagations by a distance f and multiplying by the "lens phase" in between, one readily finds

$$E(f,\boldsymbol{\rho}') = \frac{i}{\lambda f} \int \mathrm{d}^2\rho E(-f,\boldsymbol{\rho}) e^{ik\boldsymbol{\rho}\cdot\boldsymbol{\rho}'/f} \tag{4.14}$$

provided there is no clipping due to the finite size of the lens. Thus, if the phase is uniform in the incident focal plane, it will also be uniform in the outgoing focal plane. In any case, the respective electric field distributions are pure Fourier transforms of one another. This is just the focussing property of the lens: a collimated beam is converted to a strongly converging beam while a beam strongly diverging from the incident focal plane becomes collimated.

The fact that (apart from a different phase factor) the electric field in the outgoing focal plane is the Fourier transform of both the field in the incoming focal plane and the plane of the lens itself might sound contradictory since the intensity distributions in these two planes are different in general. In fact, this is a consequence of the mathematical structure of the paraxial propagator, and the phenomenon is even more general: the field distribution in the incoming focal plane can be calculated from the distribution in any other plane $\mathscr{S}$ on the same side of the lens using the appropriate (retarded or advanced) paraxial propagator. The electric field distribution in the outgoing focal plane is the Fourier transform of the distribution in the incoming focal plane and thus, by virtue of the convolution theorem, the product of the respective Fourier transforms of the field distributions in the plane $\mathscr{S}$ and the paraxial propagator. Since the Fourier transform of the paraxial propagator is a pure phase factor, we find that the field distribution in the outgoing focal plane is (apart from the phase factor) the

Fourier transform of *any* particular plane on the incoming side. Of course, this is only true for freely propagating beams. For the usage of our phase plates, this is quite advantageous since it means that as long as no clipping occurs, the position of the phase plate should not at all be critical (which is what one observes experimentally).

Using the same type of calculation, one readily finds the magnifying property of lenses: the electric field distributions between an object plane at distance d and an image plane at b on the other side of the lens, with $1/d + 1/b = 1/f$ (thin lens equation), a short calculation yields

$$E(b,\rho') = -\frac{1}{G}E(-d,-\rho'/G)\exp\left(-i\frac{k}{2b}\frac{G+1}{G}\rho'^2\right) , \tag{4.15}$$

where $G = b/d$ is the magnification factor. The electric field in the image plane is a scaled and upside down version of the one in the object plane up to a spatially varying phase. The geometric situation is illustrated in figure 4.2. When either b or d approaches f, the other one will go to infinity.

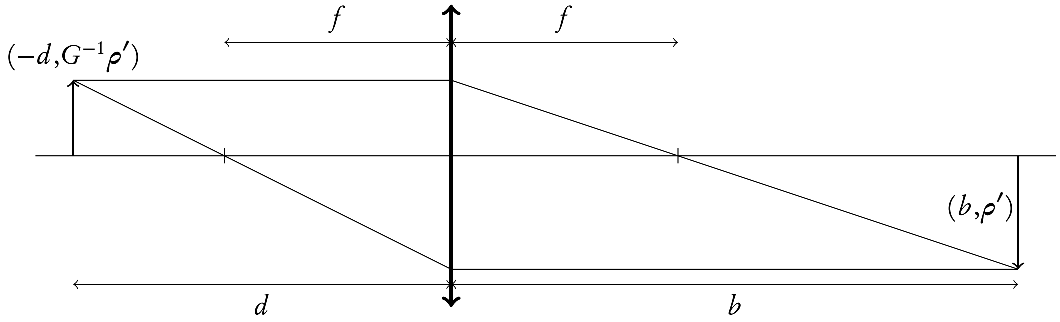

FIGURE 4.2: *Using a lens as a magnifying glass: for each object plane at a distance d of the lens there is a corresponding image plane at the distance b, with $1/b+1/d=1/f$ where the electric field distribution is a magnified (by a factor $G=b/d$) and upside down version of the object distribution.*

Phase plates generalise the principle of lenses by imprinting an *arbitrary* phase distribution $\phi(\rho)$ on the electric field:

$$E(\rho) \mapsto E(\rho)e^{i\phi(\rho)} . \tag{4.16}$$

During a subsequent propagation, the modification of the phase distribution will result in a modification of the electric field's modulus and hence of the intensity. As we will see below, this permits to create very different beam profiles. In order to appreciate the possibilities offered by these plates, we first have to look at the "carrier" of the phase, that is, the profile of the beam before the phase plate.

Gaussian beams

Since the transformation of a light beam is governed by Fourier transforms, it is natural to assume that a Gaussian intensity profile must be particularly adapted for their description: being an eigenfunction of the Fourier transform, a Gaussian can be expected to describe correctly the intensity profile of a light beam along its entire trajectory as long as no diffraction occurs. Indeed it turns out that not only this conjecture is true but also laser beams have intensity profiles which—depending on the specific laser—very nearly match a Gaussian[6]. Thus, this is one of the gratifying cases where the most convenient theoretical description corresponds at the same time to a common situation in actual experiments.

The isotropic Gaussian beam is commonly defined in the following form:

$$E(\rho,z)=E_0\frac{w_0}{w(z)}\exp\left(\frac{-ik\rho^2}{2q(z)}\right)e^{-i[kz-\zeta(z)]}\,, \tag{4.17}$$

with the amplitude E_0, the *beam parameter* $q(z)$ and the *Gouy phase* $\zeta(z)$ which are defined as follows:

$$\frac{1}{q(z)}=\frac{1}{R(z)}-i\frac{2}{kw^2(z)} \quad ; \quad \zeta(z)=\arctan\left(\frac{z}{z_0}\right)\,. \tag{4.18}$$

Here, $R(z)$ is the local radius of the wave front's curvature, and $w(z)$ is the local width. The two are given by

$$R(z)=z-z_0+\frac{z_{\mathrm{R}}^2}{z-z_0} \quad ; \quad w(z)=w_0\left[1+\left(\frac{z-z_0}{z_{\mathrm{R}}}\right)^2\right]^{1/2}\,, \tag{4.19}$$

where z_0 is the location of the plane with the smallest width, the so-called *beam waist*, w_0 is the width at the waist and z_{R} is the *Rayleigh length* defined by

$$z_{\mathrm{R}}=\frac{kw_0^2}{2}=\frac{\pi w_0^2}{\lambda}\,. \tag{4.20}$$

A graphical representation of the principal characteristics of the Gaussian beam is given in figure 4.3. The waist is the beam's plane of symmetry and the only plane in which the phase is uniform. This is equivalent to saying that it is the only wave front without finite curvature.

Despite the apparent multitude of definitions, these conventions allow a very simple description of the light beam's propagation. Indeed, for our purposes, the Gouy phase is of strictly no interest since it is constant in each plane. All that is necessary to characterise a given beam is the location of its waist z_0 and the width in this plane w_0 (in the following, we will sometimes follow the common practice of using the term "waist" meaning the width at the waist). The transformation of the beam under free propagation and when passing a lens corresponds to a simple transformation of the beam parameter $q(z)$:

$$\text{Propagation over a length } L: \quad q\mapsto q+L \quad ; \quad \text{Lens with focal length } f: \quad \frac{1}{q}\mapsto\frac{1}{q}-\frac{1}{f}\,, \tag{4.21}$$

---

[6] The deviation from a Gaussian beam is usually quantified with the M^2 number which is defined as the ratio between the angle of divergence of the laser's beam and the one of an ideal Gaussian beam having the same width. Here, the width is measured as the standard deviation of the intensity distribution. Since a Gaussian is the beam profile with minimal divergence, the M^2 number is always greater than one [114].

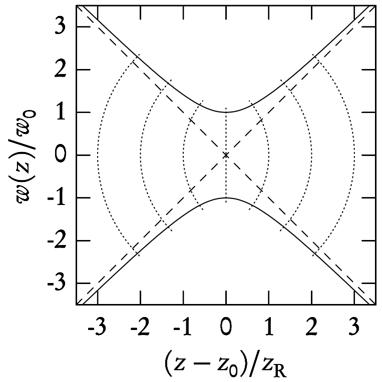

FIGURE 4.3: *Schematic representation of the main features of a Gaussian beam. The solid lines mark the radius $w(z)$ on which the electric field has fallen to $1/e$ of its original value, the dashed lines indicate the asymptotes of this width. The dotted lines show the wave front curvature.*

as can be verified by explicit calculation using the propagator (4.11). In a Gaussian beam, the intensity is well localised in any plane along its propagation, so we have here one of the cases where propagations over arbitrarily short distances can be correctly evaluated using the paraxial propagator.

Equation (4.19) shows that a Gaussian beam can never be perfectly collimated: around the waist at z_0, the width grows (linearly for large distances), the scale of variation being the Rayleigh length z_R. Table 4.1 shows how this length varies with the beam width. For large enough beam widths, the situation becomes indistinguishable from perfect collimation, which means at the same time that it becomes challenging to exactly localise the waist—at the same time, one has less and less reason to need to know its exact position. On the opposing end of the scale, the waist is easy to localise, but the beam cannot be collimated on long distances. As we shall see, both cases are of practical relevance in the actual use of phase plates.

Beam waist	Rayleigh length
5 μm	148 μm
10 μm	590 μm
50 μm	14.8 mm
100 μm	59.0 mm
500 μm	1.48 m
1 mm	5.90 m
5 mm	148 m

TABLE 4.1: *Rayleigh lengths corresponding to different beam waists for a wavelength of $\lambda = 532\,\text{nm}$, covering the entire range relevant for our experiment. Collimation is limited to submillimetric distances impossible for beam waists below ten microns. For beam waists of the order of a millimeter or more, the beam remains collimated on long distances.*

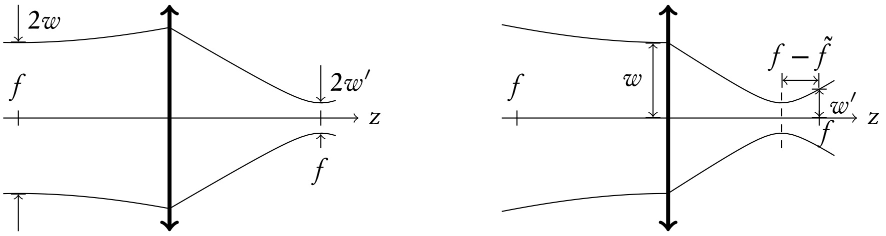

FIGURE 4.4: *Two experimentally relevant geometries when a gaussian beam is incident on a lens. Left: the incoming waist is in the incident focal plane. By symmetry, the outgoing waist is in the opposite focal plane, and the widths are related by equation* (4.22)*. Right: the incident waist is in the lens plane. In this case, the width in the outgoing focal plane is equally given by* (4.22)*, but the waist has a smaller width and lies closer to the lens (the distance $f-\tilde{f}$ has been exaggerated for illustration).*

If a Gaussian beam is incident on a lens, there are two cases of special interest which are illustrated in figure 4.4: in the first one (left panel) the incident waist is in the focal plane, where by symmetry and according to equation (4.14) the outgoing waist will equally be in the focal plane. As we stated before, the field distribution in the outgoing focal plane is just the Fourier transform of the one in the incident focal plane. The width in the outgoing focal plane will be the new waist w_0', defining a new Rayleigh length z_R'. The two are given by

$$w_0' = \frac{\lambda f}{\pi w_0} \quad ; \quad z_R' \equiv \frac{\pi w_0'^2}{\lambda} = \frac{f^2}{z_R} \,. \tag{4.22}$$

In the second case (right panel in figure 4.4) the incident waist is in the plane of the lens itself, and the outgoing waist will be at the distance $\tilde{f} = f/(1+f/z_R)$, where z_R is the Rayleigh length of the *incoming* beam. If the incoming beam is sufficiently large to have $z_R \gg f$ (the situation of a quasi-collimated beam), this plane is indistinguishable from the focal plane. In this case, the electric field in the focal plane behind the lens will be the Fourier transform of the electric field in the incident waist up to a spatially varying phase factor. The width in the outgoing focal plane is equally given by equation (4.22), but the width at the new waist and the associated Rayleigh length will be somewhat smaller. In the cases of interest for us, we can neglect this difference, *i.e.* f and $\tilde{f}$ will be almost identical.

For a given lens and wave length, one can make two useful estimations: firstly, there is an "invariant" waist given by $\sqrt{\lambda f/\pi}$ (for $\lambda = 532\,\text{nm}$ and $f = 10\,\text{cm}$ this gives 130 µm). Secondly, taking into account the finite radius R of a lens, one can estimate the smallest spot size that can be achieved with it: imposing $R \geq 2w_0$ to avoid clipping, one finds a spot size in the conjugated plane of $w_0' = 2\lambda/(\pi \tan\theta)$, where $\tan\theta = R/f$ is the *f-number* of the lens[7]. For a focal length of 10 cm and a radius of 2 cm, this minimum spot size is $w_0'^{(\text{min})} = 3.18\lambda$.

---

[7] For most practical purposes, it is almost identical to the *numerical aperture* NA $= n\sin\theta$, where n is the refractive index of the medium in which the light propagates. In our experiments, this is either air or vacuum where one has $n \simeq 1$ to a very good precision, and for typical optical configurations, $\sin\theta \simeq \tan\theta$.

The generalisation to an anisotropic Gaussian beam is straightforward since the propagation integral can be separated into two integrals over x and y. Instead of one waist situated at z_0 with width w_0 and Rayleigh length z_R, one has two waists situated at $z_0^{(x)}$ and $z_0^{(y)}$ with respective widths $w_0^{(x)}$, $w_0^{(y)}$ and associated Rayleigh lengths $z_R^{(x)}$ and $z_R^{(y)}$. The quantities along the two axes are independent from each other and transform just as the corresponding quantities in the isotropic case when the beam propagates or passes a lens.

4.3 Basic use of phase plates

We will now turn to the intensity distributions that can be generated using phase plates. To this end, we will assume the geometric situation to be the one of the right panel in figure 4.4 with the phase plate directly before the lens, *i.e.* the incident waist is on the phase plate which in turn is in the lens plane (which we define as $z = 0$). Thus, the electric field in the focal plane corresponds to the Fourier transform of the field just after the phase plate (since for dipole potentials only the intensity is important, we need not worry about the inhomogeneous phase). The electric field incident on the phase plate shall be that of a Gaussian beam carrying the power P with widths $w_0^{(x)}$ and $w_0^{(y)}$:

$$E(0,\boldsymbol{\rho}) = \sqrt{\frac{2P}{\pi w_0^{(x)} w_0^{(y)}}} \exp\left[-\left(\frac{x}{w_0^{(x)}}\right)^2 - \left(\frac{y}{w_0^{(y)}}\right)^2\right] . \tag{4.23}$$

This notation actually constitutes a slight abuse of terminology: the field which we denote by E here and in the following has the dimension of the square root of an intensity and is chosen in order to have $I = |E|^2$. The actual complex electric field amplitude is given by $E \times \sqrt{2/c\epsilon_0}$, where ϵ_0 is the dielectric constant.

The field distributions in the focal plane can be obtained by multiplying with the appropriate phase distribution and calculating the Fourier transform (since we are mainly interested in the intensity distribution, we will not bother with the inhomogeneous phase that arises in this configuration) which we will do for the four types of phase plates currently at our disposition.

The phase step plate

The simplest nontrivial phase plate is one on which the imprinted phase only takes two different values, separated by a straight line. The strongest effect will certainly be obtained when the difference between the two values equals π, *i.e.* when the plate causes a change of sign on one part of the beam. A schematic representation of such a plate is shown in figure 4.5.

For the calculation of the resulting potential, we will only consider the symmetric situation where the line of separation passes by the centre of the incident beam. In this case, the field distribution in the focal plane is given by

$$E(f,\boldsymbol{\rho}') = \frac{1}{\lambda f} \int_{-\infty}^{\infty} \mathrm{d}x \left(\int_0^{\infty} \mathrm{d}y - \int_{-\infty}^{0} \mathrm{d}y \right) E(0,\boldsymbol{\rho}) e^{ik\boldsymbol{\rho}\cdot\boldsymbol{\rho}'/f} . \tag{4.24}$$

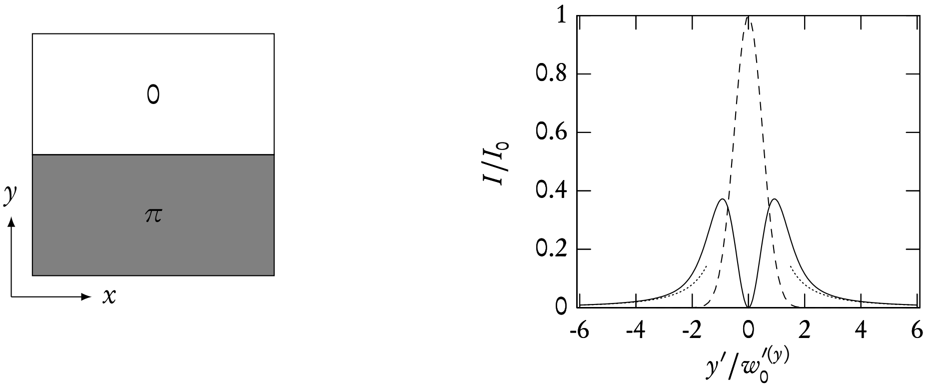

FIGURE 4.5: *Left: Schematic representation of the phase step plate. The imprinted phase makes an abrupt jump by* π *in the middle of the plate. Right: the resulting intensity distribution in the focal plane (solid line), normalised to the peak intensity of the same beam in absence of the phase plate (intensity distribution corresponding to the latter: dashed line). The dotted lines show the asymptotic behaviour for large distances.*

This integral can be evaluated analytically and gives [35]

$$E(f,\rho') = -i\sqrt{\frac{2P}{\pi w_0'^{(x)} w_0'^{(y)}}}\exp\left[-\left(\frac{x'}{w_0'^{(x)}}\right)^2 - \left(\frac{y'}{w_0'^{(y)}}\right)^2\right]\operatorname{erf}\left(i\frac{y'}{w_0'^{(y)}}\right), \tag{4.25}$$

where $\operatorname{erf}(z) = 2/\sqrt{\pi}\int_0^z \exp(-t^2)\mathrm{d}t$ is the error function. The general structure is that of a Gaussian beam "modulated" by the error function. This should not trick the reader into believing that the field will behave as a Gaussian for large y'. In fact, the Gaussian in the y' direction is compensated and replaced by a more slowly decaying function as we will see.

Since the error function is an odd function, the electric field vanishes linearly on the $y' = 0$ line (which is a very desirable feature since it guarantees the smallest possible photon scattering rate for atoms confined in the centre of the potential). This means that the intensity distribution will be harmonic in the vicinity (we set $x' = 0$ for ease of notation):

$$I(x' = 0, y' \ll w_0'^{(y)}) \simeq \frac{8P}{\pi^2 w_0'^{(x)} w_0'^{(y)}}\left(\frac{y'}{w_0'^{(y)}}\right)^2. \tag{4.26}$$

Using $U = \alpha I$ with $\alpha = 8.09 \times 10^{-37}\,\mathrm{Jm^2/W}$ and the experimentally feasible configuration $P = 1\,\mathrm{W}$, $w_0'^{(x)} = 100\,\mu\mathrm{m}$ and $w_0'^{(y)} = 5\,\mu\mathrm{m}$, one obtains a confinement of $\omega_y = 2\pi \times 4.33\,\mathrm{kHz}$, a value well suited for the creation of two-dimensional gases (see chapter 6). For the same parameters, the central intensity of the unperturbed Gaussian $I_0 = 2P/\pi w_0'^{(x)} w_0'^{(y)}$ is equivalent to a temperature of $\alpha I_0/k_\mathrm{B} = 76\,\mu\mathrm{K}$. As can be seen in figure 4.5, the barrier height is about one third of this which is large compared to experimentally feasible temperatures which range down to $\sim 50\,\mathrm{nK}$. The extreme aspect ratio $w_0'^{(x)}/w_0'^{(y)} = 20$ of this numerical example has a practical reason: since the trapping frequency decreases as a Gaussian for $x' \neq 0$, a large width is necessary to ensure that the trapping potential is uniform over the typical extension of an atomic cloud.

The asymptotic behaviour for $y' \gg w_0'^{(y)}$ can equally be calculated from (4.25) by using a suitable asymptotic expansion of the error function. Instead of doing this, we will make a little side tour that will prove quite instructive when applied to the phase barrier plate: we note that the integral (4.24) can also be written in the following form:

$$E(x',y') = \frac{2}{\sqrt{\pi w_0'^{(y)}}} \mathscr{E}(x') \int_0^\infty \mathrm{d}u \, \sin\left(\frac{2y'}{w_0'^{(y)}} u \right) e^{-u^2} , \tag{4.27}$$

where we have set

$$\mathscr{E}(x') = i \sqrt{\frac{2P}{\pi w_0'^{(x)}}} \exp\left[-\left(x'/w_0'^{(x)} \right)^2 \right] . \tag{4.28}$$

For $y' \gg w_0'^{(y)}$, the sine inside the integral is rapidly oscillating. One can now replace the integral by a sum of integrals, each over one period of the sine. Over one period, the Gaussian multiplying the sine will vary very little, permitting us to replace it by its Taylor expansion around the starting point of the period:

$$\int_0^\infty \mathrm{d}u \, \sin(\xi u) e^{-u^2} = \sum_{n=0}^{\infty} \int_0^{2\pi/\xi} \mathrm{d}u \, \sin(\xi u) \left[e^{-(2\pi n/\xi)^2} + \left(-4\pi n/\xi \, e^{-(2\pi n/\xi)^2} \right) u + \cdots \right] , \tag{4.29}$$

with $\xi = 2y'/w_0'^{(y)}$. The integral over one period of a pure sine vanishes, so the first finite contribution comes from the term linear in u leading to

$$\frac{E(x',y')}{\mathscr{E}(x')} \simeq \frac{1}{\sqrt{\pi w_0'^{(y)}}} \frac{16\pi^2}{\xi^3} \sum_{n=0}^{\infty} n e^{-(2\pi n/\xi)^2} \simeq \sqrt{\frac{w_0'^{(y)}}{\pi}} \frac{1}{y'} , \tag{4.30}$$

where we have replaced the sum by an integral in the last step. The resulting expression is a good approximation to the exact result for $y' > 3w_0'^{(y)}$. We see that the intensity decreases as $1/y'^2$, *i.e.* quite slowly. This has two consequences: firstly, a significant part of the total beam power will go into the wings where it does not participate in the confinement of the atoms. Secondly, one has to worry about clipping when for experimental reasons the phase plate cannot be positioned in the direct vicinity of the lens.

The phase barrier plate

Having seen that the phase step plate permits the creation of a single two-dimensional gas, it is natural to ask if one can generalise this principle in order to produce two such gases at a small distance from one another. This is a highly interesting configuration since it permits to observe interferences between the two gases in ballistic expansion, allowing to study the degree of coherence between the two.

It turns out this is indeed possible by using the phase distribution schematically shown in figure 4.6: a stripe of width a and phase π surrounded above and below by zero phase zones. Once more, we will only consider the case where the beam is centered on the phase plate.

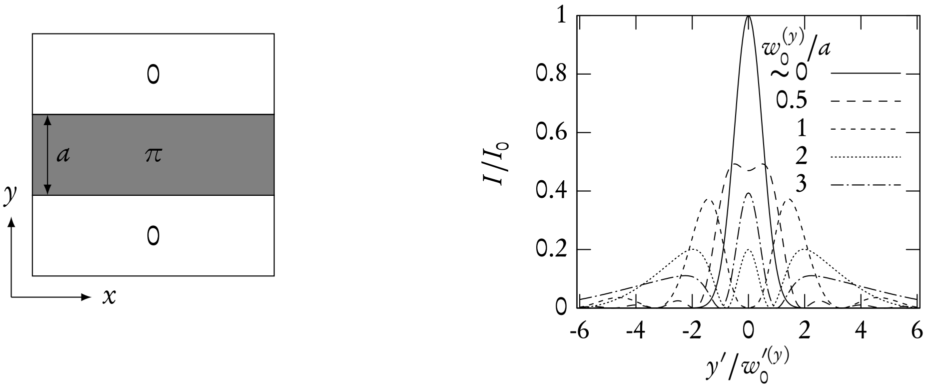

FIGURE 4.6: *Left: schematic representation of the phase barrier plate. The imprinted phase equals* π *on a limited range* a*. Right: Resulting intensity distributions in the focal plane for different values of the ratio* $w_0^{(y)}/a$*. If the ratio is small, one obtains a double peak structure, for higher values, a third peak emerges in the middle. For* $w_0^{(y)}/a \simeq 2$*, all three peaks have the same height.*

It is obvious that the resulting electric field distribution will be a function of the ratio of the incident beam width $w_0^{(y)}$ and the width of the phase barrier a and that there will be several regimes: if the beam width is small compared to that of the phase barrier, the beam will see a uniform phase distribution which leaves it unaltered, the same applies to the opposing limit when only a negligible fraction of the total power will see a phase different from zero. Obviously, we are more interested in the intermediate regime. The field in the focal plane is given by the integral

$$E(f,\boldsymbol{\rho}') = \frac{1}{\lambda f}\int_{-\infty}^{\infty} \mathrm{d}x \left(\int_{-\infty}^{-a/2} \mathrm{d}y - \int_{-a/2}^{a/2} \mathrm{d}y + \int_{a/2}^{\infty} \mathrm{d}y \right) E(0,\boldsymbol{r}) e^{ik\boldsymbol{\rho}\cdot\boldsymbol{\rho}'/f} \tag{4.31}$$

with the exact solution

$$E(x',y') = i\sqrt{\frac{2P}{\pi w_0'^{(x)} w_0'^{(y)}}} \exp\left[-\left(\frac{x'}{w_0'^{(x)}}\right)^2 - \left(\frac{y'}{w_0'^{(y)}}\right)^2\right] \times \left[\operatorname{erf}\left(\frac{a}{2w_0^{(y)}} + i\frac{y'}{w_0'^{(y)}}\right) + \operatorname{erf}\left(\frac{a}{2w_0^{(y)}} - i\frac{y'}{w_0'^{(y)}}\right) - 1\right] . \quad (4.32)$$

As we anticipated, this is a function not only of the ratio of the coordinates and the outgoing waists, but also of the ratio of the incoming vertical waist $w_0^{(y)}$ and the width of the phase barrier. For $w_0^{(y)} \ll a$, the error functions will be equal to one and one recovers a Gaussian beam. When $w_0^{(y)}$ grows, the central intensity ($y' = 0$) will diminish, forming a dip in the intensity distribution. At $w_0^{(y)}/a = 1.048$, the central intensity vanishes. When $w_0^{(y)}$ is increased further, the central electric field changes sign, creating two zero crossings which correspond to harmonic minima of the intensity distribution. As in the case of the phase step plate, the intensity vanishes in these minima, minimising the photon scattering rate. The three maxima separating the two minima are at roughly the same height for $w_0^{(y)}/a \simeq 2$. The trapping frequency in the two wells cannot be calculated analytically in the general case, but can be determined by fitting a quadratic function to the profile for a given ratio of $w_0^{(y)}/a$. For $w_0^{(y)}/a = 2$ (the case where all three maxima have about the same height), one finds that for equal power the trapping frequency is about 0.65 times the trapping frequency one finds with the phase step plate [115], *e.g.* 2.81 kHz for $P = 1\,\mathrm{W}$, $w_0'^{(x)} = 100\,\mu\mathrm{m}$ and $w_0'^{(y)} = 5\,\mu\mathrm{m}$. For $w_0^{(y)}/a = 2$, the separation of the two wells is $1.6 w_0'^{(y)}$.

The fact that the central peak only appears for certain values of the incident waist signifies that it would be possible to split an atomic cloud by passing from a single to a double well potential if one was able to vary $w_0^{(y)}/a$ between 1 and 2, typically. This is not too far-fetched since one can build the equivalent of a phase barrier plate by a succession of two phase step plates shifted with respect to each other. By putting the plates on a motorised translation stage, one would have complete control over the width of the resulting phase barrier.

The asymptotic behaviour of this electric field distribution can be calculated in the same manner as for the phase step plate. Rewriting (4.31) as

$$\sqrt{w_0^{(y)}}\frac{E(x',y')}{\mathscr{E}(x')} = e^{-\left(y'/w_0'^{(y)}\right)^2} - \frac{4}{\sqrt{\pi}}\int_0^{a/2w_0^{(y)}} \mathrm{d}u \, \cos\left(2\frac{y'}{w_0'^{(y)}}u\right) e^{-u^2} , \quad (4.33)$$

we can divide the integral into a sum of integrals in quite the same manner as above (the first term is of no interest since it falls off exponentially). However, there are two differences: firstly, the integral has a finite upper limit so that the number of cycles will not be integer. One can cope with this by dividing up the sum into an "integer" part of integrals over complete periods and a "non-integer" part with the remaining integral. Secondly, we have a cosine instead of a sine, and since $\int x \cos x \, \mathrm{d}x = 0$ for integrals over a complete period, the first contribution to the integer part comes from the quadratic term in u from the expansion of the Gaussian. The result scales as $E \sim 1/y'^2$. However, in the non-integer part, the first contribution is from the constant term so that the result scales as $E \sim 1/y'$, thus giving the asymptotic behavior of the electric field:

$$\frac{E(x',y')}{\mathcal{E}(x')} \simeq -2\sqrt{\frac{w_0'^{(y)}}{\pi}} \frac{\sin\left(\frac{y'}{w_0'^{(y)}} \frac{a}{w_0^{(y)}}\right)}{y'} e^{-\left(a/2w_0^{(y)}\right)^2} . \tag{4.34}$$

For $w_0^{(y)} = 2a$, this is a very good approximation once $y' > 6w_0'^{(y)}$.

The vortex plates

The third kind of phase plate used by our group is completely different from the first two: instead of a finite number of zones with a uniform phase, the phase is a smoothly varying function of the spatial coordinates. More specifically, it is constant as a function of the radius and varies linearly with the angle, accomplishing n complete revolutions of 2π [8]. We have two types of such plates at our disposition, with $n = 1$ and $n = 6$. Both are schematically shown in figure 4.7. Of course, this is an idealisation of the actual realisation of such plates where the total angle is subdivided into a finite number of angular sectors, the phase increasing step by step as one passes from sector to sector. For the moment, we will stick to the idealised version as it permits exact analytical calculations.

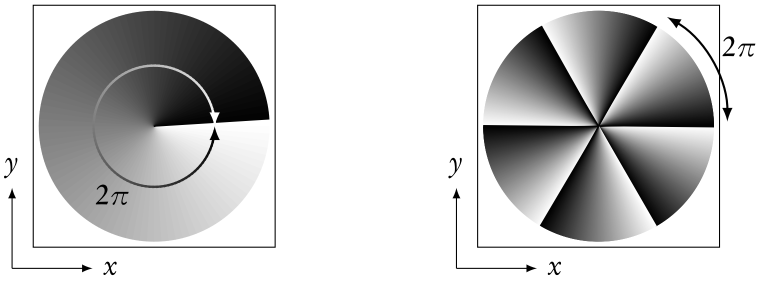

FIGURE 4.7: *Schematic representation of the two types of vortex plate available to our group. Left: a "charge one" vortex plate. The phase passes from* 0 *to* 2π *once around the plate. Right: a "charge six" type plate. Around the plate, the phase passes six times from* 0 *to* 2π.

The radial symmetry of these phase plates suggests the usage of an isotropic incident beam centered on the plate which is what we will do. The field in the focal plane is given by the

---

[8] For the case $n = 1$, such a plate has successfully been used by Denschlag *et al.* [102] to create vortices in a sodium BEC. Our use of such a plate would be a different one since we are rather interested in the far-detuned regime where no photons are absorbed so that no angular momentum can be transferred.

expression

$$E(\rho',\phi') = \sqrt{\frac{2P}{\pi w_0^2}}\frac{1}{\lambda f}\int \mathrm{d}^2\rho\, e^{-(\rho/w_0)^2} e^{in\phi} e^{ik\boldsymbol{\rho}\cdot\boldsymbol{\rho}'/f} \,. \tag{4.35}$$

This integral is most conveniently calculated in cylindrical coordinates using $\boldsymbol{\rho}\cdot\boldsymbol{\rho}' = \rho\rho'\cos(\phi-\phi')$. One can then in a first step evaluate the integral over the angle which up to a constant factor is just the integral representation of the Bessel function of the first kind $J_n(k\rho\rho'/f)$. The radial integral over the product of a Bessel function and a Gaussian can be expressed in terms of the confluent hypergeometric function ${}_1F_1(a,b,z)$ [116, 117] so that the final expression for the field reads

$$E(\rho',\phi') = i^n\sqrt{\frac{2P}{\pi w_0'^2}}e^{in\phi'}\left(\frac{\rho'}{w_0'}\right)^n \frac{\Gamma\left(\frac{n}{2}+1\right)}{\Gamma(n+1)}\,{}_1F_1\left[\frac{n}{2}+1, n+1, -\left(\frac{\rho'}{w_0'}\right)^2\right] , \tag{4.36}$$

where $\Gamma(z) = \int_0^\infty t^{z-1}e^{-t}\mathrm{d}t$ is the Gamma function. A striking feature of this solution is that the angular dependence of the phase is the same as that of the electric field just after the phase plate—the "vorticity" of the field is conserved by the Fourier transformation. The Gaussian envelope is replaced by the confluent hypergeometric function (which is traced in figure 4.8 for both relevant values of n with a Gaussian for comparison). This contains the case $n=0$ (equivalent to no phase plate at all) since ${}_1F_1(1,1,-z^2) = \exp(-z^2)$. For the two cases relevant for our phase plates $n=1$ and $n=6$, ${}_1F_1$ can equally be expressed in terms of more familiar functions:

$$ {}_1F_1\left(\frac{3}{2},2,-z^2\right) = e^{-z^2/2}\left[I_0\left(\frac{z^2}{2}\right) - I_1\left(\frac{z^2}{2}\right)\right] \tag{4.37}$$

$$ {}_1F_1(4,7,-z^2) = \frac{120}{z^{12}}\left[3z^4 - 24z^2 + 60 - e^{-z^2}(z^6 + 9z^4 + 36z^2 + 60)\right] , \tag{4.38}$$

where I_k is the modified Bessel function of the first kind.

The confluent hypergeometric function is flat and equal to one for $\rho' \to 0$ so that the behaviour in the centre will be dominated by the factor ρ'^n: the first non-vanishing term in a power expansion of the resulting intensity will by of order $2n$. Thus, the potential of the $n=1$ plate will be harmonic in the centre whereas the potential corresponding to the $n=6$ plate will be of polynomial order twelve, mimicking a box potential with a flat bottom followed by a sharp increase of the potential. Both intensity distributions are shown on the right of figure 4.8.

A straightforward calculation shows that the trapping frequency in the centre of the potential caused by the $n=1$ plate obeys the relation $\omega^2 = \alpha P/m w_0'^4$. Using the value of α stated above, a power of 1 W and a waist of 10 µm, one calculates a trapping frequency of $2\pi \times 3.80$ kHz. By focussing more, the trapping frequency can even be much higher owing to the $w_0'^2$ dependence. Thus, the $n=1$ vortex plate is an ideal tool for the production of one-dimensional gases.

For all n, the intensity vanishes in the centre so that photon scattering will not be a major concern. As in the case of the phase step, the wings of the potential exhibit no modulation—there is no feature that could cause interferences. Even before an explicit calculation, it is clear

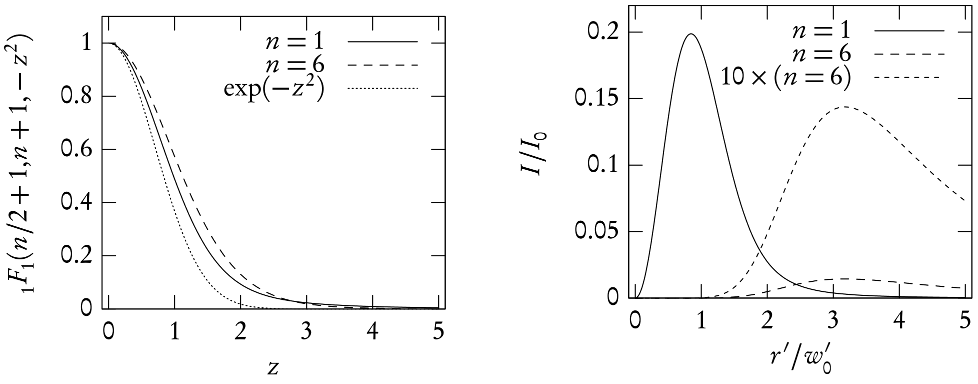

FIGURE 4.8: *Left: plots of the confluent hypergeometric function appearing in the field distribution of vortex plates for the two values of n relevant for our phase plates. A Gaussian corresponding to an unperturbed beam is shown for comparison. Right: The resulting intensity for the two types of phase plates. For optical clarity, the* $n = 6$ *profile is shown a second time multiplied by a factor of ten.*

that the decay of the intensity must be faster than for the other phase plate types since an intensity decreasing as $1/\rho'^2$ would not be normalisable in two dimensions. We expect this to be true also from a physical point of view since we have no abrupt variations of the phase (even if in the centre of the plate, they become increasingly "fast") that would cause strong diffraction. The approach we used to calculate the asymptotic behaviour of the phase step and barrier plates is not transposable since there is no simple integral involving a periodic function here, so we rather use the fact that for large and negative z, one has ${}_1F_1(a,b,z) \simeq (\Gamma(b)/\Gamma(b-a))|z|^{-a}$ [116]. The field distribution becomes

$$E(\rho',\phi') \simeq \frac{i^n n}{2}\sqrt{\frac{2P}{\pi w_0'^2}}e^{in\phi'}\left(\frac{\rho'}{w_0'}\right)^{-2}. \tag{4.39}$$

Thus, for all $n > 0$, the intensity falls off as $1/\rho'^4$ regardless of the "vortex charge" (for $n = 0$, the decay is Gaussian). In turn, its absolute value scales as n^2 so that with increasing n, an increasing fraction of the total power will go into the wings which explains the difference between the height of the respective maxima visible in figure 4.8.

4.4 *Phase plates in practice*

Having discussed the potentials that would be created by ideal phase plates, we now turn to measurements performed on their real counterparts. Of course, further theoretical investigation can in principle provide more information such as the behaviour of the potentials in planes in the vicinity of but not equal to the focal plane [115]. However, the final answer to the question about the consequences of all possible imperfections (which can come from the realisation of the phase plates as well as from an imperfect preparation of the incident beam or from the optics after the phase plate) can only be provided by an experimental test.

Preliminary tests

Imaging the intensity distribution produced by the phase plate is not trivial since we are interested in the distribution in the focal plane. One has to ensure that the waist is not too small in this plane in order to have a sufficient resolution. This is unproblematic for the phase step and vortex plates where there is no constraint on the width of the incident waist so that one can always arrange for a convenient beam size in the plane of measurement (there is still a compromise to make since it becomes increasingly difficult to centre the incident beam on the phase plate when the incident waist decreases). However, the phase barrier imposes a definite size on the incident waist so that all one can do to prevent the outgoing waist from becoming too small is to choose a large focal length for the lens. The width of the barrier being 1.7 mm, the incident waist for the case of three equal peaks will be 3.4 mm, so $w_0' = 4.98\,\mu\text{m} \times f/100\,\text{mm}$.

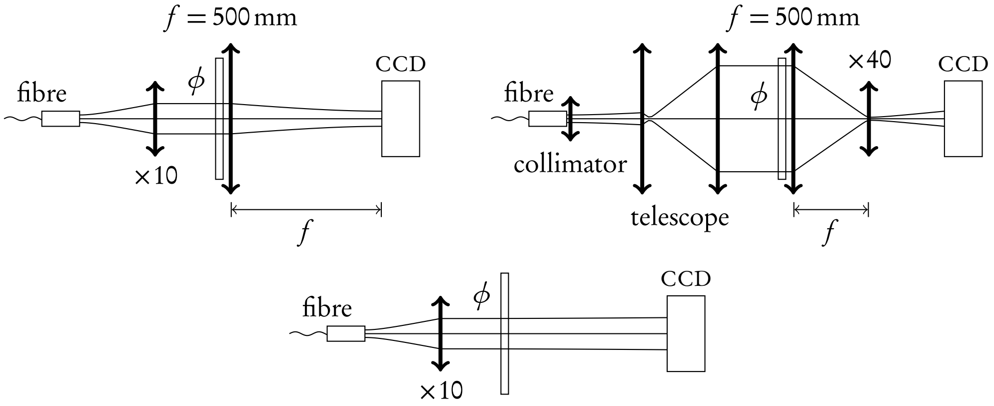

FIGURE 4.9: *The three configurations used for the preliminary tests of the phase plates (not to scale). Top: configurations 1 (left) and 2 (right), bottom: configuration 3. The difference between configurations 1 and 2 is only in the shaping of the beam wheras the third configuration probes the free propagation of the beam after the phase plate instead of its Fourier transform.*

As light source, we use a green laser pointer providing coherent light at 532 nm. Since the mode of such a device is visibly non-Gaussian (on the one used for these measurements, there is a clear subdivision into several light lobes), we inject it into a single-mode fibre and work with the beam coming out at the other end which has a profile very close to a Gaussian. At the fibre exit, we use one of three different configurations of optical elements to obtain images of the intensity distribution. In the following, we will refer to them by their respective numbers. The configurations (which are illustrated in figure 4.9) are as follows:

1. The beam is collimated using a microscope objective with a nominal magnification of 10 and a numerical aperture of 0.25, values that have been found experimentally to match

most closely the divergence of the light coming out of the fibre. The collimated beam has a width of 0.9 mm (determined by measuring the fraction of power left after a razor blade as a function of its position and fitting an error function to it). It passes a phase plate and is then focussed by a $f = 500\,\text{mm}$ lens, so one expects a width of about a hundred microns in the focal plane of the lens which allows for convenient imaging. This configuration is adapted for all plates except the phase barrier, for the reasons stated above. For all other plates, this configuration permits to measure the intensity distribution as it will be seen by the atoms.

2. The beam is collimated with a fibre outcoupler lens to a width of 350 µm. It is widened to a width of 3.2 mm using a telescope made up of two achromatic lens doublets with focal lengths 40 mm and 300 mm, respectively[9]. The beam then passes a phase plate and is focussed by a lens with $f = 500\,\text{mm}$. The image in the focal plane is magnified using a microscope objective of magnification 40 (the numerical aperture is not specified) for imaging. The beam preparation is even closer to experimental needs, but the imaging is more indirect due to the introduction of the final microscope objective. The latter may also degrade the image quality with its aberrations and finite aperture. For the phase barrier plate, this is the only choice possible among the configurations discussed here.

3. The third and last configuration is identical to the first one up to the phase plate, but instead of focussing the beam afterwards one just lets it continue to propagate and takes the image after a propagation of between one and two meters. Here one is not really in the Fraunhofer regime, but such images permit to have an idea of how the intensity distribution transforms to the final one.

In all cases, we work with an isotropic beam for simplicity. The images are taken with a Lu 055 camera fabricated by the Lumenera company. This camera has a resolution of 640 × 480 pixels, each pixel being a square with an edge length of 7.8 µm. It provides 8 bit monochrome images, *i.e.* it distinguishes 256 shades of grey, progressing linearly with increasing intensity. When in the following we express intensities in arbitrary units, these are nothing but the shades of grey (note that all images shown in this chapter have been color inversed for better reproduction). For images in the focal plane, the camera is positioned by displacing it along the optical axis until the size of the Gaussian spot is minimal.

We first discuss the intensity distribution produced by the phase step. Here, we take the images using the first configuration. To begin, we observe the beam without phase plate on the camera and attenuate the beam (by putting optical densities before the fibre entrance) until there is no more saturation. The resulting image is stored and we fit a two-dimensional Gaussian with an offset (to account for a finite background illumination) to it. Then we insert the phase plate and store the resulting image. The fitting parameters from the Gaussian permit us to subtract the offset, express the lengths in units of the unperturbed waists and the amplitude in units of the Gaussian's peak intensity. If we now take a cut through the profile (which we

---

[9] One would expect the resulting waist to be smaller, but since a beam of width 350 µm has a Rayleigh length in the sub-meter range, the beam incident on the telescope is not collimated.

average over three adjacent lines to diminish the effect of noise) and choose the origin of the spatial coordinate to coincide with the minimum, no adjustable parameter remains and the result can be directly compared to the theoretical prediction. The image taken by the camera as well as the direct comparison with theory are shown in figure 4.10.

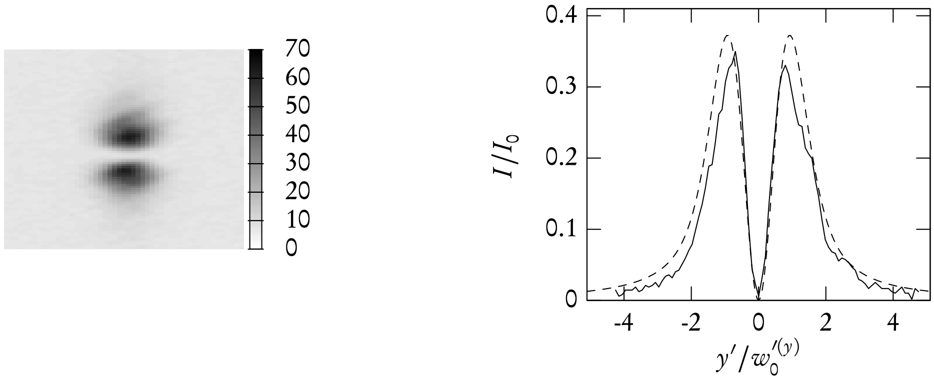

FIGURE 4.10: *Left: light intensity in the focal plane after the phase step plate as measured with a* CCD *camera, in arbitrary units. A vertical cut through this profile, averaged over three columns, is shown on the right. Solid line: measured intensity profile in units of the measured width and peak intensity of the beam in absence of the plate. Dashed line: theoretical prediction (the same data as in figure 4.5).*

The agreement between theory and measurement is fair on the whole and excellent close to the centre. The visible differences are most likely due to slight absorption of the beam on the phase plate's coating and the uncertainty of the fitted beam width. The residual intensity in the minimum is most likely caused by the pixel resolution of the camera.

As has already been anticipated, the phase barrier plate has been tested using the second configuration. For the length scale, we proceed exactly as for the phase step plate, in contrast we renounce to a properly normalised intensity. The result is represented in figure 4.11. Here, for the cut, the subtraction of the offset was done by hand, and the theoretical prediction multiplied by a factor so that the central intensity comes out equal.

On the cut, one sees that while the overall shape of the potential is reasonably close to the theoretical prediction, there is a pronounced asymmetry in the respective heights of the peaks. This is, however, not a defect of the phase plate, but rather a result of the imperfect beam preparation: when the incident waist is large, the shape of the Gaussian beam is quite sensitive to displacements of the optical elements with respect to the optical axis. Since there was some tolerance on the crossed translation stages on which they were mounted, the achievable quality of the images was limited. Later in this chapter, we will show a more symmetric image taken later with better equipment directly on the main experimental setup.

The $n = 1$ vortex plate has equally been tested in the second configuration, rather for

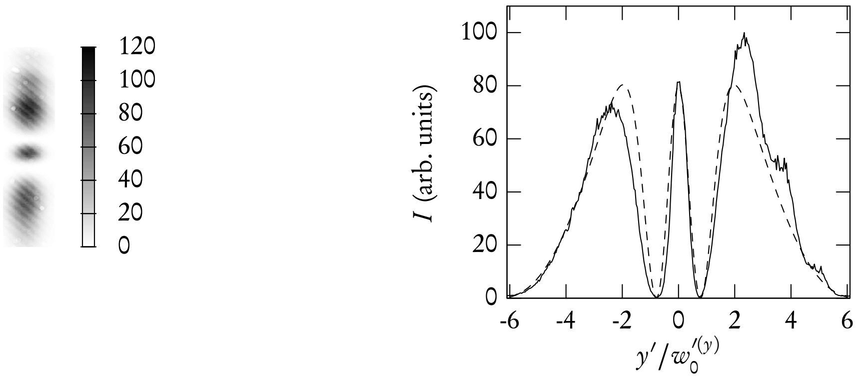

FIGURE 4.11: *Left: intensity distribution produced by the phase barrier plate as recorded with the* CCD *camera, in arbitrary units. Right: vertical cut through the distribution, averaged over 11 adjacent lines (solid line) and theoretical prediction (dashed line, same data as in figure 4.6 for* $w_0^{(y)}/a = 2$*). The latter has been multiplied by a factor to match the intensity in the centre.*

“historical” reasons since the first one would have been more adapted. Just as for the phase barrier plate, we express lengths in units of the unperturbed beam width, but leave the intensity in arbitrary units, multiplying the theoretical prediction by a factor in order to match peak values. The result can be seen in figure 4.12.

On close inspection, one remarks that the distribution of the intensity on the ring around the centre is all but equal: there are two significantly darker patches on the lower left and upper right of the intensity profile, and while the cut does not exceed an intensity of 10 in arbitrary units, one finds values of up to 27 in the two-dimensional distribution. One might try to do an angular average, but since the shape does not look perfectly round either, we shall leave it at that.

Considering these observations, one might say that the cut and the theoretical prediction are reasonably close on a qualitative level, but one should try to produce such images with a more symmetric beam in order to be able to draw conclusions on a quantitative level. A first conclusion that can be drawn from the experiences with the phase barrier and $n = 1$ vortex plate is that the preparation of the incident beam merits particular attention since it has a decisive impact on the resulting potential.

To conclude these preliminary tests, the $n = 6$ vortex plate has been tested using the first and the third configuration. In both cases, no attempt was made to provide length or intensity scales. It turns out, as is clearly visible in figure 4.13, that one needs not strive for a quantitative agreement with theory.

In both configurations, the cuts through the intensity distribution show clear qualitative differences with respect to the theoretical prediction. A common feature in both configurations

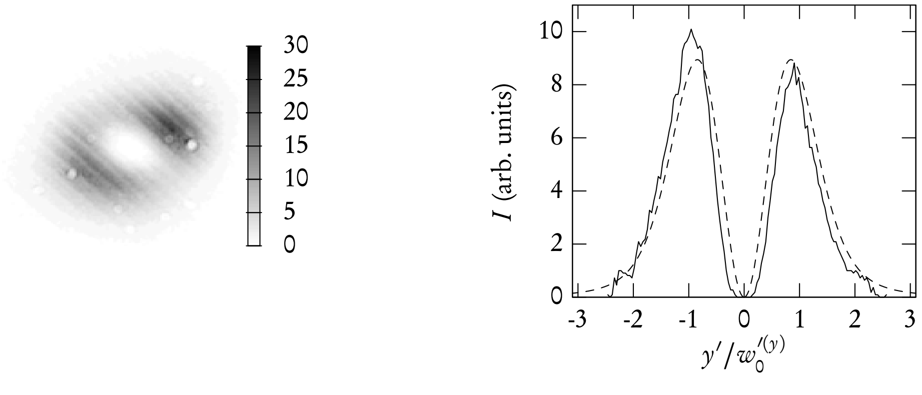

FIGURE 4.12: *Left: intensity distribution created by the $n = 1$ vortex plate as measured with the* CCD *camera. Right: Horizontal cut through the intensity distribution, averaged over three adjacent lines (solid line) and theoretical prediction (dashed line) multiplied by an appropriate factor.*

is that the “walls” are visibly steeper than in the theoretical profile for equal peak height. One also sees that the overall shape is slightly hexagonal. In the focal plane (first configuration), there is a “bump” in the centre which is absent from both theory and the intensity after free propagation.

David Jacob from the ENS sodium team has carried out further investigations on this discrepancy. His findings will be described in detail in his thesis. Here, we just summarise the main points without entering into the details: as we stated before, the actual realisation of the phase plates is not continuous, they are rather subdivided into a finite number of angular sectors each of which has a constant phase. Moreover, between these sectors there are lines of separation of finite width on which the phase is not properly defined.

From a pragmatic point of view, this does not mean that the $n = 6$ vortex plate is not usable for actual experiences: the profile after free propagation shows a very flat bottom just as desired, and if the walls increase more steeply than predicted by theory, this will only make the potential resemble more closely to a box potential. Since this is the intended use of this plate, one does not need all too small a beam width so that it is not strictly necessary that the atoms be in the focal plane.

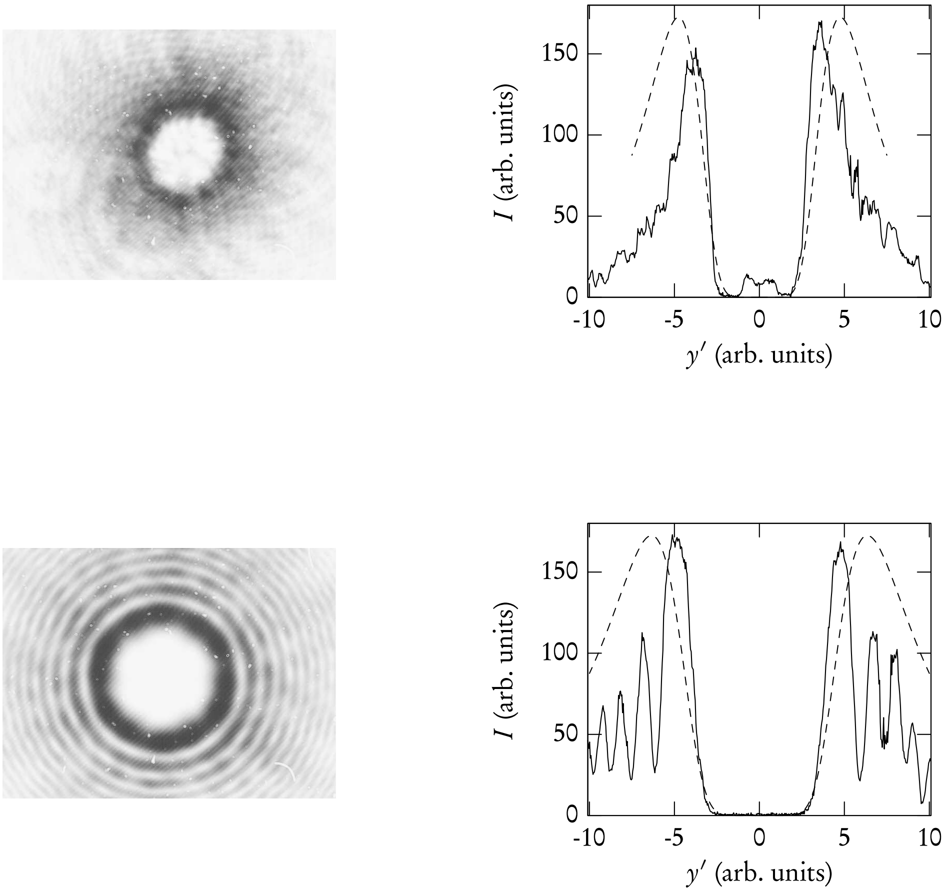

FIGURE 4.13: *Upper left: intensity distribution measured in the focal plane (first configuration). Upper right: Horizontal cut through this distribution, averaged over three adjacent lines (solid line) and the more or less adjusted theoretical prediction (dashed line). Lower left: intensity after some meters of propagation. Lower right: cut through this distribution, averaged over three adjacent lines (solid line) and a theoretical curve (dashed line) in approximate adjustment.*

One can sum up the results of these preliminary tests by saying that the behaviour of the phase step and barrier is sufficiently well understood to proceed to actual experimental use. The vortex plates, especially the $n = 6$ one, however, merit a more careful investigation beyond the one presented here in order to know how they can best be used for experiment.

Phase step and barrier in experimental use

Having gained sufficient confidence in the behaviour of phase step and barrier, the remaining problem for experimental use is the preparation of the incident beam. The experimental goal is the production of two-dimensional gases by tightly confining the atoms in one direction of space. We choose the vertical axis for this strong confinement since it is the axis of symmetry.

Taking into account the estimations for the trapping frequency stated earlier in this chapter, we strive for a vertical width of $w_0'^{(y)} = 5\,\mu\text{m}$ in the plane of the atoms. In the horizontal direction, we aim for a waist of $w_0'^{(x)} = 120\,\mu\text{m}$ to ensure that the entire atomic cloud will be tightly confined. It is more than difficult to approach the focussing lens more than up to 10 cm from the atoms, so we use an achromatic doublet (Newport PAC 073 AR.14) with $f_s = 100\,\text{mm}$ (s for "spherical") and a diameter of 38 mm. This means that the vertical and horizontal beam widths incident on the lens must be $w_0^{(y)} = 3.4\,\text{mm}$ (which is also just what is needed to produce three peaks of equal height with the phase barrier plate) and $w_0^{(x)} = 141\,\mu\text{m}$, respectively.

To produce such an anisotropic beam starting from a circular one we use cylindrical lenses which modify either only the vertical (v) or only the horizontal (h) electric field distribution. For practical reasons, it is most desirable to have the incident beam collimated in both directions on a certain part of the way because otherwise one would have to scrupulously respect fixed distances all the way from the atoms back to the source. Now, the horizontal width before the length corresponds to a Rayleigh length of only 116 mm (cf. table 4.1), so it is not possible to keep the beam collimated along the x direction far enough to permit a clean separation between the beam shaping and the focusing part.

However, this problem can easily be circumvented: for the creation of the single and double well potential, one must ensure that the electric field in the y direction be the Fourier transform of the field just after the phase plate. The same does not apply to the distribution as a function of x which remains Gaussian. Thus, the image plane must be a focal plane for the y direction, but not necessarily for the x direction. This leads to the idea of using the final lens f_s at the same time as a focusing lens on the y direction and as the second lens of a telescope along the x direction. This latter telescope reduces the waist $w_0^{(x)}$ from a size that is readily collimated to the final size in the image plane. As a consequence, before the final lens f_s, one has one "vertical" cylindrical lens f_v and two "horizontal" cylindrical lenses f_{h1} and f_{h2}. The vertical lens collimates the vertical waist to $w_0^{(y)} = 3.4\,\text{mm}$. The first (seen from the fibre exit) horizontal lens f_{h1} collimates the beam horizontally to an intermediate waist $w_0^{(x)}$ while the second one f_{h2} acts as the first lens of a telescope (the second one being, as already mentioned, the spherical lens f_s). All cylindrical lenses used in our experiment are from the Thorlabs LJ xxxx L1-A series. Putting everything together, one obtains the disposition schematically shown in figure 4.14.

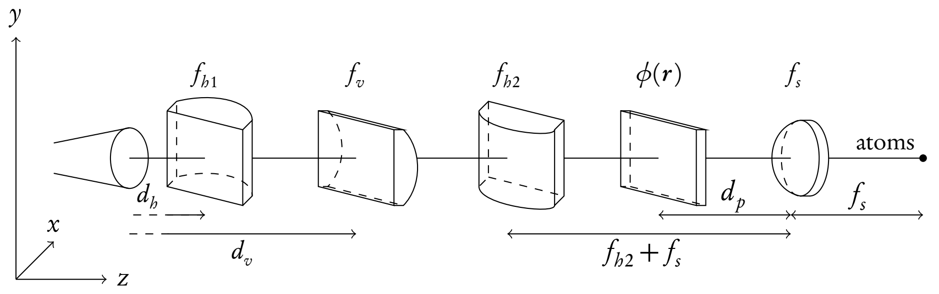

FIGURE 4.14: *Schematic representation of the beam shaping optics: a circular, slightly diverging beam is collimated horizontally and vertically by two cylindrical lenses* f_{h1} *and* f_v*. For the horizontal part, the final beam width is produced by a telescope formed by a second horizontal cylindrical lens* f_{h2} *and the focussing lens* f_s*. The vertical width is produced by focussing the collimated beam. The phase plate is at a finite distance* d_p *before the focussing lens for practical reasons.*

On the left of these optical elements, there is an incoming diverging beam with a (possibly virtual) waist at a certain distance from the first lens. By virtue of collimation, the distance between the "vertical" lens f_v and the second "horizontal" one f_{h2} can be arbitrary—on our setup, it is even negative, *i.e.* their order is inversed and there is no interval where the beam is simultaneously collimated in both directions. The diverging beam is produced using a microscope objective of magnification 10 and numerical aperture 0.25 (the same that was already used for the preliminary tests) that reduces the divergence of the beam coming out of an optical fibre without completely collimating it. We denote the distance from the objective to the first horizontal lens with d_h and the one to the vertical lens with d_v. After the experiences during our first tests, we strive for a maximum of mechanical stability of all optical elements and the best possible centering of the beam on the lenses to avoid beam deformation.

While we have seen that we have every reason to put the phase plate directly before the focussing lens to avoid clipping, practical considerations force us to place it at a finite distance d_p: the alignment of the dipole beam is by far more convenient and one has widely superior means of diagnostics if the beam is superposed with an imaging beam. Not only it is guaranteed that it will pass by the atoms, but also one can directly image the potential seen by the atoms using the camera and optics used for absorption imaging (even if one has to account for chromatic aberration between the near-infrared probe light and the green dipole beam). Since the phase shall be imprinted on the dipole beam only, the phase plate has to be moved back far enough to accommodate a dichroic plate (Melles Griot 03 BDS 003) that reflects visible light and transmits infrared[10]. All focal lengths and the (approximate) lengths are summarised in table 4.2.

In this discussion, we have so far only mentioned the elements taking an "active" part in

---

[10] The reflexion of green light by this plate is about ninety percent (according to the catalogue), so there is a visible second reflexion separated by some millimeters from the principal one, which we block with a darkened razor blade.

f_{h1}	f_{h2}	f_v	f_s	d_h	d_v	d_p
200	500	1000	100	425	1225	~ 150

TABLE 4.2: *Focal lengths and distances in our experiment. All numbers are in millimeters.*

shaping the beam. Apart from these, we also have to assure that no clipping occurs which becomes a serious issue in the vertical (y) direction where the waist on the phase plate is 3.4 mm. To be on the safe side, all mirrors are two inch diameter ones on the part of the beam trajectory where the vertical width is appreciable.

The beam thus prepared is imaged with the same imaging optics and camera (model Basler A 102f) that is used for horizontal absorption imaging. The equivalent pixel size of the camera has been measured (using an atomic cloud in free fall) to be 1.25 µm, made up of a physical pixel size of 6.45 µm and a magnification of 5.16. The latter is obtained using an achromatic doublet with a meniscus lens (Melles Griot 01 LAM 225 and 01 LAO 225). The camera has a bit depth of 12, *i.e.* it distinguishes 4096 shades of grey which will be the new "arbitrary units" for intensity. The horizontal and vertical width are measured by adjusting the optics until the central intensity is maximised and then fitting a two-dimensional Gaussian to the recorded image. We find $w_0^{\prime(x)} = 146\,\mu\text{m}$ and $w_0^{\prime(y)} = 4.54\,\mu\text{m}$, which fulfills the requirements stated above. Thanks to the careful positioning of the lenses, the beam profile is free of the asymmetries seen in the preliminary tests. If we now insert for example the phase barrier plate, we obtain the intensity distribution shown in figure 4.15 (using the fitted vertical width as a length scale).

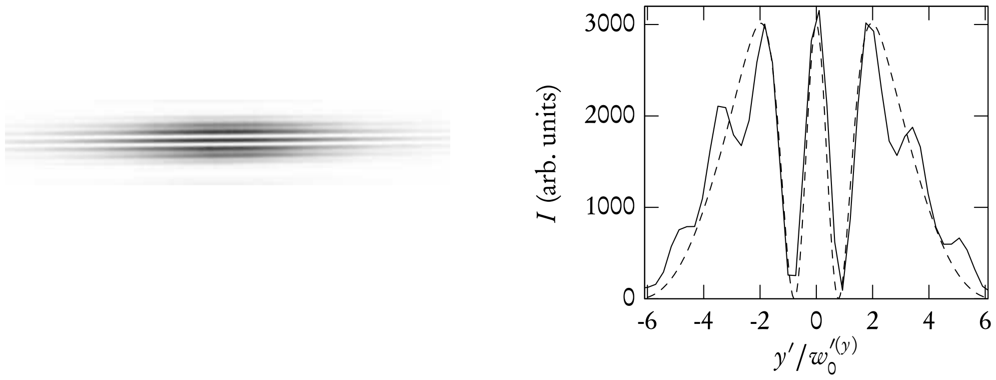

FIGURE 4.15: *Left: intensity of the phase barrier plate in the actual experimental configuration. The large horizontal extension ensures uniform vertical confinement. Right: vertical cut through the centre of this distribution (solid line) and theoretical prediction (dashed line). The visible modulation of the lateral peaks is most likely an imaging artifact.*

The agreement with the theoretical prediction is excellent in the centre, but one sees a kind of modulation on the outer slopes of the lateral peaks. This modulation disappears when one voluntarily displaces the imagery by some 50 µm, so it may be assumed that they are imaging artifacts due to aberrations of the imaging triplet f_s. However, a contribution due to clipping at the focussing achromatic doublet caused by the finite distance between the phase plate and the doublet cannot be excluded either. From this perspective, the fair agreement between measurement and theory has to be taken with a grain of salt. However, there is no reason to expect serious problems since when taking this measurement together with the preliminary one shown above, there seems to be little room for major deviations from the expected behaviour.

At this point, the characterisation of the phase step and barrier plate is about as complete as necessary for all practical purposes, so the focus of interest naturally shifts from the intensity distributions produced with the phase plates to the effect of the corresponding potentials on the atoms. As has been stated several times throughout this chapter, the very purpose of these phase plates is the production of two-dimensional Bose gases the experimental investigation of which will be the subject of chapter 6. There, we shall come back to the principles and results exposed here not only for the phase plates themselves, but also for the effects of finite resolution imaging.

Conclusion

WITH the work described in the foregoing chapters, we are quite confident that the mentioned process of "apprenticeship" as concerns the setup has come to an end. There will certainly be more technical elements to understand when the setup is progressively extended for future experiments, but at least the basic functioning is fairly well established. In particular, we have established a certain number of calibration techniques. Not all of these are helpful for every type of experiment, of course, but they provide a set of standard solutions to frequently appearing questions.

At the same time, with the prospective part of the work (on the one hand, the work described in the foregoing chapters, on the other hand, work on other aspects of the setup such as the usage of an optical "plug" to circumvent Majorana losses in a quadrupole), we have acquired a certain advance with respect to our actual needs so that we have a certain amount of solutions ready to tackle experimental problems that might appear in future applications.

Part II

Thermodynamics of the quasi-two-dimensional Bose gas

Introduction

> By “height” I mean a Dimension like your length: only, with you, “height” is not so easily perceptible, being extremely small.
>
> EDWIN ABBOTT ABBOTT (1838–1926)
> *Flatland. A romance of many dimensions*

WHILE the first part of this thesis was rather heterogeneous in that it contains descriptions of commonly used experimental techniques, actual experiments and prospective studies, this second part completely revolves around recent experiments on quasi-two-dimensional gases which constitute the most important part of my thesis work.

The data acquisition part of this work mainly took place from March to May 2009 and was accompanied—and succeeded—by an elaborate data processing part which continued all through the rest of the year. I was much involved in the data acquisition and even more so in its processing for which I held almost full responsibility. The data’s processing taking so long and not even being finished at the writing of this manuscript is owed to the fact that the data contained some surprises of which we only gradually became aware. It is the purpose of this part to explain the original motivation of these experimental studies, present the results and discuss our findings and possible explanations for them as far as they are known at the time this manuscript is finished.

The central chapter in this part is chapter 6 which presents our data along with the experimental procedure followed for its acquisition, our original motivation for taking it and our results as far as they are understood. It is preceded by an overview of some elements of theory concerning two-dimensional Bose gases in chapter 5 which provides the theoretical bases as well as concrete predictions for what we expected to find.

It turned out that our experimental data has clear qualitative and quantitative deviations from theoretical predictions. The second part of chapter 6 is dedicated to the description of these discrepancies as well as the discussion of possible causes. Our first suspect was the imaging optics, so I carried out a detailed analysis which is described in chapter 7 (along with general considerations on how absorption imaging works for quasi-two-dimensional systems where the standard derivation of the Lambert-Beer absorption law does not seem applicable). It may be anticipated that the result of this particular study is that quite clearly the observed effects cannot be explained in this way. Thus, we presently believe that their explanations has rather to be searched in the collective interaction of the atoms with the probe light. We have reasons to believe that the latter is highly nontrivial since the inter-particle spacing in our samples is notably smaller than the probe light's wavelength.

In parallel with these experimental studies, there have been ongoing prospective studies (both experimental and theoretical) which will give rise to future experiments. A brief survey of these studies and the associated experiments that are planned for the near future is given in chapter 8.

Chapter Five

Two-dimensional Bose gases: elements of theory

> Der Philosoph, der tritt herein
> Und beweist Euch, es müßt so sein:
> Das Erst wär so, das Zweite so,
> Und drum das Dritt und Vierte so;
> Und wenn das Erst und Zweit nicht wär,
> Das Dritt und Viert wär nimmermehr.
>
> JOHANN WOLFGANG
> VON GOETHE (1749–1832)
> *Faust I*

FOR a proper appreciation of experimental findings, it is helpful to have some theoretical background. Thus, the intention of the present chapter is to give a minimal overview of the theory of two-dimensional Bose gases. Considering the amount of literature on the subject, we have to limit ourselves to some selected aspects that are most relevant for our actual experimental work—a more comprehensive overview may be found in recent reviews [118, 16, 119].

It has been noticed by Peierls as early as 1935 that the dimensionality of a system may strongly affect its properties [120]. This is certainly the case of the Bose gas where one finds the celebrated Bose-Einstein condensation in the three-dimensional case, but not in lower dimensions (for homogeneous systems): as noted by Mermin and Wagner [121] and by Hohenberg [122], there cannot be any long range order (corresponding to a broken continuous symmetry) in systems of dimension lower than three if the potential satisfies certain sum rules [122], which inhibits Bose-Einstein condensation. However, there is a different phase transition in an interacting two-dimensional Bose gas (the Berezinskii-Kosterlitz-Thouless (BKT) transition [123, 124]) in which the sample passes from a normal to a superfluid state. First experimental evidence for this transition has been given by Bishop and Reppy in 1980 in a sample of superfluid helium [125]. It has also been demonstrated to occur in arrays of Josephson Junctions [126] and two-dimensional hydrogen [127]. More recently it has been extensively studied with ultracold atoms [41, 128, 43].

For our purposes, both phase transitions are relevant only as regards their impact on the *equation of state* which is our principal object of interest. In a first step, we will review the derivation of the equation of state for the ideal Bose gas for arbitrary dimensions, permitting to get a first impression of the peculiar character of the two-dimensional regime. In typical experiments with ultracold gases the degrees of freedom in the third direction cannot be completely frozen [129], leading to a "quasi-two-dimensional" regime. We will then briefly discuss the role of dimensionality on the collisional interactions (concentrating on our experimental geometry [130, 131]) and discuss the equation of state on a mean field level. We will discuss how the quasi-2d character of experimentally feasible systems can be taken into account within mean field theory. The existence of the BKT transition makes mean field theory fail for high densities where one has to use more elaborate theories. In the last section of this chapter we will briefly review some theoretical results for the equation of state in this regime which are of direct relevance to our experiments [132, 47, 48].

5.1 The ideal Bose gas

Einstein was the first to analyse the equation of state of an ideal gas using not the classical Boltzmann statistics, but the quantum statistics introduced by Bose for the description of the photon gas [133]. In particular, Einstein showed that in an ideal gas of bosonic particles, there may be a phase transition towards a state in which a macroscopic fraction of the atoms occupy the fundamental single-particle state [6]—today, this fraction goes by the name of *Bose-Einstein condensate* (BEC). Since the notion of a BEC has been used in more subtle contexts in the meantime, we will speak of a BEC in the Einstein sense[1] meaning a macroscopic fraction of atoms in the fundamental state *in the thermodynamic limit.*

Bose-Einstein condensation

Einstein's original argument can be presented in quite a synthetic way as follows: within the grand canonical ensemble, the total number of particles in a gas is given by

$$N = \int_0^\infty \mathrm{d}\epsilon f(\epsilon - \mu) D(\epsilon) \tag{5.1}$$

where μ is the chemical potential,

$$f(\epsilon) = \frac{1}{\exp(\beta\epsilon) - 1} \tag{5.2}$$

is the Bose-Einstein distribution function (with $\beta = 1/k_\mathrm{B}T$) and

$$D(\epsilon) = \sum_{\{\alpha\}} \delta(\epsilon - E_\alpha) \tag{5.3}$$

is the *density of states*. The parameter α stands for the quantum numbers characterising the gas, and E_α are the corresponding eigenenergies.

---

[1] A natural generalisation of Einstein's definition has been brought forward by Penrose and Onsager who associate Bose-Einstein condensation with the presence of a macroscopic eigenvalue in the reduced single-particle density matrix [134]. This definition includes Einstein's, but is also valid for interacting or finite-size systems. Thus, there are examples of systems who Bose-condense in the Penrose-Onsager, but not the Einstein sense—for example the interacting 2d Bose gas in a finite-size square potential [135].

From the form of the Bose-Einstein-distribution, it is obvious that all physically reasonable values for the chemical potential must be smaller than the energy of the single-particle fundamental (otherwise one would get negative occupations for low-lying states which is unphysical). The maximum values for $f(\epsilon-\mu)$ are achieved when μ is just equal to the lowest single-particle energy. For ease of notation, we choose the origin of energies to coincide with this energy in the following. In this situation, for $\mu=0$, the Bose-Einstein distribution converges exponentially to zero for $\epsilon \to \infty$ and diverges as $1/\epsilon$ for $\epsilon \to 0$. It now depends on the form (more precisely, the asymptotic form for $\epsilon \to 0$) of the density of states $D(\epsilon)$ whether the integral (5.1) converges or diverges. If it converges, this means that one may only put a finite number of particles in the excited single-particle states[2]. The energy of the fundamental being chosen as zero, just as the chemical potential, it does not cost any energy to put particles in the fundamental which can thus always host an arbitrarily large number of atoms. All particles beyond the number that can be put in excited states must go into the fundamental where they will accumulate as a Bose-Einstein condensate. Note that this is a sufficient, but not forcibly a necessary condition for the existence of a macroscopic fraction in the fundamental state. This is exactly the point where more subtle definitions of BECs in finite size or interacting systems enter [134]. For an example, one does not expect a Bose-Einstein condensate in a two-dimensional system in a harmonic trap in the thermodynamic limit according to [122, 121]. In a finite-sized system, one nonetheless finds macroscopic eigenvalues of the reduced one-particle density matrix [48].

To know whether an ideal gas exhibits Bose-Einstein condensation in the Einstein sense or not it is thus sufficient to calculate the density of states to see whether or not the integral (5.1) is infrared convergent (the density of states actually gives access to all fundamental properties of the trapped gas [29], but we will only regard the question of Bose-Einstein condensation and the equation of state). Since f diverges as $1/\epsilon$, it is sufficient that $D(\epsilon)$ scale as ϵ^{α} with any $\alpha>0$ to render the integral convergent and make Bose-Einstein condensation occur.

Let us first consider the case of the homogeneous ideal gas in a d-dimensional box of volume L^d with periodic boundary conditions. In this case, the quantum number is the discretised momentum $\hbar \boldsymbol{k}$, where each component of $\boldsymbol{k}$ is an integer multiple of $2\pi/L$, and the energy is $E_{\boldsymbol{k}}=\hbar^2\boldsymbol{k}^2/2m$ (the kinetic energy of an atom, the potential being zero). In the thermodynamic limit ($N\to\infty$ and $L\to\infty$ with N/L^d held constant), these values get increasingly close so that we may replace the discrete sum in (5.3) by an integral. Using $\delta[g(x)]=\sum_{x_i}\delta(x-x_i)/|g'(x_i)|$ (where x_i are simple zeros of g) and the fact that the surface of the $(d-1)$-sphere is $2\pi^{d/2}/\Gamma(d/2)$, one finds

$$D_{\text{hom}}(\epsilon)=\frac{L^d}{\Gamma(d/2)}\left(\frac{m}{2\pi\hbar^2}\right)^{\frac{d}{2}}\epsilon^{\frac{d}{2}-1}\,. \tag{5.4}$$

Thus, the density of states diverges for $d=1$, is constant for $d=2$ and proportional to $\sqrt{\epsilon}$ for $d=3$: a BEC in the Einstein sense only occurs in three (or more) dimensions. Note however that the two-dimensional case is marginal—an ever so slight increase of the exponent of ϵ

---

[2] Rigorously speaking, one would have to take out the fundamental of this integral explicitly, but in the thermodynamic limit its contribution to the integral vanishes so that one may think of (5.1) of being the total number of atoms in the *excited* single-particle states.

would be sufficient to produce Bose-Einstein condensation. In the three-dimensional case, a Bose-Einstein condensate is present when $n^{(3)}\Lambda^3 \geq g_{3/2}(1) \simeq 2.612$, with $n^{(3)} = N/L^3$, the thermal wavelength $\Lambda = (2\pi\hbar^2\beta/m)^{1/2}$ and $g_\alpha(x) = \sum_{n=1}^{\infty} x^n/n^\alpha$, *i.e.* when there are several particles per thermal wavelength.

The second relevant case (especially for experiment) is the case of a harmonically trapped gas. For ease of notation, we will consider an isotropic trap with trapping frequency ω. In this case, the energy levels (relative to the fundamental) are $E_{\boldsymbol{n}} = \hbar\omega \sum_{i=1}^{d} n_i$, so the quantum numbers are the occupation numbers $n_1 \ldots n_d$. In this case, the thermodynamic limit corresponds to $N \to \infty$ and $\omega \to 0$ with $N\omega^d$ held fixed[3]. The density of states can then be written as

$$D_{\text{ho}}(\epsilon) = \frac{1}{(\hbar\omega)^d} \int \mathrm{d}^d E\, \delta\left(\epsilon - \sum_{i=1}^{d} E_i\right) = \frac{1}{(\hbar\omega)^d} \int \mathrm{d}^{d-1} E\, \theta\left(\epsilon - \sum_{i=1}^{d-1} E_i\right) . \tag{5.5}$$

The anisotropic case with d distinct trapping frequencies $\omega_1 \ldots \omega_d$ leads to the same expression by appropriate substitutions, with $\omega = (\omega_1 \cdots \omega_d)^{1/d}$. From a geometrical point of view, (5.5) is just a $d-1$-dimensional volume integral, more precisely it is the volume under a regular $d-2$-simplex, so

$$D_{\text{ho}}(\epsilon) = \frac{1}{(d-1)!} \frac{\epsilon^{d-1}}{(\hbar\omega)^d} . \tag{5.6}$$

Plugging this result into the integral (5.1), we see that in the presence of a harmonic trap, one has a BEC in the Einstein sense for $d \geq 2$, *i.e.* only in one dimension Bose-Einstein condensation is absent. In particular, the critical atom number in two dimensions is (using $\sum_{n=1}^{\infty} n^{-2} = \pi^2/6$)

$$N_{\text{c}}^{(2\text{d})} = \frac{\pi^2}{6} \left(\frac{k_{\text{B}} T}{\hbar\omega}\right)^2 . \tag{5.7}$$

The equation of state

For our purposes, the main quantity of interest is the density. For the homogeneous case, it can be obtained be evaluating the integral (5.1) using the density of states for the homogeneous gas (5.4) (the integral converges for any d for $\mu < 0$) and dividing by L^d. One finds

$$n^{(d)}\Lambda^d = g_{d/2}\left(e^{\beta\mu}\right) \tag{5.8}$$

which is the *equation of state* for the homogeneous ideal Bose gas in d dimensions. In particular, one obtains a quite simple relation for $d = 2$ since $g_1(x) = -\log(1-x)$:

$$n^{(2)}\Lambda^2 = -\log\left(1 - e^{\beta\mu}\right) . \tag{5.9}$$

An analogous expression for the harmonically trapped gas can be derived in two ways: the first consists in using the *local density approximation* (LDA) which amounts to replacing the constant

---

[3] In the case of a Boltzmann gas where the density is given by $n^{(d)} = N(\beta m\omega^2/2\pi)^{d/2} \exp(-\beta m\omega^2 r^2/2)$, the central density remains constant when taking this limit.

chemical potential by a *local* chemical potential $\mu(\boldsymbol{r}) = \mu - V(\boldsymbol{r})$, where μ now is the chemical potential in the center of the gas. The physical idea behind this is that if the external potential $V(\boldsymbol{r})$ is varying slowly enough, it can be regarded as approximately constant over a volume large enough so that the particles inside it can be considered to be in the thermodynamic limit, their behaviour should be just as in a homogeneous sample. The other possibility is to treat the integral (5.1) in a semi-classical way by writing the energy as $\epsilon = \boldsymbol{p}^2/2m + V(\boldsymbol{r})$ and treating $\boldsymbol{p}$ and $\boldsymbol{r}$ as classical variables so that $\mathrm{d}\epsilon/(\hbar\omega) = \mathrm{d}^2 r\, \mathrm{d}^2 p/(2\pi\hbar)^2$. Carrying out the integration over the momentum leaves the spatial integral over the density distribution which is just the same as the one obtained using the LDA, *i.e.*

$$n\Lambda^2 = -\log\left(1 - e^{-\beta[V(\boldsymbol{r})-\mu]}\right) . \tag{5.10}$$

Here and in the following, n without a superscript is the two-dimensional density.

The total number of atoms for a harmonic trap $V(\boldsymbol{r}) = m\omega^2 r^2/2$, obtained by integration of (5.10), is

$$N(\mu) = g_2\left(e^{\beta\mu}\right)/(\beta\hbar\omega)^2 . \tag{5.11}$$

In the limit $\mu \to 0$ this reproduces the critical atom number (5.7). Note that in the same case, the density in the trap center will diverge. This unphysical divergence is a consequence of the replacement of the discrete sum in equation (5.1) by an integral—the numerical evaluation of the discrete sum converges to a finite value [136]. Anyway, equation (5.10) cannot give a correct account of the density distribution in the presence of a Bose-Einstein condensate since it only "holds" the non-condensed atoms whose number saturates at $N_\mathrm{c}^{(2\mathrm{d})}$ (the same argument holds for any $d \geq 2$).

Note that the equation of state of the d-dimensional ideal Bose gas (5.8) is *scale invariant* [137]. Mathematically speaking, a function f of n variables $x_1, x_2, \ldots, x_n$ is said to be scale invariant if

$$f(\lambda x_1, \lambda x_2, \ldots, \lambda x_n) = \lambda^{-\Delta} f(x_1, x_2, \ldots, x_n) , \tag{5.12}$$

for some exponent Δ. For a function of exactly two variables, a possible way to achieve scale invariance is that the function depends only on the *ratio* of the two, *i.e.* $f(x_1, x_2) = g(x_1/x_2)$, where g is an otherwise arbitrary function. In fact, the equation of state (5.8) is just of this form, since the d-dimensional *phase space density* $n^{(d)}\Lambda^d$ is a function of $\beta\mu = \mu/k_\mathrm{B}T$ only.

Another remark worthwhile to make is that unlike in three dimensions, the density can be directly measured using absorption imaging in one and two dimensions. In three dimensions, absorption imaging only gives access to the column density, that is, to the density integrated along the axis perpendicular to the image whereas in two dimensions, there is nothing to integrate over if the imaging plane is chosen as the plane of the sample itself, and in one dimension the same is true for any imaging plane perpendicular to the extension of the sample. Now, if the sample is large enough for the LDA to hold, and it has the mentioned property of scale invariance, this means that a single image of a sample trapped in a known potential constitutes a complete measurement of the equation of state: since the phase space density depends only on $\mu/k_\mathrm{B}T$, it is sufficient to measure for one temperature, and the trapping potential $V(\boldsymbol{r})$ "automatically" varies the chemical potential which can be calculated explicitly since $V(\boldsymbol{r})$ is supposed to be known. At this stage, this remark seems of purely academic interest since in reality one deals with interacting gases, thus introducing a supplementary energy scale and breaking the scale invariance. However, we will see that this does not forcibly happen in a two-dimensional Bose gas.

The thermally quasi-two-dimensional regime

Up to this point, we have taken the existence of Bose gases with dimension lower than three for granted. The world in which we live is three-dimensional, so systems of lower dimensionality can only exist as subsystems in three-dimensional space.

In classical mechanics with solid bodies, such systems are easily realised by imposing mechanical constraints which eliminate one or more degrees of freedom (such as attaching a mass to a rod fixed at the other end so that it may only move on a sphere). The closest analog for the situation of a quantum gas is to impose an external potential which is very tightly confining along one or more directions of space, so that the associated excitation energy is large compared to all typical energies of the system, thus freezing the degrees of freedom in the corresponding direction.

For concreteness (and because the experimental realisation comes more than close to it) let us suppose that we impose a harmonic potential $U(\boldsymbol{r}) = m\omega_z^2 z^2/2$ which is constant in the xy plane, but tightly confining in the z direction. Instead of the free wave eigenstates of the three-dimensional Schrödinger equation $\Psi(\boldsymbol{r}) = e^{i\boldsymbol{k}\cdot\boldsymbol{r}}/(2\pi)^{3/2}$ with eigenenergies $\hbar^2\boldsymbol{k}^2/2m$ one obtains the factorised eigenstates

$$\Psi_{\nu,\boldsymbol{\kappa}}(\boldsymbol{r}) = \psi_\nu(z)\frac{e^{i\boldsymbol{\kappa}\cdot\boldsymbol{\rho}}}{2\pi} \quad ; \quad E_{\nu,\boldsymbol{\kappa}} = \left(\nu + \frac{1}{2}\right)\hbar\omega_z + \frac{\hbar^2\boldsymbol{\kappa}^2}{2m} \,, \tag{5.13}$$

where $\psi_\nu(z)$ are the one-dimensional harmonic oscillator eigenstates, and $\boldsymbol{\kappa}$ and $\boldsymbol{\rho}$ are two-dimensional vectors in the xy plane.

The dynamics in the plane and along the confined direction are completely decoupled. Typically, $\hbar\omega_z > k_\mathrm{B}T$ so that one must retain the quantum-mechanical treatment for the z direction, but one can make the semi-classical approximation for the x and y directions. For large enough ω_z, the z degree of freedom is completely frozen out and one has an effectively two-dimensional gas whose density distribution is given by (5.10). As has been pointed out by Holzmann *et al.* [129], actual experiments on cold atoms are not really in this regime since one typically has $k_\mathrm{B}T \lesssim \hbar\omega_z$, but not $k_\mathrm{B}T \ll \hbar\omega_z$. In this case, one may still make the semi-classical approximation for each energy level in the z direction and the total density distribution takes the form

$$n(\boldsymbol{r}) = -\frac{1}{\Lambda^2}\sum_{\nu=0}^{\infty}\log\left(1 - e^{-\beta(\nu\hbar\omega_z - \mu)}\right)|\psi_\nu(z)|^2 \,, \tag{5.14}$$

where we have absorbed the zero-point energy $\hbar\omega_z/2$ in the chemical potential which is measured with respect to the state with the lowest energy. Since the states $\psi_\nu(z)$ are normalised, equation (5.14) can be integrated along the z direction to obtain the *quasi-two-dimensional* (in the thermal sense[4]) density distribution

$$n(\boldsymbol{\rho}) = -\frac{1}{\Lambda^2}\sum_{\nu=0}^{\infty}\log\left(1-e^{-\beta[\nu\hbar\omega_z+V(\boldsymbol{\rho})-\mu]}\right)\,, \tag{5.15}$$

where we have made use of the LDA to allow for a slowly varying trapping potential in the xy plane. In the limit $\omega_z \to \infty$, one recovers equation (5.10).

In the limit $|\beta[\mu - V(\boldsymbol{\rho})]| \gg 1$, $\beta[\mu - V(\boldsymbol{\rho})] < 0$, one may expand the logarithm in equation (5.15). The sum then becomes a geometric series and the quasi-2d density $n(\boldsymbol{\rho})\Lambda^2 \simeq \exp\{-\beta[V(\boldsymbol{\rho})-\mu]\}/[1-\exp(-\beta\hbar\omega)]$ which is the limit of a pure Boltzmann gas. If the temperature is sufficiently low so that $\beta\hbar\omega_z \gg 1$, one may expand the logarithm for all $\nu \geq 1$ as long as $\beta[\mu - V(\boldsymbol{\rho})]$ does not become large compared to unity and the density reads

$$n(\boldsymbol{\rho})\Lambda^2 \simeq -\log\left(1-e^{-\beta[V(\boldsymbol{\rho})-\mu]}\right)+\frac{e^{-\beta[V(\boldsymbol{\rho})-\mu]}}{e^{\beta\hbar\omega_z}-1}\,, \tag{5.16}$$

i.e. one retains the ideal Bose gas description for the fundamental along z and describes all other levels in the Boltzmann approximation.

Rigorously speaking, the residual thermal excitation along z breaks the before-mentioned scale invariance since it introduces the additional energy scale $\hbar\omega_z$. As long as temperatures are sufficiently low, though, this effect remains rather small, especially for high phase space densities where the population of the excited states along z becomes negligible with respect to the fundamental due to Bose statistics.

5.2 The interacting two-dimensional Bose gas

Real gases differ from the ideal ones discussed up to now in that the atoms interact by colliding with one another. Since we are considering very dilute gases, we only need to consider binary collisions which may be described by a single-particle Schrödinger equation [138]. The collision is then characterised by a *scattering amplitude* which depends on the energy of the colliding particles. In cold atom experiments, one may frequently regard the limit of this quantity for vanishing energies. In the case of a three-dimensional interacting gas, collisions are then completely characterised by the *s wave scattering length* a_s (for our ^{87}Rb atoms, $a_s = 5.1\,\mathrm{nm}$ [60]).

The collisionally quasi-two-dimensional regime

The situation is different in the case of a two-dimensional sample. Indeed, the dimensionality has so large an impact on the scattering properties that we have to refine a bit our terminology: from a *thermodynamic* point of view, the gas can be considered as being two-dimensional when

---

[4] We will see later in this chapter that the term “quasi-two-dimensional”, or “quasi-2d”, is also employed with a different meaning when discussing interactions.

$k_B T \ll \hbar\omega_z$. However, this criterion does not determine whether *collisions* can be regarded as two-dimensional. For collisions, the relevant quantities are the extension of the wave function in the vertical direction l_z and the typical range of the interaction potential. If the temperature is sufficiently low to be in the regime of pure s wave scattering, the latter is given by the scattering length a_s. Thus, a gas is two-dimensional from a *collisional* point of view if $l_z \ll a_s$.

It turns out that this is not the case in typical experiments with (quasi-)2d cold atoms such as those reported in [41, 42, 43, 139] or those described in chapter 6. On the contrary, in these experiments one typically has $l_z \gg a_s$ (typical numbers on our setup: $l_z = 180\,\text{nm}$, $a_s = 5.1\,\text{nm}$) so that the gas remains three-dimensional from the collisional point of view. We can thus qualify these gases as "collisionally quasi-2d" even if the temperature is so low that they are thermally purely two-dimensional. For currently accessible experimental parameters, the samples are quasi-two-dimensional both from the thermal and from the collisional point of view. Therefore we will often in the following refer to "quasi-2d" gases without specifying in which sense since there is no risk of confusion.

In order to be able to have a self-contained theory for the gas, one has to derive an effective 2d coupling constant g from three-dimensional scattering. Petrov *et al.* have carried out such a derivation [130, 131] and shown that when $l_z \gg a_s$, the coupling constant is given [130] by

$$g = \frac{\sqrt{8\pi}\hbar^2}{m} \frac{1}{l_z/a_s - \log(\pi q^2 l_z^2)/\sqrt{2\pi}}, \tag{5.17}$$

where $q^2 = 2m\mu/\hbar^2$ depends in turn on the density via the chemical potential μ. It is convenient to use the quantity $\tilde{g} = mg/\hbar^2$ which is just a dimensionless number.

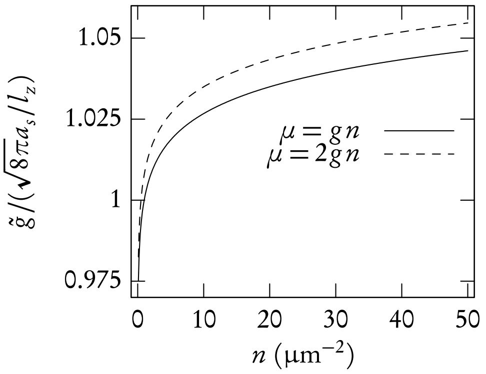

FIGURE 5.1: *Variation of the dimensionless coupling $\tilde{g} = mg/\hbar^2$ with the 2d density n for two different choices of $\mu(n)$, corresponding to the pure condensate and the mean field regime. Over the entire experimentally relevant range, $\tilde{g}$ remains equal to $\sqrt{8\pi}a_s/l_z$ to within better than five percent. These curves have been calculated using $l_z = 180\,\text{nm}$ and $a_s = 5\,\text{nm}$.*

Since we have $l_z \gg a_s$ (for our experimental numbers, $l_z/a_s \simeq 36$), the logarithmic term is usually small against l_z/a_s. This is not completely evident due to the self-consistent character of equation (5.17), but as one can see in figure 5.1, where we have represented the solution of this equation for $l_z = 180\,\mathrm{nm}$, $a_s = 5\,\mathrm{nm}$ and two different choices for $\mu(n)$,$\tilde{g}$ remains constant to a good approximation over the experimentally relevant range of densities (it falls to zero for very low densities, but they are so low that they vanish in noise for our parameters). Thus, in the following, we will treat $\tilde{g}$ as a constant, with

$$\tilde{g} = \frac{\sqrt{8\pi} a_s}{l_z} \,. \tag{5.18}$$

Note that one arrives at the same value using the following "naïve" argument [136]: the three-dimensional mean-field interaction energy is given by

$$E_{\mathrm{int}} = \frac{1}{2}\frac{4\pi\hbar^2 a_s}{m}\int \mathrm{d}^3 r\, |\Psi(\boldsymbol{r})|^4 \,. \tag{5.19}$$

Factorising $\Psi(\boldsymbol{r})$ into $\Psi(\boldsymbol{r}) = \psi(\boldsymbol{\rho})e^{-z^2/2l_z^2}/(\pi l_z^2)^{1/4}$, one may carry out the integration over z to obtain

$$E_{\mathrm{int}} = \frac{1}{2}\frac{\hbar^2}{m}\frac{\sqrt{8\pi} a_s}{l_z}\int \mathrm{d}^2\rho\, |\psi(\boldsymbol{\rho})|^4 \,, \tag{5.20}$$

where the interaction is indeed characterised by $\tilde{g}$. Typical experimental values for $\tilde{g}$ are 0.02 (reported by the NIST group from experiments on sodium [43]) and 0.14 (our group, [41, 42] and the data presented in chapter 6) so that current experiments are in the weakly interacting regime.

While this means that the interactions in a quasi-2d gas behave just as in a three-dimensional one at the mean field level, there is one important difference: in three dimensions, the interaction defines a length scale (the scattering length a_s) whereas in the quasi-2d regime the interaction constant is dimensionless (within the "naïve" derivation, the length dimension of the scattering length is cancelled by the integral over z) and cannot serve to define a characteristic length[5]. This means that *a priori* there is no breaking of scale invariance due to interactions, unlike in three (or one) dimensions. Thus, the equation of state is expected to be scale invariant provided the temperature is low enough to warrant a negligible population of the excited states in the z direction.

5.3 Hartree-Fock mean field theory

The most elementary way to take into account interactions is to do this at a Hartree-Fock mean field level. The idea of the Hartree-Fock method is to obtain an approximate, self-consistent

---

[5] In fact, this is not entirely true since one *can* define a two-dimensional scattering length $a_2 = l_z\sqrt{C}\exp(-\sqrt{\pi/2}l_z/a_s)$ [140, 119], where C is a constant of order unity. However, for typical experimental parameters, a_2 is *very* small—for $l_z = 180\,\mathrm{nm}$ and $a_s = 5\,\mathrm{nm}$, $a_2 \sim 10^{-19}\,\mathrm{m}$. It is thus hard to imagine that it might be a characteristic length scale of the problem for typical experimental parameters.

solution to the many-body Schrödinger equation by a variational approach [138]: The energy functional

$$E(\Psi) = \frac{\langle\Psi|H|\Psi\rangle}{\langle\Psi|\Psi\rangle} \tag{5.21}$$

is minimised using a trial wave function that is a symmetrised product of orthonormal single-particle states ϕ_α. The variational problem can be recast in the form of an integro-differential equation (in three dimensions):

$$\begin{aligned}\left(-\frac{\hbar^2}{2m}\Delta + V(\boldsymbol{r})\right)\phi_\alpha + \int \mathrm{d}^3r'\, U(\boldsymbol{r}-\boldsymbol{r}')\sum_\mu |\phi_\mu(\boldsymbol{r}')|^2\phi_\alpha(\boldsymbol{r}) \\ + \sum_\mu \int \mathrm{d}^3r'\, \phi_\mu^*(\boldsymbol{r}')U(\boldsymbol{r}-\boldsymbol{r}')\phi_\mu(\boldsymbol{r})\phi_\alpha(\boldsymbol{r}') = E_\alpha\phi_\alpha(\boldsymbol{r})\,,\end{aligned} \tag{5.22}$$

(the *Hartree-Fock equations*), where $U(\boldsymbol{r}-\boldsymbol{r}')$ is the two-particle interaction potential. Equation (5.22) simplifies considerably in the case of a contact potential $U(\boldsymbol{r}-\boldsymbol{r}') = g\delta(\boldsymbol{r}-\boldsymbol{r}')$: using the fact that $\sum_\mu |\phi_\mu(\boldsymbol{r})|^2 = n(\boldsymbol{r})$, it takes the form

$$\left(-\frac{\hbar^2}{2m}\Delta + V(\boldsymbol{r})\right)\phi_\alpha + 2gn(\boldsymbol{r})\phi_\alpha(\boldsymbol{r}) = E_\alpha\phi_\alpha(\boldsymbol{r})\,. \tag{5.23}$$

This has the same form as a single-particle Schrödinger equation in which the potential $V(\boldsymbol{r})$ is replaced by an *effective potential* $V_{\text{eff}} = V(\boldsymbol{r}) + 2gn(\boldsymbol{r})$. Thus, within these approximations (the Hartree-Fock approximation and the contact potential) we can take into account interactions by replacing V par V_{eff} and solving the resulting self-consistent equations for the density. Note that the Hartree-Fock approximation does not take into account correlations between different particles since it starts out from a factorised wave function. It is thus not surprising that it breaks down at high phase space densities where particles become strongly correlated, as in the case of a Bose-Einstein condensate.

Mean field theory for a thermally two-dimensional Bose gas

In the case of a gas that is collisionally quasi-2d, but thermally 2d so that there is only one populated level along z, taking interactions into account at the mean field level amounts to subtracting a term $2gn$ from the chemical potential in equation (5.9). It then becomes an implicit equation for the density n, or rather for the phase space density $D = n\Lambda^2$:

$$D = -\log\left(1 - e^{\beta\mu - \tilde{g}D/\pi}\right)\,. \tag{5.24}$$

While this expression cannot be solved for D in closed form, it can be solved for the chemical potential:

$$\beta\mu = \log\left[e^{\tilde{g}D/\pi}\left(1 - e^{-D}\right)\right]\,. \tag{5.25}$$

Thus, one can calculate the density numerically by evaluating equation (5.25) for a suitable set of values which gives $\mu(D)$. Inversing the roles of the two parameters yields $D(\mu)$. In the following, we will refer to this theory as the *single level mean field* (SLMF) theory to distinguish it from more elaborate theories which take into account the thermally quasi-two-dimensional character of the gas.

From a physical point of view, the difference between equations (5.9) and (5.24) is far more than cosmetic: it is easy to see that when D is varied from 0 to ∞, $\beta\mu$ as given by equation (5.25) takes on all values from $-\infty$ to ∞ which is equivalent to saying that equation (5.24) has a finite solution for D for *any* value of μ, unlike the ideal gas where D diverges for $\mu \to 0$ and is not defined for $\mu > 0$. From equation (5.25) we see that for $D \ll 1$ one recovers the ideal gas (5.9). In the case of a trapped gas (which can also be described using equation (5.24) by making use of the LDA), this means that the wings of the density distribution will be increasingly close (with increasing distance to the trap centre) to those of an ideal gas.

With some efforts [141], one can calculate the atom number in a harmonically trapped gas (with trapping frequency ω) corresponding to this density distribution:

$$N = \frac{1}{(\beta\hbar\omega)^2}\left\{ g_2\left(-e^{\beta\mu - \tilde{g}D(0)/\pi}\right) + \frac{\tilde{g}}{2\pi}\left[D(0)\right]^2 \right\} . \tag{5.26}$$

This relation was first presented as a perturbative result in [142], but it is in fact exact within SLMF theory [141]. Using equation (5.25) [replacing D by $D(0)$] one can express the atom number either as a pure function of $\beta\mu$ or of $D(0)$. Either way (μ is a monotonic function of D) one sees that N increases monotonically with μ or $D(0)$ and there is no saturation. This means that there is no BEC in the Einstein sense in the harmonically trapped quasi-2d Bose gas within SLMF theory, in contrast to what one finds for the *ideal* harmonically trapped 2d Bose gas (a more rigorous proof is presented in [143]).

Multi-level mean field theory

As we already stated, the typical experimental situation is that of a thermally quasi-2d Bose gas so that one has to find a means to integrate the thermal excitation along z into the mean field picture. Within a short time span, three versions of such a theory have been presented by the groups of Werner Krauth [129], Peter Blakie [144] (essentially a variant of the preceding) and ours [136]. All three approaches yield very similar results [144, 145], so for our purposes we limit ourselves to a brief review of the theories [144, 136]. For ease of notation, we will write our equations for a gas that is homogeneous in the plane, knowing that we can recover the trapped gas by making use of the LDA.

The basic idea in [129, 144] is to introduce a coupling term of the form $2gn$ into each term in equation (5.15). Since the total density is divided up into different contributions n_ν which correspond to different wave functions along z, the effective two-dimensional interaction will depend on this level structure. An intuitive approach is to start out from the three-dimensional interaction energy (5.19) and to substitute

$$|\Psi(\boldsymbol{r})|^2 = \sum_\nu n_\nu |\psi_\nu(z)|^2 \quad ; \quad n_\nu = \log\left\{1 - \exp\left[-\beta\left(\nu\hbar\omega_z + 2\sum_{\nu'} g_{\nu\nu'} n_{\nu'} - \mu\right)\right]\right\} , \tag{5.27}$$

so that the energy takes the form

$$E_{\text{int}} = \frac{1}{2}\sum_{\nu,\nu'} g_{\nu\nu'} n_\nu n_{\nu'} \,, \tag{5.28}$$

where the interaction constants $g_{\nu\nu'}$ are essentially $\tilde{g}$ multiplied by an overlap integral between the density associated to the states $\psi_\nu(z)$ and $\psi_{\nu'}(z)$:

$$g_{\nu\nu'} = \frac{\hbar^2 \tilde{g}}{m}\sqrt{2\pi l_z^2}\int \mathrm{d}z |\psi_\nu(z)|^2 |\psi_{\nu'}(z)|^2 \,, \tag{5.29}$$

with $\tilde{g}$ as given above. We have already seen that $g_{00} = \hbar^2\tilde{g}/m$, the two following values are $g_{01} = g_{10} = g_{00}/2$ and $g_{11} = 3g_{00}/4$. With these definitions, one has a self-consistent set of equations for the densities n_ν (5.27) which can be numerically solved without difficulty.

This version of a multi-level mean field (MLMF) theory uses the unperturbed eigenstates along z which in reality may be modified due to interactions. This is exactly the point where the more elaborate versions presented in [136] and [145] come into play. The approach in [136] consists in numerically solving the eigenvalue problem

$$\left[-\frac{\hbar^2}{2m}\frac{\mathrm{d}^2}{\mathrm{d}z^2} + V_{\text{eff}}\right]\psi_\nu(z) = E_\nu \psi_\nu(z) \,, \tag{5.30}$$

where $\psi_\nu(z)$ denotes the eigenfunctions along z and

$$V_{\text{eff}} = 2g^{(3)} n^{(3)}(\boldsymbol{r}) \,, \tag{5.31}$$

with the three-dimensional coupling constant $g^{(3)} = 4\pi\hbar^2 a_s/m$ and the three-dimensional spatial density

$$n^{(3)}(\boldsymbol{r}) = -\frac{1}{\lambda^2}\sum_\nu |\psi_\nu(z,\boldsymbol{\rho})|^2 \log\left(1 - e^{\beta[\mu - E_\nu]}\right) \,. \tag{5.32}$$

As before, the two-dimensional density is obtained by integrating over z which gives the same equation without the $|\psi_\nu|^2$ since they are normalised.

This system of equations can be solved by starting out with an intelligent guess for the density distribution (*e.g.*, a Boltzmann gas) and then iterating until a stable configuration is reached. When we refer to MLMF theory in the following, it is this version of it that is meant.

Note that this version of MLMF theory differs from SLMF theory even at zero temperature [which is not the case of the simpler version described above, equations (5.27) to (5.29)] since interactions will modify the eigenfunctions $\psi_\nu(z)$ regardless of the temperature. The theory presented in [145] works in a similar way, but is formulated in terms of matrices with respect to the base formed by the unperturbed wave functions along z. Another important remark concerns the application of MLMF theory to trapped gases using the LDA: Since the effective potential depends on the three-dimensional density, it depends in particular on the position in the plane so that in the system of equations (5.30) to (5.32) both the wave functions ψ_ν and the energies E_ν become functions of $\boldsymbol{\rho}$.

As far as the resulting density profiles are concerned, all three theories mentioned here give very close results over the experimentally relevant parameter range [145]. One can go even further by considering a "poor man's MLMF theory" in which one just adds a thermal gas in the states $\psi_{\nu>1}(z)$ to the SLMF density distribution—since the interaction parameter is small for current experiments and temperatures are at most of the order of some $\hbar\omega_z/k_\mathrm{B}$, the densities in the excited levels are only weakly affected by the effects of interaction. Explicitly, the density in this approach is given by

$$n\Lambda^2 = D^{(0)} - \sum_{\nu\geq 1} \log\left(1 - e^{-\beta(\nu\hbar\omega_z - \mu)}\right) \simeq D^{(0)} + \frac{e^{\beta\mu}}{e^{\beta\hbar\omega_z} - 1}\,, \tag{5.33}$$

where $D^{(0)}$ is the solution of the self-consistent equation (5.24) and we have carried out the integration over z to obtain the quasi-2d density. The approximation on the right hand side is again that of a Boltzmann gas in the excited levels.

In figure 5.2 we have represented the phase space density profiles obtained using MLMF theory for the experimentally relevant range of temperatures and $\omega_z = 2\pi \times 3.58\,\mathrm{kHz}$, in direct comparison to the ideal gas. At vanishing temperature, there is no visible difference to the latter for $\beta\mu < -1$. We equally show the direct comparison between the full MLMF result and the one obtained using equation (5.33) (using the approximated version on the right-hand side). The last plot in figure 5.2 serves to estimate when one may safely use the Boltzmann approximation for the excited levels: for the range of chemicals potentials where mean field theory is appropriate, its usage induces a negligible error. However, for $\beta\mu > 0$, the quality of the approximation rapidly deteriorates so that one must use the expression using the ideal Bose gas.

5.4 Beyond mean field theory

While mean field theory permits an accurate description of the (quasi-)two-dimensional Bose gas for low enough phase space densities ($D \lesssim 4$), it fails at high phase space densities. In fact, it has been shown by Berezinskii [123] and by Kosterlitz and Thouless [124] that while there is no Bose-Einstein condensation in a homogeneous 2d system in the thermodynamic limit, there is a phase transition from a normal (at high temperatures) to a superfluid (at low temperatures) state. This transition has many intriguing properties a comprehensive review of which would be far beyond the scope of the present work. Rather, we will content ourselves with its existence, its location and its consequences on the density distribution.

As concerns the "location" of the transition, Prokof'ev, Ruebenacker and Svistunov have shown [132] that in a weakly interacting two-dimensional Bose gas the critical point of this transition lies at a critical chemical potential and phase space density

$$\beta\mu_c = \frac{\tilde{g}}{\pi}\log\left(\frac{\xi_\mu}{\tilde{g}}\right) \quad ; \quad D_c = \log\left(\frac{\xi_D}{\tilde{g}}\right)\,. \tag{5.34}$$

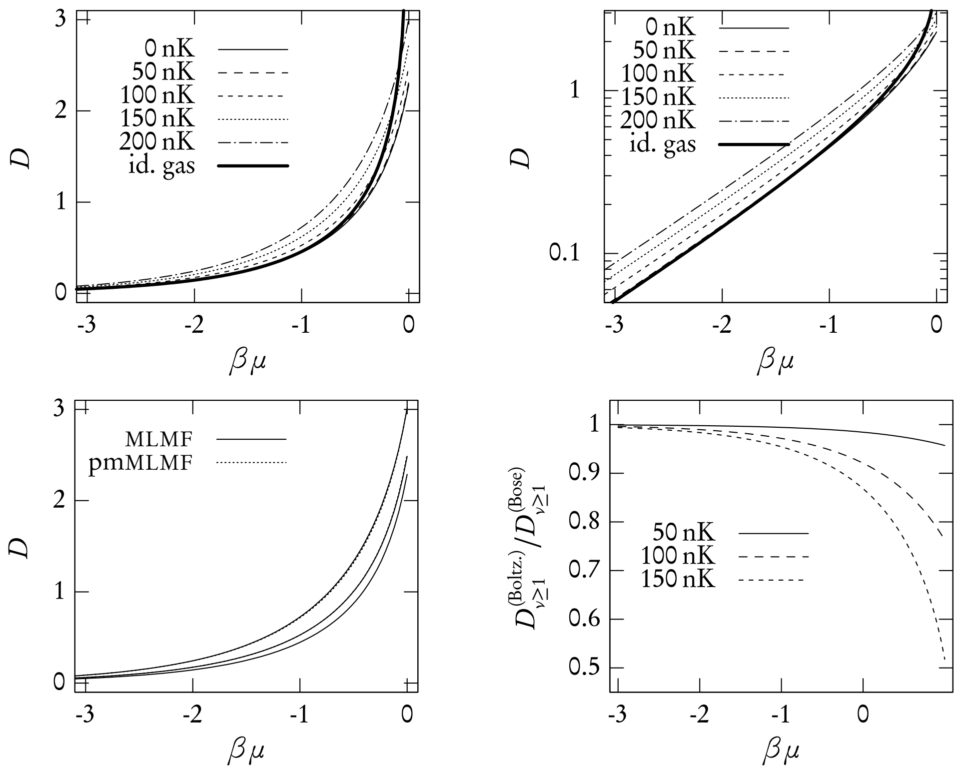

FIGURE 5.2: *Left: Phase space densities according to* MLMF *theory (the curve at* 0 nK *essentially reproduces* SLMF *theory) compared to the ideal gas prediction. Right: the same data in semi-log representation. Bottom left: comparison between the elaborate* MLMF *method and the approximate pm*MLMF *result (with the Boltzmann approximation for the excited levels) for* 0 nK, 100 nK *and* 200 nK. *In the experimentally relevant temperature range, the two are almost indistinguishable. Bottom right: ratio of the phase space density contained in the excited states as obtained using the Boltzmann approximation or the ideal Bose gas.*

The authors have numerically calculated the constants ξ_μ and ξ_D using classical Monte Carlo algorithms and found $\xi_\mu = 13.2(4)$ and $\xi_D = 380(3)$. For our experiment, $\tilde{g} = 0.14$ so that the critical chemical potential satisfies $\beta\mu_c \simeq 0.2$ and the critical phase space density is $D_c \simeq 8$.

Around the critical point, there is a fluctuation region where mean field theory breaks down. Outside this region, the gas is well described by either the mean field theory discussed above (for low D values) or the interaction-dominated (Thomas Fermi or TF) limit where $\mu \simeq gn$ (with $g = \hbar^2\tilde{g}/m$)[6] so that the density distribution of a harmonically trapped gas within

---

[6] This relation is the simplest approximation to which there are corrections even at vanishing temperature. There has been considerable theoretical research on the equation of state in this regime both analytically [146, 147, 148] and numerically using QMC methods [149, 150]. Of those recent results, the analytical results of [148] are in excellent agreement with the numeric ones [149, 150]. However, all these corrections are so small that they can be

the local density approximation takes on the shape of an inverted parabola with curvature $\partial n/\partial r^2 = (2\tilde{g}a_{\text{ho}}^4)^{-1}$. There is no simple theory for the equation of state in the fluctuation region, but Prokof'ev and Svistunov have calculated it numerically [47] in extension of their former work [132]. Their results are given in the form of tabulated values for two universal quantities called X and $\theta(X)$. In our notations, their definitions read

$$X = \frac{1}{\tilde{g}}(\beta\mu - \beta\mu_c) \quad ; \quad \theta(X) = \frac{D}{\pi} - \frac{\beta\mu}{\tilde{g}} \, . \tag{5.35}$$

Using these definitions, one can calculate the phase space density D from these two quantities:

$$D = \pi\frac{\beta\mu_c}{\tilde{g}} + \pi[\theta(X) + X] \, . \tag{5.36}$$

For the lowest values of X, the authors recommend to use the mean field expression $D = -\log[1 - \exp(\beta\mu - \tilde{g}D/\pi)]$ instead which is readily parameterised as

$$D = -\log\left(1 - e^{-\tilde{g}\theta(X)}\right) \, . \tag{5.37}$$

Equations (5.36) and (5.37) become equal at $X = -1.7$, so this is where we pass from the first (higher X) to the second (lower X) when calculating D from the tabulated values. In the following, we will refer to profiles obtained in this way as "PS profiles".

In order to compare the results by Prokof'ev *et al.* to experiment, one has to cope with two issues: firstly, all the results in [132, 47] are derived for a very weakly interacting Bose gases and the authors "expect that universal expressions established in this study are likely to work without limitations only for mU significantly smaller than 0.1" [47], where mU corresponds to $\tilde{g}$ in our notation. Thus, it is *a priori* not clear that these results are really valid for our experiments with $\tilde{g} = 0.14$. Secondly, the theory considers a thermally perfectly two-dimensional Bose gas. For a meaningful comparison, one must have an idea about the deviations from these results that may be caused by the quasi-two-dimensional character of our samples.

Both issues have been addressed in the quantum Monte Carlo (QMC) calculations carried out by Holzmann and Krauth [48] and later on by Holzmann, Chevallier and Krauth [145]. They succeeded in calculating density profiles for a quasi-two-dimensional geometry in close correspondence to preceding experiments of our group [41, 42]. In terms of atoms numbers, they were even able to go beyond experimentally feasible system sizes.

Using a set of QMC profiles that Werner Krauth kindly met at our disposition, we could make the following observations (note that one has to apply the LDA on the PS profiles in order to compare them since Prokof'ev *et al.* consider a homogeneous system whereas Holzmann *et al.* carried out their calculations for a trapped gas):

- At temperatures low enough that MLMF essentially coincides with SLMF, the QMC profiles are in agreement with the profiles calculated by Prokof'ev *et al.* to a precision

---

ignored in the present context.

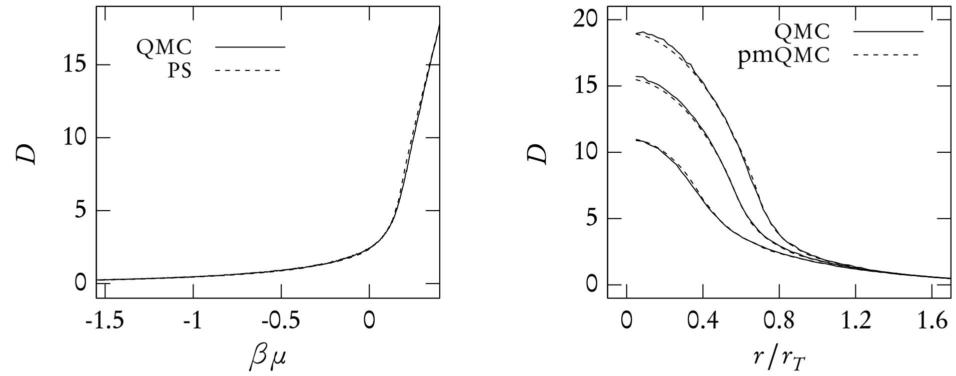

FIGURE 5.3: *Left: comparison with a* QMC *profile for* $T = 60\,\mathrm{nK}$ *(where thermal excitations along z are negligible with the prediction by Prokof'ev and Svistunov (*PS*). Both curves are strikingly similar. Right: comparison of three* QMC *curves with temperatures* 77 nK, 103 nK *and* 135 nK *(from top to bottom) with "poor man's* QMC*" (*pmQMC*) curves for the same temperatures.*

that is sufficient for experimental purposes, *i.e.* the differences are notably smaller than typical experimental noise, as can be seen in the left panel of figure 5.3. In fact, the calibration of the chemical potential for the QMC profile in this plot is slightly abusive: instead of aiming for a perfect superposition at low D (corresponding to a mean field fit), we adjusted it to have the best possible superposition of the entire curves.

- At higher temperatures, one can produce very satisfactory imitations of the QMC profiles by adding the density distribution of an ideal quasi-two-dimensional gas in the excited levels to the PS profile just as we did in the case of mean-field theory. The density profile would then be given by equation (5.33) (without making the Boltzmann approximation), but this time using the PS profile for $D^{(0)}$ instead of the SLMF one. Here again, the differences are smaller than typical experimental noise so that in the following, we can use such curves [which one could call "poor man's QMC profiles" (pmQMC)] for comparison with experiment. This is very convenient since the profiles are rapidly calculated numerically once the precalculated values by Prokof'ev *et al.* have been entered. A comparison between pmQMC and real QMC data is shown in the right panel in figure 5.3 for experimentally relevant parameters.

Thus, the QMC profiles provided to us by Werner Krauth give at the same time the answer as concerns the applicability of the theory of Prokof'ev *et al.* on our data and provides us with a "cooking recipe" to generate with modest numerical effort density profiles that closely match the QMC ones for any experimentally relevant temperature or atom number. When in the following chapters we refer to "theory" we mean pmQMC unless otherwise stated.

The inflexion point of the equation of state

A common qualitative feature of the QMC and Prokof'ev-Svistunov predictions is the existence of an inflexion point of $D(\beta\mu)$ (equivalently, using the LDA, it corresponds to a maximum of the curvature at the origin of a trapped gas profile [48]). Its position seems to be at least very close to the BKT transition [48], and using an idea put forward by Zhou and Ho in a different context [151] one can attribute still another physical meaning to this intriguing point: it can be directly related to particle number fluctuations[7] by making use of the relationship between the equation of state and the cumulants of the atom number [155].

We recall the definition of the cumulants of a statistical quantity X: if X is distributed according to some distribution function $f(X)$, the generating function of the cumulants of X is defined as $g(t) = \log(\langle e^{tX}\rangle)$, where $\langle\cdots\rangle$ denotes the expectation value with respect to the function $f(X)$. The cumulants $\langle X^k\rangle_c$ are defined by expanding this function in a power series:

$$g(t) = \sum_{k=1}^{\infty} \langle X^k\rangle_c \frac{t^k}{k!} \quad \Longrightarrow \quad \langle X^k\rangle_c = \left.\frac{\mathrm{d}^k g}{\mathrm{d}t^k}\right|_{t=0} . \tag{5.38}$$

The cumulants are directly related to the moments $\langle X^k\rangle$, in particular, the first two cumulants are nothing but the expectation value and variance of X.

In a finite-size homogeneous system (we may imagine it to be a subvolume inside a larger system), expectation values may be calculated using the grand canonical partition sum

$$Z_G = \sum_N \sum_{\{j\}} e^{\beta\mu N} e^{-\beta E_j} , \tag{5.39}$$

where $\{j\}$ represents the quantum numbers of the system's eigenstates.

Owing to the mathematical structure of Z_G, one has

$$\frac{\mathrm{d}^k}{\mathrm{d}t^k} \log\left(\left\langle e^{tN}\right\rangle\right)\Big|_{t=0} = \frac{\mathrm{d}^k}{\mathrm{d}(\beta\mu)^k} \log(Z_G) , \tag{5.40}$$

i.e. differentiating $\log(Z_G)$ with respect to $\beta\mu$ successively yields all cumulants of the atom number N.

Coming back to the inflexion point, the necessary condition for its existence is $\mathrm{d}^2N/\mathrm{d}(\beta\mu)^2 = 0$ (since the inflexion point appears at constant temperature, one may regard the atom number just as well as the phase space density). According to our reasoning above, the kth derivative of the (average) atom number with respect to $\beta\mu$ is the $(k+1)$th cumulant. Specifically, $\mathrm{d}N/\mathrm{d}(\beta\mu) = \sigma_N^2$, *i.e.* the variance of the atom number. The inflexion point thus corresponds to a situation where the variance of the atom number has a stationary point—one intuitively expects it to be a maximum since it lies well inside the fluctuation region, but not necessarily at the critical point. We could localise the inflexion point between $\beta\mu = 0.17$ and $\beta\mu = 0.21$

---

[7] Particle number (or density) fluctuations in very cold samples have first been considered by Price in 1954 [152]. The particular case of a Bose-Einstein condensate has more recently been investigated by Giorgini *et al.* [153] and by Astrakharchik *et al.* [154].

in the following way: we calculated the numerical derivative of an interpolated version of the PS profiles and searched for its maximum. The involved interpolation notwithstanding, the precision of the result is in fact limited by the discretisation of the original tabulated data. Thus, we may say that the location of the inflexion point is compatible with the critical point without being able to give more precise information. The same conclusion has been reached by Holzmann and Krauth based on their QMC data [48].

Scale invariance and universality

The theory by Prokof'ev and Svistunov is actually universal beyond the scale invariance that we stated: using the quantities stated in equation (5.35) (and other quantities defined in a similar way that we do not use here) they could construct their theory in a way that it is universal with respect to the coupling constant as well whereas the scale invariance we were discussing only implies the temperature and the chemical potential.

However, for our purposes, the interest of universality with regard to the coupling constant is essentially academic: the easiest way to vary the value of $\tilde{g}$ is to change the trapping frequency along z. With our current setup, we cannot go far beyond the value 3.6 kHz (at which the majority of our data is taken, as described in chapter 6)—and if we could, it might raise new problems since the atom number one can charge into the quasi-2d potential decreases with increasing trapping frequency. In contrast, it is very easy to reduce the trapping frequency (and thus $\tilde{g}$), but in this case scale invariance will quickly disappear due to the increasing population of excited levels along z. A different albeit technologically very involved possibility to vary $\tilde{g}$ is to change the scattering length using a Feshbach resonance. However, this would necessitate considerable magnetic fields (the broadest Feshbach resonance for ^{87}Rb lies at a magnetic field of 1007 G [156]) and our present setup does not have any coils that can easily be used to this end. Thus, we are essentially capable of realising one unique value of the coupling constant and can only verify the universality with regard to temperature and chemical potential.

A question of particular interest is to which degree the scale invariance of the PS theory is preserved at finite temperature in a quasi-2d system. Since we have seen that the resulting density profiles may be described quite satisfactorily by our pmQMC approach, it is straightforward to give a quantitative answer to this question: the density corresponding to the particles in the fundamental state along z actually *is* scale invariant to experimental precision. There is a slight breaking of this scale invariance due to the particles in the excited states $\nu \geq 1$ which is to a very good approximation given by $D_{\nu\geq 1}$ as given by equation (5.33) (without the Boltzmann approximation). For experimentally relevant parameters, this is maximally of the order of one. Thus, it is comparable to density as given by mean field theory, but will be small against the phase space density as given by PS theory.

This can be seen in figure 5.4: at a scale permitting to see the high phase space density region, profiles for different temperatures superpose almost perfectly over the whole range relevant for our experiment. Of course, by zooming in, one would find the deviations (shown in figure 5.2) in the low density regime which is accurately described by mean field theory.

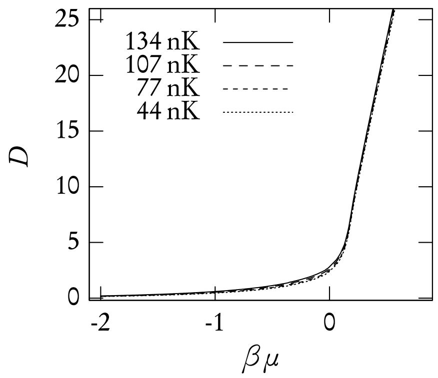

FIGURE 5.4: *pm*QMC *profiles for temperatures covering the experimentally relevant range. Notwithstanding the factor of three between the extreme temperatures, all profiles are practically superposed at this scale.*

With these considerations we conclude our review of the aspects of two-dimensional Bose gas theory most relevant for our purposes. To sum up the points that are most important for the following chapter, we have seen that experimental systems are quasi-two-dimensional both thermally (entailing the necessity to heed the residual excitation along z in the mean field limit) and collisionally (permitting to account for interactions by means of the dimensionless constant $\tilde{g}$). The equation of state exhibits scale invariance which should only marginally be broken for experimentally achievable temperatures. Finally, we have concrete predictions for the equation of state that should be directly comparable to experimental findings.

Chapter Six

Experiments with two-dimensional Bose gases

> Vous voyez bien. Passer d'une joie absurde à une mélancolie aussi absurde. Tout ça ne repose sur rien.
>
> YASMINA REZA (*1959)
> *Trois versions de la vie*

DURING our short review of 2d Bose gas theory in chapter 5, we have laid special emphasis on the aspect of scale invariance in the 2d Bose gas's equation of state. Indeed, the presumed existence of this scale invariance in a quantity that is experimentally directly measurable on our new setup—the two-dimensional density—was the very motivation of the experimental studies that are presented in this chapter.

As we stated in chapter 5, given the scale invariance and the local density approximation, one single measurement would be sufficient to determine the equation of state for all densities from zero to the central density of the measured sample. Our idea was to scan the experimentally accessible range of temperatures and atom numbers and use this data to verify whether there is indeed scale invariance. The experimental sequence we used for the production and measurement of our samples along with the necessary calibrations is described in the first part of this chapter.

When we obtained our first results in this respect (which necessitates a somewhat involved data processing that we shall describe in detail), they essentially corresponded to our expectations. This ceased to be the case when we began to do direct comparisons to theoretical predictions: it turned out that there were differences on both the qualitative and the quantitative level which need to be explained. In trying to understand them, we carried out further studies of our data which will be described in the second part of this chapter. The particular question of the influence of the imaging optics gave rise to extensive study the description of which needs a lot of space so that we dedicate a separate chapter (chapter 7) to it, all other aspects that we have studied up to now are described in this chapter[1]. In order to avoid jumping back and forth between phenomena and possible explanations with different degrees of plausibility, we first describe all the effects we observed on our data and then discuss the explanations we considered.

---

[1] The last aspect we discuss—the collective interaction between the atoms and the probe light—is actually far more complex than the imaging optics aspect, but in the available time, we could not carry out an extensive study on it so that we have to limit ourselves to a brief qualitative discussion here.

In the course of our more profound investigations, we were sometimes led to analyse data that was originally not supposed to serve other than quick calibration purposes and is therefore of inferior quality, or data the quality of which in itself is satisfactory, but which has been taken only once. We try to mark explicitly those cases where a certain scepticism is appropriate.

6.1 *Preparation of a single two-dimensional Bose gas*

The production of our objects of study takes several steps: first, we produce a cold (degenerate or near-degenerate) three-dimensional cloud in the science cell using a sequence as described in chapter 1. Then we add the optical potential so that the atoms become very strongly confined in the vertical direction, thus entering the quasi-2d regime. However, only a fraction of the total sample can be loaded into the plane, the remaining atoms are pushed outside the optical potential, but remain confined by the magnetic trap. In order to make images along the axis perpendicular to the plane (*i.e.* the vertical axis), one has to remove those side planes since otherwise they would by far dominate the signal.

Loading the atoms into the optical potential

The optical potential is generated using a 10 W Verdi laser operating at 532 nm using the optics described in the last section of chapter 4. The actual beam power can be varied between zero and a maximum which is in practice given by what we can inject into the fibre. For most of the data presented in this chapter, the total beam power on the atoms was 1.3 W. The variation of the power is achieved by changing the modulation power in an acousto-optical modulator (AOM). In order to obtain a given intensity "on demand", the power of the AOM is controlled by a feedback-loop circuit which compares a reference signal coming from the control computer to the signal of a photodiode which monitors the actual power.

The dipole potential is ramped up slowly over 1.5 s, the value which we found to minimise heating. In fact, it is very hard to be adiabatic in practice when covering such a large range of frequencies (from $\sim 60\,$Hz—the vertical frequency in the TOP trap—to $\sim 4\,$kHz) since one would have to increase the power so slowly that other heating effects (especially due to the residual intensity fluctuation of the beam) would dominate. To limit the effect of heating, the ramp takes place in the presence of the evaporation rf field. The frequency of the latter remains constant during the ramp and a subsequent hold time phase of 4 s, thus determining the final temperature.

The adjustment of the Verdi beam is quite delicate: in order to charge the maximum number of atoms in the central plane, one wants the beam to hit the center of the cloud as precisely as possible (the horizontal alignment is far less sensitive, but needs some care as well). In order to facilitate the beam adjustment, the dichroic plate which serves to superpose the Verdi with the imaging beam—and which is at the same time the last reflecting element on the Verdi's path before reaching the atoms—is fitted with a pair of graduated precision actuators (Newport DS-4F).

While the optical potential one can observe in a given plane perpendicular to the propagation direction corresponds nicely to the theoretical prediction, we observed a peculiar

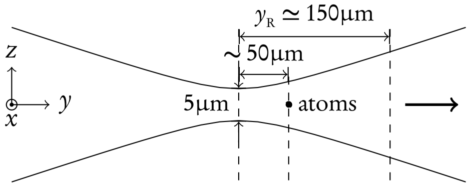

FIGURE 6.1: *Schematic representation of the geometry of the dipole beam on the atoms (not to scale): the beam propagates along the y axis and is focussed to a size of* $\simeq 5$ μm. *The atoms are about* 50 μm *further "downstream".*

behaviour when trying to load an atomic sample in the optical potential with the focal plane in the middle of the atomic sample: the cloud shape in the plane becomes strongly anisotropic, and the centre is displaced in the y direction by up to ~ 20 μm whereas the Verdi beam should not create any significant potential in the horizontal (xy) plane. We thus judged it preferable to work with a slightly reduced trapping frequency by voluntarily displacing the focal plane from the atoms by ~ 50 μm, *i.e.* by a third of a Rayleigh length (see figure 6.1 for an illustration). In this situation, the cloud is still slightly compressed along the propagation direction (the ratio of the trapping frequencies is about 1.11) of the Verdi beam, but the centre coincides with the one in the absence of the beam.

Cleaning the single plane

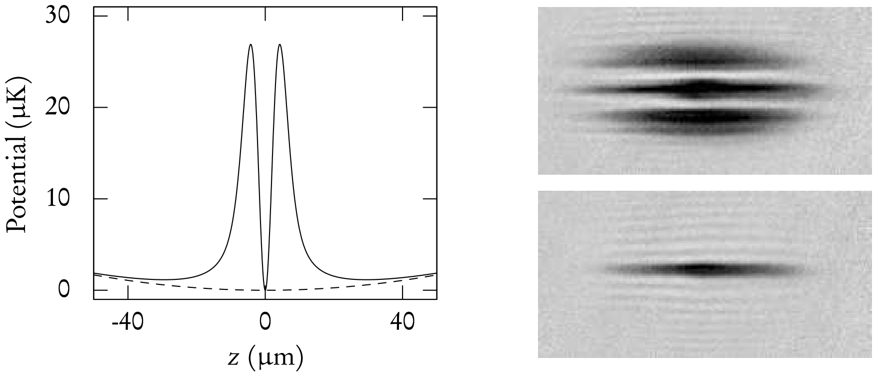

FIGURE 6.2: *Left: combined (magnetic and optical) potential in the vertical direction. There are three distinct minima: a very narrow one in the center corresponding to the quasi-2d plane and two shallower ones corresponding to the upper and lower side planes. Right: Horizontal absorption images of the quasi-2d plane before (top) and after (bottom) cleaning. These images were taken with a vertical trapping frequency considerably lower than the data presented throughout the remainder of chapter for better visibility. The horizontal lines above and below the cleaned sample are caused by diffraction.*

While we had to find a means to ensure that the atoms in the side planes do not perturb the measurement of the atoms in the plane, one has to note that in order to do this it is not mandatory to physically remove these atoms—it is sufficient to transfer them to an internal state in which they will have no appreciable interaction with the probe beam.

Our solution to this problem is to use a laser beam tuned to the $F = 2 \mapsto F' = 2$ transition (the same transition that is used for optical pumping which permits to use the same laser). After a few absorption cycles, the atoms will be in the $F = 1$ hyperfine state which does not interact with the imaging beam. Of course, in doing so, one has to avoid making the atoms in the quasi-two-dimensional plane suffer the same fate. To this end, we used a telescope of magnification 7.5 to image the shadow cast by a piano string of diameter 200 μm on the plane. The power in the center of the shadow is lower than the maximum power by a factor of more than 100. In order to use the available power efficiently, we broaden the beam using an anamorphic prism pair to match more closely the shape of the atomic distribution.

As is easy to imagine, the "protection" of the atoms in the plane is quite sensitive to the vertical adjustment of this "cleaning beam". In order to facilitate this adjustment, we decided to superpose the cleaning beam with the imaging beam which in turn (as already mentioned in chapter 4) is superposed with the dipole potential beam on the horizontal axis perpendicular to the magnetic transport axis. Thus, we can take a horizontal absorption image of the atoms without cleaning beam in the presence of the optical potential (taking care that the system is properly warmed up), mark the position of the atoms on the screen and use this reference to align the cleaning beam while observing it on the screen. After adjustment, one can immediately verify using horizontal absorption imaging that the side planes are well cleaned. The power of the cleaning beam is reduced as much as possible, *i.e.* we make sure that the side planes are well cleaned for the highest used temperature (where the extension of the "side lobes" is largest), but reappear when the duration of the cleaning pulse is reduced by more than 10%. A typical duration is 60 μs. During data acquisition, the cleaning is the object of periodic verification: since our data is mostly taken with vertical imaging where there is no means to know whether cleaning is still in order, we return to horizontal imaging from time to time to make sure the side planes have not reappeared (either due to a drift of the cleaning beam relative to the atoms or to a decrease in the cleaning beam's intensity).

Time of flight measurements

As usual in experiments on cold atoms, we take our absorption images either in the trap (in situ) or after a certain duration of ballistic expansion after rapidly switching off the trap [the time of flight (TOF) method]. In the present context, we additionally introduce a variant to the standard TOF scheme (where all trapping potentials are simultaneously switched off) which consists in switching off the *magnetic* trapping potential while keeping the *optical* potential constant. In this configuration, the atoms remain strongly confined in the vertical direction so that the free expansion can only take place in the plane. In the following, we refer to this situation as "2d TOF" whereas the usual TOF will be called a "3d TOF".

The 2d TOF is of special interest since it has been predicted by Kagan *et al.* [157] and by Pitaevskii and Rosch [158] that in this special configuration the expansion of the density distribution after being released from an isotropic in-plane trap with trapping frequency ω follows a simple scaling relation[2]:

$$n(\boldsymbol{\rho},t)=\frac{1}{\gamma(t)}n\left(\boldsymbol{\rho}/\sqrt{\gamma(t)},0\right) \quad ; \quad \gamma(t)=1+(\omega t)^2\,. \tag{6.1}$$

If this result holds for our data (there may be limits to its applicability since it has been derived using a delta interaction potential which can cause problems in two dimensions), this means that one may acquire data after a 2d TOF and then use the scaling relation (6.1) to obtain the exact in situ density distribution. This has two advantages with respect to a direct in situ measurement: firstly, the imaging takes place in the absence of an external magnetic field so that there is no inhomogeneous Zeeman broadening, thus enhancing the signal to noise ratio (of course, for longer expansion time the measured peak optical density will eventually fall below its in situ value). Secondly, one is less prone to imaging artifacts of all kinds since the object to be imaged is larger.

In taking our data, we made use of this relation, albeit with some caution. On the one hand (as described on pp. 132 ff.), our data cannot serve as an experimental verification of equation (6.1), on the other hand, the experimental situation is more complicated due to the slow variation of the vertical trapping frequency in the plane which may be expected to cause deviations from the predicted behaviour once the cloud has expanded sufficiently to explore a larger part of the potential. Thus, we usually took our data after a short 2d TOF of 3 ms which is sufficient to ensure the absence of a magnetic field, but will change the linear size of the cloud by only 6% so that the overall shape cannot have evolved substantially (of course, the same would be true for a short 3d TOF, but to a lesser extent). Many measurements were repeated both with and without 2d TOF, and we will show some examples throughout this chapter.

One may wonder whether absorption imaging still works in the same way in our particular geometry where the extension of the sample along the imaging direction (z) is comparable to the typical distance between atoms [$(n^{(3)})^{-1/3}$ or $(n^{(2)})^{-1/2}$, whichever is larger] so that there is typically at most one atom in a given column. Thus, the standard derivation of the Lambert-Beer absorption law cannot be applied. However, as we will show in chapter 7, one can derive the same equations by an alternative argument so that absorption imaging may be expected to work in the same way for quasi-2d samples as it does for three-dimensional ones at least in the dilute limit and with non-saturating probe laser light.

We also made use of 3d TOF measurements to characterise our samples. While there is no global scaling law for the density distribution during a three-dimensional ballistic expansion, the general behaviour can be understood by noting that due to the strong vertical confinement the cloud will expand very rapidly in the vertical direction so that after less than 1 ms interactions within the sample become negligible. Hence, during the observable part of the TOF, the cloud should expand as an ideal gas. As concerns the expansion in the xy plane, one may divide

---

[2] More precisely, Kagan *et al.* presented a rigorous proof of the scaling relation within a Bogoliubov approach (for the condensate mode and the Bogoliubov excitations) whereas Pitaevskii and Rosch derived it for the entire density distribution, but put it under the reserve that the interaction between atoms can be represented as a delta potential.

the sample into a thermal (which will expand with a typical time scale of $\omega^{-1} \sim 8\,\mathrm{ms}$) and a condensed part (which will expand with a typical time scale of $m\Delta x\Delta y/\hbar \sim 550\,\mathrm{ms}$ for $\Delta x \sim 20\,\mu\mathrm{m}$). This means that for typical experimental time scales from 0 to 30 ms the thermal part will expand appreciably while the condensed part will remain practically unaltered.

Trapping frequencies

After these discussions of the production and cleaning of a single quasi-2d gas and our methods to image it, the only missing elementary characterisation of the system is to give the trapping frequencies in the three directions of space. This is most important for the tightly confining potential since it determines the quasi-2d coupling constant $\tilde{g}$. Before measurement we only have the theoretical estimate based on the beam power and measured waist, but this is certainly overestimated since we voluntarily displaced the focal plane from the atoms. It is also important for the in-plane frequencies since they are modified by the presence of the optical dipole potential: as has been pointed out in [136], the inhomogeneity of the vertical trapping frequency over the plane causes a renormalisation of the frequencies in the plane, so they should be measured as well.

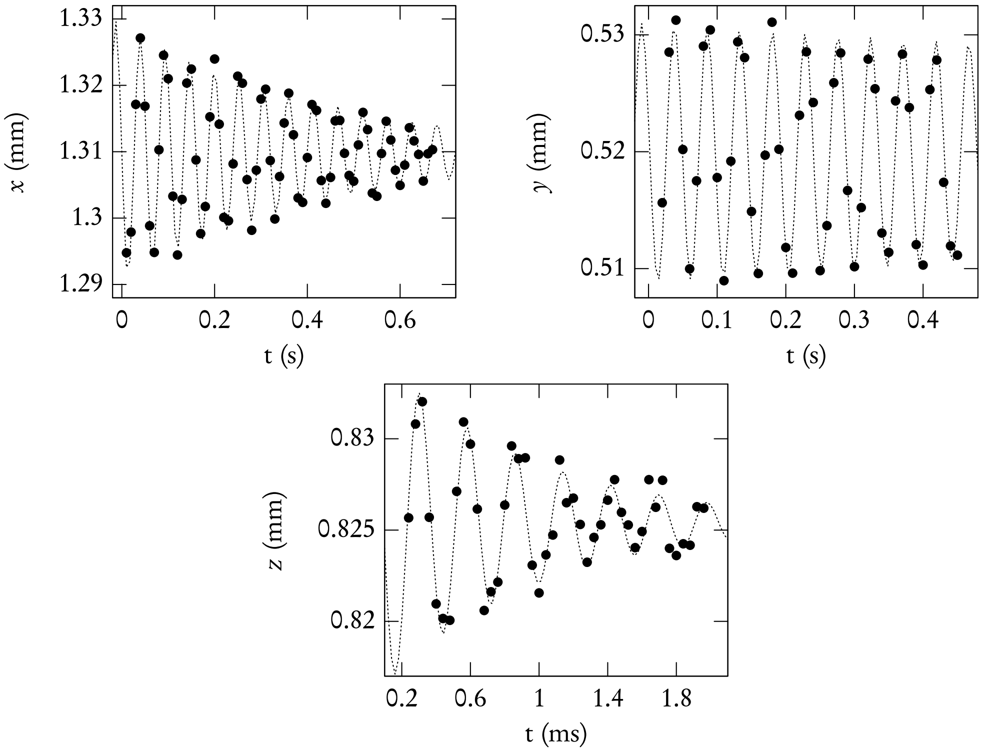

FIGURE 6.3: *Center of mass oscillations used to determine the trapping frequencies along all three axes. Note that the time scale for the oscillations along z is in milliseconds whereas it is in seconds for the other two directions. The dotted lines show least square fits with damped sines.*

axis	frequency (Hz)	damping time (s)
x	18.8	0.46
y	21.0	2.94
z	3580	0.91×10^{-3}

TABLE 6.1: *Trapping frequencies and phenomenological damping times corresponding to the plots shown in figure 6.3. The "damping" in the plane might be nothing but the start of a beat note, in the vertical direction it is plausible to assume that it is due to the sample's exploring anharmonic parts of the trapping potential.*

The procedure for the measurement of the frequencies is just as it has been described in chapter 3, *i.e.* by exciting and observing centre of mass oscillations along all three axes. A typical example for such a measurement is shown in figure 6.3, the numerical value extracted from least square fits using a phenomenological damped sine function are given in table 6.1.

The vertical trapping frequency corresponds to a harmonic oscillator length of $l_z = (\hbar/m\omega_z)^{1/2} = 180\,\text{nm}$ [the geometric mean frequency in the plane $\omega = (\omega_x\omega_y)^{1/2} \simeq 19.9\,\text{Hz}$ in turn leads to a length of $a_{\text{ho}} = (\hbar/m\omega)^{1/2} = 2.41\,\mu\text{m}$] and thus to a coupling constant $\tilde{g} = \sqrt{8\pi}a_s/l_z = 0.14$.

6.2 *Data processing*

In order to be able to do meaningful comparisons to theory, we first have to convert our experimental data to the form proposed by theory. In particular, we need to express our density distributions as functions of the radial distance from the cloud centre, and calibrate the temperature and chemical potential so that we may convert the density and the radius to a phase space density and an equivalent chemical potential, using the LDA for the latter. In the following sections, we describe the processing and the calibration of our data that permit to cast it in the desired form.

Image processing

Directly after acquisition, we dispose of a set of absorption images such as those shown in the two upper rows in figure 6.4, *i.e.* a grid of discrete optical density (D_o) values (see chapter 7 for the definition of the optical density). For quantitative analysis, we want to have our data in the form of radial profiles which can be compared to theoretical predictions. These profiles are obtained in several steps: in a first step, we fit a 2d Gaussian to the images to determine the position, anisotropy and tilt angle of each sample. Around its position, we extract a region of interest (ROI) of 216 × 216 pixels, corresponding to an equivalent physical extension of $(315\,\mu\text{m})^2$.

We then calculate the average value in four 40 × 40 pixel squares situated at the corners of the ROI (like this, the distance between two opposing "inner corners" of these squares is only 12% smaller than the full width of the region of interest, see figure 6.5). This value is subtracted

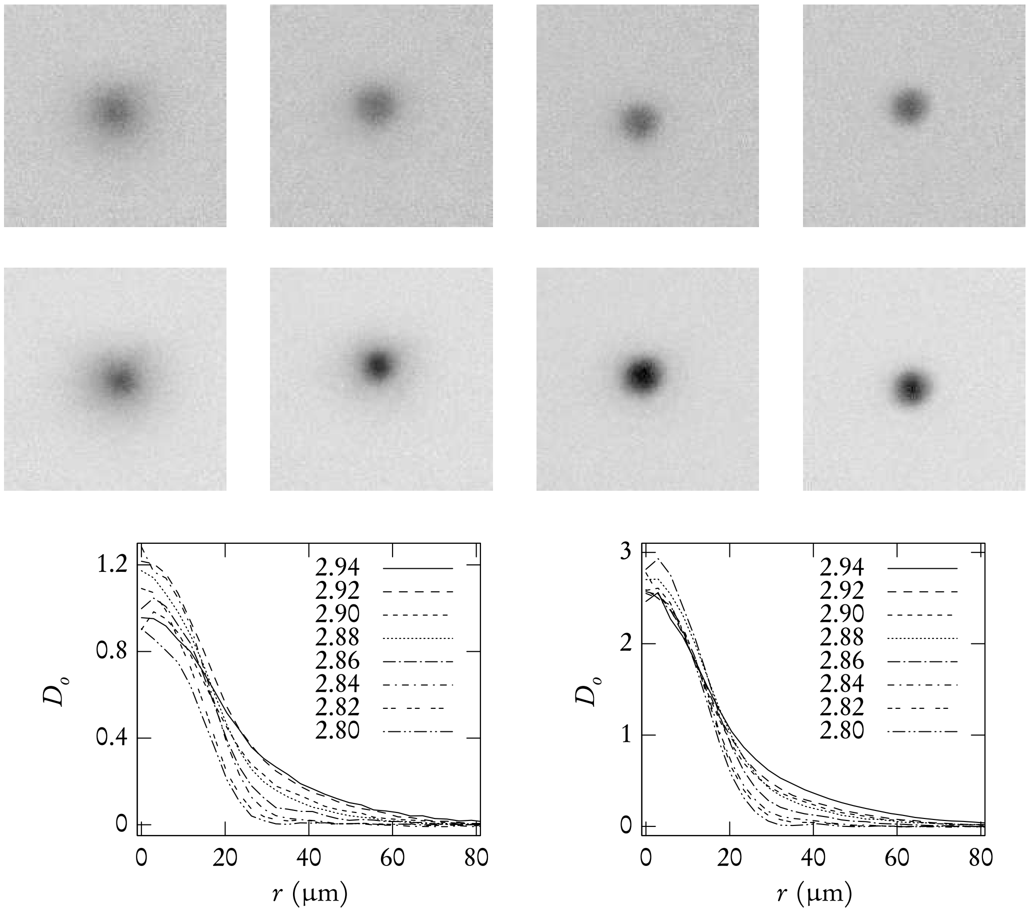

FIGURE 6.4: *Top row: in situ absorption images of quasi-2d samples for* 2.94 MHz, 2.90 MHz, 2.86 MHz *and* 2.82 MHz *(from left to right). The offset has not yet been subtracted and the centering for these images is done by hand (for data analysis, this is done using a gaussian fit). Middle row: the same after a 2d* TOF *of* 3 ms. *The grey scale has been slightly adapted with respect to the top row. Bottom row: averaged profiles from data taken in situ (left) and after a 2d* TOF *of* 3 ms *(right). The plots show the measured optical density* D_0 *without any corrective factors. The two graphs are extracted from one same series in which the 2d* TOF *duration was alternating between* 0 *and* 3 ms. *The radio frequency determining the temperature ranges from* 2.94 MHz *(highest temperature) down to* 2.80 MHz *(lowest temperature).*

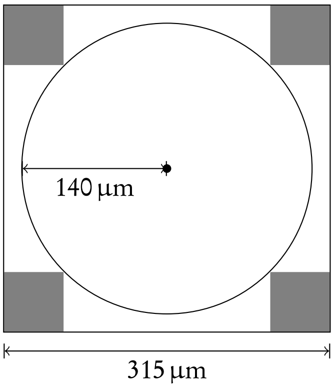

FIGURE 6.5: *Schematical illustration of the region of interest (*ROI*): the four shaded squares in the corners indicate the areas used for the calculation of the offset. Their inner corners touch a circle of radius* 140 µm *which is larger than any measured sample.*

as an offset which works to a precision of typically better than $\Delta D_o = 0.02$. The ROI is then rotated to compensate for the tilt angle (typically $\lesssim 10°$) using a bicubic-spline algorithm from the MATLAB library.

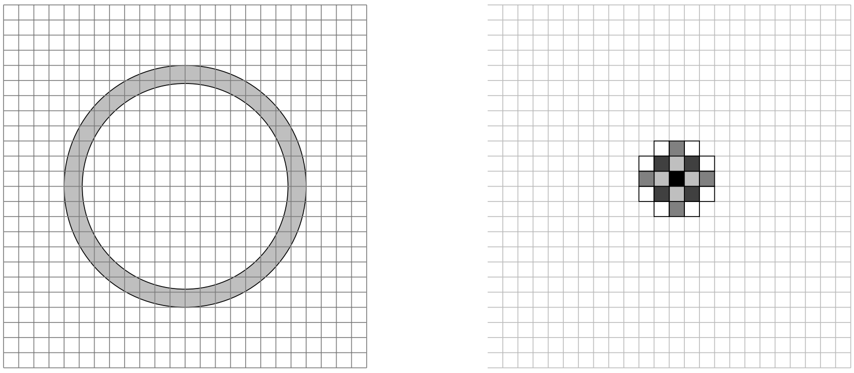

FIGURE 6.6: *Schematical illustration of the two approaches to obtain a radial profile. Left: the average is carried out by explicitly calculating the integral over the pixels contained between two ellipses (shaded area), taking into account the fact that most pixels will only partially lie inside the considered area. Right: pixels are sorted according to their distance from the centre, illustrated here for the first five distances. Pixels having the same color are at the same distance from the centre. The average is then carried out over each such subset of pixels.*

After these preparations, we are ready to do the angular average to obtain a radial profile. We have tried out two complementary algorithms to do this (the first one has been developed by Kenneth Günter and the other by myself). Their principles are as follows (see also figure 6.6):

1. The pixels of the ROI are sorted according to their distance from the centre (measured

in discrete pixels), then an average is carried out within each set of pixels at an equal distance from the centre. If one wants to enhance the resolution of this procedure, one can subdivide the original pixels into $4, 9, 16, \ldots$ pixels and use the algorithm in the same way.

2. The ROI is considered as a continuous surface on which the pixels take up a finite area each. One calculates the surface integral over the surface between two ellipses centered on the ROI using analytical formulas. Each pixel contributes with the fraction of its area that is covered by the considered surface. The radii of the ellipses may be chosen arbitrarily, but the most natural choice seems to be to keep the total surface equal so that the resolution becomes finer towards the outside of the cloud.

While both methods allow to calculate the averages to an arbitrary precision (*i.e.* to a precision limited by the fluctuations of the original image), each has its respective advantage: the first method is *much* faster whereas the second method allows to take into account the ellipticity in a natural way by imposing the measured ellipticity on the integration surfaces (which has to be implemented by a suitable binning algorithm with the first method). Apart from these details, both algorithms yield identical results, as one should expect. The profiles shown in the bottom row of figure 6.4 have been generated using the first method, as is the case for the majority of the data shown in this chapter.

Fixing the detectivity factor

In an ideal realisation of absorption imaging with linearly polarised resonant light, the atomic density would be given by

$$n = D_o \left(\frac{7}{15} \frac{3\lambda^2}{2\pi} \right)^{-1} , \tag{6.2}$$

where $7/15$ is the average of the squares of the relevant Clebsch-Gordan coefficients (see chapter 7) and $3\lambda^2/2\pi$ is the cross section of the atoms for the absorption of light with a Clebsch-Gordan coefficient of one ($\lambda = 780.24\,\mathrm{nm}$ in our case). In actual experiments, the measured optical density D_o is diminished with respect to the ideally expected value (the *optical depth* d_o, see chapter 7) due to various imperfections such as broadening of the resonance line due to the Zeeman effect in inhomogeneous magnetic fields. We account for this by multiplying the optical density with an appropriate factor $\xi > 1$.

We will now discuss the role of the imaging beam intensity in our experiment. In order to have a precise idea of the intensity on the atoms, we carried out a calibration of the total efficiency of our pixelfly qe camera, *i.e.* we determined the number of counted photoelectrons as a function of the number of photons really arriving at the camera (which can be calculated from the exposure time together with the beam power measured using a power meter and the beam width). We found that the ratio between the numbers of present photons and counts is 7.69. Knowing this number and the magnification G (since the intensity on the atoms is G^2 times the intensity on the camera), we can determine the intensity on the atoms directly from our raw images.

Most of our data has been taken with an intensity of 0.5 mW/cm^2 on the atoms which corresponds to 1/6 of the equilibrium saturation intensity for linearly polarised probe light $I_{\mathrm{sat}} = 3.05\,\mathrm{mW/cm^2}$ [159]. In the following, we will refer to this as the "high intensity" scheme. We equally took data using a "low intensity" scheme where the power was a factor of 4.5 lower and the exposure time a factor of 4.3 longer to have an approximately equal number of detected photons. In direct comparison after 3 ms of 2d TOF we measured 1.27 times more atoms in the low intensity scheme than in the high intensity scheme (determined in a series in which the intensity was changed at some point without interrupting the sequence. The ratio is that between the averages of five consecutive shots for each intensity).

There are several reasons which made us prefer the "high intensity" imaging scheme: firstly, its designation notwithstanding, it is still in the weakly saturating regime so that the line width cannot be reduced much by reducing the intensity even more; Secondly, it permits to take our absorption images using shorter exposure times so that the atoms have less time to move—we shall illustrate on pp. 136 how such a motion can alter the observed density distribution. A third reason is an effect that has yet to be understood: while when imaging after a finite TOF duration, the observed optical density increases with decreasing intensity as one should expect since saturation broadening becomes less and less pronounced, we found that in the case of in situ imaging the observed atom number actually has a *maximum* close to the intensity of the high intensity scheme and then rapidly decreases with decreasing intensity. We thus decided to attribute a greater weight to TOF data, but frequently acquired data with series alternating between in situ and 2d TOF sequences to have the direct comparison.

Since the measured factor of 1.27 constitutes more of a lower bound than an exact correction factor (one would have to be able to carry out the limit towards vanishing intensity in order to obtain it) and the resonance curves we measured are compatible with the natural line width, but seem to be slightly broadened even in the low intensity scheme, we decided to "leave a margin" of 10% to roughly account for these extra effects and used $\xi = 1.4$ for data taken after TOF. This is most likely still slightly underestimated, but should not be far from the truth. In the following section, we will discuss the influence of the value of ξ on subsequent calibrations.

For in situ data, the detectivity is dominated by inhomogeneous Zeeman broadening. In direct comparison, we measure 2.21 as many atoms after 3 ms of 2d TOF than in situ. Thus, for in situ images, we use a value for ξ which is a factor of 2.21 larger than the TOF value, *i.e.* $\xi = 3.1$.

Determining the temperature

Since the natural quantity for the theoretical description of the (quasi-)2d Bose gas is the phase space density $D = n\Lambda^2$ rather than the density n, a meaningful comparison between experiment and theory requires a reasonably precise estimate of the temperature. The simplest method to obtain such an estimate is a gaussian fit: since $g_\alpha(x) \simeq x$ for $x \ll 1$ and any α, the density distribution of a harmonically trapped Bose gas in any dimension will approach a Gaussian in the outer regions where the density is low enough.

On three-dimensional samples, this method works quite well if one takes care to exclude the very centre of the sample from the fit. In two dimensions, this is considerably less true since the coefficients in the power series of g_1 decrease more slowly than those of $g_{3/2}$. In trying to restrict the fit to a region sufficiently far out for the Gaussian approximation to work (to be precise to within 5%, one needs to restrict the fit to $r > 2r_T$, where $r_T = (k_B T/m\omega^2)^{1/2}$ is the typical length scale of the trapped gas), one ends up with a poor signal to noise ratio and a high sensitivity to imperfections in the offset subtraction, rendering the fit temperature prone to strong fluctuations and systematic errors.

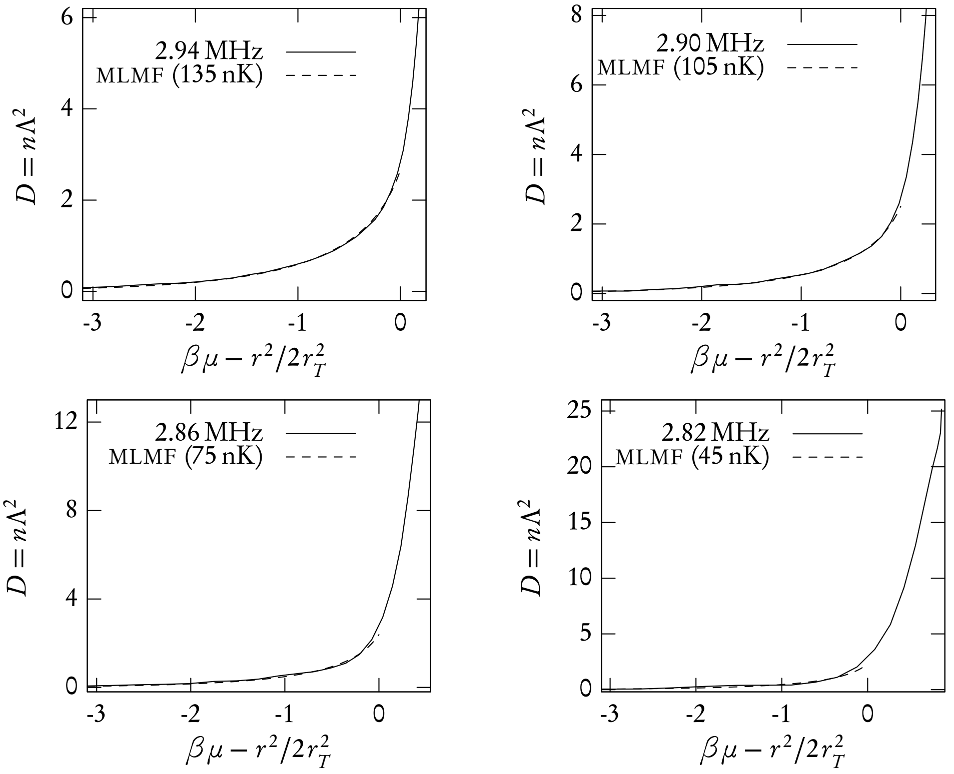

FIGURE 6.7: *Temperature calibration using multi-level mean field (*MLMF*) profiles. The plots show four typical profiles (taken after* 3 ms *of 2d* TOF*) after calibration, with the closest mean field profile for comparison.*

In order to have a more reliable means of estimating the temperature, we developed an algorithm based on multi-level mean field (MLMF) theory: first we generate a set of $D(\beta\mu)$ curves for temperatures ranging from 5 nK...200 nK in steps of 5 nK as a gauge. These profiles are calculated up to a maximal chemical potential $\mu_{\max} = 0$, corresponding to a maximum phase space density of between 2 and 3. To estimate the temperature for a given sample, we take its radial profile $n(r)$ which we convert to $n(\mu_0/k_B T_0 - r^2/r_{T_0}^2)\Lambda_0^2$ using an arbitrary initialisation temperature T_0 and thermal wavelength $\Lambda_0 = (2\pi\hbar^2/mk_B T_0)^{1/2}$, and $\mu_0 = 0$. Note that we are relying on the LDA for this calibration. The experimental profile is adjusted to the MLMF profile whose temperature comes closest to T_0 by using the temperature and chemical

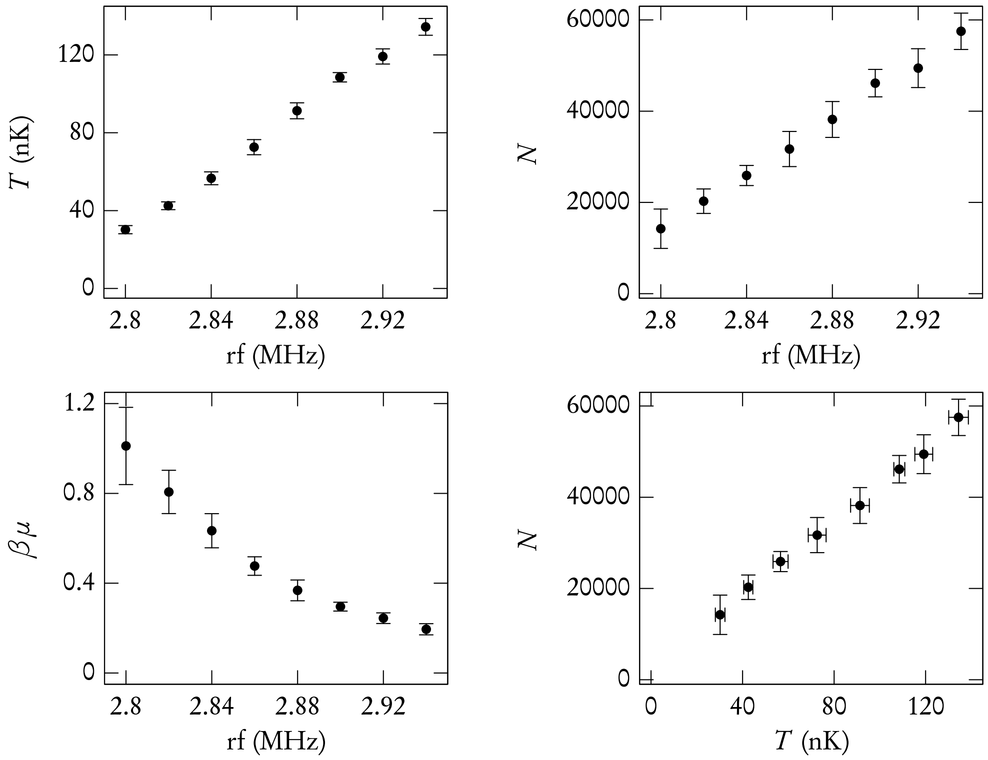

FIGURE 6.8: *Top left: temperatures obtained from multi-level mean field fits on data taken after* 3 ms *of 2d* TOF *(after* TOF *correction). Top right: atom numbers for the same series. Bottom left:* $\beta\mu$ *as a function of the radio frequency as obtained from the* MLMF *fit. Bottom right: atom number as a function of temperature to illustrate how the two correlate due to the production of the samples using evaporative cooling. For all four plots, a detectivity factor* $\xi = 1.4$ *has been used, error bars indicate statistical uncertainties.*

rf (MHz)	T (nK)	N	$\beta\mu$
2.80	30.2 ± 2	14200 ± 4300	1.01 ± 0.17
2.82	42.5 ± 2	20300 ± 2700	0.81 ± 0.10
2.84	56.6 ± 3	25900 ± 2200	0.63 ± 0.08
2.86	72.6 ± 4	31700 ± 3900	0.48 ± 0.04
2.88	91.3 ± 4	38200 ± 3900	0.37 ± 0.05
2.90	109 ± 3	46100 ± 3000	0.30 ± 0.02
2.92	119 ± 4	49400 ± 4300	0.24 ± 0.02
2.94	134 ± 4	57500 ± 4000	0.19 ± 0.02

TABLE 6.2: *The same data as in the plots in figure 6.8 in absolute numbers.*

potential attributed to the experimental profile as fitting parameters, yielding at couple (T_1, μ_1) corresponding to the best fit. From this point on we can iterate the procedure by choosing the MLMF profile whose temperature is closest to T_1, adjusting the experimental profile [which yields a couple (T_2, μ_2)] and so on. In most cases, this procedure will converge after a few iterations (typically two or three), but it also happens occasionally that the temperature ends up oscillating between two values so alternates between two different reference curves. In this case, we take the average between the two (T, μ) couples (the temperatures are maximally 5 nK apart anyway so that the difference between the two reference profiles is small).

In figure 6.7, we show four examples (covering the range of experimentally explored temperatures) of experimental density profiles together with the closest MLMF profile. The temperatures attributed to the images of the corresponding series (with nine repetitions of each point) are shown in figure 6.8. One immediately sees that the attributed temperatures are quite reproducible, which means that both the experimental sequence (determining the real temperature) and our fitting procedure work reproducibly. Note that this is less the case for the atom numbers that show stronger fluctuations—for similar temperatures, N can vary by up to a factor of two between extreme values.

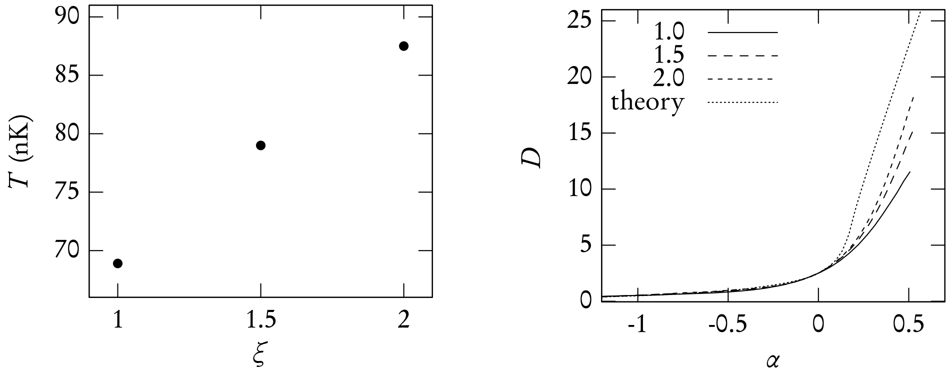

FIGURE 6.9: *Influence of the detectivity factor ξ on the temperature measured by a multi-level mean-field fit. The starting point is a given profile (rf* 2.86 MHz, 3 ms *of 2d* TOF*) which is multiplied by a trial factor ranging from* 1.0 *to* 2.0 *before making a temperature calibration. The left plot shows the resulting temperature which for the chosen example changes appreciably over the relevant range between* 1.0 *and* 2.0. *The second plot shows the corresponding phase space density profiles after calibration as a function of $\alpha = \beta\mu$, with a theoretical profile (with temperature* 79 nK *corresponding to the fit to the $\xi = 1.5$ profile) for comparison.*

One should note, however, that this stability in itself does not give any information about *systematic* uncertainties. We have identified two possible causes of such systematic uncertainties. The first is the subtraction of the offset which is a minor issue for images with a good signal to noise ratio (such as the images taken after 2d TOF). The second one is the detectivity factor ξ with which we multiply the measured optical densities to account for the reduction of the effective cross section of the atoms with respect to the ideal value.

Unlike the case of a Boltzmann gas (the density profile of which in a harmonic trap is Gaussian) where the temperature enters only in the width of the distribution, temperature information is contained both in the width and the amplitude of the distribution already when considering an ideal, perfectly two-dimensional Bose gas. This is even more true in our quasi-two-dimensional regime. Thus, changing ξ will cause the temperature attributed to a given profile to change as well. In figure 6.9 we show the consequences for a typical profile, both for the attributed temperature and the resulting $n\Lambda^2$. One sees that the uncertainty on the detectivity factor ξ enters as an important systematic uncertainty into the temperature calibration.

6.3 First results

Having finished our calibrations, we are now ready for a direct comparison to theoretical predictions. The results of this comparison are exposed in the following sections. In this presentation, we try to separate the effect of the LDA from the effect of scale invariance as best we can, even if this is only marginally possible with our data.

Test of the local density approximation

The first thing to verify once the data has been processed to a usable form is that the LDA which has been used for the calibrations is indeed valid for our data. An ideal verification would consist in producing a large number of samples at equal temperature, but with atom numbers differing by at least one order of magnitude. However, due to the production of our samples using evaporative cooling, temperature and atom number are always closely correlated, as can be seen in figure 6.8 (bottom panel). Thus, to obtain an approximate verification of the LDA, we produced a large number of samples at constant temperature (as we already stated, the temperature is well reproducible on our setup) and selected samples with substantially different atom numbers *a posteriori*.

N	T (nK)	$\beta\mu$
18 600	62.9	0.39
13 700	69.6	0.20
9 900	67.3	0.11

TABLE 6.3: *Atom numbers (using $\xi = 1.4$) and fitted temperature and chemical potential for the three samples shown in figure 6.10. Since the numbers concern individual images rather than ensembles, we cannot provide a statistical error estimate.*

The result of this procedure is shown in figure 6.10 (left panel): from the available data, we selected three profiles with temperatures (as obtained from the procedure described above) between 63 nK and 70 nK (see table 6.3 for details). The atom numbers (as always in this chapter unless stated otherwise) were obtained by summing over all pixels in the regions of interest (for

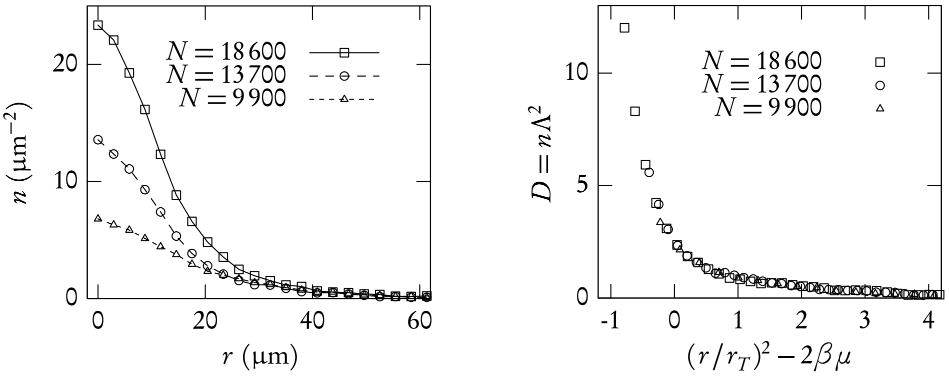

FIGURE 6.10: *Test of the local density approximation (*LDA*): a set of three profiles with atom numbers up to a factor of two apart, but similar temperature, shown as $n(r)$ (left panel) and $D(r/r_T)$ (right panel). The data has been taken after* 3 ms *of 2d* TOF *(which has been corrected for), the plots have been made using a detectivity factor* $\xi = 1.4$. *One clearly sees that the three curves superpose flawlessly in the second plot.*

which, as we said, the offset is already subtracted). Thus, they are directly proportional to the detectivity factor ξ (which is of no consequence for the test of the LDA).

The right panel of the same figure shows the same data in the form $D(\beta\mu)$ (using the MLMF calibration of chemical potential and temperature). As one can see, all three profiles superpose perfectly except for minor fluctuations. Note that this result does not depend in a critical way on this particular method of temperature calibration: since the temperature enters into the relation between $n(r^2)$ and $D(\beta\mu)$ as a mere scaling parameter, one may equally well attribute an arbitrary temperature and chemical potential to one of the curves and use temperature and chemical potential as fitting parameters to adjust the two other ones on the first.

Of course we cannot claim that this data constitutes a "proof" for the validity of the LDA for the considered system—for such a claim, the explored range of parameters is far too small, with only one temperature and just a factor of two between the extreme atom numbers. Note that the extreme atom numbers of typical data covering several temperatures are notably farther apart (up to a factor of five), but the extreme atom numbers correspond to the extreme temperatures so that the difference between these profiles cannot be explained by the LDA alone. However, we judge the data shown in figure 6.10 to be sufficient to give confidence that the LDA is valid for the range of parameters explored in our experiment.

Scale invariance and comparison to theory

At this point we are all set for a comparison of our experimental data with theoretical predictions: temperature and chemical potential have been calibrated using MLMF theory and we have reason to believe that the LDA which is a crucial hypothesis for the interpretation of our data should be valid to the precision of our measurements. Without supplementary assumptions, this leaves us with no free parameter and we can compare theory and experiment directly.

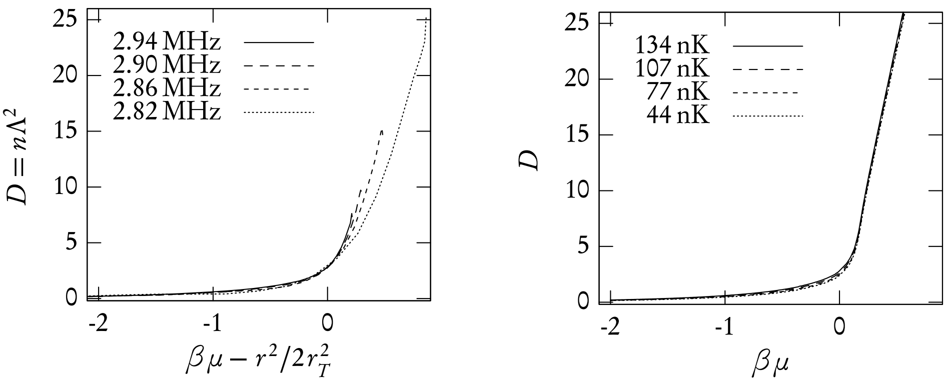

FIGURE 6.11: *Left: the four profiles from figure 6.7 superimposed on one plot. Right: pm*QMC *prediction for the temperatures attributed to these profiles using the* MLMF *fit. The theoretical data shows only minor differences due to thermal excitation along the z direction (they are strongest in the region* $-1 \lesssim \beta\mu \lesssim 0$ *where* D *is still fairly low, so the deviations do not leap to the eye). The experimental curves are fairly close to one another for the three higher temperatures. The "coldest" profile is visibly deformed.*

In figure 6.11 we see such a comparison (the profiles shown in the left panel are the same that have already been shown in figure 6.7). Here we have separated experimental and theoretical profiles for optical clarity. The right plot shows that at the scale for D given by the curve with the highest phase space density, the profiles should be essentially superposed. This is the case to a reasonable degree for the profiles corresponding to rf values ≥ 2.86 MHz. The profile at 2.82 MHz deviates significantly from the others for higher D values. We found this to be systematic for our data at temperatures determined by rf values ≤ 2.84 MHz—there is a progressive effect of deformation which becomes increasingly strong with decreasing temperature. For the "higher half" of our data, there is no visible evidence for deformation on the profiles themselves whereas for the "lower half" one notices slight artifacts such as the kink on the "coldest" profile in figure 6.11 where the separation from the other curves takes place.

Even if we set aside the lower temperature profiles, there remain differences between the experimental data and the theoretical prediction on both the qualitative and the quantitative level: none of our experimental curves shows the characteristic inflexion point that is visible on all theoretical curves, and a plot of experiment and theory on one same graph shows considerable deviations. An example for such a direct comparison is shown in figure 6.9. This same graph holds at the same time the answer to the question whether this discrepancy might be due to a faulty calibration of the detectivity factor ξ: within reasonable limits for its value, there seems to be no way to achieve a better agreement with theory. Furthermore, this effect could not account for the absence of the inflexion point.

At this point it is clear that there is a substantial difference between the predicted and the measured density profiles. This puts our calibrations described in the preceding sections on unstable ground: before knowing their cause, one cannot guarantee that the deformations affect only the high density region. The fact that the mean field fits work well in itself cannot be considered a strong evidence for such an assumption since the shape of the mean field profiles offers few "landmarks". Thus, it is desirable to complement further analysis of the data with representations that are less dependent on a particular calibration.

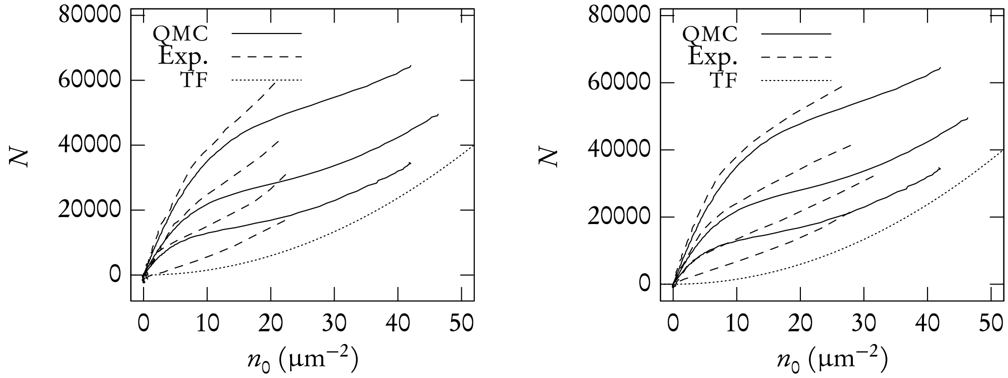

FIGURE 6.12: *Atom number as a function of the central density. Solid lines correspond to the* QMC *prediction [145] for the temperatures* 77 nK, 103 nK *and* 135 nK *(from bottom to top), dashed lines are calculated from experimental data in situ with* $\xi = 3.1$ *(left panel) and after* 3 ms *of 2d* TOF *using* $\xi = 1.4$ *(right panel). For both datasets, we show the profiles corresponding to rf values of* 2.94, 2.90, 2.86 *and* 2.82 MHz. *The dotted line shows the Thomas-Fermi limit. The in situ data presents some numerical artefacts at low temperature since due to the low signal to noise ratio the subtraction of the constant offset is not entirely satisfactory.*

One example for such a complementary representation is shown in figure 6.12: one may plot the atom number N as a function of the peak density n_0. Using the LDA, one obtains a curve $N(n_0)$ from a single profile by representing it as $n(r^2)$ and integrating from a variable inner radius r_0^2 [which determines $n_0 = n(r_0^2)$] to "infinity", *i.e.* to a point far enough outside the sample. The detectivity factor ξ enters such a plot in a transparent way since it corresponds to a simultaneous scaling of both axes by the same factor. Another advantage is that such a plot allows the comparison of several sets of data without having to calibrate their temperatures, *i.e.* one can judge whether or not two sets of curves are mutually compatible without having to have a one to one correspondence of their temperatures and chemical potentials. In figure 6.12 we show two of these plots, comparing in situ and TOF data to curves calculated from QMC density profiles that have been given to us by Werner Krauth. The disadvantage of this type of plot is that a faultily compensated offset enters in a complicated manner. The left panel of figure 6.12 shows some examples of this effect (erratic jumps and negative atom numbers close to the origin).

6.4 *Further characterisation of our data*

At this point, we may clearly state that our observations do not agree with theoretical predictions. Now, as we have seen in chapter 5, there are two theoretical predictions (the one by Prokof'ev and Svistunov [47] and the one by Holzmann and Krauth [48]) which have been derived using different methods and agree very well with each other. Thus, there is good reason to have faith in these predictions which means that in our data there are effects outside the considered theoretical framework. These may be either mere technical imperfections or physical effects that have an interest in themselves. In order to tell which case is true for our data, we have carried out a more thorough analysis which we present in the following sections. Afterwards, we will present the possible elements of explanation that we have considered. Of course, these two parts are all but independent since the aspects we investigated were always influenced by our hypotheses and vice versa so that the order of the two parts might just as well be the inverse.

A pure density effect?

Up to this point, our characterisation of the differences between experiment and theory was rather qualitative. While this had the advantage of avoiding an overly sensitivity to particular calibrations, it is helpful to be more quantitative in order to identify the effects at work. The first question we want to address is whether or not what we observe is a pure density effect.

To this end, we take our data after 3 ms of 2d TOF and calibrate it (*i.e.*, we determine both the temperature and the chemical potential) as described above using a detectivity factor $\xi = 1.4$. The temperature and chemical potential attributed to a given profile completely determine the theoretical curve that one is supposed to measure. We can thus calculate the ratio between the theoretically expected and the experimentally measured density profile.

One should remark that taking the ratio between two functions will yield meaningful results when the difference between the two has an essentially local character. If this is not the case, *e.g.* if the second function is the convolution of the first with a not too narrow function, there is no telling how exactly this affects the ratio of the two functions.

The result (averaged over nine runs) is shown in figure 6.13. We plot the ratio of the densities as a function of the expected density. In the ideal case, this would just give one. In the case of a purely local density-dependent effect, the resulting curve would have a nontrivial shape, but should not depend on the temperature, *i.e.* the curves taken for different temperatures should superpose. However, as we see in the first panel of figure 6.13, this is not what we find: the curves for different temperatures clearly separate when plotted as a function of the expected density, but quite surprisingly this is far less the case when plotting the same ratio (which is, of course, at the same time the ratio of the expected and the measured *phase space* density) as a function of the expected phase space density $D^{(\mathrm{theo})}$ (as shown in the second panel in figure 6.13). Here, most curves superpose within the error bars. The clear deviation of the "coldest" curve might be owed to the fact that the temperature calibration becomes marginally reliable there. The third panel of this figure shows the ratio of the expected and measured atom number (since the measured density is smaller than the expected one, the same is true for

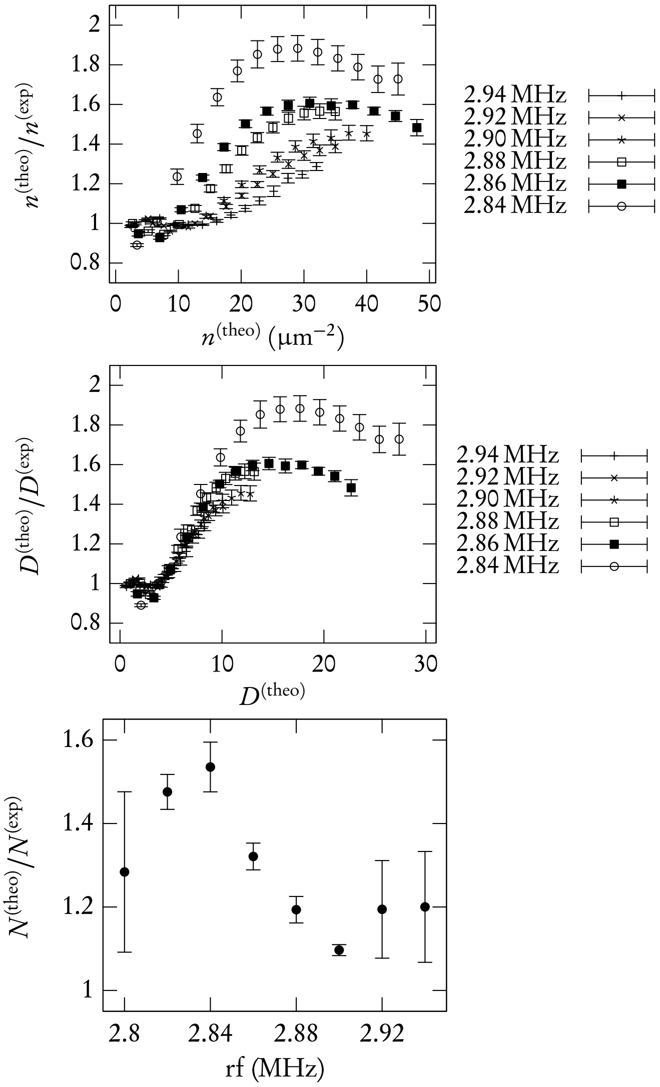

FIGURE 6.13: *Top: Ratio of the theoretically expected and the measured density as a function of the expected density for six different temperatures. The experimental profiles (taken after* 3 ms *of 2d* TOF *which is corrected for) have been calibrated using multi-level mean field fits. For not too low temperatures, there is a plateau close to one corresponding to the range where the fit well reproduces the data. For high densities, one sees that the experimental cloud shapes are considerably less peaked than the theoretical ones. One equally sees that for the lowest shown temperature, the mentioned plateau vanishes,* i.e. *the data can no more be well reproduced by the fit over a non-negligible range. Middle: the same data with the theoretical phase space density on the horizontal axis. Bottom: Ratio of the atom numbers corresponding to the theoretical and experimental profiles.*

the respective atom numbers): as the measured temperature decreases, the ratio $N^{(\mathrm{theo})}/N^{(\mathrm{exp})}$ increases up to a certain point, then seems to plunge while the error bars become quite large. Here again, it is well imaginable that the dependence should in fact be monotonic and that the "coldest" points are displaced due to unreliable calibrations of the temperature and chemical potential.

Central curvature

When we first determined the central curvature of our data, it was supposed to serve a different purpose: according to the LDA and for large atom numbers, the centre of the density distribution should be in the Thomas-Fermi regime and thus take a parabolic shape with curvature $\partial n/\partial r^2 = (2\tilde{g}a_{\mathrm{ho}}^4)^{-1}$ as we mentioned in chapter 5. This expected curvature only depends on the trapping frequencies along z (through $\tilde{g}$) and in the plane (through a_{oh} which can be determined independently, as described earlier in this chapter). Thus, it would provide a means to fix the detectivity factor. Since we know that the shape of our density distributions differs in shape from theoretical expectations, and seemingly more so in the centre than in the wings[3], it is clear that we cannot use this data for such a calibration. However, the information contained in it may still be useful to characterise our findings. In particular, the inflexion point of the equation of state mentioned in chapter 5 corresponds to a maximum of the curvature at the origin, so it is worthwhile to check for its presence.

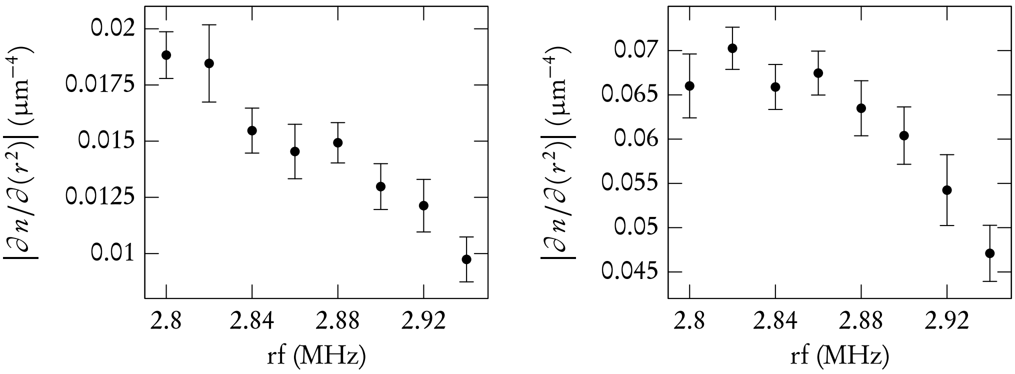

FIGURE 6.14: *Central curvature of data taken in situ (left) and after* 3 ms *of 2d* TOF *(right). The latter is corrected for ballistic expansion, otherwise no corrective factors have been applied. The curvature was calculated by fitting a parabola to the central disk of radius* 10 µm *of each image. For the experimental values* $\omega = 2\pi \times 19.9\,\mathrm{Hz}$ *and* $\tilde{g} = 0.14$*, one expects the curvature to converge to* 0.106 *(pure Thomas-Fermi limit). While the* TOF *data shows a plateau at low rf (corresponding to low temperatures) indicating a detectivity factor of* 1.4*, the situation for the in situ data is far less clear.*

---

[3] Our calibrations are equivalent to superposing theory and experiment in the low-density regime. Throughout our entire analysis, we stick to this choice since it seems reasonable that whatever the nature of the effect, it should be stronger in dense samples than in very dilute ones where one essentially deals with single-particle physics.

To obtain the curvatures, we fitted a two-dimensional parabola to the centre of our samples (more precisely, to the central disk of radius 10 µm. We verified that the results do not depend in a critical manner on the precise radius), using the two Thomas-Fermi radii as fitting parameters. The result is shown for the data from our principal series (both in situ and after 3 ms of 2d TOF, the latter is rescaled using equation (6.1) to be comparable to in situ data) in figure 6.14. Having accepted that the density distribution is altered by some unknown effect, is surprising to find that the data after TOF effectively shows a plateau for low temperatures (note that the temperature calibration does not at all enter in these graphs, they use nothing but the raw image data) at a value which is about a factor 1.4 lower than the expected value 0.106—*i.e.*, just what one would have expected to find from the previously stated value $\xi = 1.4$ if there was no deformation. Two remarks are in order. On the one hand, it is not unimaginable that there is an effect which reduces the central amplitude without altering much the curvature: for an example, this is what happens when one convolves a parabola (extending to infinity) with a Gaussian. On the other hand, the impression of a plateau relies on the presence of the "coldest" point which is lower than its immediate neighbour, giving the impression that the curvature has stabilised, but this might be coincidental. This latter hypothesis is supported by the fact that there is no discernible plateau in the left plot in figure 6.14 which shows the in situ data. Neither of the two data sets shows a clear maximum (corresponding to the inflexion point of the equation of state)—however, one would have to take more data to reduce the error bars to draw definite conclusions about its absence.

It is worthwhile to note that the difference in curvature between in situ and TOF data [we recall that the TOF expansion is already accounted for using equation (6.1)] is significantly larger than the difference in the detected atom number: the factor between TOF and in situ atom number is 2.21 (averaged over the whole series) while the factor between the curvatures is (apart from not being constant) higher than three. This supports the impression that the effects at work are stronger at higher densities.

Change of shape during two-dimensional time of flight

The differences observed between in situ and 2d TOF data naturally leads to the question of how the measured density distribution evolves as a function of the expansion time. Of course, we have to be aware that we cannot separate the effects we are looking for from possible deviations from the scaling relation (6.1).

To this end, we consider a series in which we varied the duration of the 2d TOF expansion from 0 to 16 ms while keeping the rest of the sequence constant. The maximum time is chosen so that the cloud stays in the harmonic regime of the optical potential during the whole TOF—in practice, this is limited not so much by the expansion of the cloud, but to a center of mass motion of the entire sample.

To characterise the evolution of the density profile, we fitted a heuristic bimodal function to it: the sum of a gaussian and a Thomas-Fermi parabola. For our purposes, the exact form of the two functions is of little interest since we are mainly interested in possible differences in their evolution: ideally, no matter how one subdivides the total density profile, each component should expand according to equation (6.1). When the cloud undergoes nontrivial deformations during its expansion, this results in different evolutions for the different components.

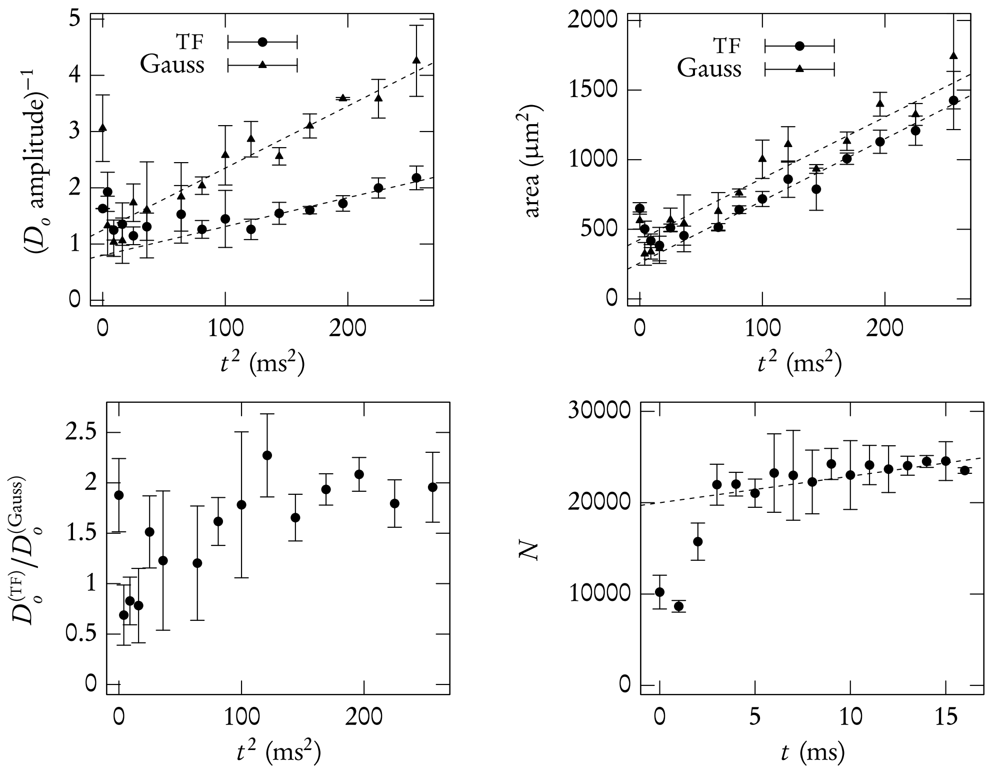

FIGURE 6.15: *Analysis of data in which the samples were identically prepared and probed after increasingly long 2d* TOFs. *To extract quantitative results, the images were fitted with a bimodal "Gauss + Thomas-Fermi" distribution. Top left: inverse optical density amplitudes for both components as a function of the squared expansion time (with $\xi = 1$). The short-dashed lines correspond to linear fits. Top right: the corresponding areas $R_x R_y$ and $\Delta x \Delta y$. The short-dashed lines come from linear fits. All fit results can be found in table 6.4. Bottom left: ratio of* TF *and Gaussian amplitudes. Bottom right: Evolution of the detected atom number (obtained by a pixel count using $\xi = 1$) with the expansion time. The short-dashed line shows a linear fit for $t \geq 3$ ms and indicates that the number of detected atoms increases at a rate of* 290/ms. *In all four plots, error bars show statistical uncertainties.*

The results are shown in figure 6.15. We plotted the area of the fit function (the product of the two Thomas-Fermi radii or the two Gaussian widths, respectively) and the inverses of the peak optical densities as a function of the squared expansion time. Thus, according to equation (6.1), one should obtain straight lines with an offset corresponding to the in situ values and a slope which is determined by the in-plane trapping frequency. Indeed, it is possible to fit straight lines to our data if one disregards the very first points. It is not unreasonable to do so because the detectivity for the first points is affected by the magnetic trapping field which takes a few milliseconds to completely disappear.

	from D_0^{-1}	from area
TF	$(13.8 \pm 3)\,\mathrm{Hz}$	$(18.8 \pm 1)\,\mathrm{Hz}$
Gauss	$(14.8 \pm 1)\,\mathrm{Hz}$	$(15.4 \pm 2)\,\mathrm{Hz}$

TABLE 6.4: *"Effective trapping frequencies" obtained by fitting a law of the form* $1+(\omega t)^2$ *to the evolution of the two components. Clearly, only the frequency derived from the "Thomas-Fermi area" agrees with the expected value* 19.3 Hz *within the error bars.*

Quite interestingly, there is a certain variety of values for the trapping frequencies that we obtain from these fits. We have summarised them in table 6.4. Note that the value for the Gaussian area is not very reliable since it easily changes by adding or removing single points to the fitted set at either end. As the third panel in figure 6.15 shows, the fit is dominated by the TF component, increasingly so for longer expansion times.

The evolution of the Thomas-Fermi component is intriguing: the central density behaves as if the trapping frequency was significantly lower than the measured 20.3 Hz while the area is in agreement with the measured value, as if the parabola was cut off at its tip, but steadily less so with increasing expansion time. If one fits a single Gaussian function to the entire image, one obtains even lower frequencies (between 13 Hz and 14 Hz), indicating that the distribution (after TOF correction) becomes narrower with increasing expansion times.

At the same time, the number of detected atoms is steadily increasing even after the complete disappearance of the magnetic field as can be seen in the fourth panel of figure 6.15: after a short rapid increase corresponding to the switching off of the magnetic trap, the atom number does not saturate, but increases steadily at a rate of about 290 atoms/ms (for $\xi = 1$).

An illustration for both phenomena is provided in figure 6.16 where we show two profiles after different 2d TOF durations after rescaling so that we have two versions of an "effective in situ profile". With all the caution that is appropriate when comparing two profiles selected out of a limited set (for each value, there were three to four measurements), it is clear that the wings are in good agreement, but that there is a considerable discrepancy in the centre. The imaging optics was not optimally focussed the day this very series was acquired which explains the irregularities present on the wings of both profiles.

One may use the following reasoning to see whether we may expect to have recovered full detectivity in the center after 15 ms of expansion: we see in figure 6.16 that the two experimental curves are essentially superposed for $D_0 \leq 0.8$. This corresponds to a measured optical density of 0.71 on the 3 ms profile (and considerably less on the 15 ms one). This leads us to suppose that for optical densities equal to or lower than this 0.71, one has full detectivity. Now, the scaling factor for 15 ms is $1+(\omega t)^2 \simeq 4.31$ so that a measured optical density of 0.7 becomes an optical density of 3.06 after rescaling. The 15 ms profile does not exceed this value by far, so we may expect the reduction of detectivity to have essentially disappeared.

For comparison, we equally show a pmQMC profile for the atom number corresponding to the 15 ms profile (taking into account $\xi = 1.4$) and the temperature 91.3 nK which according to table 6.2 corresponds to the radio frequency of 2.88 MHz used throughout this series. Quite

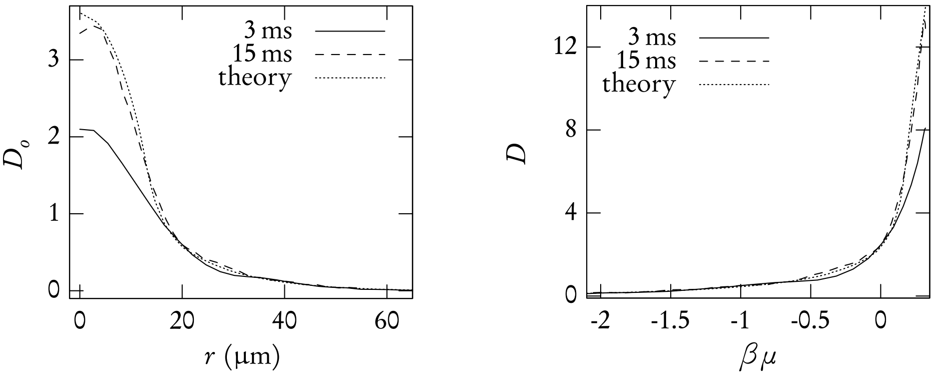

FIGURE 6.16: *Left: optical density profiles measured after* 3 ms *and* 15 ms *of 2d* TOF, *respectively, after rescaling both axes using the scaling law* (6.1) *with the measured trapping frequency* 19.3 Hz. *Each of the two profiles has been selected to have an optical density near the average to render them comparable. A theoretical (pm*QMC*) profile for the atom number* 34 000 *and a temperature of* 91.3 nK *is shown for comparison. Right: the same data after converting to* $D(\beta\mu)$.

clearly, the 15 ms profile is a lot nearer to the theoretical prediction than the 3 ms one. However, the apparent agreement between the theoretical and the 15 ms profile might in part be accidental since the calibrations are not this precise.

While we do not have enough data taken after longer 2d TOFs to make stronger claims, this particular result is encouraging in the sense that by taking a comprehensive set of data after 15 ms of 2d TOF, one might actually obtain a good agreement with theory. Of course, one has to be aware that in doing so, the scaling relation (6.1) is taken for granted unless one finds a means to verify it separately.

Two-dimensional and three-dimensional time of flight

Another observation we made is that the optical density measured after three-dimensional ballistic expansion was systematically higher than after a two-dimensional expansion. Up to a certain point, this is to be expected: in the 2d TOF case, the whole distribution obeys the scaling law (6.1) so that the central density decreases as $[1+(\omega t)^2]^{-1}$. In the 3d TOF case, only the thermal component will expand whereas the horizontal size of the condensed component should remain almost constant. Thus, in three-dimensional TOF, once the thermal fraction is sufficiently dilute, the central optical density (in vertical imaging) should not vary appreciably which is indeed compatible with our observations. However, it turns out that this reasoning cannot explain the differences we find between profiles obtained after 2d or 3d TOF on a quantitative level.

Figure 6.17 shows a typical case, *i.e.* images of identically prepared atomic samples probed either after a short 2d TOF or a longer 3d one. In this plot, the peak optical density after 4 ms of 2d TOF is ~ 1.5. Using equation (6.1), we conclude that the in situ peak optical density should

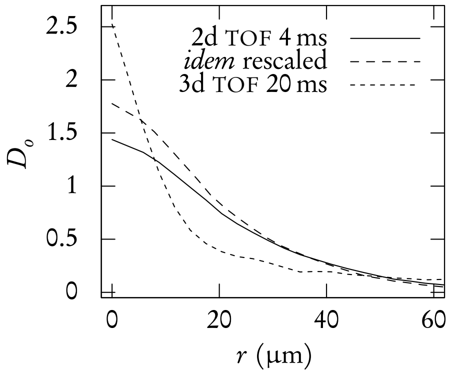

FIGURE 6.17: *Direct comparison of the optical density profiles after* 4 ms *of 2d* TOF *and after* 20 ms *of 3d* TOF *under otherwise identical conditions. The optical density after 3d* TOF *is significantly greater than what one would expect from the 2d* TOF *data even after rescaling the latter which is supposed to yield the in situ distribution.*

be ~ 1.85. But we see that the optical density after 20 ms of 3d TOF is actually significantly higher than that.

There is no apparent reason why one should believe that the central density is actually increasing during a three-dimensional ballistic expansion, so we should rather try to find a reason for the measured optical density's being lower than expected from the scaling law (6.1).

Influence of the imaging beam's intensity

As we stated at the beginning of this chapter, we used two different imaging schemes as regards the intensity, a "low intensity" and a "high intensity" one. In the high intensity scheme, the atoms are exposed to an intensity of 0.5 mW/cm^2 during 60 µs while in the second case, the intensity is a factor of four lower and the exposure a factor of four longer so that the number of absorbed photons remains equal.

In the high intensity scheme, there is a marginal saturation effect since $I/I_{\text{sat}} \simeq 1/6$ (using the saturation intensity for linear light [60]) whereas it should be completely negligible in the case of the low intensity scheme. However, due to the prolonged exposure time, the low intensity scheme gives the atoms more time to move under the influence of the acceleration due to the absorption and reemission of photons. It is thus instructive to do a direct comparison of both schemes to have an idea of the respective impacts of the mentioned effects.

An example of such a comparison is shown in figure 6.18: the atomic sample is prepared using an identical sequence with final radio frequency 2.85 MHz for all runs and then imaged after 3 ms of 2d TOF. During the first half of the sequence, the images are taken using the low intensity scheme, then, without interrupting the sequence, we switch to the high intensity scheme by increasing the beam power and decreasing the exposure time of the CCD camera.

For our comparison, we produce radial profiles for all the images and then average over the five last "low intensity profiles" and the first five "high intensity profiles" (which should be

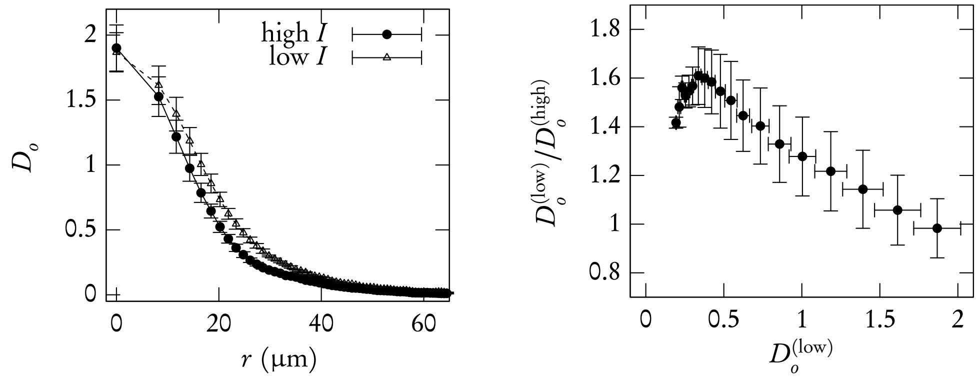

FIGURE 6.18: *Direct comparison of optical density (D_o) profiles measured with "low" and "high" imaging intensity. Left: averages over five consecutive shots under identical conditions. The "low intensity" images were acquired directly after the "high intensity" ones without interrupting the sequence. Right: ratio of the two as a function of the "low intensity" optical density. There is a clear influence of the intensity on the measured cloud shape. In this figure, error bars show statistical uncertainties.*

the most comparable since the latter have been taken directly after the former). The resulting profiles are shown in the first panel of figure 6.18. It is clear that their differences significantly exceed the error bars. Quite interestingly, the central optical density is practically equal for both, the differences show up mostly on the "steep descent" part of the profiles. The second panel of the same figure shows the *ratio* of the two optical density profiles as a function of the low intensity optical density.

Concerning the data shown in this figure, a note of caution is in order: in fact, the experiment was not yet in its stationary regime during the series (the atom number was visibly increasing during the low intensity shots, but seemed to have stabilised by the time we changed the intensity). While we believe the general effect, *i.e.* the existence of a significant difference in the shape of the profile, to be independent of this since we limited our analysis to some shots taken during a comparatively short time at a moment where the stabilisation was already close to being finished, the actual numbers might be affected by the experiment's not having reached its stationary state. From a larger perspective, it would be instructive to have similar data for more than one temperature, but currently we only have the shown data at our disposition.

Judging from this data set, it seems that the difference between high and low intensity imaging is less a saturation effect (which should result in a constant factor), but the result of a real deformation of the sample that is taking place during the imaging process.

Imaging with finite detuning

Still another effect shows up in the "resonance series" we regularly took to make sure that our imaging beam was still tuned to the atomic resonance. In these series, we prepared an atomic sample using an identical sequence (with a final radio frequency of 2.88 MHz, *i.e.* at a temperature approximately in the centre of the investigated range) for each shot and imaged it (after a given TOF scheme) with the imaging beam's frequency as the varying parameter. To find the resonance, we plot the atom number as a function of the frequency and fit a Lorentzian to the resulting curve which yields the resonance frequency and the width of the resonance.

Instead of the atom number, one can just as well regard the peak optical density which usually shows more fluctuations, but should vary with the frequency in the same way as the atom number [in the absence of optical aberrations, the shape of the sample should remain invariant and just be multiplied by a factor reflecting the reduction of the effective cross section (see chapter 7)]. However, we found a systematic and significant displacement of the maximum of the peak optical density with respect to the maximum of the atom number, as can be seen in figure 6.19 and 6.20.

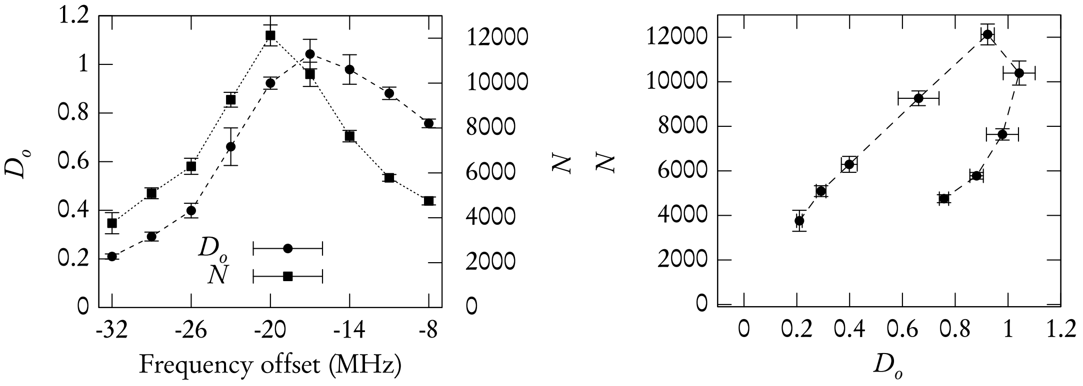

FIGURE 6.19: *Peak optical density D_0 and atom number N (wihout any corrective factors) for a resonance series on a two-dimensional samples evaporated down to* 2.88 MHz, *with in situ imaging. Left: both physical quantities as functions of the imaging offset frequency (with respect to a reference frequency chosen for technical convenience). The two maxima clearly are not in the same place. Right: Atom number as a function of the peak optical density. The "loop" accomplished by these data points shows the extent of the deformation in the observed cloud shape.*

One may either compare the resonance curves corresponding to the atom number and the peak optical density, as is done in the first panel in figure 6.19, or plot one as a function of the other, as can be seen in the second panel in figure 6.19 and in figure 6.20. For in situ imaging, one can see in the first panel of figure 6.19 that the resonance of the peak optical density is displaced with respect to the one of the atom number by about 3 MHz, *i.e.* half a natural line width which is far from negligible.

The same is true for a resonance taken after 3 ms of 2d TOF: if one normalises atom number and peak optical density by their respective maximum values, the "loops" corresponding to the two cases come out practically superposed (first panel in figure 6.20). Moreover, we also have data that shows that the effect is equally present after a short *3d* TOF (5 ms), as can be seen in

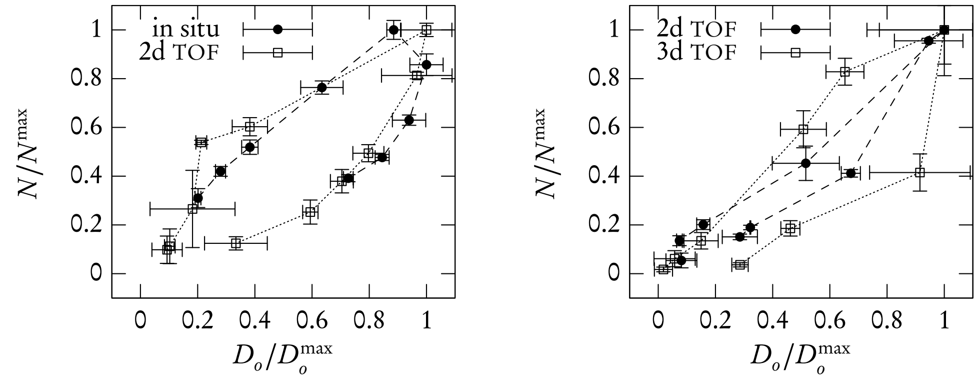

FIGURE 6.20: *The appearance of the "loop" shown in figure 6.19 is not limited to in situ imaging, as these plots show. Left: the in situ data from figure 6.19 in direct comparison to a resonance curve taken after* 3 ms *of 2d* TOF. *Both series are taken at "high" imaging intensity. Right: comparison between resonance curves after 2d and 3d* TOF, *both taken at "low" imaging intensity. Here the "loop size" does seem to differ, but the quality of the data is far less than that of the left plot so that one should be careful with quantitative claims. In any case, it is without question that the "loop" is present also after 3d* TOF.

the second panel in figure 6.20: the quality of the data is not outstanding (in fact, more so in the case of the 2d TOF data shown for comparison that has been taken the same day as the 3d TOF data), but the "loop" effect is undeniably present.

Most interestingly, the effect is absent (to the precision of our measurement) when instead of a quasi-two-dimensional atomic sample we probe a three-dimensional one, *i.e.* in the absence of the optical dipole potential. This can be seen in figure 6.21 which is the 3d counterpart to figure 6.19. The data is strongly affected by saturation at resonance so that $N(D_0)$ is not a straight line as it would be in the ideal case, but there is no discernible loop. This alone precludes the observed loops to be mere imaging artifacts—as we will show in chapter 7, there are other reasons as well to refute this explanation.

The data thus seems to indicate that the presence of "resonance loops", *i.e.* significant deformation of the observed cloud shape as a function of imaging frequency, is in some way related to the quasi-two-dimensional character of the probed system. Perhaps the most intriguing fact in this respect is the presence of the loop in the case of a 3d TOF measurement: if the gas is initially confined to a harmonic oscillator size of 200 nm, it should have expanded to a size of 18 µm after 5 ms of free expansion which is comparable to the in-plane sizes. However, we should not attribute too much weight to this particular result since it it based on only two series which might be faulty (*e.g.*, one could have accidentally programmed a 2d TOF instead of a 3d one). A final answer to this question will have to wait until new data has been acquired. When doing so, it might be interesting as well to do it for different temperatures (all resonance series that were made during the data acquisition period in question were made at the same radio frequency) to see whether or not the effect has a visible temperature dependence.

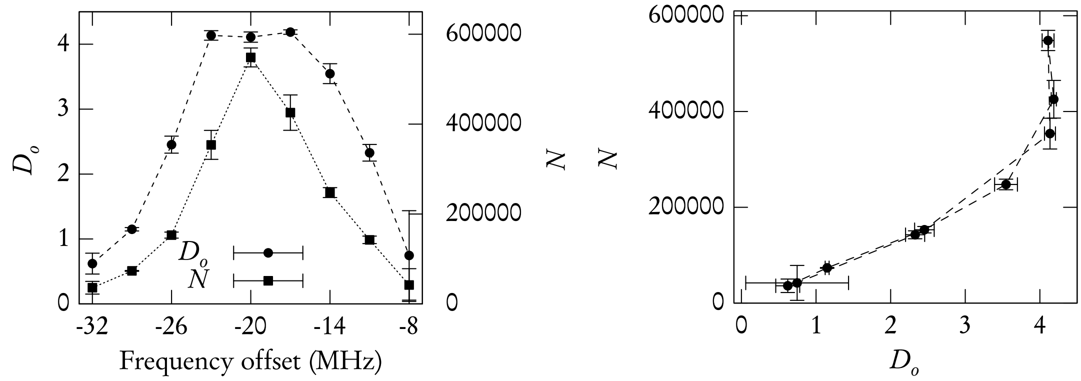

FIGURE 6.21: *Resonance curve taken on a three-dimensional sample (the cloud in the* TOP *trap before ramping up the optical potential). Left: Peak optical density* D_0 *and atom number* N *as a function of the imaging beam's frequency. Right: Atom number as a function of the peak optical density. No corrective factors have been applied on either plot. Note that the curves are deformed by saturation (especially clear on the left plot). Unlike the curves from quasi-2d samples, there is no evidence for a finite-sized "loop" in the second plot. The data displayed in these plots has been acquired the same day as the data in the right panel of figure 6.20.*

6.5 Possible causes for the observed effects

After this review of unexpected effects, we pass to an overview of the possible causes we were able to identify. They can be divided into two groups: on the one hand, detection effects, *i.e.* phenomena that happen during absorption imaging and that may stem either from a real deformation of the atomic sample due to collective interactions with the imaging beam or from a deformation of its *image* due to imperfections of the imaging optics. The second group are effects that are independent of the measurement process, *i.e.* they occur within the sample even before we probe it. This would be equivalent to say that there are physical processes at work in the sample itself which are not contained in the model solved theoretically in [47, 48].

In fact, our first suspect was the imaging optics: their net effect is that of a convolution with a response function, so it is well imaginable that the imperfections of our optics might cause the observed flattening in the centre of our samples. We have thus investigated this question in detail. Since the description of the employed methods and their results takes up considerable space, we put it in a separate chapter (chapter 7). Here, we only state the main result that to our best knowledge, the imperfections of our imaging optics cannot explain the observed effects. Rather, one may assume that most of our images (with the possible exception of the ones showing the very coldest samples and a general question mark on data taken after a long 3d TOF[4]) are essentially faithful, *i.e.* what looks like small artifacts most likely really are small

---

[4] The analysis in chapter 7 assumes that there is a unique "object plane", *i.e.* a plane directly after the sample where the absorption process is finished. After a long 3d TOF, the vertical extension of the sample is of the order of the depth of focus, and we have made no attempt to analyse the consequences of this fact in our analysis which was

artifacts and not the small visible symptoms of much larger deformations.

Population of several hyperfine states

The first effect we want to discuss belongs to the group of "in-sample" effects. One can produce a certain effect of "flattening" by adding atoms in hyperfine states other than $F = 2, m_F = 2$. The only possible states are $F = 2, m_F = 1$ and $F = 1, m_F = -1$ since only those can be magnetically trapped. Of these two, atoms in $F = 2, m_F = 1$ would absorb photons from the imaging beam and thus contribute to absorption images while the atoms in the $F = 1, m_F = -1$ hyperfine state would be "invisible", but can nonetheless influence the shape of the density distribution because they interact with the atoms in other hyperfine states. Both of these states see a magnetic trapping potential that is only half the one seen by the $F = 2, m_F = 2$ hyperfine state due to their lower magnetic moment.

However, there is little reason to believe in a significant population of these states: it could be produced at two moments, the first being the optical pumping before transport which does not transfer all atoms to the desired state and the second the cleaning pulse after loading the atoms into the optical potential. Both are preferentially eliminated by radio-frequency evaporation since they see only half the trapping potential: they will have larger oscillation amplitudes while the evaporation surface is the same for all hyperfine states so that atoms in hyperfine states other than $F = 2, m_F = 2$ hit the evaporation surface more frequently and thus have a higher probability of being evaporated. Undesired atoms from imperfect optical pumping usually do not "survive" the first phase of evaporation for the preparation of the initial sample. Those who might appear due to the cleaning pulse may expect a similar fate since we let the sample thermalise for at least 4 s after ramping up the optical potential.

One has to note, however, that there is no simple way to verify this experimentally since the standard experimental methods to probe the hyperfine distribution are the following: for $F = 2, m_F = 1$, one can reduce the current in the magnetic trap coils until their gradient compensates gravity for particles with $\mu = \mu_B$, but no more for such with $\mu = \mu_B/2$, then restoring the initial value, take an absorption image and see how many atoms are lost in the process. For $F = 1$ atoms, one can shine light tuned to the "repumping transition" $F = 1 \longleftrightarrow F' = 2$ on the atoms before taking the absorption image and observe the increase in atom number. The first method does not work in our case since the vertical confinement is mainly due to the optical potential. The second one would be applicable if one could obtain reliable atom numbers from horizontal imaging: in vertical imaging, there is no way to distinguish atoms appearing in the plane from atoms appearing in the side wells in which there is almost certainly a certain population. However, in horizontal imaging the optical density is so high that the signal is strongly saturated so that one cannot extract quantitative information in this way. We have not yet come up with more reliable methods, so for the moment being we have to trust in the argument that due to rf evaporation, it is unlikely to have a non-negligible population of undesired hyperfine states.

---

focused on quasi-2d samples. In particular, we cannot exclude that the high optical densities observed after 3d TOF could in fact at least partly be the result of imaging aberrations which can lead to a significant increase of the peak optical density when the imaged distribution is sharply peaked [160].

Three-body losses

A second scenario we considered concerns the role of three-body losses: given the fact that there are constantly atom losses in the centre of the trap due to this mechanism, one has to check that the time scale on which the atomic sample gains its equilibrium scale is sufficiently short compared to the time scale set by the loss rate to ensure that the observed distributions are really at equilibrium.

Three-body collisions are a loss mechanism that is always present in ultracold gases—if the vacuum is sufficient, it is usually the limiting factor for the lifetime of a BEC. An extensive study of the three-body losses in a three-dimensional BEC has been carried out by Söding *et al.* in 1999 [161] who found that the rate of atoms lost from a BEC in the presence of a thermal component can be well described by a law of the form

$$\frac{1}{N}\frac{\mathrm{d}N}{\mathrm{d}t} = -L\left(\langle n^2\rangle + 6\langle n n_{\mathrm{th}}\rangle + 6\langle n_{\mathrm{th}}^2\rangle\right) - G\left(\langle n\rangle + 2\langle n_{\mathrm{th}}\rangle\right) - \frac{1}{\tau} \tag{6.3}$$

(in this equation, all densities are three-dimensional ones) and determined the constant associated to three-body losses to be $L = 1.8 \times 10^{-29}\,\mathrm{cm}^6/\mathrm{s}$. This should give the relevant order of magnitude for our system, but one should not forget that the dimensionality of the system may modify the collisional behaviour—for an example, the NIST group found that in a one-dimensional geometry the three-body loss rate may be reduced by up to a factor of seven [162]. Four our estimations, we will take the value of L "as is". Moreover, we will ignore the interplay between condensed and non-condensed particles and just regard a generic $\langle n^2\rangle$ term for an order of magnitude estimation.

The three-dimensional density $n^{(3)}$ of our samples can be calculated from the surface density n by using the Gaussian density distribution associated to the ground state along z (ignoring for our estimations the residual excitations in this direction) so that $n^{(3)} = n/(\pi l_z^2)^{1/2}$, with $l_z = 180\,\mathrm{nm}$. Thus, the theoretically expected maximum surface density of $40\,\mu\mathrm{m}^{-2}$ leads to a maximum three-dimensional density $n^{(3)}_{\mathrm{max}} = 125\,\mu\mathrm{m}^{-3}$. Using this value, we find $L(n^{(3)}_{\mathrm{max}})^2 = 0.281\,\mathrm{s}^{-1}$, corresponding to a time scale of 3.56 s.

This time scale set by three-body losses is still far larger than that corresponding to the atomic motion in the plane which is characterised by the inverse trapping frequency, *i.e.* 0.052 s. Thus, the atoms may undergo several oscillations on the time scale set by the loss mechanism so that we may expect the density profile to be at equilibrium provided the mean free path is long enough that the atoms can "make use" of this time.

Dimensionally speaking, the mean free path is equal to $1/n^{(3)}\sigma$, where $\sigma = 8\pi a_s^2$ is the scattering cross section. Plugging in $n^{(3)}_{\mathrm{max}}$ as defined above, we find a mean free path of 12.2 µm. This should be sufficient to permit an efficient redistribution of the atoms (note that we are reasoning in terms of peak densities so that the mean free path should be compared to the typical extension of the very dense part of the cloud) so that we do not expect major out-of-equilibrium phenomena.

Interaction with the imaging light

Finally, we turn to the question of the deformation of the atomic sample due to interaction with the imaging light. *A priori*, it is not surprising that such a phenomenon occurs, but we initially expected it to be a small effect as we will explain presently.

When an atom absorbs a photon, the photon momentum is added to the original one of the atom which is accelerated in the propagation direction of the photon. In contrast, there is no preferred direction for the emission of a photon. Thus, the motion of the atom due to the spontaneous emission of photons can be regarded as a random walk. On each spatial axis, it can be described by a set of coupled differential equations:

$$\frac{\mathrm{d}\overline{x^2}}{\mathrm{d}t} = 2\overline{xv} \quad ; \quad \frac{\mathrm{d}\overline{xv}}{\mathrm{d}t} = \overline{v^2} \quad ; \quad \frac{\mathrm{d}\overline{v^2}}{\mathrm{d}t} = 2\mathscr{D} \, , \tag{6.4}$$

where $\mathscr{D}$ is the velocity diffusion constant. Starting with the third one, they may be integrated successively so that one finds

$$\overline{v^2} = 2\mathscr{D}t \quad ; \quad \overline{xv} = \mathscr{D}t^2 \quad ; \quad \overline{x^2} = \frac{2\mathscr{D}t^3}{3} = \frac{\overline{v^2}t^2}{3} \, . \tag{6.5}$$

Thus, all we need to now is the width of the velocity distribution due the spontaneous emission of photons (since the mean of v is zero, the average of its square equals the variance). The number of scattered photons per atom is

$$N_{\mathrm{ph}} = \frac{\Gamma}{2} \frac{I/I_{\mathrm{sat}}}{1 + I/I_{\mathrm{sat}}} t \, . \tag{6.6}$$

With $\Gamma = 2\pi \times 6\,\mathrm{MHz}$, $t = 60\,\mu\mathrm{s}$ (the exposure time used for high intensity imaging) and $I/I_{\mathrm{sat}} = 1/6$, we find $N_{\mathrm{ph}} = 160$. Then, using $\overline{v^2} = (\hbar k/m)^2 N/3$ (with a factor of 1/3 corresponding to an even distribution of the original total momentum over all three axes. For a more sophisticated treatment, one might take the directivity of dipolar radiation at this point), we get $\Delta x = \sqrt{N_{\mathrm{ph}}}/3(\hbar k/m)t \simeq 1.5\,\mu\mathrm{m}$. Thus, the expansion of the atomic sample due to the scattering of photons should correspond to a convolution with a Gaussian of width Δx. But Δx is small against the characteristic scale of variation in our density profiles so that this in itself is far from sufficient to explain the differences between experiment and theory that we have seen.

A second phenomenon that could in principle occur is that due to the absorption of the imaging photons the sample is accelerated so much in the propagation direction that either the imaging optics is focussed only on a part of its trajectory or the Doppler effect causes the atoms to become effectively detuned with respect to the probe beam. As concerns the latter, the recoil velocity acquired by the atom at the absorption of each photon is $\hbar k/m = 5.86\,\mathrm{mm/s}$ so that the final velocity after the absorption of 160 photons is $v_f = 0.94\,\mathrm{m/s}$. For comparison, the "Doppler velocity" at which the Doppler detuning becomes equal to the natural line width is $\Gamma/k = 4.7\,\mathrm{m/s}$ which is considerably larger than even the final velocity. Thus, we do not expect the Doppler detuning to play a significant role. As concerns the sample's going out of focus, the total displacement is $\Delta z = v_f t/2 \simeq 28\,\mu\mathrm{m}$ which is smaller than the sensitivity of our focussing procedure (described in chapter 7) so that once again this does not seem to be a problem.

However, all this discussion is based on the assumption that each atom interacts with the imaging light independently of all others. This hypothesis is customary when one considers ultracold Bose gases since normally they are so dilute that the interatomic distance is larger then the probe light's wavelength. This is clearly not the case for our quasi-two-dimensional samples where the theoretically expected in-plane density climbs up to $\sim 40\,\mu\mathrm{m}^{-2}$, corresponding to the three-dimensional density $n^{(3)}_{\mathrm{max}} \simeq 125\,\mu\mathrm{m}^{-3}$ and thus $kn^{(3)}_{\mathrm{max}} \simeq 1.61$. This means that the interaction between the induced dipoles of two different atoms may become non-negligible since the interaction potential scales as $\hbar\Gamma/(kr)^n$ [163, 164]. More precisely, there are three terms ($n = 1, 2, 3$) which will all be of comparable order of magnitude for our maximal densities. A meaningful manner of taking this effect into account will therefore require considerable theoretical effort which goes beyond what could be done in the time currently at our disposal. Here we limit ourselves to a brief qualitative discussion of the consequences one may expect from this mechanism.

A first consequence of such an interaction would be a splitting up of the atoms' resonance frequencies [generally, if more than two atoms are involved, one would obtain as many different frequencies as atoms and the typical width of the spectrum would be $\Gamma/(kr)^n$] so that the probe beam would become effectively detuned with respect to them, resulting in a reduction of the absorptive cross section.

Furthermore, the interaction potential would produce a force between the atoms. Let us just regard the term $\hbar\Gamma/(kr)^3$. It will give rise to a force of magnitude $3\hbar k\Gamma/(kr)^4$. We can estimate the displacement of an individual atom due to the interaction with one incident photon in the presence of a second atom by assuming a uniformly accelerated motion during the time scale which characterises photon diffusion, *i.e.* Γ^{-1}:

$$\Delta x \sim \frac{1}{2}\frac{F}{m}\Gamma^{-2} = \frac{3}{2\Gamma}\frac{\hbar k}{m}\frac{1}{(kr)^4}\,. \tag{6.7}$$

We recognise the recoil velocity $\hbar k/m = 5.86\,\mathrm{mm/s}$, the factor multiplying it is equal to $5.92\,\mathrm{ns}$ for $kr = 1.61$ so that the total displacement becomes $0.035\,\mathrm{nm}$. The acquired velocity according to the same argument is $\hbar k/m \times 3/(kr)^4 \simeq 2.62\,\mathrm{mm/s}$. These numbers seem to suggest that the effect should be comparable to the effect of photon recoil—we should not forget that there are two more terms giving rise to contributions of equal order of magnitude.

It is worthwhile to stress that the deformations caused by this effect have a nonlinear character (since the force depends on the density) and cannot be modeled by a simple convolution with an appropriate function in the same way as the photon recoil. Instead, one would have to carry out actual simulations.

An important argument for the plausibility of this effect's being an explanation for the observed phenomena is that it might actually provide an explanation for the "resonance loops" as well: due to the dipole interaction, the energy levels inside the atoms (and hence the resonance frequencies) will be shifted by $\sim \pm\hbar\Gamma/(kr)^n$, where the sign depends on the relative orientation of the two induced dipoles (at the same time, it determines whether the resulting force between the atoms will be attractive or repulsive). Thus, if the fraction of equally oriented pairs is different from the fraction of pairs with opposite dipole moments, a positive detuning will result in different deformations than a negative one which might account for the observed loops.

Of the effects discussed in section 6.4, there is one that does not seem to be explainable in terms of this collective atom-photon interaction: in figure 6.13, we see that our data is more compatible with an effect depending on $n\Lambda^2$ than with a pure density effect whereas the collective atom-photon interaction as we have discussed it here should be a pure density effect. However, as we stated, this assertion is based on the hypothesis of a *purely local* effect. The reduction of the effective cross section is such a local effect, but the motion of the atoms due to the interaction potential is not. While this is an issue to be observed, it is not clear at present whether the apparent temperature-dependence is a real effect. A quantitative prediction of the effects of collective atom-photon interactions should permit to resolve this question.

As we already stated, these arguments are purely qualitative at present and have to be supplemented with far more detailed investigations to find out whether this effect is really what we are looking for. Such an investigation should also address the question if it is appropriate to restrict the analysis to atom pairs or if one has to take into account correlations involving even more atoms.

Chapter Seven

A closer look on absorption imaging

> But optics sharp it needs, I ween,
> To see what is not to be seen.
>
> JOHN TRUMBULL (1750–1831)
> *McFingal*

ONE of the first candidates for a possible explanation for the discrepancies between theory and experiment exposed in chapter 6 is the influence of the imaging optics. Indeed, since the object of our measurement is the *shape* of the atomic sample, it is essential to have a clear idea of whether or not the measured profiles are deformed by the optics and if yes, in which way.

To this end, we try to model the imaging process as realistically as possible, taking into account the finite size of the imaging triplet, its aberrations as well as imperfect focusing. However, we will restrict ourselves to the case where the atomic distribution itself remains unaltered by the interaction with the imaging beam. The purpose of the present chapter is rather to provide a good comprehension of the "basic" functioning of the imaging system which can then be extended by adding the aspects discussed at the end of chapter 6.

The first part of this chapter addresses a question that comes even before and has been raised several times throughout this manuscript: for the interpretation of absorption images, one relies on the Lambert-Beer absorption law according to which the intensity transmitted by a sample decreases exponentially with its column density, *i.e.* the density integrated along the light beam. The standard derivation of this law makes use of a differential argument by dividing up the sample into a succession of infinitely thin layers. As we have seen in chapter 6, this division makes no sense for our typical samples in which the thickness is smaller than the inter-particle spacing. We show that the Lambert-Beer law should nonetheless be valid by deriving it without relying on differential arguments. We then discuss the consequences of the nonlinear relation between density and transmitted intensity for the sensitivity towards small deviations which can become a serious issue at high densities.

In the second part of the chapter we analyse how the electric field distribution after the atoms is transformed by the imaging optics. We give some general analytical expressions before turning to a numerical treatment of the problem in order to derive results that can be directly compared to experimental findings. We reproduce the focusing procedure and a typical resonance series to see whether the observed phenomena can be explained by imperfect imaging optics.

7.1 The Lambert-Beer absorption law

In absorption imaging, the measurement process amounts to determining the number of photons missing from a probe beam due to their interaction with the probed sample. In order to reconstruct the density from this information, one needs a theory about the interaction between the light beam and the sample. For the case of dilute atomic gases, this interaction is characterised by the Lambert-Beer law.

Standard derivation of the Lambert-Beer law

The Lambert-Beer law describes the absorption of a probe beam by a dilute disordered medium of absorbers characterised by their absorptive cross section σ and number density $n(x,y,z)$. Atoms are regarded as classical absorbers, in particular we ignore the effects of coherent and Bose-stimulated scattering [165] and density correlations arising from the quantum statistics of the sample [163]. In typical cold atoms experiments these quantum corrections to a purely classical treatment are small, so we will not take them into account here.

Let us imagine a uniform beam of intensity I_0 propagating along the z axis through such a medium. We consider a layer of thickness Δz which we choose so small that between any z and $z+\Delta z$ there are so few atoms that their respective cross sections will not touch. The total number of scatterers per unit area between z and Δz is then given by $n(x,y,z)\Delta z$, and the intensity of the probe beam will decrease as

$$I(x,y,z+\Delta z) = I(x,y,z) - I(x,y,z)\sigma n(x,y,z)\Delta z \; . \tag{7.1}$$

Of course, due to the finite life time of the excited state, each absorbed photon will eventually be reemitted. In all that follows, we suppose that these reemitted photons will not reach the detector, *i.e.* that they are emitted at an angle outside the numerical aperture of the detection optics. At the same time, we neglect multiple scattering that could "drive back" a photon inside the detected solid angle. Thus, each absorbed photon is lost from the detected signal.

In the limit $\Delta z \to 0$, (7.1) becomes a differential equation:

$$\frac{\mathrm{d}}{\mathrm{d}z} I(x,y,z) = -n(x,y,z) I(x,y,z)\sigma \; . \tag{7.2}$$

If the cross section itself is just a constant, this readily gives the solution (outside the sample)

$$I(x,y,\infty) = I_0 \exp\left[-\sigma \int_{-\infty}^{\infty} \mathrm{d}z\, n(x,y,z)\right] \; . \tag{7.3}$$

In the case of non-negligible saturation of the atomic transition, the cross section σ becomes a function of intensity incident on the atom. Equation (7.2) remains valid if the dependence of σ on the intensity is taken into account [166]: with $\sigma(I) = \sigma_0/(1+I/I_{\mathrm{sat}})$, where I_{sat} is the *saturation intensity*, the solution of equation (7.2) becomes

$$\log\left(\frac{I(x,y,\infty)}{I_0}\right) + \frac{I(x,y,\infty)-I_0}{I_{\mathrm{sat}}} = -\sigma_0 \int_{-\infty}^{\infty} \mathrm{d}z\, n(x,y,z) \, . \tag{7.4}$$

Henceforth, we will call the quantity $d_o(x,y) \equiv \sigma_0 \int_{-\infty}^{\infty} \mathrm{d}z\, n(x,y,z)$ the *optical depth*. Here, σ_0 is the resonant cross section for the interaction with linearly polarised light including the associated Clebsch-Gordan coefficient[1]:

$$\sigma_0 = \frac{7}{15}\frac{3\lambda^2}{2\pi} \simeq 0.135\,\mu\mathrm{m}^2\,. \tag{7.5}$$

In actual experiments, the detectivity is always reduced with respect to the ideal case by some factor ξ due to imperfections in the realisation of the imaging system. In our equations, this amounts to replacing σ by σ/ξ, the saturation intensity I_{sat} by an effective saturation intensity $I_{\mathrm{sat}}^{\mathrm{eff}} = \xi I_{\mathrm{sat}}$ and, as a consequence d_o by ξd_o—in this manner, the definition of d_o remains unchanged and the optical depth is still a property of the atomic sample only.

In the experimental implementation of absorption imaging, one normally strives to reduce the incident intensity far enough that $I_0 \ll I_{\mathrm{sat}}$ so that (7.4) reduces to (7.3)[2]. In this case, the *optical density*

$$D_o \equiv -\log(I/I_0) \tag{7.6}$$

is equal to the optical depth d_o up to the factor ξ: $D_o = d_o/\xi$. This is convenient since the optical density is easy to determine: it is sufficient to have one image of the unperturbed beam and one where the beam is absorbed by the sample to calculate it. If saturation is non-negligible, the relation between optical depth and optical density becomes nonlinear and one has to do a precise calibration of ξ in order to be able to calculate d_o from the measured intensities.

Since this derivation relies on the subdivision of a sample of finite thickness into a succession of thin layers, it is not clear whether or not the results will hold for a two-dimensional system where such a subdivision is not possible. It turns out that at least for the case of negligible saturation, one can derive the same equations without making use of a differential argument.

An alternative derivation

Let us consider a surface A (for simplicity, let us imagine it to be a square) with a probe beam of homogeneous intensity I incident on it. On this surface, let there be a single atom with its absorptive cross section σ (as shown in the left panel in figure 7.1). The probability for a given photon to be scattered by the atom is then just σ/A provided $\sigma \ll A$ so that we do not have to worry about the exact position of the atom within the square (otherwise, if the atom was near the border, part of its cross section might be outside the square). That means that every photon has a probability of $1-\sigma/A$ *not* to be absorbed.

Now let us consider the case of N atoms with uncorrelated positions, each coming with its own cross section. The probability for a given photon not to be absorbed by any of these atoms is then $(1-\sigma/A)^N$. This remains true when the cross sections of the atoms overlap since it is nothing but the expectation value of the fraction of the total surface covered by the atoms'

---

[1] The coefficient 7/15 used here and in the following corresponds to a π transition between two levels with $J=2$ and $J'=3$ under the assumption that the populations of the magnetic substates of the ground state are equal.

[2] However, Reinaudi *et al.* have experimentally demonstrated that for optically dense clouds, it may be advantageous to be in the opposite limit where the linear term in (7.4) dominates [166].

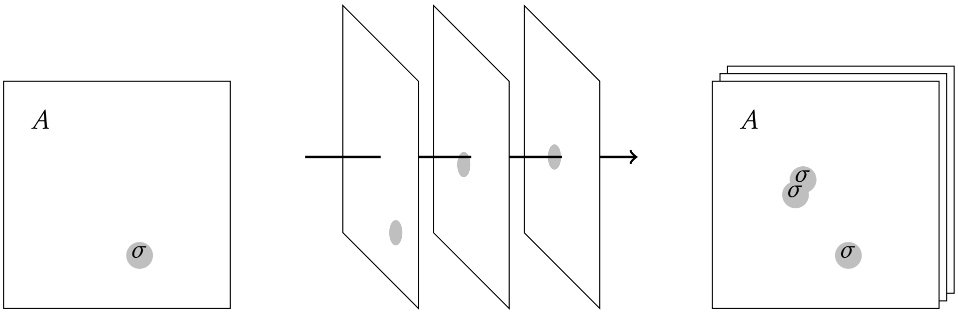

FIGURE 7.1: *Left: the scattering cross section of an individual atom on a surface A covers the fraction σ/A of the total area, so a photon has a probability of $1-\sigma/A$ to pass the square without being absorbed. Center: A sample containing more than one atom can be considered as an ensemble of transparent sheets of area A, each "carrying" an individual atom. A light beam passing through such a succession of layers sees the situation illustrated on the right (for negligible saturation), regardless of whether the atoms are dispersed over a finite volume or concentrated in a plane.*

cross sections. Reexpressing the atom number in terms of the 2d density $n_{2\mathrm{d}}$, the probability for a photon to pass the sample is

$$P(n_{2\mathrm{d}})=\left(1-\frac{\sigma}{A}\right)^{n_{2\mathrm{d}}A}=\left[\left(1-\frac{\sigma}{A}\right)^{A/\sigma}\right]^{\sigma n_{2\mathrm{d}}}\equiv\eta^{-\sigma n_{2\mathrm{d}}}\,. \tag{7.7}$$

We find the same functional form as in equation (7.3) without making use of the extension of the sample along the probe beam. Evidently, the initial intensity multiplied by the probability for an individual photon to pass the sample is nothing but the final intensity. From standard calculus we know that in the limit $\sigma/A\to 0$, we have $1/\eta=(1-\sigma/A)^{A/\sigma}\to 1/e$ so that equation (7.3) is completely reproduced with the column density $\int_{-\infty}^{\infty} n\,\mathrm{d}z$ replaced by the surface density $n_{2\mathrm{d}}$. Note that otherwise the ratio between η and e can be absorbed in a constant factor multiplying the cross section, *i.e.* it would be a constant correction to the detectivity.

At this point one has to ask what meaning to give to our surface A. A sensible choice should satisfy $A\gg\sigma$ so that $\eta\simeq e$ (besides its being our initial assumption to avoid having to account for the exact position of the atoms within the surface) and at the same time be small compared to the typical scale of variation of experimentally observed samples so that one can assume the density to be constant over the surface. A convenient response from an experimentalist's point of view is to choose A as the equivalent size of a pixel on the CCD chip that is used to record the images, "equivalent" meaning that the edge length is divided by the magnification factor of the imaging optics. In our setup this equivalent edge length is 1.46 µm, made up of a physical pixel size of 6.45 µm and a magnification of 4.42. This pixel size has been chosen to be smaller than typical features of atomic samples, so it remains to verify that we have $A\gg\sigma$: the resonant cross section of our ^{87}Rb atoms interacting with linearly polarised light (including the Clebsch-Gordan coefficient) is 0.135 µm^2 (see (7.5)) so that $A/\sigma\simeq 15.8$, leading to $\eta/e\simeq 0.97$.

Thus, we are really in a situation where the conventional Lambert-Beer solution (7.3) holds.

In fact, this alternative derivation makes no assumption about the geometry of the sample along the direction of the probe beam and is thus equally valid for 2d and 3d systems. In order to better understand how this comes about, one may imagine that each atom's cross section is printed on an individual, otherwise transparent sheet, and the whole gas is obtained by making a stack of such sheets (as illustrated in the center and right panels in figure 7.1). For the absorption of the probe beam, it makes no difference whether there is a finite distance between successive sheets (case of a 3d sample) or not (2d sample) as long as one remains in the regime of negligible saturation[3].

In a situation of non-negligible saturation, the two- and three-dimensional cases are no more equivalent: while in the 3d case, each layer of atoms sees an intensity that is reduced by the absorption in the preceding layers, the atoms in a 2d systems are all concentrated in one unique layer so that they all see the incident intensity. Thus, within the validity of our assumptions, we expect equation (7.7) to hold for any incident intensity by plugging in the appropriate expression for $\sigma(I)$.

Summing up, for our experiments on quasi-2d Bose gases we expect to be in a situation where (apart from a constant factor) the shape of the atomic sample is accurately rendered by the optical density. However, for a better understanding of experimental results, it is worthwhile having a closer look on the functional form of the optical density as well as the influence of discretisation by the CCD.

Numerical aspects of the optical density

As we can see from its definition (7.6), the optical density is a nonlinear function of the dimensionless variable $\mathscr{I} \equiv I/I_0$. This makes that the optical density is quite sensitive to fluctuations of the measured signal due to shot noise and may have a tendency to amplify distortions of the intensity distribution caused by imaging aberrations. We therefore judge it worthwhile to put some numbers on this sensitivity. According to standard error propagation, a deviation $\Delta\mathscr{I}$ in the dimensionless intensity will cause a deviation

$$\Delta D_o \equiv \frac{\mathrm{d}D_o}{\mathrm{d}\mathscr{I}} \Delta\mathscr{I} = -\frac{\Delta\mathscr{I}}{\mathscr{I}} = -e^{D_o} \Delta\mathscr{I} \,. \tag{7.9}$$

One sees that with increasing optical density, the sensitivity increases *exponentially*. Let us now see the consequences of shot noise on this quantity. Here, the figure of merit is the *dynamic range* which is nothing but the maximum number of counted photoelectrons and sets the scale

---

[3] To complete this discussion, we show that using the same reasoning one recovers the differential equation (7.2) in the case where the reduction of the intensity as the beam passes through the sample must be taken into account: When going from z to $z + \Delta z$, one passes by $N = n(z)A\Delta z$ particles (or sheets) so that the intensity decreases as

$$I(z + \Delta z) = I(z) \left(1 - \frac{\sigma}{A}\right)^{n(z)A\Delta z} \,. \tag{7.8}$$

In this case, N will be quite small so that one can make the approximation $(1-\sigma/A)^{n(z)A\Delta z} \simeq 1-n(z)\sigma\Delta z$. Plugging this into equation (7.8) yields equation (7.1) (or equation (7.2) in the limit $\Delta z \to 0$), where σ may depend on I.

of the intensity resolution of the CCD. If one uses the complete available range on a 12 bit device (distinguishing 4096 different intensity values), one has $\Delta\mathscr{I} = 0.244 \times 10^{-3}$, the complete dynamic range of an 8 bit device (256 different values) corresponds to $\Delta\mathscr{I} = 3.91 \times 10^{-3}$. While the pixelfly qe camera (PCO company) we used as a CCD is a 12 bit device, we did not use the complete dynamic range in order to prevent saturation of the atoms, but only a range of ~ 320 corresponding to $\Delta\mathscr{I} = 3.13 \times 10^{-3}$. In table 7.1 we show the correspondence between optical density, the number of counted photoelectrons N and the resulting fluctuations. The quantity ΔD_o in this table is calculated as $\Delta D_o = [D_o(\langle N\rangle - \Delta N) - D_o(\langle N\rangle + \Delta N)]/2$.

D_o	$\langle N\rangle$	$\Delta N = \sqrt{\langle N\rangle}$	ΔD_o	$\Delta D_o/D_o$
0	320	17.9	0.06	∞
0.01	317	17.8	0.06	6.0
0.1	290	17.0	0.06	0.6
0.5	194	13.9	0.07	0.14
1	118	10.9	0.09	0.09
2	43.3	6.58	0.15	0.08
3	15.9	3.99	0.26	0.09
4	5.86	2.42	0.44	0.11
5	2.16	1.47	0.95	0.19
6	0.79	0.89	∞	∞

TABLE 7.1: *Uncertainty of the optical density due to the shot noise associated to the number N of counted photoelectrons on the* CCD *for a dynamic range of* 320*. The relative uncertainty is lowest for optical densities between* 1 *and* 4*.*

One finds a noise level of 0.06 which is in good agreement with our absorption images. One sees that it is desirable to avoid optical densities superior to 4 in this configuration. As concerns the maximum values, in our images of 2d Bose gases, the optical density rarely significantly exceeds 3, so we do not expect to run into problems this way.

Of course, the discretisation in the CCD and the associated shot noise is not the only source of deviations of the measured intensity from its ideal value, and the sensitivity stated here concerns all such sources that may occur. In particular, if the optical density is altered due to aberrations of the imaging optics, the effect on the absorption image will be much stronger on optically dense clouds. To put it another way, the nonlinear character of the optical density makes optically dense clouds more sensitive to imaging aberrations than more dilute samples.

7.2 *Imaging with imperfect optics*

Now that we have made some basic considerations about how the optical signal is created by the atoms and interpreted after being measured in a CCD, we turn to the question of how the signal is transmitted from the atoms to the camera, *i.e.* to the working of the imaging optics. In our experiment, we are using an achromatic doublet with a meniscus lens (Melles Griot 01 LAM 225 and 01 LAO 225) with an effective focal length of $f = 107\,\mathrm{mm}$. The distance from the atoms to the triplet is $d = 132\,\text{mm}$, the distance from the triplet to the camera $b = 581\,\text{mm}$, resulting in a magnification of 4.42.

If the triplet was the equivalent of an ideal lens, the electric field distribution in the camera plane would be given by equation (4.15) which we reproduce here for convenience:

$$E(b,\rho') = -\frac{1}{G}E(-d,-\rho'/G)\exp\left(-i\frac{k}{2b}\frac{G+1}{G}\rho'^2\right) ,$$

with $G = b/d$. In this ideal case, the modulus of the image distribution is a scaled version of the modulus of the object distribution, independently of the phase distribution, *i.e.* the field curvature in the object plane.

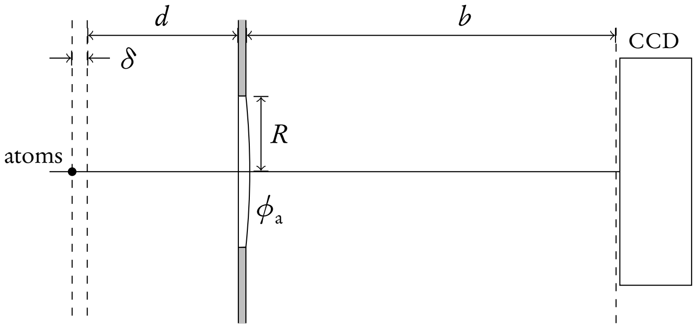

FIGURE 7.2: *A more realistic model for the imaging situation: the distance between the atoms and the lens differs by an amount δ from the ideal d fulfilling the thin lens equation, the lens has a finite radius (outside which the light beam is clipped) and gives rise to aberrations.*

For real imaging, there are three effects that cause deviations from this ideal behaviour (see figure 7.2 for an illustration): (i) the finite size of the lens which will cause the electric field to be clipped at a certain radius R (for our triplet, $R = 19\,\text{mm}$), (ii) imperfections in the focusing, *i.e.* the thin lens equation is only nearly fulfilled and $1/b + 1/d - 1/f \neq 0$, (iii) aberrations of the lens triplet, *i.e.* the phase imprinted on the field distribution arriving at the lens plane is not purely quadratic, $\phi_{\text{lens}} - k\rho^2/2f \neq 0$. In the following sections, we will see how these three effects influence the electric field in the camera plane.

The point transfer function—a Green function approach

From a mathematical point of view, the most transparent approach is certainly to cast the entire imaging process into a single response function to a point source input. At the same time, this permits to get a certain intuition about the behaviour of the system since it is usually not too hard to estimate the consequences of a convolution with a given function.

The equations of paraxial wave optics we recalled in chapter 4 permit to calculate such a function. Using the paraxial propagator (4.11) (again we reproduce this equation for convenience)

$$\mathscr{G}(\boldsymbol{\rho}' - \boldsymbol{\rho}) = \frac{i}{\lambda L} e^{-ikL} e^{-ik(\boldsymbol{\rho}'-\boldsymbol{\rho})^2/2L} \,,$$

we can decompose the process of imaging into three steps: a propagation of the object field from the atoms to the lens (representing the triplet), the phase imprinting and clipping at the lens itself and finally the propagation from the lens to the camera. There is a certain ambiguity on where one wants to include the imperfect focusing (of course, all ways to do it are strictly equivalent). In all that follows, we will take it into account by replacing the object distance d by a distance $d + \delta$. The electric field in the camera plane is then given by

$$\begin{aligned} E(b,\boldsymbol{\rho}) = \frac{i}{\lambda b} \int \mathrm{d}^2\rho' e^{-ik(\boldsymbol{\rho}-\boldsymbol{\rho}')^2/2b} e^{ik\boldsymbol{\rho}'^2/2f} e^{i\phi_\mathrm{a}(\boldsymbol{\rho}'/R)} \theta(R-\rho') \\ \times \frac{i}{\lambda(d+\delta)} \int \mathrm{d}^2\rho'' e^{-ik(\boldsymbol{\rho}'-\boldsymbol{\rho}'')^2/2(d+\delta)} E[-(d+\delta), \boldsymbol{\rho}''] \,. \end{aligned} \quad (7.10)$$

The finite size of the lens is taken into account by the Heaviside function $\theta(R - \rho')$, aberrations are absorbed in the function $\phi_\mathrm{a}(\rho'/R)$. We will discuss the form of this function in greater detail later on, for the moment we just remark that it is real and radially symmetric.

To simplify the expression (7.10), we first note that in practice, the error in the focussing is very small compared to the object distance, *i.e.* $\delta \ll d$ so that $1/(d+\delta) \simeq 1/d - \delta/d^2$. This permits to gather together the exponentials in $\boldsymbol{\rho}'^2$ and to simplify them using the thin lens equation so that only one exponential $\exp(ik\boldsymbol{\rho}'^2\delta/2d^2)$ is left. If we then inverse the order of integration, we may write

$$E(b,\boldsymbol{\rho}) = e^{-ik\boldsymbol{\rho}^2/2b} \int \mathrm{d}''\rho E[-(d+\delta), \boldsymbol{\rho}''] e^{-ik\boldsymbol{\rho}''^2/2(d+\delta)} \mathscr{G}_\mathrm{ptf}(\boldsymbol{\rho}, \boldsymbol{\rho}'') \,, \quad (7.11)$$

with the *point transfer function*

$$\mathscr{G}_\mathrm{ptf}(\boldsymbol{\rho}, \boldsymbol{\rho}'') = \frac{-1}{\lambda^2 b(d+\delta)} \int \mathrm{d}^2\rho' \theta(R-\rho') e^{i[\phi_\mathrm{a}(\rho'/R) + k\boldsymbol{\rho}'^2\delta/2d^2]} e^{ik\boldsymbol{\rho}'\cdot[\boldsymbol{\rho}''/(d+\delta) + \boldsymbol{\rho}/b]} \,. \quad (7.12)$$

The general structure of equation (7.12) is that of a Fourier transform passing from the variable $\boldsymbol{\rho}'$ to the variable $\boldsymbol{\rho}''/(d+\delta) + \boldsymbol{\rho}/b$. We can render the expression somewhat more compact by regarding the equivalent field, *i.e.* the image field rescaled by the magnification $b/(d+\delta)$:

$$\begin{aligned} \tilde{E}(\boldsymbol{\rho}) &\equiv \frac{b}{d+\delta} E\left(b, \frac{b}{d+\delta}\boldsymbol{\rho}\right) \\ &= e^{ik\boldsymbol{\rho}^2/2(d+\delta)} \int \mathrm{d}^2\rho'' e^{ik\boldsymbol{\rho}''^2/2(d+\delta)} E[-(d+\delta), -\boldsymbol{\rho}''] g(\boldsymbol{\rho} - \boldsymbol{\rho}'') \,, \end{aligned} \quad (7.13)$$

where we have made the substitution $\boldsymbol{\rho}'' \mapsto -\boldsymbol{\rho}''$ to obtain a convolution integral, and

$$g(\boldsymbol{\rho} - \boldsymbol{\rho}'') = \frac{b}{d+\delta} \mathscr{G}_\mathrm{ptf}\left(\frac{b}{d+\delta}\boldsymbol{\rho}, -\boldsymbol{\rho}''\right) \,. \quad (7.14)$$

Note that the fact that we can write (7.13) in the form of a convolution is a consequence of our usage of the paraxial approximation. If one considers objects that have a significant distance to the optical axis, one cannot use this approximation any more and the point transfer function will depend on the distance to the optical axis. For our purposes, the paraxial approximation can be expected to hold since our samples are small and approximately (to the precision of our calibrations) centered on the optical axis.

If we now use the radial symmetry of the transformed function in equation (7.12) to evaluate the radial part of the integral, we can give the following expression for g (setting the global phase to $+1$ for aesthetics which does not change anything about the physics):

$$g(\rho) = \frac{2\pi}{\lambda^2(d+\delta)^2}\int_0^R \mathrm{d}\rho'\rho' J_0\left(\frac{k\rho\rho'}{d+\delta}\right)\exp\left[i\left(\phi_\mathrm{a}(\rho'/R) + \frac{k\delta\rho'^2}{2d^2}\right)\right]. \tag{7.15}$$

This expression contains all three imperfections of the imaging optics: diffraction causes the integral to be cut off at R while focusing and aberrations show up in the complex exponential. We see that from a mathematical point of view, imperfect focusing can be regarded as a special type of aberration.

One can use equation (7.15) to estimate the depth of focus of the imaging optics in the following way: if we define it as the distance at which $\exp(ik\delta_\mathrm{df}R^2/2d^2) = -1$ (*i.e.* the contribution on the border of the lens has the inverse sign of the contribution in the centre), we readily find (for $R = 19\,\mathrm{mm}$, $d = 132\,\mathrm{mm}$ and $\lambda = 780\,\mathrm{nm}$) $\delta_\mathrm{df} = \lambda d^2/R^2 = 38\,\mu\mathrm{m}$. Note that the depth of focus is proportional to the inverse square of the lens's f number.

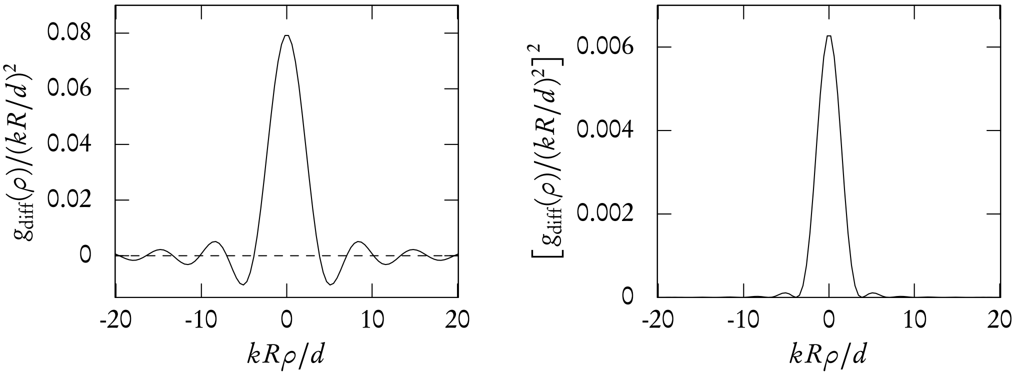

FIGURE 7.3: *Imaging point transfer function (left) and its square (right) in the diffraction-limited case. Naturally, the secondary extrema are considerably more pronounced for the non-squared version, especially the "undercut" following the first zero plays a non-negligible role in the deformation of the imaged distribution. For our parameters,* $(kR/d)^{-1} = 1.16\,\mu\mathrm{m}$.

To get an impression of the type of function we are dealing with, g can be evaluated analytically in the simplified case where both ϕ_a and δ are zero. Physically, this means that there are no aberrations, the focusing is perfect and the only deviation from the ideal case is the diffraction due to the finite lens size. In this limiting case, g reads

$$g_{\mathrm{diff}}(\boldsymbol{\rho}) = \frac{R}{\lambda d \rho} J_1\left(\frac{kR\rho}{d}\right) . \tag{7.16}$$

In the limit $R \to \infty$, g_{diff} becomes a Dirac delta function, as one would expect. In figure 7.3, one can see the behaviour of g (left) as well as its square (right).

One readily verifies that $\int \mathrm{d}^2\rho\, g_{\mathrm{diff}}(\boldsymbol{\rho}) = 1$ so that a constant electric field is unchanged by the imaging process. In fact, even if it is less obvious, the same is true for the general function g: in its expression (7.15), only the Bessel function depends on ρ, all other functions depend on ρ' only. Writing the integral over g as

$$\int \mathrm{d}^2\rho\, g(\boldsymbol{\rho}) = 2\pi \lim_{r\to\infty} \int_0^r \mathrm{d}\rho\, \rho\, g(\rho) , \tag{7.17}$$

and then changing the order of integration, we see that the integral over ρ gives a function of the form (7.16), with R replaced by r. As we said, this becomes a delta function in the limit $r \to \infty$ so that the exponential is evaluated at $\rho' = 0$ and the integral over g is indeed equal to one.

Frequently, when discussing imaging properties, opticians reason in terms of $|g|^2$ which is the point transfer function for a point source input *intensity* rather than a point source input *field*. This is because most basic imaging applications (such as standard microscopy) use incoherent light: the equivalent intensity incident in the detector plane is

$$I(b,\boldsymbol{\rho}) = \frac{\omega}{2\pi}\int_0^{2\pi/\omega} \mathrm{d}t \int \mathrm{d}^2\rho' E(-d,\boldsymbol{\rho}-\boldsymbol{\rho}',t) g(\boldsymbol{\rho}') \int \mathrm{d}^2\rho'' E^*(-d,\boldsymbol{\rho}-\boldsymbol{\rho}'',t) g(\boldsymbol{\rho}'') . \tag{7.18}$$

In the case of incoherent light, one has $\omega/2\pi \int \mathrm{d}t E(\boldsymbol{\rho},t)E^*(\boldsymbol{\rho}',t) = \delta(\boldsymbol{\rho}-\boldsymbol{\rho}')|E(\boldsymbol{\rho})|^2$ and thus

$$I_{\mathrm{incoh}}(b,\boldsymbol{\rho}) = \int \mathrm{d}^2\rho' |E(-d,\boldsymbol{\rho}-\boldsymbol{\rho}')|^2 |g(\boldsymbol{\rho}')|^2 = \int \mathrm{d}^2\rho' I(-d,\boldsymbol{\rho}-\boldsymbol{\rho}') |g(\boldsymbol{\rho}')|^2 . \tag{7.19}$$

In our case, however, we are dealing with *coherent* light where $\omega/2\pi \int \mathrm{d}t E(\boldsymbol{\rho},t)E^*(\boldsymbol{\rho}',t) = E(\boldsymbol{\rho})E^*(\boldsymbol{\rho}')$ and have to stick to the point transfer function for the electric field.

Having to regard the electric field rather than the intensity means that one may expect considerably stronger deformation of the imaging signal: while the modulus square of the response function is strictly positive by definition and secondary maxima are significantly suppressed, neither of these two affirmations is true for the response function itself. Indeed, one clearly sees in figure 7.3 that in the diffraction-limited case, the first zero of g is followed by a marked "undercut". On a qualitative level, this can *amplify* a maximum of the signal whereas a strictly positive response function will always flatten such maxima. If we take into account aberrations (including imperfect focusing) at the same time, the point transfer function will be complex. On a qualitative level, its behaviour will be close to the one of g_{diff} (as opposed to a strictly positive function), but on a quantitative level one has to take concrete examples to see its consequences.

Characterisation of aberrations

In order to evaluate our equations numerically, we must supply an explicit expression for the aberration phase ϕ_a. The general idea is to express it in terms of the difference between the actual and the ideal optical path length ΔL_OP [167], so that $\phi_\mathrm{a} = k\Delta L_\mathrm{OP}$, and to expand it in a power series in $\boldsymbol{\rho}$ and $\boldsymbol{\eta}$ which are the 2d coordinates in the lens and object planes, respectively:

$$\Delta L_\mathrm{OP} = \sum_{\ell,m,n=0}^{\infty} C_{\ell mn} \boldsymbol{\rho}^{2\ell} (\boldsymbol{\rho}\cdot\boldsymbol{\eta})^m \boldsymbol{\eta}^{2n} \,. \tag{7.20}$$

the so-called *Seidel expansion* with the *Seidel coefficients*[4] $C_{\ell mn}$. In our case, we are dealing with very small objects so that $h \ll r$, *i.e.* the distance to the optical axis is small compared to typical distances along the optical axis, and the only coefficients of interest are the coefficients $C_{\ell 00}$. For the simplest possible case of a single spherical lens, there are analytical expressions for these coefficients which rapidly become quite unwieldy with increasing order. We expect our multi-element lenses to perform better than this, but these expressions are a good means to derive an upper bound and to test our numerical means (given by the OSLO software) to obtain the Seidel coefficients for our actual lenses.

For a single spherical lens, the first non-trivial Seidel coefficient C_{200} (C_{100} would be a mere correction to the focal length) characterises the so-called *spherical aberration* and is explicitly given by [167]

$$C_{200} = -\frac{n^3 + (n-1)^2(3n+2)p^2 + 4(n+1)pq + (n+2)q^2}{32 f^3 n (n-1)^2} \,, \tag{7.21}$$

where n is the refractive index of the lens material, f is the focal length on the image side, q is the *shape factor* which characterises the respective curvatures of the two lens surfaces ($q = 0$ for a symmetric lens and $q = \pm 1$ for plano-convex lenses) and $p = 1 - 2f/b$ is the *position factor*. We see that aberrations are determined not only by the physical properties of the lens itself, but also by the geometry of the imaging configuration, *i.e.* by the chosen magnification and the lens's orientation. If we plug in our parameters $f = 107\,\mathrm{mm}$ and $b = 581\,\mathrm{mm}$ (which correspond to $p = 0.632$) and choose a refractive index $n = 1.5$, we obtain

$$C_{200} = \begin{cases} -3.51\lambda\,\mathrm{cm}^{-4} & q = 0 \\ -12.51\lambda\,\mathrm{cm}^{-4} & q = +1 \\ -1.486\lambda\,\mathrm{cm}^{-4} & q = -1 \end{cases} \tag{7.22}$$

using our detection wave length $\lambda = 780\,\mathrm{nm}$. This gives a good example of how much it may deteriorate image quality to use a plano-convex lens in the wrong sense. More importantly, the

---

[4] There is sometimes a certain confusion between these coefficients and the *Zernike* coefficients which are the coefficients corresponding to the expansion on a set of modes which are orthonormal on the unit disk [111, 168]. When higher-order aberrations are negligible, one can calculate the Seidel coefficients from the Zernike coefficients (or vice versa) with some effort, but in general this is not true and it is better to keep in mind that they are conceptually incompatible.

value for $q = -1$ constitutes an upper bound of what we may expect from our imaging triplet (which has been optimised to reduce spherical aberrations). The choice of units is convenient since the radius of our lens is close to 1 cm, so the aberration phase on the border is just $k\lambda = 2\pi$ times the numerical value, *i.e.* the number directly indicates the number of phase "rollovers" from the centre to the border due to spherical aberrations. Note that this interpretation corresponds to a worst case scenario since in actual imaging applications the signal is usually concentrated close to the lens's centre so that the contribution from the lens border is smaller than in these estimations which amount to considering a uniformly illuminated lens.

A similar analysis has been carried out by the Houston group in 1997 [160]. It turns out they were using the same imaging triplet as we do, albeit in a $G = 2.4$ configuration. They obtained $C_{200} = -0.875\lambda_{\mathrm{Li}}\,\mathrm{cm}^{-4}$ (with $\lambda_{\mathrm{Li}} = 671\,\mathrm{nm}$. Using our wavelength, this would read $C_{200} = -1.017\lambda\,\mathrm{cm}^{-4}$) which indeed is better than the most favourable number obtained for a spherical lens. Using the OSLO software, we find that for our magnification C_{200} comes out almost a factor of two lower (the triplet is optimised for infinity, so higher magnifications are bound to reduce aberrations): we find $C_{200} = -0.542\lambda\,\mathrm{cm}^{-4}$ which is the value that we will use in the following.

We will not take into account higher order aberrations here which seems hard to justify—since $kC_{200}R^4$ is not small compared to one, one may well expect the following coefficients to be non-negligible. In fact, this decision is rather a pragmatic one: higher-order coefficients are a lot harder to come by since there is no pre-programmed means in OSLO to calculate them (whereas C_{200} can be obtained directly). However, the Houston group did calculate the coefficient C_{300} and found (for their configuration) $C_{300} = 0.0066\lambda_{\mathrm{Li}}\,\mathrm{cm}^{-6}$ [160]. It seems reasonable that in passing from a magnification of 2.4 to one of 4.4, this coefficient will not increase by more than a factor of order unity, so we expect that breaking off the Seidel expansion at fourth order is not entirely unreasonable.

While there is no general analytic expression for the g in the presence of aberrations, one can calculate $g(0)$ for our special case where aberrations are only considered up to fourth order in ρ since the integral in (7.15) becomes Gaussian when using ρ^2 as the integration variable. The explicit solution is

$$g(0) = \frac{\pi^{3/2}}{2\lambda^2(d+\delta)^2\sqrt{ik|C_{200}|}} \exp\left[i\left(\frac{k\delta}{4d^2\sqrt{k|C_{200}|}} \right)^2 \right] \times \left[\mathrm{erf}\left(\sqrt{i}\frac{k\delta}{4d^2\sqrt{k|C_{200}|}} \right) - \mathrm{erf}\left(\sqrt{i}\frac{k\delta - 4k|C_{200}|d^2R^2}{4d^2\sqrt{k|C_{200}|}} \right) \right] . \quad (7.23)$$

This expression is useful to estimate the position of the best focus: for $\delta \ll d$, the prefactor can be regarded as a constant as a function of δ while the expression in brackets is of the form $g(\delta) = f(\delta + A) - f(\delta)$, with $A = 4C_{200}d^2R^2$ and f is an odd function because the error function is one. Thus, $g(-A/2+\delta) = g(-A/2-\delta)$ and the modulus of $g(0)$ will be symmetric with respect to the point $\delta_{\mathrm{sym}} = -2C_{200}d^2R^2$. Note that the choice $\delta = \delta_{\mathrm{sym}}$ corresponds to the situation where the exponential inside the integral in equation (7.15) is equal to one for $\rho = R$, *i.e.* one would arrive at the same value for δ by using a stationary phase argument to maximise the central amplitude. We stress that this symmetry only applies to $|g(0)|$ and is not true for arbitrary ρ values, as is illustrated in the right panel in figure 7.4. The profiles shown in this plot were obtained by numerically evaluating the integral (7.15) with the Mathematica software.

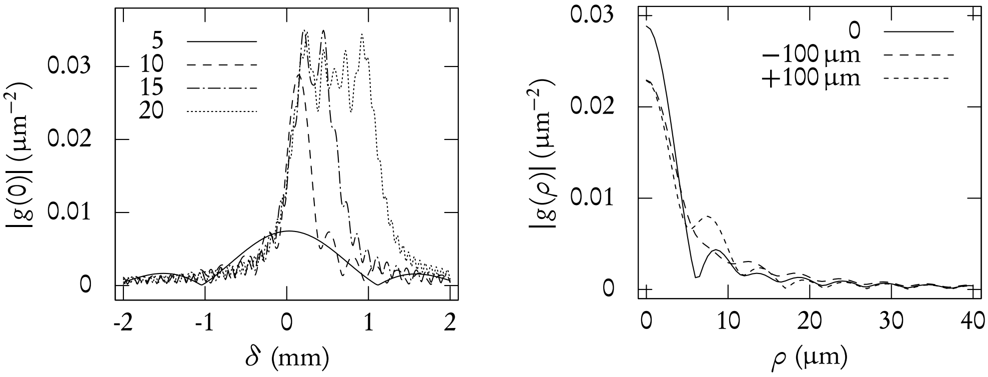

FIGURE 7.4: *Left: modulus of the point transfer function for* $\rho = 0$ *as a function of the sample position* δ *for four different values of the effective radius* R *(in* mm*). The point of symmetry moves to higher* δ *values for higher* R*. The shape of the curve becomes increasingly complex as one passes from the diffraction-dominated to the aberration-dominated regime. Right: numerically calculated point transfer functions* $g(\rho)$ *for our experimental geometry,* $R = 10\,$mm *and three values of the focussing parameter* $\delta - \delta_{\text{sym}}$ *(*0, $-100\,\mu$m *and* $+100\,\mu$m*).*

A graphical representation of $|g(0)|$ for different values of R covering the experimentally relevant range is shown in figure 7.4. Note that R is not necessarily the physical radius of the lens for experimental purposes: if the light coming from the probe and the sample only explores a part of the lens, one may just as well use a point transfer function corresponding to a smaller R. As long as no clipping occurs at the lens, this changes nothing about the physical result. Of course, the point transfer function itself *will* change as a function of R, but the physical result is not the point transfer function, but the result of a convolution with it.

It is important to know the size of the incident light distribution on the lens since we clearly see that it determines the position of the best focus. The reason is the following: the best focus is the position where the two considered aberrations maximally compensate each other over the explored lens area. Since the spherical aberration becomes stronger farther from the lens centre, the best focus becomes progressively more displaced with respect to the position $\delta = 0$ which represents the optimum for a lens without aberrations.

Numerical aspects of imaging convolution

For the numeric evaluation of a convolution integral, the most favorable case (which is often realised in practical applications) is the one where at least one of the two functions rapidly falls to zero so that the integral needs only be evaluated over a restricted domain. In our case, the response function typically falls off as a power law (since $J_n(z) \sim z^{-1/2}$, multiplied by a cosine [116]) while the signal E/E_0 actually converges to *one* instead of zero when one quits the atomic sample. Thus,if one wants to calculate the convolution of the two directly, one must take into account a domain large enough for the response function to give negligible contributions. Even so, this approach is disadvantageous since the weight of the signal is maximum outside the cloud and minimum in its center, *i.e.* just the inverse of the desired behaviour.

For numerical reasons, it is thus preferable to regard the quantity $\mathcal{E} = 1 - E/E_0$ rather than E/E_0 itself. Like this, one can calculate separately the convolutions of the point transfer function with a constant function equal to unity (which is just the integral over the point transfer function and, as we stated above, gives one) and with $\mathcal{E}$ which converges to zero so that the integral will not be dominated by large ρ contributions from the point transfer function. Both contributions can then be summed to give the final result. Note that this only works because the integral over the point transfer function is known analytically which avoids the numerical calculation of this poorly converging integral.

Decomposition on Laguerre-Gauss modes

While the approach using the point transfer function is certainly elegant from a mathematical point of view and very useful to get an intuitive understanding of the imaging process, it is not the most adapted for numerical applications: in order to obtain the response function, one first has to numerically evaluate an integral over a certain part of the lens surface and then numerically convolve the result with the object distribution in order to obtain an "image distribution", *i.e.* one has to successfully carry out two numerical integrations before being able to verify whether the used lens surface was large enough to avoid the introduction of artificial clipping. More importantly, the precision of the two integrals cannot easily be checked separately. It is thus worthwhile to look for an alternative (mathematically equivalent) evaluation scheme that might be more transparent.

In using the point transfer function, we let the object distribution "unchanged" and wrap up all subsequent processes, notably the propagation to the lens and the multiplication with the lens phase and clipping, into the response function. From a physical point of view, it is more transparent to combine the object distribution with the propagation to the lens and then use a transfer function from the lens to the detection plane. This would permit to verify the distribution arriving at the lens before continuing the propagation and thus facilitate the choice of an appropriate cut-off radius[5].

The solution we chose is the following: we expand the electric field in the object plane on a suitable set (characterised by an arbitrarily chosen waist with its width and position) of Laguerre-Gauss functions which permits to calculate semi-analytically the electric field in the lens plane. Having obtained this field, this leaves us with one two-dimensional integral to

---

[5] From a mathematical point of view, one could just work with the whole lens surface and ignore the fact that the light does not explore all of it. For numerical reasons, it is preferable to restrict numerical integrals to the regions that really contribute since the rest will only add artifacts—especially in our case where the lens phase goes as ρ^4, leading to a rapidly oscillating integrand that is difficult to tackle numerically.

evaluate, using explicit input functions which permit to benefit from the spatial localisation of the beam. By “semi-analytical” we mean that the propagation of each Laguerre-Gauss mode is calculated using an exact analytical formula, and the total field is obtained by summing over a finite set of such modes using coefficients obtained by the numerical expansion of the field in the object plane. In this way, there are still two integrals to calculate on the whole (one for the projection on Laguerre-Gauss modes and one for the propagation from the lens to the detection plane), but they are “well separated” and the accuracy of the first one can be easily checked by comparing the sum over the Laguerre-Gauss modes to the initial function.

For the radially symmetric case, the Laguerre-Gauss modes read [113]

$$u_p(\rho, z) = \frac{1}{\sqrt{\pi w(z)^2}} \left[\frac{q_0}{q_0^*} \frac{q(z)^*}{q(z)} \right]^{\frac{2p+1}{2}} L_p\left(\frac{2\rho^2}{w(z)^2} \right) \exp\left[-i \frac{k\rho^2}{2q(z)} \right] , \tag{7.24}$$

where $q(z)$ and $w(z)$ are the beam parameter and width we already used in chapter 4. We recall here their definitions:

$$\frac{1}{q(z)} = \frac{1}{R(z)} - i\frac{2}{kw(z)^2} \quad ; \quad R(z) = z - z_0 + \frac{z_R^2}{z - z_0} \quad ; \quad w(z) = w_0 \left[1 + \left(\frac{z - z_0}{z_R} \right)^2 \right]^{1/2} . \tag{7.25}$$

The gaussian beam (4.17) is recovered in the case $p = 0$ (the factor depending on q and its complex conjugate reproduces the Gouy phase). The propagation phase e^{-ikz} which is common to all modes has been dropped for ease of notation.

Each individual mode propagates independently without changing the shape of the associated intensity distribution except for the scaling with the width $w(z)$. However, the shape of a general beam made up of several modes is not constant since the relative phase between the modes changes with z.

The Laguerre polynomials are orthonormal with respect to an exponential weight function:

$$\int_0^\infty \mathrm{d}x e^{-x} L_m(x) L_n(x) = \delta_{mn} . \tag{7.26}$$

Substituting $x = 2\rho^2/w(z)^2$ we can rewrite this as

$$\frac{2}{w(z)^2} \int_0^\infty \mathrm{d}(\rho^2) \left[L_m\left(\frac{2\rho^2}{w(z)^2} \right) e^{-\rho^2/w(z)^2} \right] \left[L_n\left(\frac{2\rho^2}{w(z)^2} \right) e^{-\rho^2/w(z)^2} \right] = \delta_{mn} . \tag{7.27}$$

Thus, if we want to decompose our electric field in the object plane as

$$E(-d, \rho) = \sum_{n=0}^{\infty} E^{(n)} L_n\left(\frac{2\rho^2}{w(z)^2} \right) e^{-\rho^2/w(z)^2} , \tag{7.28}$$

the mode amplitudes $E^{(n)}$ are given by

$$E^{(n)} = \frac{4}{w(z)^2} \int_0^\infty \mathrm{d}\rho \rho E(-d, \rho) L_n\left(\frac{2\rho^2}{w(z)^2} \right) e^{-\rho^2/w(z)^2} , \tag{7.29}$$

or, written as a two-dimensional integral,

$$E^{(n)} = \frac{2}{\pi w(z)^2} \int \mathrm{d}^2\rho E(-d,\rho) L_n\left(\frac{2\rho^2}{w(z)^2}\right) e^{-\rho^2/w(z)^2} \,. \tag{7.30}$$

It turns out such two-dimensional integrals are numerically better suited for the calculation of the coefficients than one-dimensional ones, especially the center of the distribution is rendered more accurately using two-dimensional integrals.

For the expansion, one has to fix the position and width of the waist. For simplicity, we choose the position of the waist to coincide with the plane of the atomic sample. Like this, each mode has a plane phase profile in the object plane. However, this does not mean that one cannot reproduce an electric field with finite curvature in this configuration: since the coefficients from the Laguerre-Gauss expansion may be complex, the phase of the sum over several modes is not necessarily homogeneous. As concerns the width, we adapt it for a given input profile so that we can reproduce it satisfactorily with a limited number (between 10 and 30) of modes. Since we know the propagation of each mode up to the lens exactly, this means that we know the field distribution in the lens plane to the same precision as that of our initial Laguerre-Gauss expansion.

One can equally take into account the effects of finite detuning at the level of the Laguerre-Gauss expansion by introducing the imaginary part of the cross section σ so that

$$\sigma = \frac{1+2i\Delta/\Gamma}{1+(2\Delta/\Gamma)^2}\sigma_0 \tag{7.31}$$

where σ_0 is the resonant cross section, Γ is the resonance width (not necessarily the natural line width, but the total width including potential broadening) and $\Delta \equiv \omega_\mathrm{L} - \omega$ the difference between the laser and the resonance frequency. The electric field in the object plane will thus have a non-uniform phase and the expansion coefficients $E^{(n)}$ will be complex. Otherwise, the calculation scheme remains unchanged.

More numerical aspects

The Laguerre-Gauss expansion permits to calculate the electric field in the lens plane $E(0,\boldsymbol{\rho})$ to an arbitrary precision. All that remains to do to obtain the equivalent field distribution in the imaging plane is to multiply with the lens and aberration phases (the focusing imperfection is already contained in the incident field) and do the propagation integral. Actually, the numerically most efficient way to do the latter is to use the fact that the propagation integral is a convolution:

$$E(b,\boldsymbol{\rho}) = \left\{ \left[E(0,\boldsymbol{\rho}')\theta(R-\rho')e^{i[\phi_\mathrm{a}(\rho'/R)+k\rho'^2/2f]} \right] * \left[\frac{1}{\lambda b} e^{ik\rho'^2/2b} \right] \right\}(\boldsymbol{\rho}) \,. \tag{7.32}$$

We recall that b is the distance between the lens and the detection plane and f is the focal length.

Now, instead of evaluating the convolution directly, one can make use of the convolution theorem, *i.e.* calculate the Fourier transforms of both brackets, multiply the two and transform back the result. Standard algorithms such as the ones implemented in MATLAB (which we used) succeed in doing this for considerably larger matrices than the ones they are able to convolve directly.

The question of numeric efficiency is of some importance here since it turns out that one has to use quite large matrices to obtain accurate results. The size of the matrix is determined by the physical size of the relevant region (the surface of the lens or a fraction of it if the beam does not explore it in its entirety) and the step size of the grid in the lens plane. Since we are making use of the convolution theorem which implicitly assumes periodic boundary conditions, one has to make sure that no "wrap-around" effects appear (which would show up on the wings of the distribution). We found that for our parameters, we can work with a disk of radius 10 mm (which means amongst other things that diffraction due to the finite lens size is not an issue for our configuration), or rather a square of edge length 20 mm since we want to work with square matrices.

The grid size has to be adjusted to the function with the fastest variation in (7.32). For our parameters, $(2b/k)^{1/2} = 380\,\mu\mathrm{m}$, $(2f/k)^{1/2} = 163\,\mu\mathrm{m}$ and $(kC_{200})^{-1/4} = 7.7\,\mathrm{mm}$. Thus, the step size of the grid used for the numeric calculation should be such that there are of the order of ten points on 163 µm. We choose a step of 10 µm which satisfies this criterion. While this certainly gives a satisfactory resolution in the centre, one finds that it corresponds to a variation of $\sim \pi$ between two successive pixels on the border of the considered surface and would certainly lead to erroneous results if this surface was uniformly illuminated. However, for the objects of interest for us, we verified that the results do not change appreciably when slightly changing the grid spacing.

Taking the grid step and area we find that we need matrices with 2001×2001 elements for our numerical calculations (we prefer to have an uneven number of rows and columns so there is a unique central pixel). Since each matrix element is a complex number made up of two double precision floating point numbers, the memory occupied by such a number is $2 \times 8 \times 2001^2 = 64\,064\,016$ bytes. In itself, this is not a challenge for modern computers, but the entire process uses certain number of such matrices (even more so because MATLAB does not do its Fourier transform "in place". In the script we wrote to this end there are 10 such matrices which are explicitly declared to which one has to add the implicitly appearing ones as well as all the variables that are already in the memory) so that we are actually close to the limits of what can be done with straightforward MATLAB implementation—of course, more sophisticated programming techniques would permit to go well beyond this, but since it turns out we can work like this, our efforts are better spent elsewhere.

7.3 Simulation results

Having put into place our numeric tools, we are now ready to discuss the effects of imaging on realistic atom clouds. The experimental findings presented in chapter 6 suggest two principal questions, which are (i) how much the measured profiles are typically deformed by aberrations and (ii) whether zero detuning corresponds rather to the maximum atom number or the maximum optical density. We will address both question in the following sections. To have meaningful results, we try to follow as closely as possible the corresponding experimental method in both cases.

Best focus

The experimental procedure to find the best focus is the following: we produce a very cold sample (evaporation frequency 2.80 MHz) and observe it after 3 ms of 2d TOF. We then vary the position of the imaging triplet (by typically 100 µm) and observe the evolution of the cloud shape. In order to avoid being led astray by fluctuations of the atom number, our criterion is not the peak optical density, but the appearance of diffraction artifacts on the wings of the profile. We localise the position of the focusing translation stage corresponding to the appearance of these artifacts on both sides and then take the centre between those two as the position of best focus.

We mimic this experimental procedure by starting out with a theoretical profile corresponding to a temperature of 40 nK and an atom number of 20 000 (corresponding to the lowest values in our calibrations shown in figure 6.8). To take into account the time of flight expansion, we scale this profile using equation (6.1) with a time constant of 3 ms. From the density distribution and the temperature, we can calculate the optical depth d_0 which permits to calculate the electric field after the sample. In the following, we will show the quantity $\mathcal{E} = 1 - E/E_0$ for convenience. In calculating the electric field distribution from the optical depth, one has to make a choice about the reduction of the absorptive cross section due to the effects discussed in chapter 6, *i.e.* fix the value of the parameter ξ. Here we decide to regard the most difficult case (so that the results we obtain should correspond to the worst one could expect) by setting $\xi = 1$. Thus, the peak optical density is slightly greater than 4 whereas experimentally measured optical densities hardly exceed 3.

The results are shown in figure 7.5. The first to third panel illustrate the quality of the Laguerre-Gauss expansion. It is important to have a very good approximation where $\mathcal{E}$ is close to one because of the nonlinear dependence of the optical density on the intensity—small deviations in $\mathcal{E}$ easily create large deviations in D_0. The fourth panel shows image distributions for three values of the focus position, one close to the optimum[6], the others on both sides of it at a distance of 250 µm. "Close to the optimum" means that we followed the experimental procedure by localising diffraction artifacts (clearly visible in figure 7.5) and then chose the middle instead of fine-tuning the shape of the profile in direct comparison to the object profile. By following the latter procedure, one can get an even better agreement between the two, but one could not do this experimentally (since one does not have a reference profile handy), so the profile shown in figure 7.5 is closer to experimental reality.

From these results, one may draw the following conclusions:

---

[6] The position of this optimum permits us to verify *a posteriori* that the chosen cutoff radius R was sufficiently large: since $R = 10$ mm, the best focus according to the symmetry argument explained on page 158 would be at 150 µm if the whole surface inside R was explored (see figure 7.4). The found value for the best focus is three times smaller, indicating that not all the "available" surface is explored.

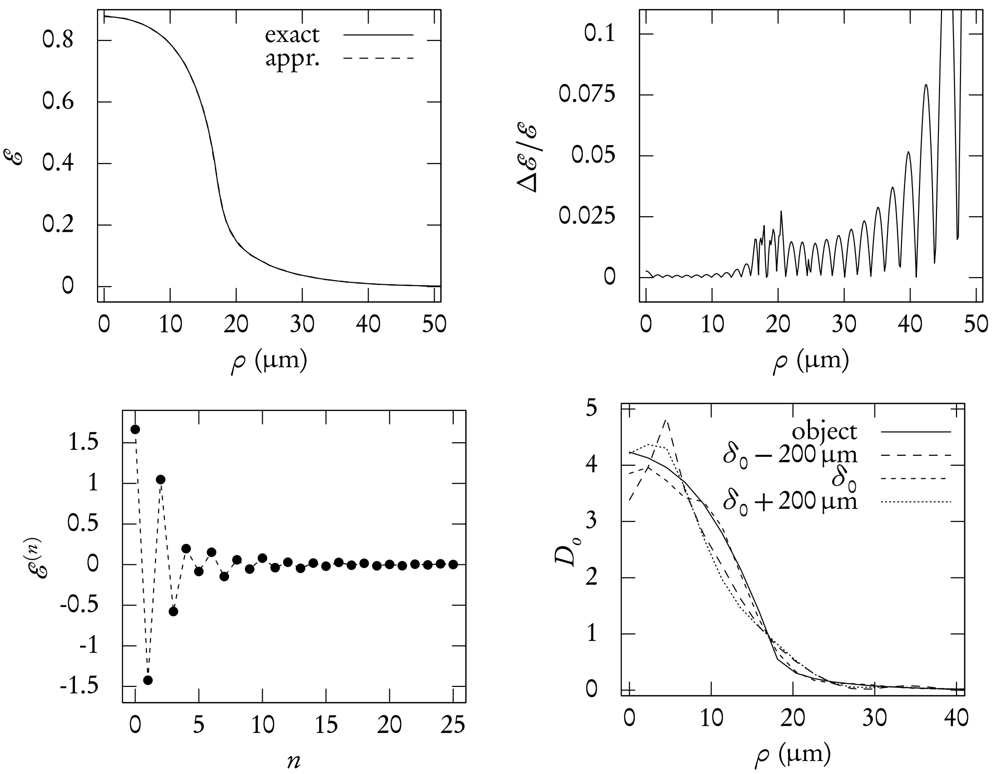

FIGURE 7.5: *Top left: field distribution $\mathcal{E}$ in the object plane for a cloud with $T = 40\,\mathrm{nK}$ and $N = 20000$ together with the approximation by a sum over 25 Laguerre-Gauss modes. The waist used for the Laguerre-Gauss expansion is 7 μm. In the range of appreciable signal, the approximation is accurate to better than 3%. Top right: relative precision of the approximation which is indistinguishable from the original on the top left plot. Lower left: the corresponding expansion coefficients. The dotted line is a guide to the eye. Bottom right: optical depth d_0 in the object plane and scaled image optical densities D_0 for three focusing positions relative to the optimum δ_0 found using the "experimental" procedure. For our case, we found $\delta_0 = 50$ μm.*

- Even for our coldest samples, it is possible following the experimental procedure to find a focus in which the profiles are only slightly deformed in the center (note that when one takes into account the reduction of the absorptive cross section, these deviations will become smaller since they are amplified by the logarithmic dependence of the optical density on the intensity). For higher temperatures (not shown here, but we verified it using the same procedure) the image quality becomes less sensitive to the lens position, as one should expect.

- Deformations first show up in the center of the cloud. For the focus found using the "experimental" procedure, the wings are almost unchanged—one sees some slight deviations in figure 7.5, but they are small and rapidly disappear for higher temperature profiles. This gives some confidence in the validity of our temperature calibrations since those rely solely on the low density part of the cloud.

- Close to the best focus, the central optical density will rather increase than decrease (the fact that the shown profile at $\delta = \delta_0$ lies below the prediction is rather an accident when one regards the evolution of the profile in the vicinity), an effect we already mentioned as a possible consequence of the point transfer function's not being strictly positive. It has also been reported by the Houston group [160].

Thus, within the validity of our simulations, we may conclude that the systematic reduction of the observed optical density in the centre of experimental samples with respect to theoretical predictions at all temperatures is not primarily caused by the imaging optics.

Resonance curves

We now turn to the case of finite detuning of the imaging beam with respect to the atomic resonance. Since, as has been shown in chapter 6, in experimental resonance curves taken on quasi-2d samples the respective maxima of the optical density and atom number do not coincide, the most important question is which one is closer to the actual resonance. At the same time, one can try to determine in which geometry one should expect to see such a big difference between the two as shown in chapter 6, figures 6.19 and 6.20.

Physically, the difference between the two maxima can arise from a "lens effect": at finite detuning, the imaginary part of the absorptive cross section (7.31) makes that the cloud does not only attenuate the incident light beam but will also imprint a phase distribution on it just as a lens. This would change strictly nothing about the image if the resulting field distribution was then imaged using perfect optics—as we stressed earlier in this chapter, a perfect lens will produce a scaled and upside down version of the *modulus* of the electric field. The phase distribution would be modified in this case, but this is of no interest to us since we are only interested in the intensity distribution. Thus, the lens effect only becomes visible when using imperfect imaging optics—it is the result of the interplay between the modification of the curvature of the object field and imaging imperfections since the light will explore different parts of the lens which in turn will change the effect of clipping and aberrations. This means that in order to reproduce this effect, we cannot separate out the effect of the detuning, but have to consider the full imaging system as above.

Here again we mimic the experimental procedure which is the following: we generate a moderately cold cloud (in the middle of the range shown in chapter 6) and regard it either in situ or after a short 2d or 3d TOF. Since this does not change much about the shape of the sample, we consider the case of a 2d TOF of 3 ms in the following as a representative case. We calculate a theoretical profile for a temperature of 80 nK and an atom number of 35 000 (corresponding to the approximate centre of the experimentally explored range as shown in figure 6.8) and scale it as described above. Once again, we do not apply any corrective factor to the cross section ($\xi = 1$) so that the results will be the "worst case" in that any appearing effect will be amplified by the nonlinearity between intensity and optical density. We calculate the electric field distribution using the profile, the temperature and a variable detuning Δ, then expand it on Laguerre-Gauss modes (now, the expansion coefficients are complex numbers). The calculation of the image distributions is done exactly as when we regarded the question of best focus.

Some typical results are shown in figure 7.6. For convenience, atom number and optical density have been scaled by their respective maxima with respect to Δ. The plots show that one can indeed produce the "loops" shown in figure 6.20 with the lens effect. Depending on the sign of δ, the maximum of the optical density[7] is displaced towards positive or negative detunings. The maximum of the atom number, however, proves to be quite stable. Thus, the choice made in our experiments, *i.e.* always taking the maximum of the atom number as reference, seems to be the correct one.

However, the third panel in figure 7.6 clearly shows that nonetheless the loops observed on our data cannot be explained by this phenomenon: to produce loops of the size shown in figure 6.20 one would have to displace the imaging optics from the best focus by of the order of 500 µm—but we have seen (both experimentally and from our simulations in the preceding section) that we already see serious diffraction artifact at less than half this distance so that it is not conceivable that our optics should have been so far out of adjustment (which was verified periodically). We recall that the effect is also absent from a resonance series taken on a three-dimensional sample (see figure 6.21), although the column density was *higher* than the two-dimensional density of the quasi-2d samples so that one would expect the lens effect to be stronger. Thus, we conclude that the loops shown in figure 6.20 cannot be explained by a conventional "lens effect".

In summary, the results shown in this chapter indicate that the effects observed on our quasi-two-dimensional gases are most likely not primarily caused by the imperfections of our imaging optics. Of course, our results are only valid within our basic assumptions, in particular the used form of the aberrations and, just as importantly, the assumption that the probe beam was perpendicular to the optics to a sufficient precision to justify our usage of the paraxial approximation. However, we have reason to believe both assumptions to be sufficiently well

---

[7] Note that this maximum, just as in the experimental case, is not necessarily the central value since the lens effect can cause a "dip" in the centre of the distribution.

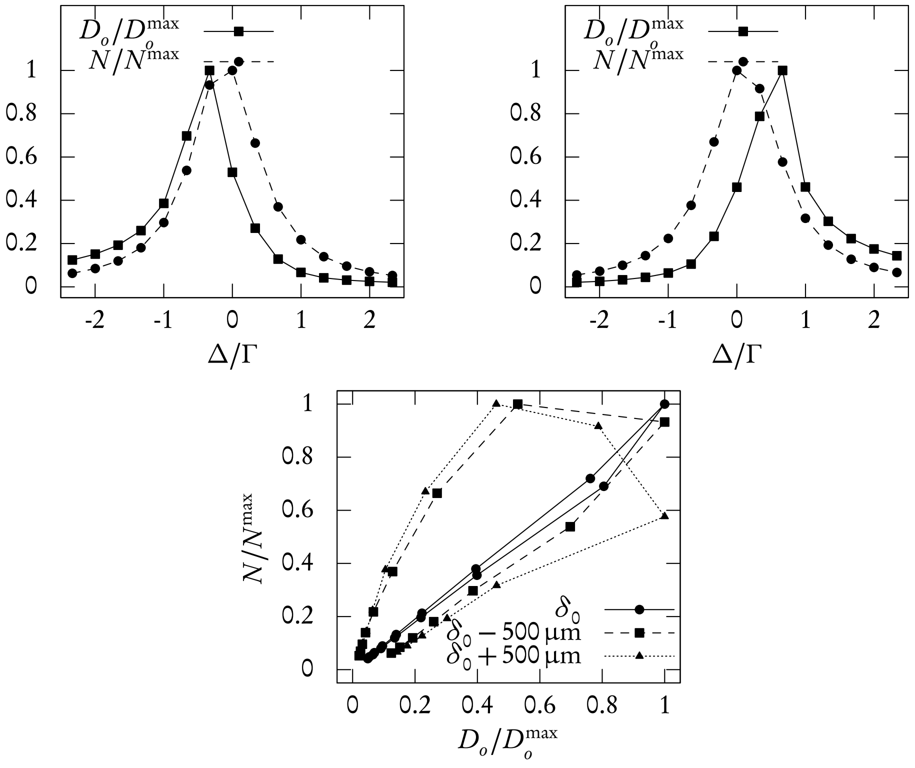

FIGURE 7.6: *Top: resonance curves for* $\delta = \delta_0 - 500\,\mu\text{m}$ *(left) and* $\delta = \delta_0 + 500\,\mu\text{m}$ *(right). We recall that for our parameters,* $\delta_0 = 50\,\mu\text{m}$. *The maximum of* N *remains close to resonance whereas the maximum of the optical density* D_o *is displaced to negative detunings for negative* δ *and to positive ones for positive* δ. *Bottom: atom number as a function of the maximum optical density for three values of* δ. *For values near the best focus, there is almost no discernible loop. In all three plots, the lines are a guide to the eye.*

verified that our conclusions should not be affected in their essence, even more so since we "took a margin" by carrying out our numerical simulations using $\xi = 1$ where imperfections become more visible due the nonlinear relation between optical density and intensity.

As a result, this is not necessarily negative—quite on the contrary, since it indicates that the differences between theory and experiment are in fact due to nontrivial physical processes that have yet to be understood. At the same time, we may have some confidence that our measurements of these effects are mostly unspoilt by the imaging optics: since the cloud is flattened with respect to theoretical predictions, it becomes even less sensitive to imperfections of the imaging optics. In this respect, the results are actually very convenient since they confirm that we may investigate the more interesting physics without having to complicate matters by considering the role of imaging optics.

Chapter Eight

Perspectives

> Ou bien, machiniste autant qu'artificier,
> Sur une sauterelle aux détentes d'acier,
> Me faire, par des feux successifs de salpêtre,
> Lancer dans les prés bleus où les astres vont paître !
>
> EDMOND ROSTAND (1868–1918)
> *Cyrano de Bergerac, Act III, Scene 13*

IT IS customary to end a scientific document such as a thesis with some words about plans for future work and possible continuations of the work described in the document itself. In the present context where the central content (presented in chapter 6) turns out to be still "work in progress", the most proximate continuation is almost evident, all the more so since we explicitly stated where supplementary data would be helpful to provide further insight. Thus, we will not dwell further on this obvious aspect and rather give a brief overview of the experimental projects outside this scope which are planned for the near future.

8.1 Further investigations on 2d Bose gases

Of the multitude of possibilities offered by the method discussed in chapter 4, up to now we have only put to use the phase plate serving to create a single quasi-two-dimensional gas. However, with the plates at our disposition, we are equally able, for instance, to create two such gases at a distance of some micrometres (8 µm for a beam waist of 5 µm. Such a configuration permits to let the two gases thus produced overlap and interfere in ballistic expansion, revealing coherence properties both within each cloud and between the two samples.

Interference experiments to reveal the coherence properties within a single sample have been a powerful technique in the cold atom community ever since the groundbreaking experiments by the MIT group [169] who was the first to demonstrate interference between two (three-dimensional) Bose-Einstein condensates. Polkovnikov, Gritsev, Altman and Demler have shown that in the case of one- and two-dimensional systems, the interference contrast contains profound information about the higher-order coherence properties [170, 171]. In the case of one-dimensional Bose gases, their theory is in excellent agreement with experimental results obtained by the Heidelberg group [83].

Considerably less is known for the two-dimensional case. On the theoretical side, the published results stop with [170], *i.e.* only the expectation value for the contrast itself is known and there is no equivalent for the far more detailed analysis of the one-dimensional case in [171] where explicit expressions for all higher-order modes of the contrast were obtained. On the experimental side, the expectation value of the interference contrast has been used as a means of thermometry [41] and there are some unpublished results aiming at the determination of higher order correlations [172], but they are unsatisfactory in several respects: since the sample was created by slicing up an elongated Bose-Einstein condensate using a one-dimensional optical lattice (the same procedure as described in [41]), there was no precise control over the number of planes in a given realisation (the actual number varied between two and four). At the same time, the elongated geometry might cause the phonon modes to be partly in the one-dimensional regime. Thus, the acquisition of more data using our new setup would permit to address both concerns thanks to the new preparation scheme using a phase plate and a cleaning beam as well as its inherently nearly isotropic geometry in the plane.

Aside from the coherence properties within a single sample at equilibrium (where interference is in effect a heterodyning technique), interference experiments can also be used to probe the coherence between two samples (which manifests itself in the degree of reproducibility of the fringe position). For sufficient spatial separation, the equilibrium state is that of no coherence between the two samples. If the two are produced from a single coherent sample, this means that the initial coherence must decay to the final state, and it turns out the dynamics of this process depends on the dimensionality of the system [173]. In particular, in two dimensions the long-time decay of coherence scales as $t^{-T/8T_{\mathrm{BKT}}}$, where T_{BKT} is the BKT critical temperature, *i.e.* algebraically and not subexponentially as in the one-dimensional case.

The dynamics of this decoherence process between two *one-dimensional* systems has been studied by the Heidelberg group [38]. The predictions of the two-dimensional case, however have yet to be verified. First attempts in this direction carried out in our group showed that the experimental challenge lies in the preparation of an initially coherent sample[1] so that we rather turned to the study of a single two-dimensional gas which is simpler as a physical system (precisely the study described in chapter 6).

A third possible line of study on two-dimensional systems is related to the trapping potential in the plane: instead of carrying out our measurements in a harmonic trap (provided by the magnetic trap), we could make use of the $n = 6$ vortex plate to create a "box potential", thus realising a finite-size homogeneous system. Since in such a system it is "harder" to achieve Bose-Einstein condensation (in an infinite system it would be absent even at vanishing interaction strength) this could shed new light on the relationship between the BKT transition and Bose-Einstein condensation which are hard to separate in a harmonic trap.

---

[1] We did not investigate the reasons for these difficulties in detail at the time, but judging from our experiences with a single two-dimensional sample, it seems probable that a major contribution to the absence of coherence in our measurements was due to the fact that at this time, we did not yet use a cleaning beam so that there may well have been some coherence between the planes, but the signal was drowned by the contribution of the atoms above and below the two quasi-2d planes.

8.2 *Cold atoms in geometric potentials*

Since cold atoms are often considered to be model systems that can be used to simulate effects from solid state physics (see [16] for a review), one subject of constant interest is the creation of gauge potentials that act on our neutral atoms in the same way a magnetic field acts on charged particles. One possibility to create such a gauge potential, as has been briefly mentioned in chapter 2, is to set a slightly anisotropic trap into rotation (see, *e.g.*, [18, 19]). In the corotating frame, one finds an effective Hamiltonian containing a constant gauge field, mimicking a constant magnetic field.

An alternative route to obtaining of the same Hamiltonian is the use of *geometric potentials* [174, 175, 176, 177] where the accumulation of a Berry phase [178] by the atoms on closed trajectories creates an effective vector potential. In particular, there has been a concrete proposal by the Vilnius group [179] for a realisation of such a gauge potential with cold atoms. The apparition of a Lorentz-type force from such effective potentials may seem mysterious, but our group was able to reproduce them using a semi-classical reasoning [180].

While the Vilnius proposal certainly showed the way, it cannot be directly realised using alkali atoms because of the complex level structure of real atoms (the authors of [179] use a Lambda scheme as a simplified model). The essential ingredient of their proposal is that the atoms are transferred in a position-dependent internal state which in their case is a "dark state" in which the atoms do not absorb photons due to the destructive interference of the transition amplitudes to the excited state from the two base states. With real atoms, one has to take into account spontaneous emission which leads to the loss of atoms and thus to a limited lifetime for the atomic sample in the dark state. To circumvent this problem, we have put forward an alternative proposal [181] in which there actually is no dark state and the gauge potential is generated using far-detuned light so that photon scattering becomes considerably less important.

So far there is little experimental work on this topic. The NIST group reported the realisation of a constant gauge vector potential [182]. They have equally reported the observation of non-constant vector potentials and vortices [183]. Beyond this hallmark result, there are a lot of open questions on this subject (like the one whether or not it is easier with this method to reach the lowest Landau level). Our group has already invested major efforts to realise the proposal [181] and my successors will probably start the work on these experiments in the near future.

Closing remarks

> Lascio questa scrittura, non so
> per chi, non so più intorno a che
> cosa: stat rosa pristina nomine,
> nomina nuda tenemus.
>
> UMBERTO ECO (*1932)
> *Il nome della rosa*

SINCE the discussion in chapters 6 and 7 does not converge towards one unique key aspect, but rather resembles an enumeration of observed phenomena and possible explanations which cannot yet be definitely linked to each other, it seems worthwhile to conclude with a short summary.

We have carried out experiments in which quasi-two-dimensional Bose gases were produced and imaged using absorption imaging perpendicularly to the atomic plane. The resulting profiles—once temperature and chemical potential are properly calibrated—can be directly compared to theoretical predictions, and it turns out that there are clear differences between our measurements and theory.

Since there is no reason to distrust the theoretical predictions, we have conducted a more detailed analysis of our data (section 6.4). In parallel, we have modeled our imaging optics to see whether the observed discrepancy could be caused by optical aberrations (chapter 7). The result of this latter investigation being essentially negative, we are quite confident that our observations correspond to actual physical effects taking place in our atomic sample.

In particular, we may quite safely assert a reduction of the detectivity in the centre of our samples. This assertion is supported both by 2d (pp. 132 ff.) and 3d (pp. 135 ff.) TOF measurements. Likewise, there is no ambiguity on the presence of a strong dependence of the observed density profiles on the detuning of the probe beam with respect to the atomic transition (pp. 137 ff.). We have equally clear evidence for a deformation of the sample during longer imaging pulses (pp. 136 ff.).

Taken together, these effects lead us to the hypothesis that we are in fact observing the consequences of a collective interaction of the atoms with the probe light (pp. 143 ff.). It remains unclear, however, how this can be reconciled with the observation that the deviations from theory seem to depend on density and temperature rather than only on the density as one would expect under these assumptions (pp. 129 ff.). But as we already explained, this latter observation should not be attributed too much weight.

Among these results, the evolution of the observed density distribution with increasing 2d TOF duration gives some hope that it might actually be possible to circumvent the deformation of the observed density distribution by allowing for a sufficiently long two-dimensional expansion. Hopefully, there will soon be more data on this particular aspect so that we may see clearer.

Acknowledgements

> Habt Dank für die Zeit,
> Die ich mit euch verplaudert hab
> Und für eure Geduld,
> Wenn es mehr als eine Meinung gab,
> Dafür, daß ihr nie fragt,
> Wann ich komm oder geh,
> Für die stets offene Tür,
> In der ich jetzt steh.
>
> REINHARD MEY (*1942)
> *Gute Nacht, Freunde*

ACCOMPLISHING a PhD thesis is a difficult enterprise, and it is certain that I never would have been able to see the end of it without all the help and moral support I received both inside and outside the laboratory. It is thus not an obligation, but a necessity and a pleasure to address my thanks to all those helpful hands.

First of all, I want to thank Jean Dalibard for letting me join his team when there was little evidence that I was apt for this work, and for his ongoing faith when there was abundant evidence for the contrary. I learnt a lot of passionating physics from him during these three years and I was always impressed by his ability to spontaneously produce precise and pedagogic explanations even for brand new results. In particular, I thank him for having the patience of listening to so many ideas that were only half thought-through. Most of all I was impressed by his unrelenting perseverance when facing difficult moments where I alone would have given up a long time before.

I further address my thanks to the members of the team, that is, my fellow PhD students and the postdocs I had the pleasure to work with during my stay. At the beginning of my thesis, when the experiment was still under construction, I spent most of my time with Baptiste Battelier. I appreciated very much his quiet and unpretentious yet efficient way of doing his work and that he treated me as his equal from the first day on. During that time, I received a lot of advice from Peter Krüger who always took care of the cohesion not only of the experimental apparatus, but also of the team working on it. He left us at the same time as Zoran Hadzibabic with who I rarely had the pleasure of interacting, but when I had, it was always a great experience to see him sparkling with physical ideas. Later on, I worked principally with Marc Cheneau who always impressed me with his discipline and his determination to do everything with a maximum of care and precision. Even when he was gone, his work greatly facilitated mine, since it reduced the number of elements I had to worry about when things were not going as they were supposed to. When I was on the team for a year, we were joined by Tarik Yefsah who quickly turned out to be a natural engineer (apart from being a physicist, of course!). In the same way he transformed the experiment he transformed the atmosphere in the team with his entering jingles, his "castrato arias" and his inexhaustible good humour—however, I still do not believe that Einstein was in reality a Kabyle.... Two years after him, Rémi Désbuquois joined the team. Rather on the quiet side, he nonetheless quickly earned the respect and sympathy of the other group members, even if at first he was grilling laser diodes at about the same velocity. In order for a team composed by such different temperaments to stick together, one always needs one who has the gift of equilibrating them, and we are lucky to have our present postdoc Kenneth Günter to fulfill this delicate task (along with his work on the experiment). I appreciated a lot his excellent sense of humour and his letting me steal his coffee—at least, up until the moment when we agreed to gang up on Rémi.

Outside the team, the contact with PhD students, Postdocs and group leaders from other experiments in the cold atoms group was always enriching. In particular, I am thankful to Fabrice Gerbier for countless hints for experimental practice, to Emmanuel Mimoun for lots of informatics assistance, David Jacob for making jokes that are even worse than mine, Luigi De Sarlo for providing me Italian goods of all kinds, Juliette Simonet for our "PhD anonymous" sessions, Leticia Tarruell and Jason McKeever for teaching me how to inject an optical fibre in an efficient way and Martin Teichmann for all those weird coffee break discussions he broke loose. Special thanks go to Werner Krauth for many enlightening discussions and for putting some of his QMC profiles at our disposal which proved invaluable for direct comparisons between experiment and theory.

My work could not have been carried out without the help of the people working in the laboratory's workshops and offices. In particular, my thanks go to Christophe Bernard, Didier Courtiade, Jean-Michel Issac, Jean-Marc Jusseau, Linda Krikorian, Jack Olejnik, Richard Pescari, Michel Quidu-Tronscoff, Thierry Tardieu and Françoise Tarquis. In contrast, no thanks to the people who were drilling holes all day and demolishing an external staircase right outside my window while I was trying to concentrate on my work...

On a larger scale, I want to address my thanks to the organisations that have financed my work, the French ministry of research, the German Academic Exchange Service (in particular Ursula Bazoune without whose aid my grant would almost surely have been rejected) and the Institut francilien de recherche sur les atomes froids (IFRAF).

While I received a lot of help and support inside the laboratory, I would not have been able to live unscathed through all those times of mysterious technical problems without all those people I could meet outside the laboratory. In the first place, I want to thank my parents and grandparents as well as my sister Corinna for their patience and understanding, and for supporting to see my only twice to three times a year. I further thank my flatmates Christian, Frédéric and Katharina for all the meals, conversations and movies we shared.

I equally thank those people with whom I shared the pleasure of teaching at two summer academies in Germany in 2007 and 2008: Thank you Anke, Annick, Björn, Christian, Christoph, Dietmar, Eva, Henning, Karoline, Katrin, Kerry, Marion, Martin, Mirko, Nadine, Simon, Stefanie, Sven and Till, thanks also to all my pupils who so willingly delved into the unknown depths of physics with me. Having to explain physics to others surely has made some aspects of it a lot clearer to me.

Nothing was more important to "recharge my batteries" than the numerous occasions I had to make music, enjoying both the pleasure of the music itself and the society of so many extraordinary people. I cannot possibly reproduce the names of everyone I shared these moments with, however I have to yield to the need of at least thanking those with whom I shared most of these moments: Adam, Adrien, Alexandra, Anna, Anne-Laure, Anne-Lise, Astrid, Aude, Benjamin, Blaise, Capucine, Claire, Constance, Cyril, David, Etienne, Fabio, Florence, François, Gabrielle, Jean-Christophe, Joëlle, Julien, Julien, Justine, Justine, Kerry, Léopold, Laetitia, Louise, Ludivine, Maéva, Magali, Marie, Marion, Martin, Maximilien, Mireille, Murielle, Pierre, Pierre, Quentin, Sébastien, Simon, Simon, Sophie, Sophie, Stephanie, Sylvain, Sylvine, Théo, Victoire, Vicens, Vincent, Vincent, Virginie, Vsevolod, I thank you.

Finally, I thank those friends who I met outside any common institution and with whom I shared so many glasses of wine and enriching conversations: thank you Anne, Axel, Chiara, Christina, Emmanuel, Eva, Florence, Hanno, Katharina and Nastasja.

Bibliography

[1] M. H. Anderson, J. R. Ensher, M. R. Matthews, C. E. Wieman and E. A. Cornell, *Observation of Bose-Einstein Condensation in a Dilute Atomic Vapor*, Science **269**, 198 (1995).

[2] K. B. Davis, M. O. Mewes, M. R. Andrews, N. J. van Druten, D. S. Durfee, D. M. Kurn and W. Ketterle, *Bose-Einstein Condensation in a Gas of Sodium Atoms*, Phys. Rev. Lett. **75**, 3969 (1995).

[3] F. London, *On the Bose-Einstein Condensation*, Phys. Rev. **54**, 947 (1938).

[4] F. London, *The Lambda-Phenomenon of Liquid Helium and the Bose-Einstein Degeneracy*, Nature **141**, 643 (1938).

[5] V. F. Sears and E. C. Svensson, *Pair Correlations and the Condensate Fraction in Superfluid* ^{4}*He*, Phys. Rev. Lett. **43**, 2009 (1979).

[6] A. Einstein, *Quantentheorie des einatomigen idealen Gases*, Sitz. Ber. Preuss. Akad. Wiss. (Berlin) **22**, 261 (1924).

[7] L. D. Landau and V. L. Ginzburg, *On the theory of superconductivity*, JETP **20**, 1064 (1950).

[8] E. P. Gross, *Structure of a quantized vortex in boson systems*, Il Nuovo Cimento **20**, 454 (1961).

[9] L. P. Pitaevskii, *Vortex lines in an imperfect Bose gas*, Sov. Phys. JETP **13**, 451 (1961).

[10] F. Dalfovo, S. Giorgini, L. P. Pitaevskii and S. Stringari, *Theory of Bose-Einstein condensation in trapped gases*, Rev. Mod. Phys. **71**, 463 (1999).

[11] A. J. Leggett, *Bose-Einstein condensation in the alkali gases: Some fundamental concepts*, Rev. Mod. Phys. **73**, 307 (2001).

[12] C. J. Pethick and H. Smith, *Bose-Einstein Condensation in Dilute Gases* (Cambridge University Press, 2002).

[13] L. P. Pitaevskii and S. Stringari, *Bose-Einstein Condensation* (Clarendon Press, 2003).

[14] B. DeMarco and D. S. Jin, *Onset of Fermi Degeneracy in a Trap Atomic Gas:*, Science **285**, 5434 (1999).

[15] S. Giorgini, L. P. Pitaevskii and S. Stringari, *Theory of ultracold atomic Fermi gases*, Reviews of Modern Physics **80**, 1215 (2008).

[16] I. Bloch, J. Dalibard and W. Zwerger, *Many-body physics with ultracold gases*, Rev. of Mod. Phys. **80**, 885 (2008).

[17] R. P. Feynman, *Simulating Physics with Computers*, Int. J. Th. Phys. **21**, 467 (1982).

[18] V. Bretin, S. Stock, Y. Seurin and J. Dalibard, *Fast Rotation of a Bose-Einstein Condensate*, Phys. Rev. Lett. **92**, 050403 (2004).

[19] V. Schweikhard, I. Coddington, P. Engels, V. P. Mogendorff and E. A. Cornell, *Rapidly Rotating Bose-Einstein Condensates in and near the Lowest Landau Level*, Phys. Rev. Lett. **92**, 040404 (2004).

[20] N. R. Cooper, N. K. Wilkin and J. M. F. Gunn, *Quantum Phases of Vortices in Rotating Bose-Einstein Condensates*, Phys. Rev. Lett. **87**, 120405 (2001).

[21] P. Courteille, R. S. Freeland, D. J. Heinzen, F. A. van Abeelen and B. J. Verhaar, *Observation of a Feshbach Resonance in Cold Atom Scattering*, Phys. Rev. Lett. **81**, 69 (1998).

[22] S. Inouye, M. R. Andrews, J. Stenger, H.-J. Miesner, D. M. Stamper-Kurn and W. Ketterle, *Observation of Feshbach resonances in a Bose-Einstein condensate*, Nature **392**, 151 (1998).

[23] E. Tiesinga, B. J. Verhaar and H. T. C. Stoof, *Threshold and resonance phenomena in ultracold ground-state collisions*, Phys. Rev. A **47**, 4114 (1993).

[24] S. Jochim, M. Bartenstein, A. Altmeyer, G. Hendl, S. Riedl, C. Chin, J. Hecker Denschlag and R. Grimm, *Bose-Einstein Condensation of Molecules*, Science **302**, 2101 (2003).

[25] M. W. Zwierlein, C. A. Stan, C. H. Schunck, S. M. F. Raupach, S. Gupta, Z. Hadzibabic and W. Ketterle, *Observation of Bose-Einstein Condensation of Molecules*, Phys. Rev. Lett. **91**, 250401 (2003).

[26] T. Bourdel, L. Khaykovich, J. Cubizolles, J. Zhang, F. Chevy, M. Teichmann, L. Tarruell, S. J. J. M. F. Kokkelmans and C. Salomon, *Experimental Study of the BEC-BCS Crossover Region in Lithium 6*, Phys. Rev. Lett. **93**, 050401 (2004).

[27] D. Jaksch, C. Bruder, J. I. Cirac, C. W. Gardiner and P. Zoller, *Cold Bosonic Atoms in Optical Lattices*, Phys. Rev. Lett. **81**, 3108 (1998).

[28] M. Greiner, O. Mandel, T. Esslinger, T. Hänsch and I. Bloch, *Quantum phase transition from a superfluid to a Mott isolator in a gas of ultracold atoms*, Nature **415**, 39 (2002).

[29] V. Bagnato, D. E. Pritchard and D. Kleppner, *Bose-Einstein condensation in an external potential*, Phys. Rev. A **35**, 4354 (1987).

[30] A. Görlitz, J. M. Vogels, A. E. Leanhardt, C. Raman, T. L. Gustavson, J. R. Abo-Shaeer, A. P. Chikkatur, S. Gupta, S. Inouye, T. Rosenband and W. Ketterle, *Realization of Bose-Einstein Condensates in Lower Dimensions*, Phys. Rev. Lett. **87**, 130402 (2001).

[31] T. Kinoshita, T. Wenger and D. S. Weiss, *Observation of a One-Dimensinoal Tonks-Girardeau Gas:*, Science **305**, 1125 (2004).

[32] D. Rychtarik, B. Engeser, H.-C. Nägerl and R. Grimm, *Two-Dimensional Bose-Einstein Condensate in an Optical Surface Trap*, Phys. Rev. Lett. **92**, 173003 (2004).

[33] C. Orzel, A. K. Tuchman, M. Fenselau, M. Yasuda and M. A. Kasevich, *Squeezed States in a Bose-Einstein Condensate*, Science **291**, 2386 (2001).

[34] Z. Hadzibabic, S. Stock, B. Battelier, V. Bretin and J. Dalibard, *Interference of an Array of Independent Bose-Einstein Condensates*, Phys. Rev. Lett. **93**, 180403 (2004).

[35] N. L. Smith, W. H. Heathcote, G. Hechenblaikner, E. Nugent and C. J. Foot, *Quasi-2D confinement of a BEC in a combined optical and magnetic potential*, J Phys. B **38**, 223 (2005).

[36] O. Zobay and B. M. Garraway, *Two-Dimensional Atom Trapping in Field-Induced Adiabatic Potentials*, Phys. Rev. Lett. **86**, 1195 (2001).

[37] Y. Colombe, E. Knyazchyan, O. Morizot, B. Mercier, V. Lorent and H. Perrin, *Ultracold atoms confined in rf-induced two-dimensional trapping potentials*, Europhys. Lett. **67**, 593 (2004).

[38] S. Hofferberth, I. Lesanovsky, B. Fischer, T. Schumm and J. Schmiedmayer, *Non-equilibrium coherence dynamics in one-dimensional Bose gases*, Nature **449**, 324 (2007).

[39] M. Köhl, H. Moritz, T. Stöferle, C. Schori and T. Esslinger, *Superfluid to Mott insulator transition in one, two, and three dimensions*, J. Low. Temp. Phys. **138**, 635 (2005).

[40] I. B. Spielman, W. D. Phillips and J. V. Porto, *Mott-Insulator Transition in a Two-Dimensional Atomic Bose Gas*, Physical Review Letters **98**, 080404 (2007).

[41] Z. Hadzibabic, P. Krüger, M. Cheneau, B. Battelier and J. Dalibard, *Berezinskii-Kosterlitz-Thouless crossover in a trapped atomic gas.*, Nature **441**, 1118 (2006).

[42] P. Krüger, Z. Hadzibabic and J. Dalibard, *Critical Point of an Interacting Two-Dimensional Atomic Bose Gas*, Phys. Rev. Lett. **99**, 040402 (2007).

[43] P. Cladé, C. Ryu, A. Ramanathan, K. Helmerson and W. D. Phillips, *Observation of a 2D Bose Gas: From Thermal to Quasicondensate to Superfluid*, Phys. Rev. Lett. **102**, 170401 (2009).

[44] B. Battelier, *Gaz bidimensionnel de bosons ultra-froids – Nouvelle expérience de condensation de Bose-Einstein*, Ph.D. thesis, Université Pierre et Marie Curie (Paris VI) (2007).

[45] M. Cheneau, *Transition BKT et potentiels géométriques dans le gaz de Bose bidimensionnel*, Ph.D. thesis, Université Pierre et Marie Curie (Paris VI) (2009).

[46] L. Boltzmann, *Wissenschaftliche Abhandlungen*, vol. II (J. A. Barth, Leipzig, 1909).

[47] N. Prokof'ev and B. Svistunov, *Two-dimensional weakly interacting Bose gas in the fluctuation region*, Phys. Rev. A **66**, 043608 (2002).

[48] M. Holzmann and W. Krauth, *Kosterlitz-Thouless Transition of the Quasi-Two-Dimensional Trapped Bose Gas*, Phys. Rev. Lett. **100**, 190402 (2008).

[49] M. Greiner, I. Bloch, T. W. Hänsch and T. Esslinger, *Magnetic transport of trapped cold atoms over a large distance*, Phys. Rev. A **63**, 031401 (2001).

[50] E. L. Raab, M. Prentiss, A. Cable, S. Chu and D. E. Pritchard, *Trapping of Neutral Sodium Atoms with Radiation Pressure*, Phys. Rev. Lett. **59**, 2631 (1987).

[51] C. G. Townsend, N. H. Edwards, C. J. Cooper, K. P. Zetie, C. J. Foot, A. M. Steane, P. Szriftgiser, H. Perrin and J. Dalibard, *Phase-space density in the magneto-optical trap*, Phys. Rev. A **52**, 1423 (1995).

[52] P. D. Lett, R. N. Watts, C. I. Westbrook, W. D. Phillips, P. L. Gould and H. J. Metcalf, *Observation of Atoms Laser Cooled below the Doppler Limit*, Phys. Rev. Lett. **61**, 169 (1988).

[53] J. Dalibard and C. Cohen-Tannoudji, *Laser cooling below the Doppler limit by polarization gradients: simple theoretical models*, J. Opt. Soc. Am. B **6**, 2023 (1989).

[54] F. Schreck, *Mixtures of ultracold gases: Fermi sea and Bose-Einstein condensate of Lithium isotopes*, Ph.D. thesis, Université Pierre et Marie Curie (2002).

[55] S. P. Rath, *Towards a new generation BEC experiment* (2006), internship report.

[56] P. Horowitz and W. Hill, *The art of electronics*, 2nd ed. (Cambridge University Press, 1989).

[57] W. Petrich, M. H. Anderson, J. R. Ensher and E. A. Cornell, *Stable, Tightly Confining Magnetic Trap for Evaporative Cooling of Neutral Atoms*, Phys. Rev. Lett. **74**, 3352 (1995).

[58] M.-O. Mewes, M. R. Andrews, N. J. van Druten, D. M. Kurn, D. S. Durfee and W. Ketterle, *Bose-Einstein Condensation in a Tightly Confining dc Magnetic Trap*, Phys. Rev. Lett. **77**, 416 (1996).

[59] M. D. Barrett, J. A. Sauer and M. S. Chapman, *All-Optical Formation of an Atomic Bose-Einstein Condensate*, Phys. Rev. Lett. **87**, 010404 (2001).

[60] D. A. Steck, *Rubidium 87 D Line Data*, available online at `http://steck.us/alkalidata` (2009).

[61] L. D. Landau, *Theory of energy transfer II*, Phys. Z. Sowjetunion **2**, 46 (1932).

[62] C. Zener, *Non-Adiabatic Crossing of Energy Levels*, Proc. R. Soc. London **137**, 696 (1932).

[63] R. Franzosi, B. Zambon and E. Arimondo, *Nonadiabatic effects in the dynamics of atoms confined in a cylindric time-orbiting-potential magnetic trap*, Phys. Rev. A **70**, 053603 (2004).

[64] E. W. Hagley, L. Deng, M. Kozuma, J. Wen, K. Helmerson, S. L. Rolston and W. D. Phillips, *A Well-Collimated Quasi-Continuous Atom Laser*, Science **283**, 1706 (1999).

[65] J. H. Müller, D. Ciampini, O. Morsch, G. Smirne, M. Fazzi, P. Verkerk, F. Fuso and E. Arimondo, *Bose-Einstein condensation of rubidium atoms in a triaxial TOP trap*, J. Phys. B **33**, 4095 (2000).

[66] E. Hodby, G. Hechenblaikner, O. M. Marago, J. Arlt, S. Hopkins and C. J. Foot, *Bose-Einstein condensation in a stiff TOP trap with adjustable geometry*, J. Phys. B **33**, 4087 (2000).

[67] F. G. Major and H. G. Dehmelt, *Exchange-Collision Technique for the rf Spectroscopy of Stored Ions*, Phys. Rev. **170**, 91 (1968).

[68] R. V. E. Lovelace, T. J. Mehanian, T. J. Tommila and D. M. Lee, *Magnetic confinement of a neutral gas*, Nature **318**, 30 (1985).

[69] R. V. E. Lovelace and T. J. Tommila, *Theory of Bose-Einstein condensation of atomic hydrogen in a dynamic trap*, Phys. Rev. A **35**, 3597 (1987).

[70] E. A. Cornell, C. Monroe and C. E. Wieman, *Multiply loaded, ac magnetic trap for neutral atoms*, Phys. Rev. Lett. **67**, 2439 (1991).

[71] S. Gov and S. Shtrikman, *Dynamic stability of the time-averaged orbiting potential trap: Exact classical analysis*, J. App. Phys. **86**, 2250 (1999).

[72] J. H. Müller, O. Morsch, D. Ciampini, M. Anderlini, R. Mannella and E. Arimondo, *Atomic Micromotion and Geometric Forces in a Triaxial Magnetic Trap*, Phys. Rev. Lett. **85**, 4454 (2000).

[73] M. R. Matthews, B. P. Anderson, P. C. Haljan, D. S. Hall, C. E. Wieman and E. A. Cornell, *Vortices in a Bose-Einstein Condensate*, Phys. Rev. Lett. **83**, 2498 (1999).

[74] K. W. Madison, F. Chevy, W. Wohlleben and J. Dalibard, *Vortex Formation in a Stirred Bose-Einstein Condensate*, Phys. Rev. Lett. **84**, 806 (2000).

[75] C. Raman, J. R. Abo-Shaeer, J. M. Vogels, K. Xu and W. Ketterle, *Vortex Nucleation in a Stirred Bose-Einstein Condensate*, Phys. Rev. Lett. **87**, 210402 (2001).

[76] J. Arlt, O. Marago, E. Hodby, S. A. Hopkins, G. Hechenblaikner, S. Webster and C. J. Foot, *Bose-Einstein condensation in a rotating anisotropic TOP trap*, J. Phys. B **32**, 5861 (1999).

[77] E. Hodby, G. Hechenblaikner, S. A. Hopkins, O. M. Maragò and C. J. Foot, *Vortex Nucleation in Bose-Einstein Condensates in an Oblate, Purely Magnetic Potential*, Phys. Rev. Lett. **88**, 010405 (2001).

[78] T.-L. Ho, *Bose-Einstein Condensates with Large Number of Vortices*, Phys. Rev. Lett. **87**, 060403 (2001).

[79] D. Guéry-Odelin, *Spinning up and down a Boltzmann gas*, Phys. Rev. A **62**, 033607 (2000).

[80] N. V. Vitanov and K.-A. Suominen, *Time-dependent control of ultracold atoms in magnetic traps*, Phys. Rev. A **56**, R4377 (1997).

[81] O. Morizot, C. L. G. Alzar, P.-E. Pottie, V. Lorent and H. Perrin, *Trapping and cooling of rf-dressed atoms in a quadrupole magnetic field*, J. Phys. B **40**, 4013 (2007).

[82] T. Schumm, S. Hofferberth, L. M. Andersson, S. Zildermuth, S. Groth, I. Bar-Joseph, J. Schmiedmayer and P. Krüger, *-wave interferometry in a double well on an atom chip*, Nature Physics **1**, 57 (2005).

[83] S. Hofferberth, I. Lesanovsky, T. Schumm, A. Imambekov, V. Gritsev, E. Demler and J. Schmiedmayer, *Probing quantum and thermal noise in an interacting many-body system*, Nature Physics **4**, 489 (2008).

[84] I. Lesanovsky and W. von Klitzing, *Time-Averaged Adiabatic Potentials: Versatile Matter-Wave Guides and Atom Traps*, Phys. Rev. Lett. **99**, 083001 (2007).

[85] S. Hofferberth, B. Fischer, T. Schumm, J. Schmiedmayer and I. Lesanovsky, *Ultracold atoms in radio-frequency dressed potentials beyond the rotating-wave approximation*, Phys. Rev. A **76**, 013401 (2007).

[86] R. K. Easwaran, L. Longchambon, P.-E. Pottie, V. Lorent, H. Perrin and B. M. Garraway, *RF spectroscopy in a resonant RF-dressed trap*, J. Phys. B **43**, 065302 (2010).

[87] F. Chevy, V. Bretin, P. Rosenbusch, K. W. Madison and J. Dalibard, *Transverse Breathing Mode of an Elongated Bose-Einstein Condensate*, Phys. Rev. Lett. **88**, 250402 (2002).

[88] D. Guéry-Odelin, F. Zambelli, J. Dalibard and S. Stringari, *Collective oscillations of a classical gas confined in harmonic traps*, Phys. Rev. A **60**, 4851 (1999).

[89] S. Stringari, *Collective Excitations of a Trapped Bose-Condensed Gas*, Phys. Rev. Lett. **77**, 2360 (1996).

[90] M.-O. Mewes, M. R. Andrews, N. J. van Druten, D. M. Kurn, D. S. Durfee, C. G. Townsend and W. Ketterle, *Collective Excitations of a Bose-Einstein Condensate in a Magnetic Trap*, Phys. Rev. Lett. **77**, 988 (1996).

[91] D. S. Jin, J. R. Ensher, M. R. Matthews, C. E. Wieman and E. A. Cornell, *Collective Excitations of a Bose-Einstein Condensate in a Dilute Gas*, Phys. Rev. Lett. **77**, 420 (1996).

[92] M. Edwards, P. A. Ruprecht, K. Burnett, R. J. Dodd and C. W. Clark, *Collective Excitations of Atomic Bose-Einstein Condensates*, Phys. Rev. Lett. **77**, 1671 (1996).

[93] P. A. Ruprecht, M. Edwards, K. Burnett and C. W. Clark, *Probing the linear and nonlinear excitations of Bose-condensed neutral atoms in a trap*, Phys. Rev. A **54**, 4178 (1996).

[94] D. M. Stamper-Kurn, H.-J. Miesner, S. Inouye, M. R. Andrews and W. Ketterle, *Collisionless and Hydrodynamic Excitations of a Bose-Einstein Condensate*, Phys. Rev. Lett. **81**, 500 (1998).

[95] S. Giorgini, *Collisionless dynamics of dilute Bose gases: Role of quantum and thermal fluctuations*, Phys. Rev. A **61**, 063615 (2000).

[96] Y. Castin and R. Dum, *Bose-Einstein Condensates in Time Dependent Traps*, Phys. Rev. Lett. **77**, 5315 (1996).

[97] C. E. Wieman, D. E. Pritchard and D. J. Wineland, *Atom cooling, trapping, and quantum manipulation*, Rev. Mod. Phys. **71**, S253 (1999).

[98] P. Lemonde, O. Morice, E. Peik, J. Reichel, H. Perrin, W. Hänsel and C. Salomon, *An Opto-electric Trap for Cold Atoms*, Europhys. Lett. **32**, 555 (1995).

[99] P. Krüger, X. Luo, M. W. Klein, K. Brugger, A. Haase, S. Wildermuth, S. Groth, I. Bar-Joseph, R. Folman and J. Schmiedmayer, *Trapping and Manipulating Neutral Atoms with Electrostatic Fields*, Phys. Rev. Lett. **91**, 233201 (2003).

[100] R. J. C. Spreeuw, C. Gerz, L. S. Goldner, W. D. Phillips, S. L. Rolston, C. I. Westbrook, M. W. Reynolds and I. F. Silvera, *Demonstration of neutral atom trapping with microwaves*, Phys. Rev. Lett. **72**, 3162 (1994).

[101] G. A. Turnbull, D. A. Robertson, G. M. Smith, L. Allen and M. J. Padgett, *The generation of free-space Laguerre-Gaussian modes at millimetre-wave frequencies by use of a spiral phaseplate*, Opt. Comm. **127**, 183 (1996).

[102] J. Denschlag, J. E. Simsarian, D. L. Feder, C. W. Clark, L. A. Collins, J. Cubizolles, L. Deng, E. W. Hagley, K. Helmerson, W. P. Reinhardt, S. L. Rolston, B. I. Schneider and W. D. Phillips, *Generating Solitons by Phase Engineering of a Bose-Einstein Condensate*, Science **287**, 97 (2000).

[103] N. R. Heckenberg, R. McDuff, C. P. Smith, H. Rubinsztein-Dunlop and M. J. Wegener, *Laser beams with phase singularities*, Opt. Quant. Elect. **24**, S951 (1992).

[104] M. A. Clifford, J. Arlt, J. Courtial and K. Dholakia, *High-order Laguerre-Gaussian laser modes for studies of cold atoms*, Opt. Comm. **156**, 300 (1998).

[105] E. R. Dufresne and D. G. Grier, *Optical tweezer arrays and optical substrates created with diffractive optics*, Rev. Sci. Inst. **69**, 1974 (1998).

[106] E. R. Dufresne, G. C. Spalding, M. T. Dearing, S. A. Sheets and D. G. Grier, *Computer-generated holographic optical tweezer arrays*, Rev. Sci. Inst. **72**, 1810 (2001).

[107] S. Bergamini, B. Darquié, M. Jones, L. Jacubowiez, A. Browaeys and P. Grangier, *Holographic generation of microtrap arrays for single atoms*, J. Opt. Soc. Am. B **21**, 1889 (2004).

[108] J. P. Gordon and A. Ashkin, *Motion of atoms in a radiation trap*, Phys. Rev. A **21**, 1606 (1980).

[109] F. Bloch and A. Siegert, *Magnetic Resonance for Nonrotating Fields*, Phys. Rev. **57**, 522 (1940).

[110] R. Grimm, W. M and Y. B. Ovchinnikov, *Optical dipole trap for neutral atoms*, in B. Bederson and H. Walther (eds.), *Advances in atomic, molecular, and optical physics*, vol. 42 (Elsevier, 2000).

[111] M. Born and E. Wolf, *Principles of Optics: Electromagnetic Theory of Propagation, Interference and Diffraction of Light*, 7th ed. (Cambridge University Press, 1999).

[112] E. Hecht, *Optics*, 3rd ed. (Addison-Wesley, 1998).

[113] A. E. Siegman, *Lasers* (University Science Books, 1986).

[114] A. E. Siegman, *Defining, measuring, and optimizing laser beam quality*, in A. Bhowmik (ed.), *Proc. SPIE*, vol. 1868, 2–12 (SPIE, 1993).

[115] J. Dalibard, *Lames de phase* (2007), internal document.

[116] M. Abramowitz and I. A. Stegun (eds.), *Handbook of mathematical functions* (National Bureau of Standards, 1972).

[117] E. Karimi, G. Zito, B. Piccirillo, L. Marrucci and E. Santamato, *Hypergeometric-Gaussian modes*, Opt. Lett. **32**, 3053 (2007).

[118] A. Posazhennikova, *Colloquium: Weakly interacting, dilute Bose gases in 2D*, Rev. Mod. Phys. **78**, 1111 (2006).

[119] Z. Hadzibabic and J. Dalibard, *Two-dimensional Bose fluids: An atomic physics perspective*, in R. Kaiser and D. Wiersma (eds.), *Nano optics and atomics: transport of light and matter waves*, vol. CLXXIII (Enrico Fermi summer school, Varenna, 2009).

[120] R. E. Peierls, *Quelques propriétés typiques des corps solides*, Ann. Inst. Henri Poincaré **5**, 177 (1935).

[121] N. D. Mermin and H. Wagner, *Absence of Ferromagnetism or Antiferromagnetism in One- or Two-Dimensional Isotropic Heisenberg Models*, Phys. Rev. Lett. **17**, 1307 (1966).

[122] P. C. Hohenberg, *Existence of Long-Range Order in One and Two Dimensions*, Phys. Rev. **158**, 383 (1967).

[123] V. L. Berezinskii, *Destruction of long-range order in one-dimensional and two-dimension system possessing a continuous symmetry group - ii. Quantum systems*, Sov. Phys. JETP **34**, 610 (1971).

[124] J. M. Kosterlitz and D. J. Thouless, *Ordering, metastability and phase transitions in two-dimensional systems*, J. Phys. C **6**, 1181 (1973).

[125] D. J. Bishop and J. D. Reppy, *Study of the superfluid transition in two-dimensional ^4He films*, Phys. Rev. B **22**, 5171 (1980).

[126] C. Leemann, P. Lerch, G. A. Racine and P. Martinoli, *Vortex Dynamics and Phase Transitions in a Two-Dimensional Array of Josephson Junctions*, Phys. Rev. Lett. **56**, 1291 (1986).

[127] A. I. Safonov, S. A. Vasilyev, I. S. Yasnikov, I. I. Lukashevich and S. Jaakkola, *Observation of Quasicondensate in Two-Dimensional Atomic Hydrogen*, Phys. Rev. Lett. **81**, 4545 (1998).

[128] V. Schweikhard, S. Tung and E. A. Cornell, *Vortex Proliferation in the Berezinskii-Kosterlitz-Thouless Regime on a Two-Dimensional Lattice of Bose-Einstein Condensates*, Phys. Rev. Lett. **99**, 030401 (2007).

[129] M. Holzmann, M. Chevallier and W. Krauth, *Semiclassical theory of the quasi-two-dimensional trapped Bose gas*, Europhys. Lett. **82**, 30001 (2008).

[130] D. S. Petrov, M. Holzmann and G. V. Shlyapnikov, *Bose-Einstein Condensation in Quasi-2D Trapped Gases*, Phys. Rev. Lett. **84**, 2551 (2000).

[131] D. S. Petrov and G. V. Shlyapnikov, *Interatomic collisions in a tightly confined Bose gas*, Phys. Rev. A **64**, 012706 (2001).

[132] N. Prokof'ev, O. Ruebenacker and B. Svistunov, *Critical point of a weakly interacting two-dimensional Bose gas.*, Phys. Rev. Lett. **87**, 270402 (2001).

[133] S. N. Bose, *Planck's Law and Light Quantum Hypothesis*, Z. Phys. **26**, 178 (1924).

[134] O. Penrose and L. Onsager, *Bose-Einstein Condensation and Liquid Helium*, Phys. Rev. **104**, 576 (1956).

[135] S. T. Bramwell and P. C. W. Holdsworth, *Magnetization: A characteristic of the Kosterlitz-Thouless-Berezinskii transition*, Phys. Rev. B **49**, 8811 (1994).

[136] Z. Hadzibabic, P. Krüger, M. Cheneau, S. P. Rath and J. Dalibard, *The trapped two-dimensional Bose gas: from Bose–Einstein condensation to Berezinskii–Kosterlitz–Thouless physics*, New J. Phys. **10**, 04500 (2008).

[137] K. Huang, *Statistical Mechanics*, 2nd ed. (Wiley, 1988).

[138] A. Messiah, *Mécanique Quantique* (Dunod, Paris, 1959, 1964).

[139] J. I. Gillen, W. S. Bakr, A. Peng, P. Unterwaditzer, S. Fölling and M. Greiner, *Two-dimensional quantum gas in a hybrid surface trap*, Phys. Rev. A **80**, 021602 (2009).

[140] D. S. Petrov, G. V. Gangardt and G. V. Shlyapnikov, *Low-dimensional trapped gases*, J. Phys IV France **116**, 3 (2004).

[141] M. Holzmann, *On the mean-field formula of the Kosterlitz-Thouless-Berezinskii transition temperature of a trapped two dimensional Bose gas*, private communication.

[142] M. Holzmann, G. Baym, J.-P. Blaizot and F. Laloë, *Superfluid transition of homogeneous and trapped two-dimensional Bose gases*, PNAS **104**, 1476 (2007).

[143] R. K. Bhaduri, S. M. Reimann, S. Viefers, A. G. Choudhury and M. K. Srivastava, *The effect of interactions on Bose-Einstein condensation in a quasi two-dimensional harmonic trap*, J. Phy. B **33**, 3895 (2000).

[144] R. N. Bisset, D. Baillie and P. B. Blakie, *Analysis of the Holzmann-Chevallier-Krauth theory for the trapped quasi-two-dimensional Bose gas*, Phys. Rev. A **79**, 013602 (2009).

[145] M. Holzmann, M. Chevallier and W. Krauth, *Universal correlations and coherence in quasi-two-dimensional trapped Bose gases*, arXiv 0911.1704 (2009).

[146] A. Y. Cherny and A. A. Shanenko, *Dilute Bose gas in two dimensions: Density expansions and the Gross-Pitaevskii equation*, Phys. Rev. E **64**, 027105 (2001).

[147] L. Pricoupenko, *Variational approach for the two-dimensional trapped Bose-Einstein condensate*, Phys. Rev. A **70**, 013601 (2004).

[148] C. Mora and Y. Castin, *Ground State Energy of the Two-Dimensional Weakly Interacting Bose Gas: First Correction Beyond Bogoliubov Theory*, Phys. Rev. Lett. **102**, 180404 (2009).

[149] S. Pilati, J. Boronat, J. Casulleras and S. Giorgini, *Quantum Monte Carlo simulation of a two-dimensional Bose gas*, Phys. Rev. A **71**, 023605 (2005).

[150] G. E. Astrakharchik, J. Boronat, J. Casulleras, I. L. Kurbakov and Y. E. Lozovik, *Equation of state of a weakly interacting two-dimensional Bose gas studied at zero temperature by means of quantum Monte Carlo methods*, Phys. Rev. A **79**, 051602 (2009).

[151] Q. Zhou and T.-L. Ho, *Universal Thermometry for Quantum Simulation*, arXiv 0908.3015 (2009).

[152] P. J. Price, *Density Fluctuations at Low Temperatures*, Phys. Rev. **94**, 257 (1954).

[153] S. Giorgini, L. P. Pitaevskii and S. Stringari, *Anomalous Fluctuations of the Condensate in Interacting Bose Gases*, Phys. Rev. Lett. **80**, 5040 (1998).

[154] G. E. Astrakharchik, R. Combescot and L. P. Pitaevskii, *Fluctuations of the number of particles within a given volume in cold quantum gases*, Phys. Rev. A **76**, 063616 (2007).

[155] F. Schlögl and E. Schöll, *A Relation Between Cumulants of a Thermodynamic Variable and the State Equation*, Z. Phys. B **51**, 61 (1983).

[156] A. Marte, T. Volz, J. Schuster, S. Dürr, G. Rempe, E. G. M. van Kempen and B. J. Verhaar, *Feshbach Resonances in Rubidium 87: Precision Measurement and Analysis*, Phys. Rev. Lett. **89**, 283202 (2002).

[157] Y. Kagan, E. L. Surkov and G. V. Shlyapnikov, *Evolution of a Bose gas in anisotropic time-dependent traps*, Phys. Rev. A **55**, R18 (1997).

[158] L. P. Pitaevskii and A. Rosch, *Breathing modes and hidden symmetry of trapped atoms in two dimensions*, Phys. Rev. A **55**, R853 (1997).

[159] B. Gao, *Effects of Zeeman degeneracy on the steady-state properties of an atom interacting with a near-resonant laser field: Analytic results*, Phys. Rev. A **48**, 2443 (1993).

[160] C. C. Bradley, C. A. Sackett and R. G. Hulet, *Analysis of in situ images of Bose-Einstein condensates of lithium*, Phys. Rev. A **55**, 3951 (1997).

[161] J. Söding, D. Guéry-Odelin, P. Desbiolles, F. Chevy, H. Inamori and J. Dalibard, *Three-body decay of a rubidium Bose-Einstein condensate*, Appl. Phys. B **69**, 257 (1999).

[162] B. Laburthe Tolra, K. M. O'Hara, J. H. Huckans, W. D. Phillips, S. L. Rolston and J. V. Porto, *Observation of Reduced Three-Body Recombination in a Correlated 1D Degenerate Bose Gas*, Phys. Rev. Lett. **92**, 190401 (2004).

[163] O. Morice, Y. Castin and J. Dalibard, *Refractive index of a dilute Bose gas*, Phys. Rev. A **51**, 3896 (1995).

[164] E. Mandonnet, *Etude théorique d'un gaz de Bose ultra-froid : 1. Diffusion et localisation de la lumière 2. Condensation de Bose-Einstein en dimensionalité réduite*, Ph.D. thesis, Université Pierre et Marie Curie (Paris VI) (2000).

[165] H. D. Politzer, *Bose-stimulated scattering off a cold atom trap*, Phys. Rev. A **55**, 1140 (1997).

[166] G. Reinaudi, T. Lahaye, Z. Wang and D. Guéry-Odelin, *Strong saturation absorption imaging of dense clouds of ultracold atoms.*, Opt. Lett. **32**, 3143 (2007).

[167] V. N. Mahajan, *Optical Imaging and Aberrations*, vol. I, 1st ed. (SPIE, Bellingham, WA, 1998).

[168] R. J. Noll, *Zernike polynomials and atmospheric turbulence*, J. Opt. Soc. Am. **66**, 207 (1976).

[169] M. R. Andrews, C. G. Townsend, H.-J. Miesner, D. S. Durfee, D. M. Kurn and W. Ketterle, *Interference Between Two Bose Condensates*, Science **275**, 637 (1997).

[170] A. Polkovnikov, E. Altman and E. Demler, *Interference between independent fluctuating condensates*, PNAS **103**, 6125 (2006).

[171] V. Gritsev, E. Altman, E. Demler and A. Polkovnikov, *Full quantum distribution of contrast in interference experiments between interacting one-dimensional Bose liquids*, Nature Physics **2**, 705 (2006).

[172] Z. Hadzibabic, P. Krüger and J. Dalibard, *Interference contrasts between two quasi-two-dimensional Bose gases*, unpublished measurements.

[173] A. A. Burkov, M. D. Lukin and E. Demler, *Decoherence Dynamics in Low-Dimensional Cold Atom Interferometers*, Phys. Rev. Lett. **98**, 200404 (2007).

[174] C. A. Mead and D. G. Truhlar, *On the determination of Born–Oppenheimer nuclear motion wave functions including complications due to conical intersections and identical nuclei*, The Journal of Chemical Physics **70**, 2284 (1979).

[175] M. V. Berry, *Geometric Phases in Physics*, chap. The quantum phase, five years after, 7–28 (World Scientific, Singapore, 1989).

[176] J. Moody, A. Shapere and F. Wilczek, *Geometric Phase in Physics*, chap. Adiabatic Effective Lagrangians, 160–183 (World Scientific, Singapore, 1989).

[177] A. Bohm, A. Mostafazadeh, H. Koizumi, Q. Niu and J. Zwanziger, *The Geometric Phase in Quantum Systems* (Springer, Berlin Heidelberg New York, 2003).

[178] M. V. Berry, *Quantal Phase Factors Accompanying Adiabatic Changes*, Proc. R. Soc. Lond. **392**, 45 (1984).

[179] G. Juzeliūnas, J. Ruseckas, P. Öhberg and M. Fleischhauer, *Light-induced effective magnetic fields for ultracold atoms in planar geometries*, Phys. Rev. A **73**, 025602 (2006).

[180] M. Cheneau, S. P. Rath, T. Yefsah, K. J. Günter, G. Juzeliūnas and J. Dalibard, *Geometric potentials in quantum optics: A semi-classical interpretation*, Europhys. Lett. **83**, 60001 (2008).

[181] K. J. Günter, M. Cheneau, T. Yefsah, S. P. Rath and J. Dalibard, *Practical scheme for a light-induced gauge field in an atomic Bose gas*, Phys. Rev. A **79**, 011604 (2009).

[182] Y.-J. Lin, R. L. Compton, A. R. Perry, W. D. Phillips, J. V. Porto and I. B. Spielman, *Bose-Einstein Condensate in a Uniform Light-Induced Vector Potential*, Phys. Rev. Lett. **102**, 130401 (2009).

[183] Y.-J. Lin, R. L. Compton, K. Jiménez-García, J. V. Porto and I. B. Spielman, *Synthetic magnetic fields for utlracold neutral atoms*, Nature **462**, 628 (2009).

Abstract

When an ultracold bosonic gas is strongly confined along one direction of space, the corresponding degrees of freedom are "frozen" and the gas becomes effectively two-dimensional. The production of such quasi-two-dimensional Bose gases with a new experimental setup and subsequent studies of these objects are the principal subject of this thesis manuscript which is divided into two parts. The first part describes the basic experimental apparatus and techniques that permit us to create ultracold Bose gases for various purposes. The particular case of a quasi-two-dimensional Bose gas is discussed in detail in the second part where we describe the production (in which holographic phase plates play an important role) and investigation of this system. The goal of these experiments was the measurement of the quasi-two-dimensional Bose gas's equation of state. It turned out that the otherwise well-established method of absorption imaging gives rise to unexpected effects when applied to quasi-two-dimensional samples. We present a thorough characterisation and elements of possible explanations for these effects.

Keywords Bose-Einstein condensation, low dimension, equation of state, scale invariance, phase plate, aberrations.

Résumé

Lorsqu'un gaz bosonique ultrafroid est fortement confiné selon une direction de l'espace, les degrés de liberté correspondants sont « gelés » et le gaz devient effectivement bidimensionnel. Le sujet principal de ce manuscrit de thèse est la production de ces gaz quasi-bidimensionnels avec un nouveau dispositif expérimental ainsi que leur étude subséquente. Le manuscrit se divise en deux parties dont la première est consacrée à la description du dispositif expérimental et des techniques qui nous permettent la production des gaz de Bose ultrafroids. Le cas particulier de la production (pour laquelle on se sert d'une lame de phase holographique) et l'étude des gaz de Bose quasi-bidimensionnels est discuté en détail dans la deuxième partie. Le but original des expériences décrites ici était de mesurer l'équation d'état du gaz de Bose quasi-bidimensionnel. Il s'est avéré que la méthode de l'imagerie par absorption, appliquée sur un tel gaz, donne naissance à des effets inattendus. Nous donnons une caractérisation détaillée ainsi que des éléments d'explication possibles de ces effets.

Mots-clé Condensation de Bose-Einstein, basse dimension, équation d'état, invariance d'échelle, lame de phase, aberrations.